Airbursts and Cratering Impacts

2025 | Volume 3 | Pages: 1–87 | e-location ID: e20250003
DOI: 10.14293/ACI.2025.0003

Research Article

A Tunguska Sized Airburst Destroyed Tall el-Hammam a Middle Bronze Age City in the Jordan Valley Near the Dead Sea (Expanded)

Malcolm A. LeCompte[1], Steven Collins[2], Phillip J. Silvia[3], Gunther Kletetschka[4,5], Timothy Witwer[6], Robert E. Hermes[7], Christopher R. Moore[8,9], Wendy S. Wolbach[10], George A. Howard[11], A. Victor Adedeji[12], Charles Mooney[13], James P. Kennett[14], Allen West[6,*] and Ted E. Bunch[15]

[1]Center of Excellence in Remote Sensing Education and Research, Elizabeth City State University, Elizabeth City, NC, 27909, USA; [2]School of Archaeology, Veritas International University, Albuquerque, NM, 87109, USA; [3]College of Archaeology, Trinity Southwest University, Albuquerque, NM, 87109, USA; [4]Geophysical Institute, University of Alaska Fairbanks, 903 Koyukuk Drive, Fairbanks, AK, 99775, USA; [5]Faculty of Science, Charles University, Albertov 6, Prague, 12843, Czech Republic; [6]Comet Research Group, Prescott, AZ, 86301, USA; [7]Los Alamos National Laboratory (retired), Los Alamos, NM, 87545, USA; [8]South Carolina Institute of Archaeology and Anthropology, University of South Carolina, Columbia, SC, 29208, USA; [9]SCDNR Heritage Trust Program, Land, Water, and Conservation Division, South Carolina Department of Natural Resources, Columbia, SC, 27909, USA; [10]Department of Chemistry and Biochemistry, DePaul University, Chicago, IL, 60614, USA; [11]Cosmic Summit, Raleigh, NC, 27604, USA; [12]Department of Natural Sciences, Elizabeth City State University, Elizabeth City, NC, 27909, USA; [13]Analytical Instrumentation Facility, North Carolina State University, Raleigh, NC, 27695, USA; [14]Department of Earth Science and Marine Science Institute, University of California, Santa Barbara, CA, 93106, USA; [15]Northern Arizona University (deceased), Flagstaff, AZ, USA

*Correspondence to: Allen West, E-mail: CometResearchGroup@gmail.com

Received: 24 April 2025; Revised: 24 April 2025; Accepted: 4 May 2025; Published online: 24 May 2025

How to cite: LeCompte M.A., et al. A Tunguska Sized Airburst Destroyed Tall el-Hammam a Middle Bronze Age City in the Jordan Valley Near the Dead Sea (Expanded). *Airbursts and Cratering Impacts*. 2025 | Volume 3 | Issue 1 | Pages: 1–87 | DOI: 10.14293/ACI.2025.0003

ABSTRACT

We present evidence that Tall el-Hammam, a fortified Middle Bronze Age city in the Jordan Valley, was destroyed by an extraordinary high-energy event in approximately 1650 BCE. Excavations reveal that more than 12 m of a palace complex and a massive mudbrick rampart were leveled, and widespread fatalities occurred, with all skeletal remains displaying significant disarticulation. The entire city is capped by a ~1.5 m-thick charcoal-and-ash-rich destruction layer containing shock-metamorphic and high-temperature materials. This stratum yields abundant shocked quartz, vesicular melted pottery and mudbrick, diamond-like carbon, soot, Fe- and Si-rich microspherules, and $CaCO_3$ spherules derived from melted plaster. SEM/TEM imaging with EDS and electron backscatter diffraction (EBSD) identified planar deformation features and high-pressure mineral phases diagnostic of shock metamorphism. Metallic micro-droplets of platinum, iridium, nickel, gold, silver, zircon, chromite, and quartz imply transient exposure to temperatures exceeding 2000°C.

Scattered debris fields (potsherds, charred grain, charcoal, and bone fragments) exhibit a coherent southwest-to-northeast dispersal pattern consistent with a directed supersonic shock wave. Anomalously high salt concentrations

(~4 wt%) in the destruction layer provide evidence for the vaporization of Dead Sea brines or sedimentary salts, producing hypersaline soils that appear to have inhibited agriculture. This environmental breakdown coincides with an enigmatic ~300–600-year regional abandonment of Tall el-Hammam and surrounding settlements in the lower Jordan River Valley. Some researchers suggest that an oral tradition of this catastrophe may have been preserved in the biblical narrative of the destruction of Sodom.

The observed suite of shock, melt, and geochemical signatures cannot be explained by natural disasters, fires, earthquakes, lightning, anthropogenic activity, or warfare. We therefore propose a cosmic airburst by a comet or asteroid of "super-Tunguska" magnitude—several times larger than the 1908 Tunguska event. To test this hypothesis, we conducted hydrocode simulations of a Type-II "touchdown" airburst (an airburst whose fireball reaches Earth's surface), reproducing a high-velocity, high-temperature jet impacting the surface and generating meltglass, microspherules, and multi-GPa shock metamorphism. The modeled results match the evidence observed at Tall el-Hammam.

Collectively, the geological, geochemical, geophysical, and archaeological evidence converges on a super-Tunguska-scale airburst as the most likely mechanism for the city's destruction. Although such events are rare (estimated global recurrence interval of 200 to 1000 years), their capacity to devastate entire urban areas highlights the need for modern recognition and mitigation of the hazards posed by high-energy cosmic airbursts.

KEYWORDS

airburst, archaeology, asteroid, hydrocode modeling, meltglass, shocked quartz, planar deformation features, spherules, tall el-Hammam, tunguska

Editor's Note: This revised article, initially published by Bunch et al. (2021) [1] in *Scientific Reports*, now includes updated and expanded findings. Carl Sagan famously stated the often-quoted and often-misused phrase, "*extraordinary claims require extraordinary evidence.*" To clarify, he warned, "*The worst aspect is that some scientists attempt to suppress* [new] *ideas. The suppression of uncomfortable ideas may be common in religion and politics, but it is not the path to knowledge and has no place in the endeavor of science.*" Ignoring Sagan's warning, a small but vocal group of scientists has actively sought to stifle discussion on the Tall el-Hammam airburst. Such actions undermine the principles of scientific inquiry. In response, the authors updated, expanded, and republished the original article on Tall el-Hammam in this journal *Airbursts and Cratering Impacts*. This new article incorporates novel data on the SW-to-NE directionality of the blast wave, shocked quartz at both Tall el-Hammam and Tunguska, and a hydrocode model of the proposed impact event. This publication represents the merging of three previous publications relevant to Tall el-Hammam, with overlapping co-authorship. Therefore, the co-authors of Bunch et al. [1], Silvia et al. [2], Kletetschka et al. [3], and this contribution are collectively referred to here as "we."

Introduction

Since 2005, archaeological excavations at Tall el-Hammam ("TeH"), an ancient walled city in the southern Jordan Valley northeast of the Dead Sea (Figure 1), have revealed compelling evidence of catastrophic destruction approximately 3600 years ago. This study investigates potential causes of the city's terminal destruction through archaeological, geological, geophysical, and geochemical analysis.

Geographical setting

TeH is situated within the Middle Ghor, the southernmost extension of the Jordan Valley, between Lake Tiberias (~200 meters below sea level, mbsl) and the Dead Sea (~415 mbsl) (Figure 1). The region features a relatively flat plain known as the "Kikkar of the Jordan" (hakikkar hayarden) in Hebrew [5, 6].

The city is built atop a raised, two-tiered occupational mound, the largest in the southern Jordan Valley. Such ancient mounds are referred to as "tel" in Hebrew and "tell" or "tall" in Arabic. TeH preserves stratified remains of a fortified urban center and is recognized as the largest continuously occupied Bronze Age city in the southern Levant [5]. The city-state thrived for nearly 3000 years, from the Chalcolithic Period (~4700 BCE) through the Bronze Age, until its destruction around 1650 BCE (3600 cal BP). This study focuses on the Middle Bronze Age II (MB II) period (~1800–1550 BCE). See **SI Text S1** [7] for archaeological periods and chronological frameworks. All Supporting Information (SI) data are at https://zenodo.org/records/15336569. Dates are reported as BCE or calibrated years before 1950 (cal BP).

Excavations, conducted under the School of Archaeology, Veritas International University, and Trinity Southwest University, in cooperation with the Department of Antiquities of the Hashemite Kingdom of Jordan, involved a large international team [6, 8–12]. Beginning in 2005, the team spent

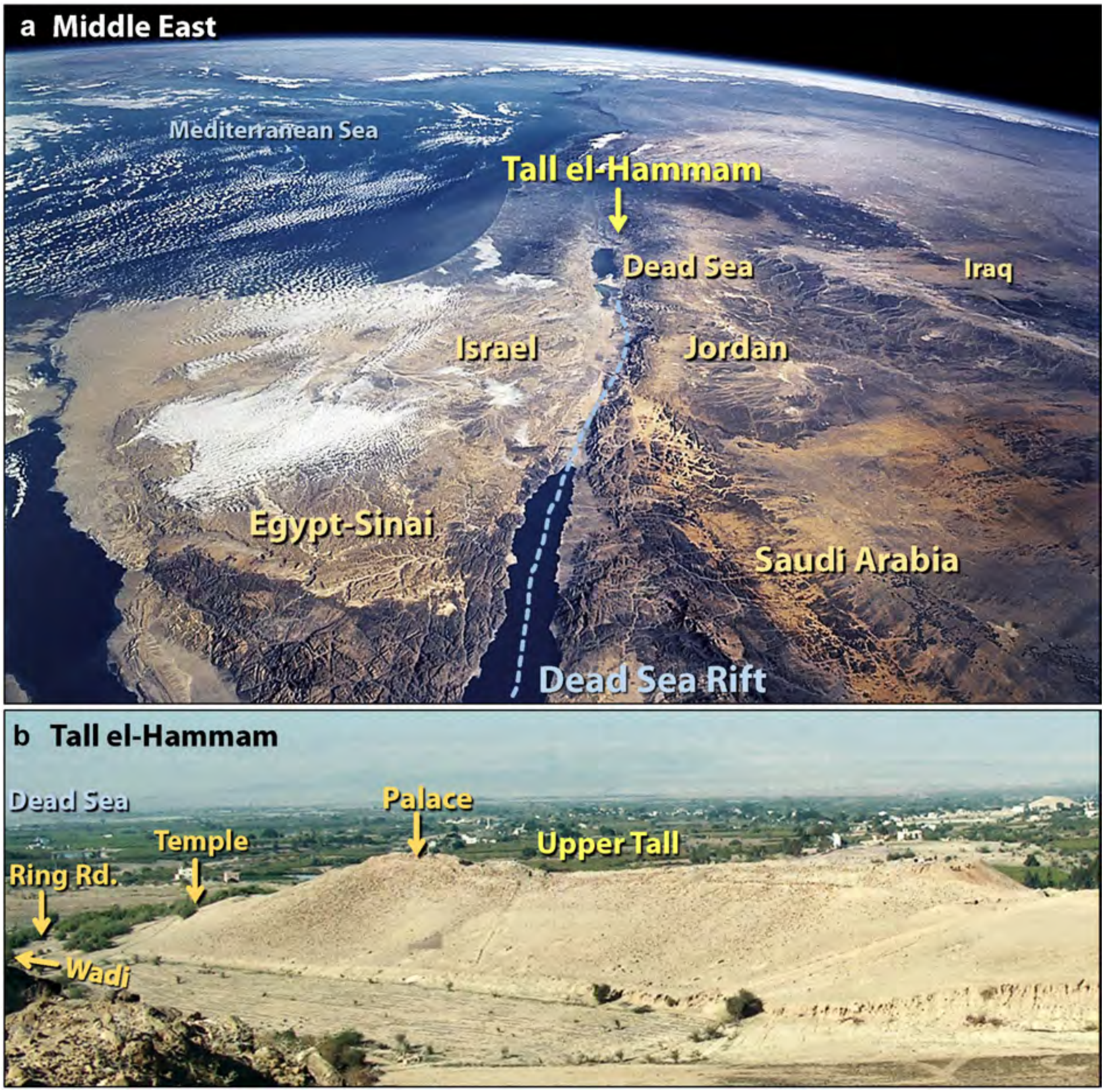

Figure 1: **Location of Tall el-Hammam. (a)** Oblique photograph of the southern Levant, facing north, showing the Dead Sea, the location of TeH, and nearby countries. The Dead Sea Rift, a major tectonic plate boundary, passes through the region. Source of base image: NASA, Space Shuttle. "The Sinai Peninsula and the Dead Sea Rift." Photo: sts109-708-024, taken 12/16/2009. (nasa.gov/topics/earth/features/astronauts_eyes/sts109-708-024.html). **(b)** West-southwest-facing view of the upper tall at TeH, showing the locations of the palace and temple. The Dead Sea is visible to the left. Photo by Dev777, Wikipedia [4].

16 seasons in the field, spanning 18 years, for a total time of 2.5 years on-site. The Tall el-Hammam Excavation Project was one of the most extensive excavations of a Bronze Age city in the history of South Levantine archaeology.

Architectural destruction evidence

The upper tall was heavily fortified with ~4-meter-thick stone foundations supporting freestanding mudbrick ramparts, monumental gateways, and multi-story structures, including a palace complex (Figure 2a). Today, almost no MB II mudbrick superstructures remain above foundation level, except for a dozen or so mudbrick courses preserved on the northeast side of the 33-meter-high mound. Surviving walls are uniformly sheared off near the stone foundation tops. The massive palace walls, originally 1.0–2.2 meters thick, likely rose ~11–15 meters in height.

The defensive system included a mudbrick rampart ~30-meter-thick at the base and a ~7–8-meter-wide crest accommodating military patrols. A 4-meter-thick defensive wall with towers surmounted the rampart, rising more than 33 meters above the lower city. A 2.2-meter-thick wall further separated the palace platform from the surrounding upper city.

Figure 2: Catastrophic leveling of the palace at TeH. (a) Artistic reconstruction of the 4–5-story palace (~52 meters × ~27 meters) before destruction. **(b)** Reconstruction of the excavation area. "MB II" marks the top of the 1650-BCE rubble layer. Most of the 4-story structure is missing, with only partial wall bases surviving. Debris from between sheared walls was cleared during excavation. Millions of mudbricks from the upper palace and adjacent buildings appear lost.

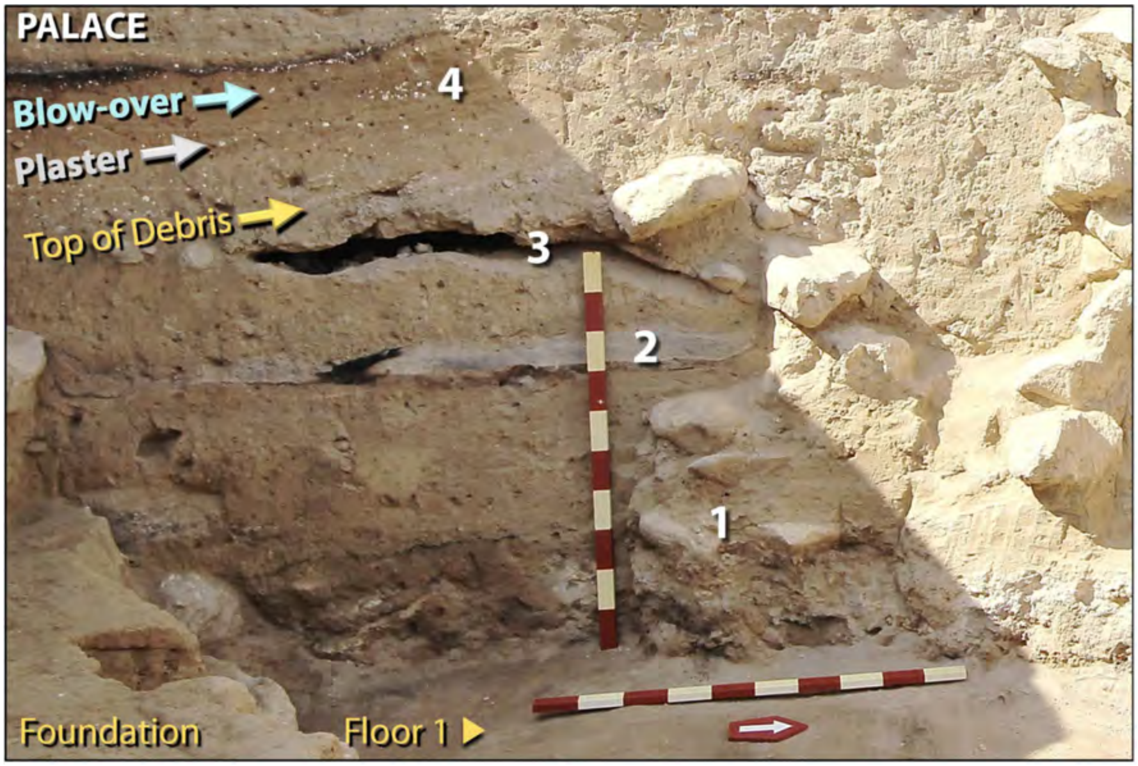

Figure 3: Destruction of the multi-storied palace. Photograph of the four-story palace ruins. Floor. #1: broken mudbricks and debris from upper stories; #2: a burned layer; #3: a void left by burned textiles (fibrous ash and carbon); Blue area marks the blow-over layer of windblown laminated deposits sealing the site for ~3600 years; #4 – fragments of white limestone plaster ($CaCO_3$) mixed with carbonate spherules from walls and ceilings. Scale bars have 10-cm divisions.

The palace complex itself, measuring ~52 meters × ~27 meters (Figure 2a), likely reached 4–5 stories tall, extending 11–15 meters above the rampart crest. Excavations reveal that most first-floor walls and all upper stories are missing. Instead of collapsed debris, small, fragmented mudbricks are randomly embedded in a ~1.5-meter-thick churned destruction layer (Figures 2b and 3; **SI Figure S1** [7]). This observation suggests that the mudbricks were pulverized and ejected under massive force, primarily moving to the northeast.

On the lower tall, similar damage is observed. MB II domestic structures, particularly in the south, southwest, and west sectors, show even more severe damage, with virtually no mudbricks remaining atop massive stone foundations. Large stones and pillar bases exhibit signs of high-temperature fracturing. Although isolated mudbrick courses survive on external towers near the monumental gateway, they do not rise much above the foundation level.

The MB II destruction matrix on the lower tall is exposed mainly at the surface, similar to the upper tall, with little evidence of erosional detritus. Salt-laden ash dominates the overlying shallow soils. Following the terminal destruction, over 98% of the lower tall was never reoccupied during the ensuing 3600 years [8].

Mudbrick survival is somewhat better in the northeastern sector of the lower tall, behind the shelter of the upper-city ramparts. This asymmetry suggests that the destructive force was more intense across the southwest-facing sectors. Across the site, MB II walls (ranging from 0.5 to >2 meters thick) are consistently sheared off at ~1.5 meters—the approximate midpoint of their first stories.

The few remaining mudbrick fragments are generally pulverized and occasionally display thermal reddening. Critically, the MB II destruction layer shows no evidence of erosion by wind or water, implying that the missing millions of mudbricks were violently removed during a catastrophic event (Figure 2b). For more geological and human history of the site, see below **Appendix A1, Geological Context and Appendix A2, Human occupation of the Jordan Valley**.

Study objectives

The primary objective of this contribution is determining the processes involved in the high-temperature/high-pressure, catastrophic destruction of Tall el-Hammam (hereafter “TeH”), a prosperous, powerful MB-II urban center. Early archaeological excavations at TeH revealed the presence of unusual materials, including melted mudbrick fragments, melted roofing clay, melted pottery, ash, charcoal, charred seeds, and burned textiles, all intermixed with fragmented and pulverized mudbrick. After eleven seasons of excavations, the site excavators independently concluded that the evidence pointed to a possible cosmic impact. They contacted our outside group of experts from multiple impact-related and other disciplines to investigate the potential formation mechanisms for the unusual suite of high-temperature evidence, which required explanation.

Potential written record of the Tall el-Hammam destruction

There is an ongoing debate about whether TeH could be the biblical city of Sodom (Silvia [6] and references therein), but this issue is beyond the scope of this investigation. Questions about the age and location of Sodom are addressed in detail elsewhere [5, 8–23] and are not directly related to the fundamental question about what processes produced the high-temperature melted materials at TeH. Silvia [6], Bunch et al. [1], and Silvia et al. [2] proposed that the destruction of this ancient urban city by a cosmic object resulted in an oral tradition that is the source of the written version of Sodom in Genesis. Thus, we consider whether the details recounted in Genesis are a reasonable match for the known details of a cosmic impact event and, therefore, may represent an ancient eyewitness account of a cosmic airburst.

Results and interpretations

Contents. To assist in understanding the complex, multidisciplinary data presented in this study, we provide the following section list:

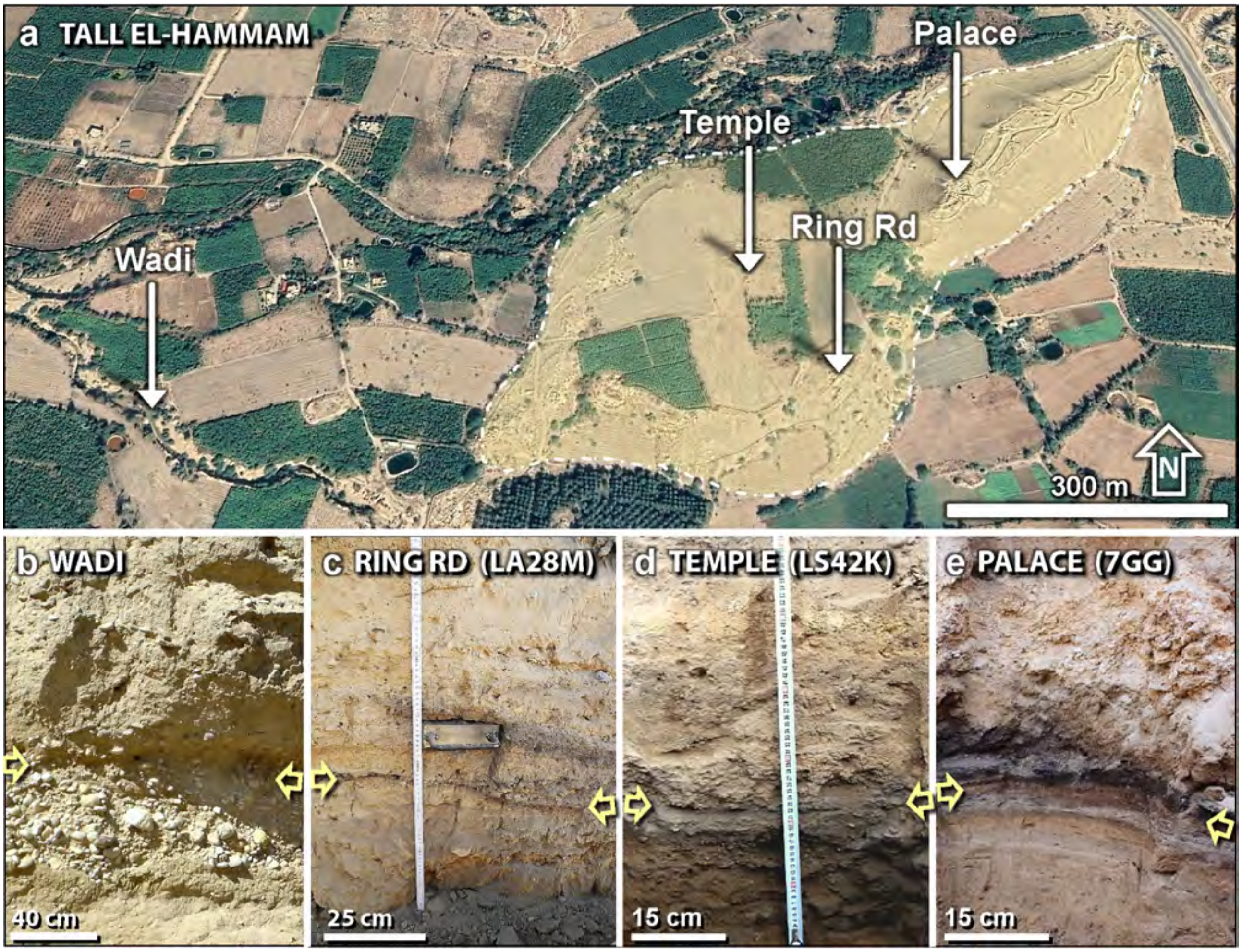

Figure 4: **Sedimentary profiles. (a)** Map of the city (white dashed line) showing sampling locations spanning ~1100 m. Source of base image: "Tall el-Hammam." 31° 50.483, N 35° 40.029 E. Google Earth; CNES/Airbus. Imagery date: 11/26/2019; accessed: 4/4/2021. **(b)** The wadi; **(c)** the ring road in Field LA; **(d)** the palace in Field LS; and **(e)** the palace in Field UA. In the wadi, yellow arrows mark the level of the 3600-year-old stratum. Inside the city, the arrows mark the location of the charcoal-and-ash-rich dark layer.

To investigate the destruction at TeH, we conducted a wide range of analyses. These included optical transmission microscopy (OPT), epi-illumination microscopy (EPI), universal stage, scanning electron microscopy (SEM), energy dispersive spectroscopy (EDS), focused ion beam milling (FIB), transmission electron microscopy (TEM), scanning transmission electron microscopy (STEM), fast-Fourier transform (FFT), electron backscatter diffraction (EBSD), cathodoluminescence (CL), and neutron activation (INAA) (see **Appendix A3, Methods** below). The group of co-authors of Bunch et al. [1], Silvia et al. [2], Kletetschka et al. [3], and of this contribution are collectively referred to below as "we." The group collected, analyzed, and interpreted melted materials across the city, including sediment, mudbricks, potsherds, meltglass, and roofing clay.

1. Stratigraphy of Tall el-Hammam

Our investigations focused on suites of samples from four representative sampling sites, spanning a lateral distance of ~1500 m across the occupational mound of TeH and into the watershed beyond (Figure 4**, SI Figure S2** [7]). Three sampling sites (the palace on the upper tall, the temple on the lower tall, and the ring road on the lower tall near the main gate) were chosen based on access to archeologically excavated squares in the key areas of interest. The wadi site was selected because of its location outside the city walls. The three sites in the city are separated by up to ~500 m laterally, covering an area of 5.7 hectares (0.057 km^2), and the wadi site extends the total horizontal distance to 1500 m for all four sites. Sample collection from more distant sites outside the tall could not be conducted due to lack of access.

All TeH sampling profiles investigated contain an MB II burn layer that is highly complex and variable across the tall but is generally composed of three parts above the previous MB occupation level. The first part is the deepest one and is mainly pulverized mudbrick mixed with larger melted and unmelted mudbrick fragments, melted and unmelted roofing clay, ash, charcoal, charred seeds, unburnt wood, burned textiles, bones, plaster fragments, broken pottery, and melted pottery. We call this the 'debris matrix.' It varies in thickness up to ~1.5 m and is only occasionally missing across the entire tall.

Immediately above the debris matrix, the second part comprises thin, windblown, fine-grained, weak laminations, including fragments of broken plaster, limestone spherules, and charcoal, radiocarbon-dated to 1650 BCE. It is not present in all locations and is typically found on the NE sides of SW-facing wall remnants at the top of the debris matrix. This extraordinary stratum is termed the 'blow-over' layer. Nothing similar has been identified in older or younger deposits, beginning in the Early Bronze Age and extending through the Iron Age.

The third part is a charcoal-and-ash-rich stratum called the 'dark layer,' which is found everywhere across the tall and is typically only a few centimeters thick or less. However, on the outer, southwest-facing side of the large city gate, it is ~1 m thick. Sometimes, the dark layer is on top of the weakly laminated blow-over layer, but other times, it is the only layer found, usually resting on top of an existing interior building floor. Its burial depth varies considerably from being near the surface on parts of the lower tall to being buried 1-4 m across most of the upper tall. The debris matrix, the blow-over layer, and the dark layer collectively comprise the interval of interest called the 'destruction layer.'

The four sites investigated, with a difference in elevation of 52 m, are listed below from SW to NE. Almost all proxies investigated here came from these four sampling sites:

(i) The wadi: the surface is at an elevation of ~197 mbsl on a short seasonal stream that drains the southern boundary of the tall (Figure 4b, **SI Figure S2** [7]). We sampled a 170-cm-thick sequence beginning ~100 cm below the surface, with the destruction layer located ~160 cm below the surface. Five discontinuous samples had an average thickness of ~13.2 cm (range: 10-20 cm). Four intermediate layers were not sampled. The average sample size for the wadi and the three following sites was 1200 g (range: 870-2000 g).

(ii) Ring road: the surface is at ~170 mbsl on the road interior to the wall that ringed the lower city (Figure 4c, **SI Figure S2** [7]). The top of the 30-cm sequence is at a depth of 22 cm, with the destruction layer at 42 cm. Six contiguous samples each had thicknesses of 5 cm.

(iii) Temple: the surface is at ~170 mbsl on the lower tall (Figure 4d, **SI Figure S2** [7]). We sampled a 43-cm sequence, with the destruction layer at 54 cm. Five contiguous samples had an average thickness of 8.6 cm (range: 6-16 cm).

(iv) Palace: the surface is at ~145 mbsl on the upper tall (Figure 4e, **SI Figure S2** [7]). We sampled a 28-cm sequence with the top of the destruction layer at ~360 cm. Five contiguous samples each had an average thickness of 5.6 cm (range: 3-13 cm).

Summary of 1. Stratigraphy of Tall el-Hammam

Proxy Types:

- Sedimentary layers (debris matrix, blow-over, dark layer)
- Melted materials (mudbrick, pottery, roofing clay)

Analysis Methods:

- Stratigraphic profiling at four sites (Palace, Temple, Ring Road, Wadi)
- Elevation mapping and lateral transect (~1500 m)
- Depth-based sediment sampling and visual analysis

Key Findings:

- The destruction layer comprises:
    - A **debris matrix** rich in pulverized, melted architectural and organic materials.
    - A **blow-over layer** of wind-deposited laminations was found mainly to the NE of structures.
    - A widespread **charcoal-rich dark layer**, up to 1 m thick in some locations.
- These layers are unique to the MB II horizon and absent in older or younger strata.
- Melted materials occur only within this destruction layer.
- Lack of erosional features suggests rapid, high-energy deposition.
- Vertical relief of sites spans ~52 m
- Destruction layer depth varies by site (e.g., 3.6 m at the Palace, 1.6 m at the Wadi).

2. Dating of the destruction layer

2.1 Radiocarbon dating of the destruction layer

The age of the destruction layer at TeH was modeled using the OxCal radiocarbon calibration program [24, 25], version 4.4 (IntCal20 calibration curve) with the 'Combine' computer routine [26] (**SI Tables S1, S2** [7]). Radiocarbon dates were obtained for 26 samples from the destruction layer, and of those, OxCal rejected three dates as outliers that are a few decades too young, and three dates were rejected as being a few decades too old. The following datable materials were extracted from the destruction layer in Field UA in and around the palace: carbonized wood, including twigs (n = 11), carbonized grains and seeds (n = 3), charred organic material (n = 4), organic sediment (n = 1), and collagen from burned bone (n = 1).

The Bayesian-modeled age for the destruction layer is 1661 ± 21 BCE (3611 cal BP) (Figure 5**; SI Tables S1 and S2** [7]) for a range of 1686 to 1632 BCE with a 68% confidence interval (CI, approximately equivalent to 1σ). Because of radiocarbon-dating uncertainties, the age of the destruction event has been rounded to the nearest half-century: 1650 BCE ± 50 (3600 cal BP).

2.2 Dating using pottery seriation

This age is consistent with seriation, a standard dating method used in archaeology based on the ages of stylistic changes in pottery and artifacts. This method provides an estimated age of ~1750-1650 BCE [6], a range that includes the calibrated radiocarbon ages.

Interpretation of the age of tall el-Hammam

Accurate dating of the destruction layer is a necessary element of the TeH evidence. For maximum accuracy, Telford et al. [27] recommended that the age of any short-term event is best constrained by using multiple dates of samples collected directly within a layer of interest. Radiocarbon dates below the destruction layer were appropriately younger or older and are not included here. At TeH, we acquired datable carbon only from the clearly defined destruction layer.

The dates were acquired from seeds representing a single year, and some of the charred wood is from twigs representing only a few years' growth. These short-lived materials are among the most desirable for accurate dating, making it likely that these samples' age range encompasses the layer's actual age.

Bayesian analysis has increasingly become the standard approach to produce archeological age-depth models [28] since this dating method minimizes potential stratigraphic complications. The OxCal calibration program, for example, uses a Combine routine that statistically tests the hypothesis that multiple radiocarbon dates relate to the same event. When multiple dates from a single stratum have differing

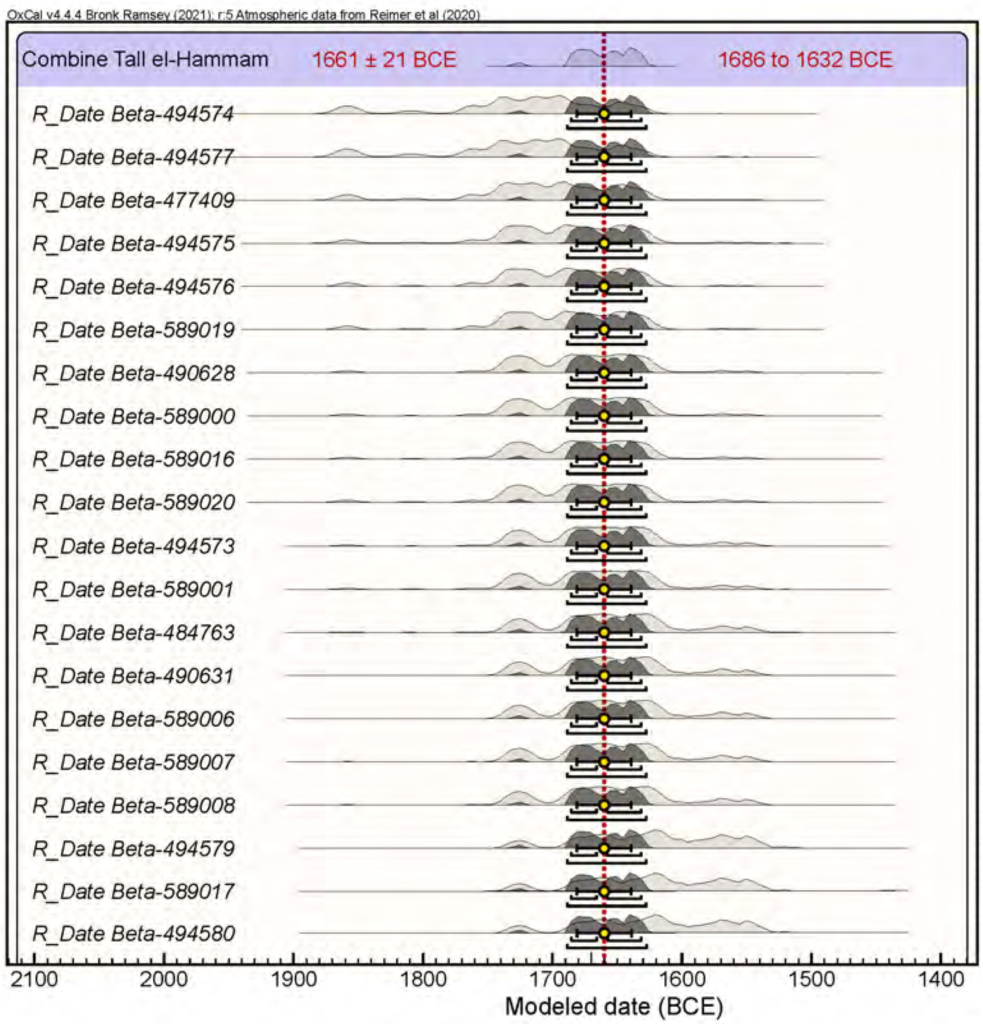

Figure 5: **Bayesian analysis.** Using OxCal v.4.4.4 [24–26], the 'Combine' computer routine determined that 20 of 26 ^{14}C dates are statistically synchronous and likely represent a single event at 1661 ± 21 BCE (1686 to 1632 BCE), rounded to 1650 BCE. Light gray curves represent unmodeled calibrated ages; dark gray represents modeled calibrated ages. The white dot beneath the curves equals the mean age, also defined by the red-dotted vertical line. Progressively longer brackets beneath curves represent 68% and 94% confidence intervals. The program performed two statistical probability tests to test the robustness of the model. The A_{comb} and Chi Sq statistical tests show a high probability, indicating that the modeled age of 1661 ± 21 BCE is likely accurate.

radiocarbon ages, the OxCal program determines which dates have the highest probability of fitting the model, and the anomalous dates are either remodeled or rejected as outliers, thus producing a statistically accurate calibrated radiocarbon age.

Summary of 2. Dating of the destruction layer

Proxy Types:

- Carbonized organic remains (wood, seeds, grains, charred materials, collagen from bone)
- Diagnostic pottery assemblages

Analysis Methods:

- Radiocarbon dating (26 samples) calibrated with OxCal v4.4 using IntCal20 curve
- Bayesian modeling and statistical outlier rejection
- Pottery seriation and typological comparison

Key Findings:

- Radiocarbon dates from short-lived organics (e.g., seeds, twigs) yielded a modeled age of **1661 ± 21 BCE**, rounded to **1650 ± 50 BCE**.
- Dates span a 68% confidence interval from **1686 to 1632 BCE**.
- Pottery styles align with a Middle Bronze Age IIa–IIb transition age of **~1750–1650 BCE**, consistent with radiocarbon dating.
- All samples were taken from the **destruction layer** itself, minimizing stratigraphic uncertainty.
- Bayesian analysis confirmed statistical coherence of 20 out of 26 radiocarbon dates, with high model robustness.

3. Evidence of widespread burning and extreme temperatures

3.1 City-wide conflagration and the charcoal-rich layer

The first evidence of city-wide burning was unearthed when excavators discovered several 6- to 7-cm-wide pieces of MB II pottery with surfaces that appeared to have been melted at high temperatures [5, 8–12]. Subsequently, the excavators uncovered a burn layer with a large number of melted mudbrick fragments and what appeared to be melted roofing clay [5, 8–12]. Such material is highly anomalous because the region's MBA inhabitants could not produce fires with temperatures high enough to melt such material. These discoveries led to the investigations described in this contribution.

Several post-MBA burn layers were found on the upper tall several meters above the MB II burn layer and dated 300 years younger at ~1400 BCE during Late Bronze Age II (Figure 6). In addition, there are two earthquake-related destruction layers buried beneath the MB II destruction layer; one dates to ~3300 BCE during the Early Bronze Age and the other to ~2100 BCE during the Intermediate Bronze Age. However, the strata marking those other events do not display the magnitude of destruction or contain any of the melted materials found in the MB II burn layer.

3.2 Charcoal, charred grains, and soot as evidence of widespread burning

Our analyses reveal a significant peak of carbon in the palace destruction layer (Figure 7), where the loss-on-ignition (LOI) value for the charcoal-rich layer is 43.7 wt% (**SI Table S3** [7]). Background LOI values in two samples above and two below the destruction layer average ~23.4 wt%, for a difference of ~20 wt%. Because strata above and below the destruction layer are light-colored in comparison, the background LOI values are inferred to represent mostly carbonate, which is common in TeH sediment; the increase of ~20 wt% in LOI value for the destruction layer is inferred to be from organic carbon, i.e., burned wood and textiles.

To further test for organic carbon content, we added water to ~100 g of sediment for 10 contiguous samples from the palace and collected the float. Inspection by optical microscopy confirmed that the float from the destruction layer contained mostly charred organic material, e.g., soot, ash, charcoal, wood, and plant fragments at 1.7 wt% of bulk sediment, while the layer beneath it contained 0.1 wt%. The other eight non-destruction strata contained no detectable float.

Sedimentary soot was analyzed in one sample of the destruction layer from Field UB, located behind the palace. The sample was mainly silty, calcareous sand with no visible charcoal, wood, or textiles. It contained an average of 1.0 wt% total organic carbon (TOC) with a high ratio of soot carbon to total organic carbon (soot/TOC), averaging 75.8% (range 55.7 to 95.8% in two aliquots). This high ratio in the destruction layer is consistent with intense biomass burning that converted most organic matter into soot via condensation of combustion-derived gases.

3.3 High-temperature diamond-like carbon (diamondoids)

Nanodiamonds and diamond-like carbon have been used as indicators of cosmic impacts, including at the Cretaceous-Paleogene boundary (K-Pg) at ~65 Ma [29, 30] and the Younger Dryas boundary (YDB) at 12.8 ka [31]. Kinzie et al. [31] concluded that impact-related nanodiamonds and diamond-like carbon (DLC or diamondoids) are produced from the pyrolysis of carbon sources, e.g., vegetation and carbonate rocks incinerated during high-temperature, high-pressure airburst/impact events. This process also occurred during the Chiemgau airburst/impact event in Germany [32]. To search for nanodiamonds in TeH sediment, we followed the protocol of Kinzie et al. [31], who used multiple reagents to remove all minerals except refractory, acid-resistant carbon.

In six samples of TeH bulk sediment from the temple (LS42J), we searched for but could not detect the presence of nanodiamonds but did observe carbon atoms clustered into irregularly shaped plate-like clumps. Examination using

Figure 6: **Multiple burned layers at Tall el-Hammam.** On the upper tall, there are three terminal burn layers: one during the Middle Bronze Age (MB II), another during Late Bronze Age II (LBA), and one higher during the Iron Age (not visible here). Each burn layer represents the end of an archaeological period at the site. A dashed white line encloses the LBA burn layer at the arrow, representing the burning of a single building at ~1400 BCE stacked atop the sheared MB-II walls. "MBA floor" marks the top of the MB II floor beneath the 1.5-m-thick destruction layer dating to 1650 BCE. Two earthquake-related destruction layers (not shown) are buried deeper than the floor of this excavation, one dated ~400 years earlier at ~2100 BCE and the other even older at ~3300 BCE. All these layers are distinctly separate from the MB II destruction layer above the bottom arrow, the only layer that contains high-temperature melted materials.

bright-field high-resolution transmission electron microscopy (HRTEM) reveals short-range carbon structures, typically composed of less than 1-2 dozen atoms (Figure 8). Analyses by transmission electron microscopy (TEM) and selected-area electron diffraction (SAD) indicate that the structures are composed of amorphous carbon that does not produce SAD patterns (Figure 8c), even though organized, short-range structures are present (Figure 8b). This material is commonly referred to as diamondoids or diamond-like carbon (DLC) [31], composed of the smallest units observed in a diamond crystal lattice. The structures are nearly as hard as diamond and are stable at temperatures up to ~1000-1200°C [31]. Diamondoids were observed in all samples investigated, but abundances peaked at ~3 ppm in the temple destruction layer. This value is >3× higher than background concentrations that average 0.9 ppm (range: 0.4-1.9 ppm) above and below the destruction layer.

When viewed using optical microscopy, these nanocrystals appear clear to translucent white (Figure 8d), as is typical of diamondoids and diamond-like carbon [33], as distinguished from opaque, non-diamond forms of carbon that are commonly black or gray. When the residue was exposed to ultraviolet light sources, the carbon-rich residue luminesced (Figure 8e) at some of the characteristic luminescence bands for diamond, 365 nm (long-wave UV) and 440 nm [34].

One fragment of melted pottery from the palace exhibits the results of the impact of a 30-µm-wide carbon-rich particle (Figure 9). Using optical microscopy, the particle is whitish and translucent-to-clear, the same as the diamondoids extracted from sediment. SEM-EDS analyses indicate that this particle is an aggregate of hundreds of discrete plate-like amorphous carbon grains, along with a few micron-sized grains of Si, Ca, and Al oxides. The individual grains are anhedral with no apparent structure, resembling TEM images of TeH diamondoids.

Diamond-like carbon or diamondoids are associated with extraterrestrial impact events [35] but are also found in hydrocarbon deposits and coal [35]. Each diamondoid typically contains carbon atoms that are sp^3-bonded (i.e., 4 bonded carbon atoms), as in diamond, rather than with sp^2 bonding (i.e., 3 bonded carbon atoms), typical of graphite [35].

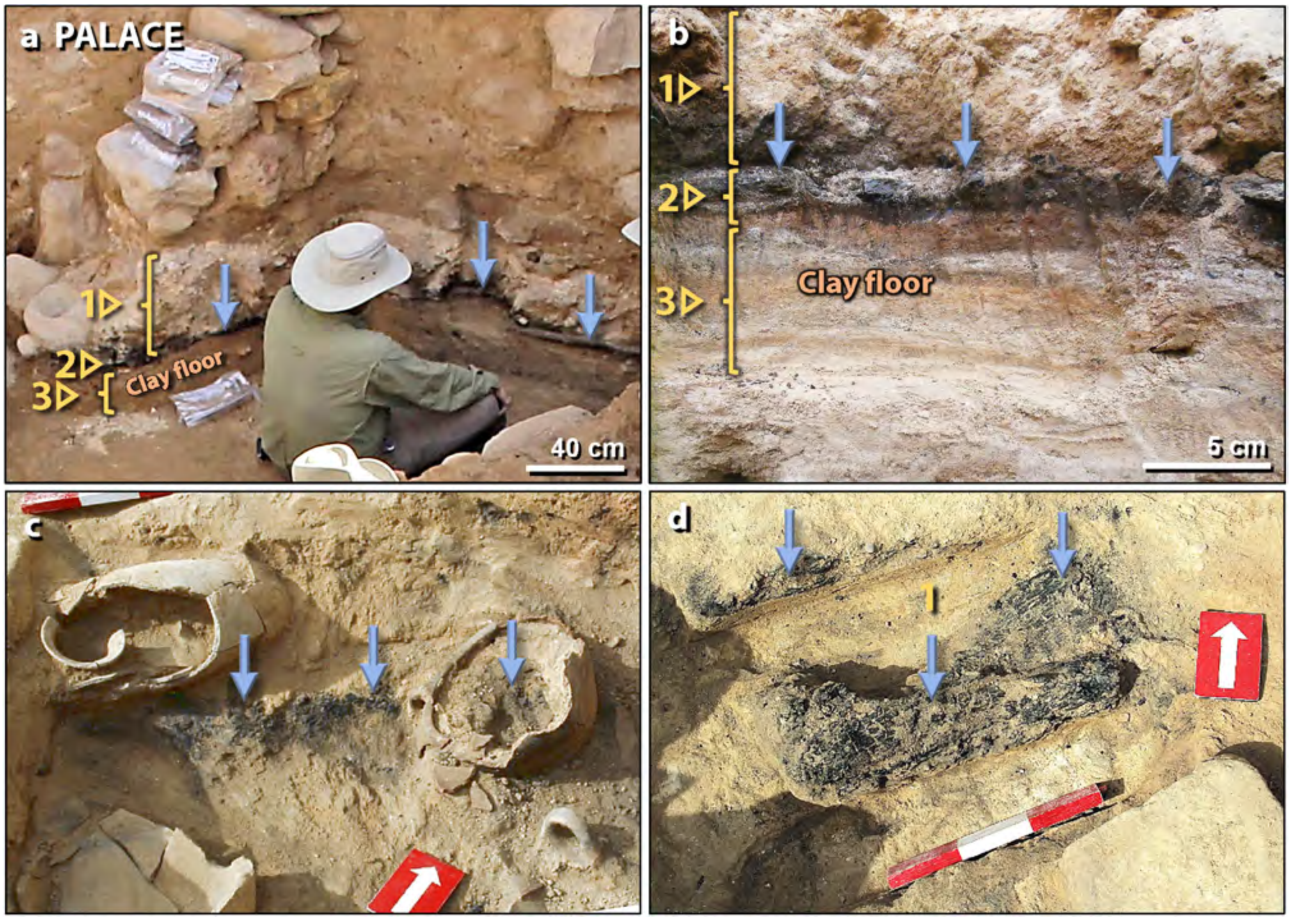

Figure 7: Destruction layer in the palace. (a) Photo of excavation in an exterior food preparation area of the palace. #1, in yellow text, marks MB II debris that was most likely deposited by post-fire erosion. #2 points to the charcoal-rich 'dark layer' indicating a major burning episode. It contains fragments of plaster and limestone spherules. Blue arrows mark its top. #3 points to the cross-section of multi-layered clay flooring. **(b)** Close-up photo of the same palace sampling sequence as in panel 'a.' **(c)** Photo of broken pots with carbonized grains embedded in MB II 1.5-m-thick debris matrix, mainly composed of pulverized mudbrick, plaster fragments, and limestone spherules. The debris matrix is found in the space between all palace walls. Note the charcoal inside the broken pot. The end of a scale stick with 10-cm divisions is at the upper left. **(d)** Charred palace roof timber surrounded by a 1.5-m-thick charcoal-rich debris matrix of pulverized mudbrick. A scale stick shows 10-cm markings.

Although diamondoids peak in the temple destruction layer, indicating likely exposure to high temperatures, they are also present at lower concentrations in all other layers. These lower concentrations may be due to the reworking of the nano-sized diamondoids, which are easily redeposited by wind and water.

The carbon-rich aggregate fused to a melted potsherd is whitish-to-clear (Figure 9), so we conclude that this object is a cluster of diamondoids. The particle appears to have had sufficient velocity to produce a crater in the molten potsherd. If so, the velocity was low enough not to have shattered the low-mass, high-energy particle and yet high enough to have pushed aside the viscous molten glass.

3.4 High-temperature melted minerals in the destruction layer

We used SEM-EDS and TEM-EDS, as further discussed in sections below, to measure 38 elements and melted high-temperature minerals (Table 1), and of these, 74% (n = 28 of 38) melted at ≥1300°C; 45% (n = 17 of 38) at ≥1600°C; and 18% (n = 7 of 38) at ≥2000°C. All represent equilibrium temperatures, usually a few hundred degrees higher than non-equilibrium temperatures commonly associated with oxygen-deficient (reducing) conditions present during impact events [36].

Interpretation of city-wide burning and destruction

We considered whether military action burned and destroyed TeH in ~1650 BCE. Typically, any evidence of the destruction through warfare is deduced by the presence of war artifacts, such as arrowheads, spear points, and sling stones. However, in the MB II matrix at TeH, no single arrow point or sling stone has been uncovered. Also, during its previous ~2850 years of occupation at TeH, there is no evidence of military activity associated with city-wide destruction or

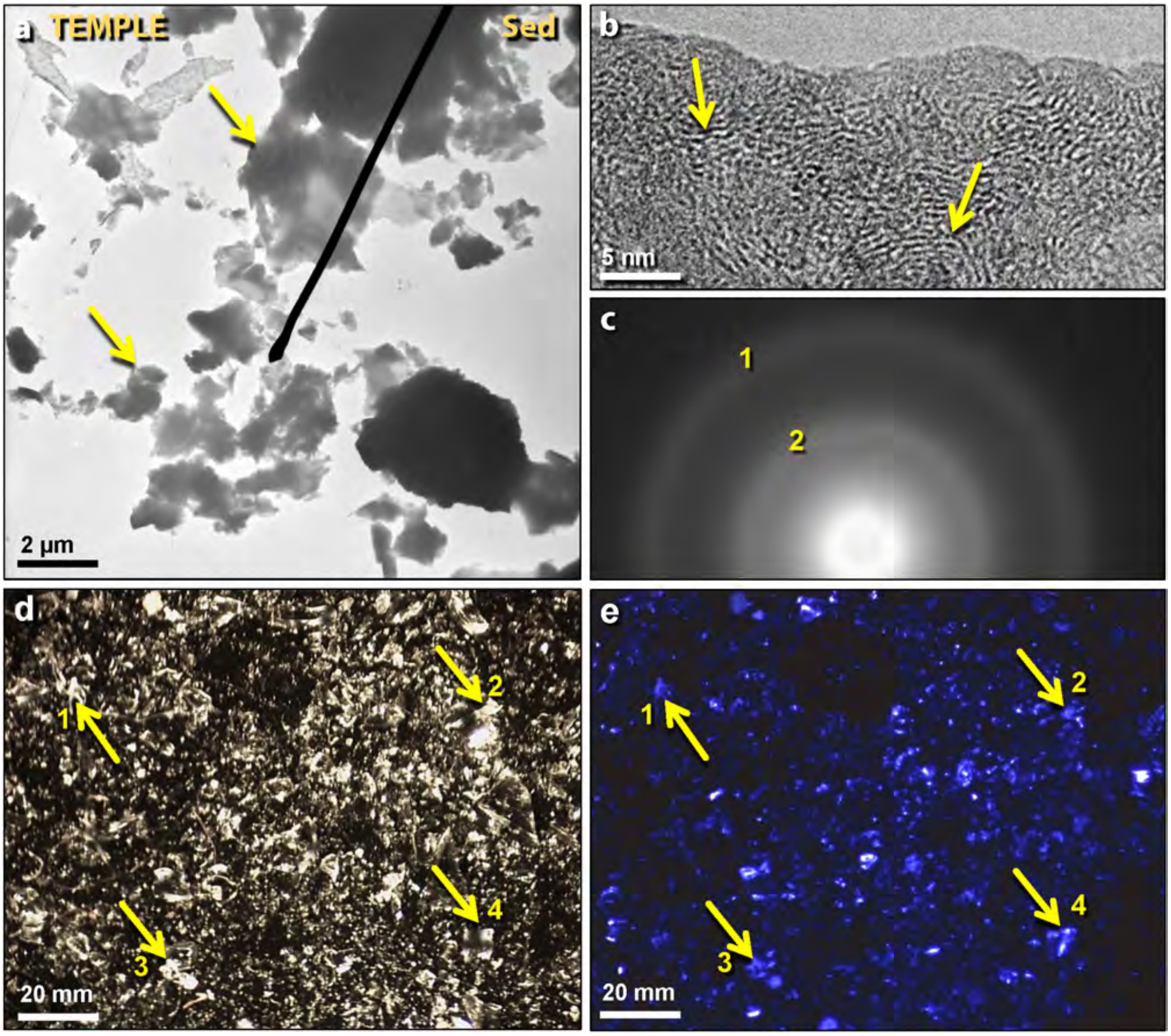

Figure 8: Diamondoids (diamond-like carbon) in temple sediment. (a) Transmission electron microscopy (TEM) image of clusters of amorphous diamondoids. **(b)** Bright-field high-resolution transmission electron microscopy (HRTEM) of acid-resistant residue shows carbon atoms' short-range ordering. **(c)** Selected-area electron diffraction (SAD) of the residue and the grid film, confirming that the residue is amorphous carbon. **(d)** Photomicrograph of diamondoids showing white to optically clear material on black carbon SEM tab; **(e)** photomicrograph of the same area as in panel 'd' showing that the diamondoids luminesce at ~440 nm, typical of cubic diamonds.

burning at any time, although there is evidence of two episodes of burning due to earthquakes.

In contrast, in Iron Age strata dating to ~1350 BCE, ~300 years following the MB II destruction event, numerous sling stones suggest military action. In addition, the Iron Age II city on the upper tall was destroyed by military conquest in the late 9th century BCE. Thus, military action has been detected at TeH but not in the 1650-BCE destruction layer. In each case of military destruction, there are no examples of melted materials, including pottery, mudbrick, meltglass, or spherules.

Military action has also been documented at nearby Jericho, 22 km west of TeH. However, no evidence of military conquest has been detected in the MB II occupation level at that site, which instead shows evidence of intense burning and destruction 1650 years ago, as at TeH. In a previous battle in ~2000 BCE, defensive walls were breached, after which the site displayed different pottery, weapons, architecture, and burial customs, as is typical of military conquest [37]. Similarly, between 1950–1800 BCE, Jericho suffered violent destruction indicative of military action [38]. Neither of these episodes is apparent at TeH, and no warfare-related melted materials have been reported at Jericho.

At Tall Nimrin, the third-largest city in the area, located ~5 km north of TeH, there is no evidence of MB II warfare at 1650 BCE, although there is evidence of destruction and possible burning, as at TeH. Also, there is evidence of military action

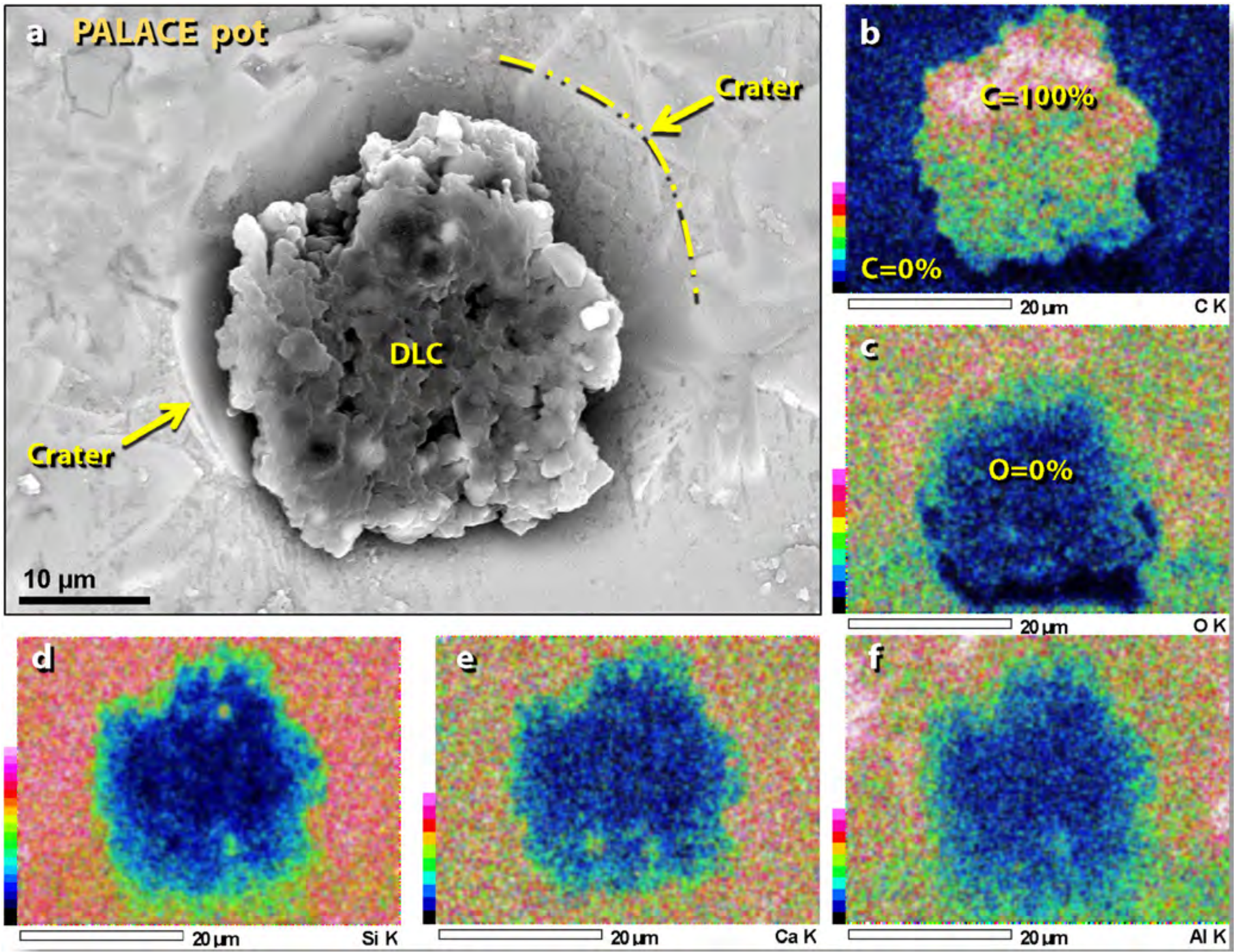

Figure 9: Diamond-like carbon embedded in pottery from the palace. (a) Pure carbon aggregate, likely a diamondoid or DLC cluster, is embedded in a crater on the melted surface of the pottery. **(b-f)** SEM-EDS elemental maps showing that the particle is composed of carbon with almost no oxygen or other elements; the object is embedded in the Ca-Al-Si pottery matrix.

during the Iron Age II period, as at TeH. Thus, the three largest urban cities in the southern Jordan Valley, TeH, Jericho [39, 40], and Tall Nimrin [41], were burned and/or destroyed simultaneously at ~1650 BCE, the end of MB II, but lack any evidence for military action as a potential cause. Of all the layers in the three cities showing evidence of military or other types of destruction, e.g., earthquakes, none contain any reported evidence of high-temperature proxies, including melted materials, such as mudbricks, pottery, and roofing clay.

Summary of 3. Evidence of widespread burning and extreme temperatures

Proxy Types:
- Melted mudbrick, pottery, roofing clay
- Charcoal, ash, soot, charred organics
- Diamond-like carbon (DLC)
- High-T minerals

Analysis Methods:
- Optical microscopy, SEM-EDS, TEM, DSC-TGA
- LOI, carbon separation, elemental analysis

Key Findings:
- A 1.5-m-thick layer contains widespread char and combustion traces.
- LOI indicates ~20 wt% rise in organic carbon; DLC peaks at ~3 ppm.
- Vesicular textures and partial melting in silicates indicate exposure to >1300–1500°C.
- 74% of elements melt at ≥1300°C, 18% at ≥2000°C (Table 1).
- Charcoal layers with a soot/TOC ratio of ~76% suggest intense biomass burning.
- Embedded DLC in meltglass points to high-T particle impacts consistent with an airburst.

Table 1: Equilibrium melting points of materials analyzed from the destruction layer at Tall el-Hammam.

Phase	Formula	~Equilib melt T (°C)
Potassium Chloride	KCl	770
Sodium chloride	NaCl	801
Calcium carbonate	$CaCO_3$	825
Silver	Ag	961
Gold	Au	1064
Copper	Cu	1085
Iron phosphide	Fe_2P, Fe_3P	1100
Iron sulfide	FeS, Fe_2S, Fe_3S	1194
Sediment	Si-Ca-rich	1250
Spherules, Si-rich	Si, Ca, Al, Fe oxides	1250
Melted mudbrick	Si-rich	1400
Silicon, native	Si	1414
Spherules, Fe-rich	Fe + Fe oxides	1420
Nickel	Ni	1455
Iron, native	Fe	1538
Wollastonite	$CaSiO_3$	1540
Titanomagnetite	$TiFe_2O_4$	1550
Iron oxide (hematite)	Fe_2O_3	1565
Iron oxide (magnetite)	Fe_3O_4	1590
Spherules, REE-rich	Fe oxides +REEs	1590
Melted pottery	Si-Ca-rich	1590
Calcium phosphide	Ca_3P_2	1600
Tin Oxide	SnO_2	1630
Calcium phosphate	$Ca_3(PO_4)_2$	1670
Zircon, dissociation	$ZrSiO_4 \geq ZrO_2$	1676
Zircon	$ZrSiO_4$	1687
Quartz	SiO_2	1713
Platinum	Pt	1768
Titanium sulfide	TiS	1780
Chromium	Cr	1907
Manganese oxide	MnO	1945
Calcium silicate	$CaSiO_3$	2130
Chromite	$(Fe)Cr_2O_4$	2190
Lanthanum (PGE)	La_2O_3	2315
Ruthenium	Ru	2334
Cerium (PGE)	CeO_2	2400
Iridium	Ir	2466
Calcium oxide	CaO	2572

Representative materials and chemical formulas observed in meltglass, melted pottery, mudbrick, and roofing clay from the destruction layer are listed. Melting temperatures reflect standard equilibrium conditions and are organized from lowest to highest. These data constrain minimum thermal exposures during the hypothesized cosmic airburst event. Notably, 74% of the analyzed materials (28 of 38) exhibit melting points ≥1300°C, with 18% ≥2000°C, indicating transient exposure to extreme temperatures consistent with a high-energy atmospheric explosion. Melting temperatures range from ~770° to 2572°C.

4. High-temperature impact-related materials

4.1 Melted potsherds indicative of extreme heat

Surface-melted potsherds were found about 15 m northeast of the palace complex in the destruction layer in Field UB (Figure 10). These were associated with numerous unmelted potsherds within a sealed MB II context that was deeply buried in undisturbed sediment beneath ~2.5 m of Iron Age walls. Their position indicates that the melted potsherds were not redeposited from younger strata. Their MB II age was determined by seriation (pottery styles) and radiocarbon dating of associated charred seeds and grains. The potsherds were mixed within a heavily churned debris matrix containing charcoal, ash, pulverized mudbrick, potsherds, roofing materials, and fragments of limestone building plaster. No melted material was found anywhere in the city in younger or older layers, spanning ~3500 years, including from the Early Bronze Age (3300-2300 BCE), Late Bronze Age (1550-1200 BCE), Iron Age (1200-332 BCE, and Early Roman times (63 BCE-135 CE).

One melted potsherd analyzed from the Square 10JJ in the palace (Figure 10a and 10b) came from the shoulder/neck transition of a wheel-made MB II storage jar. The sherd was constructed from tan, gritty, sandy clay with a maximum thickness of ~1 cm. Photomicrographs and SEM images show that the outer surface of the potsherd is relatively smooth, glossy glass. The broken edge shows that only the sherd's outer 2 mm were altered to glass, while the next 4 mm were darkened by thermal exposure but not melted; the sherd's inner 4 mm are unmelted (Figure 10e and 10f). Most of the potsherd's edges are highly vesicular (Figure 10g and 10h), and once-molten clay drapes over some of the broken edges, suggesting that melting of the sherd took place following breakage. The inner portion of the sherd visible on the broken or sliced edges appears to be original unaltered clayey sand with few voids (Figure 10f and 10g). Mineral inclusions on the interior surface of the potsherd are unmelted. On the other hand, most minerals embedded in the exposed or exterior surface of the potsherd exhibit significant melting, during which the matrix was transformed into greenish, translucent glass.

Another melted potsherd (Figure 10c and 10d), part of a typical red clay pot, was excavated from the temple in the lower tall, where it was found intermixed with sherds of unmelted MB II pottery. The average thickness of the sherd is 5 mm, but only the outside 2 mm of the sherd had been transformed into highly vesicular glass. The middle 1 mm of clay is darkened, presumably by thermal exposure, but not melted. The bottom 2 mm of clay retains its original red color from firing in a kiln and is unmelted. The curvature of the sherd shows that melting was limited to the outside of the pot's exterior or exposed surface. SEM imagery confirms that the outer surface is melted and highly vesicular, indicating exposure to high temperatures. Many minerals embedded in the surface are partially or fully melted, while most minerals within the matrix are unmelted.

SEM/energy dispersive X-ray spectroscopy (SEM-EDS), using a large spot size, and microprobe analyses of both sherds indicate similar compositions. They are dominantly composed of SiO_2 at ~48.6 average wt%; CaO at ~17.5 wt%; and Al_2O_3 at ~15.0 wt% (values for other oxides are provided in **SI Tables S4 and S5** [7]). The Ca-rich matrix contains abundant crystals of plagioclase and pyroxene. The composition of the clay used to make the pottery is smectite (montmorillonite) with a high percentage of calcium hydroxide

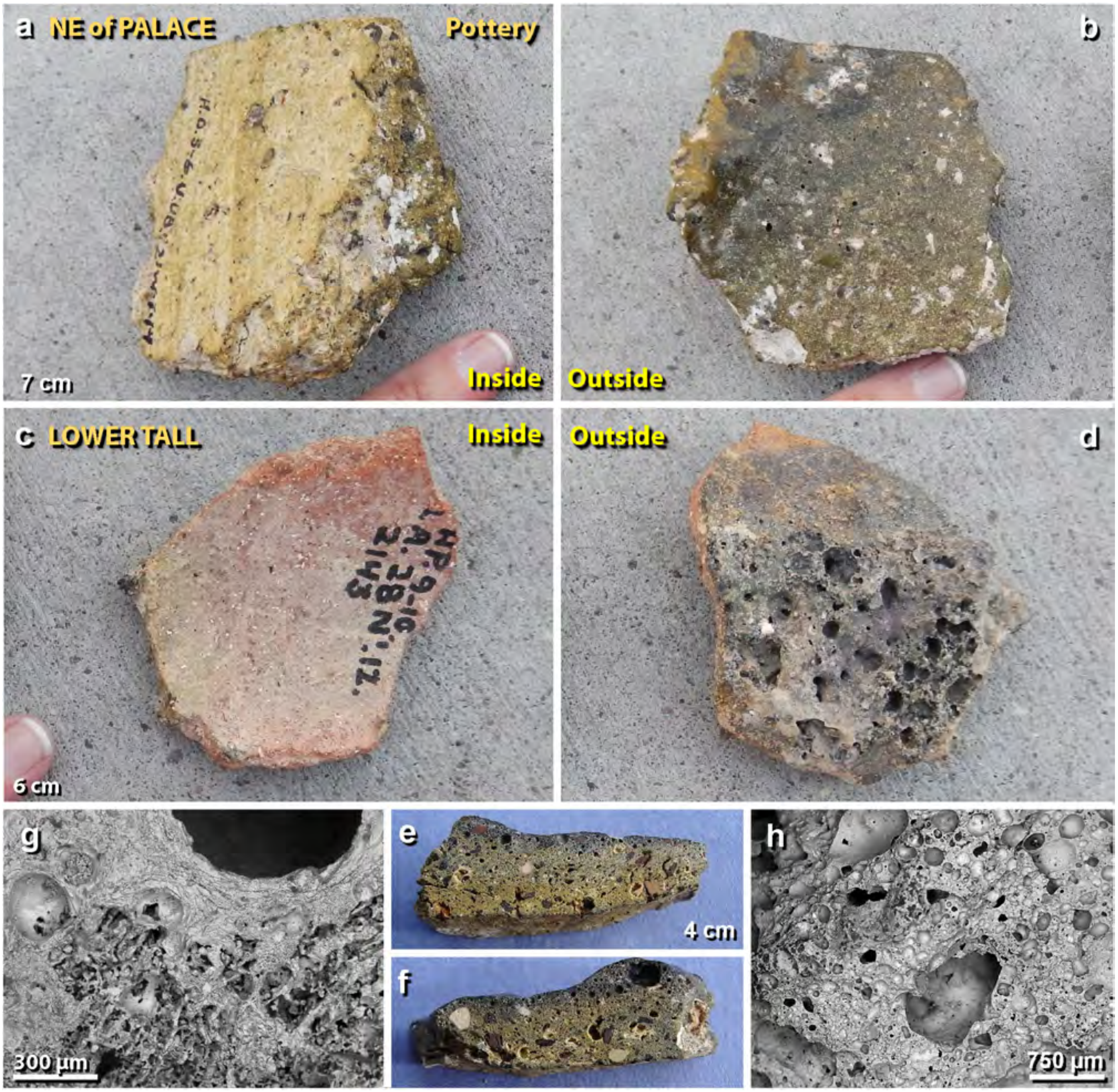

Figure 10: **Melted pottery. (a)** Photos of a 7-cm-wide potsherd from a broken storage jar from NE of the palace, showing an unmelted inner surface and **(b)** the darker melted outer surface of the potsherd. The upper-left edge in panel 'b' is the outward-curved lip of a storage jar. **(c)** Potsherd of a 6-cm-wide storage jar from the lower tall, displaying an unaltered inner surface, and **(d)** the highly vesicular outer surface. **(e-f)** Photos of both edges of the sliced section of sherd in panels 'a' and 'b' above. **(g)**, **(h)** SEM images of the highly vesicular sliced surface of sherd in panels 'a' and 'b.'

due to the weathering of the abundant local limestone. When mixed with quartz as a binding agent, this type of clay was extensively used for centuries by regional cultures as the standard raw material for pottery.

Interpretation of melted pottery and heating experiments

We investigated the melting point of TeH pottery by conducting heating experiments on unmelted pottery from the MB II destruction layer. First, we used Differential Scanning Calorimetry with Thermogravimetric Analysis (DSC-TGA). DSC measures the heat flow of a sample over a temperature range, and TGA measures the weight change of a sample over the same temperature range. We observed a 32.7 % weight loss between ~381 and 831°C but with only an additional 0.5 wt% weight loss after ~831°C during heating to ~1400°C (**SI Figure S3b** [7]). These results indicate that the powder gave off physically and chemically bound volatile materials (e.g., H_2O and CO_2) during the ramp-up to 831°C, with minimal subsequent outgassing. As expected, the sample showed no further weight change during cooling in an argon atmosphere. The DSC results demonstrated a prominent endothermic peak coinciding with the decomposition/weight loss of the sample during the temperature increase to ~831°C. There was an increase in heat flow at ~1150°C and again at ~1310°C, suggesting exothermic reactions possibly due to the recrystallization of the phases present. The powdered pottery retained its crystalline, irregular granule morphology after DSC heating to 1400°C, the maximum temperature achievable in this experiment. These results indicate that melted potteries were exposed to temperatures at TeH of >1400°C.

Independent studies show that the typical melting point of clay ranges from ~1200° to 1600°C [42]. Using the potsherd's average bulk analysis of ~17.5 wt% CaO, ~48.6 wt% SiO_2, and ~15.0 wt% Al_2O_3, the theoretical minimum melting point of the pottery is between 1300° and ~1500°C, according to the CaO-Al_2O_3-SiO_2 (CAS) ternary phase diagram [43] (**SI Figure S3a** [7]). The higher end of these theoretical calculations is consistent with the heating experiment, which showed no detectable melting at ~1400°C.

To further investigate the melting point of pottery, we conducted laboratory experiments using an oxygen/propylene torch and thermocouple. After full exposure for ~2 minutes, one fragment of unmelted Ca-rich palace pottery began melting at ~1500° ± 25°C (**SI Figure S4** [7]). Although the temperature and heat flux were sufficient to melt a small area of the potsherd, the experiment could not duplicate the extensive melting observed on melted TeH potsherds. In addition, quartz grains embedded in the pottery remained unmelted. This result suggests that the maximum exposure temperature for the excavated melted potsherds was higher than 1500°C, and the flux rate was higher than the torch provided.

4.2 Remanent magnetism of melted pottery eliminates lightning

Because storage pots were sometimes placed on the roofs of buildings at TeH, we explored the possibility that the melted pottery and mudbricks had been struck by lightning, causing flash-melting. We used the same technique as in Moore et al. [36] for measuring remanent magnetism, the magnetization remaining after Fe-rich materials cool while exposed to Earth's ambient magnetic field (i.e., geomagnetism [44]). Remanent magnetism can vary from fully magnetized, i.e., saturated, as may occur during lightning strikes, to fully demagnetized, i.e., desaturated.

Two samples of melted pottery from TeH were analyzed: TeH_VITPOT_1 at 20.6 g and TeH_VITPOT_2 at 113.5 g. The measurements of remanent magnetism in both samples were nearly the same: the samples cooled while exposed to Earth's normal geomagnetic field (**SI Figure S5** [7]). They do not exhibit any evidence of intense magnetic fields, making it highly unlikely that lightning strikes melted the TeH potsherds. For an example of the magnetization of rock by an electric discharge, see Kletetschka et al. [45–48] and Wasilewski & Kletetschka [49].

4.3 Melted mudbricks in the destruction layer

MB II mudbricks in the TeH destruction layer are present in varying states of preservation. They are occasionally found whole or partially broken but typically are highly fragmented or pulverized. Both melted and unmelted mudbricks vary in color through shades of red, brown, gray, and black (Figure 11). Because melted mudbricks are typically indistinguishable from the melted sediment, which is mainly composed of pulverized mudbricks, we refer to all of this material as 'melted mudbricks,' for simplicity. The abundances of melted material spanned a wide range: ~0.6 g/kg along the ring road (Figure 12a); ~0.1 g/kg in the temple (Figure 12b); ~5 g/kg in palace location 7GG (Figure 12c); and ~150 g/kg in palace room 7HH (Figure 12d) (**SI Table S3** [7]). No mudbricks were observed in the wadi outside the city walls.

On the upper tall, melted mudbricks were found in the MB II destruction layer in Field UA within the palace in six different excavation squares. Typically, the depth of melting is ~1-5 mm, similar to that of the melted pottery. Melted materials (mudbricks, pottery, and roofing clay) were found ~2 m below the surface, mixed within a 30-cm-thick matrix of broken pottery and decomposed unmelted mudbrick. The destruction matrix also contained ash, charcoal, charred and unburnt roofing beams, charred and uncharred grains, and burned and unburned fabric and bedding. The density of mudbrick melt-glass in the most concentrated pockets reached >50% by volume, and in some cases, fractured chunks of melted material were found in pockets several meters in diameter and up to 30 cm thick. Between these pockets, the density trailed off to 10-15% by volume. The melted mudbrick fragments were typically surrounded by decomposed mudbrick and were rarely found with ash or charcoal, suggesting that they had melted before falling into their final locations.

A layer of melted mudbrick was often overlain by ~15-30 cm of melted and unmelted roofing clay. Typically, this melted clay was many times more abundant than melted mudbricks. In a 12 m × 12 m part of Field UA, melted clay MB II roofing material was covered by a variable thickness of up to 1 m of relatively homogeneous, decomposed-to-whole, unmelted mudbricks of the Late Bronze Age.

Unbroken upper surfaces of the melted material were typically relatively smooth, and the broken surfaces were often highly vesicular, as shown in SEM images (Figure 11d–11f). The lower surfaces sometimes displayed partially fused sand grains. Optical microscopy and SEM imagery revealed that the broken interior surfaces typically contained mineral inclusions that were mainly unmelted, although some were partially melted. The outer melted surfaces often contained mineral grains that were partially to fully melted. Scratch

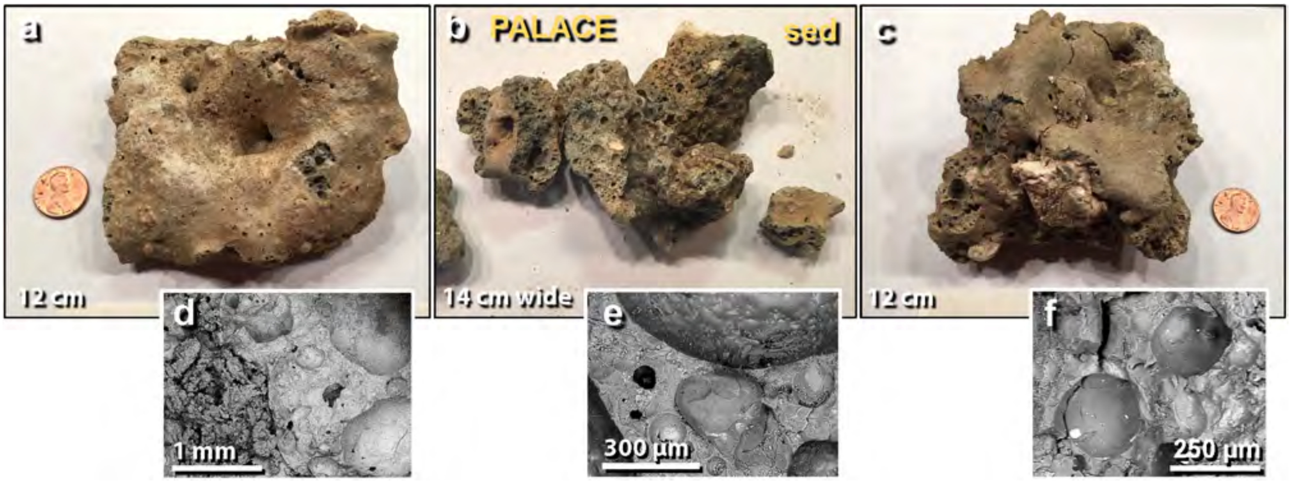

Figure 11: **Melted mudbrick from the palace. (a)** The upper surface of meltglass shows non-vesicular 'skin'; (b) broken surfaces of meltglass display vesicular texture. **(c)** The photo shows the upper surface and broken faces of meltglass. Note large, unmelted, light-colored mineral inclusions. **(d-f)** SEM images of highly vesicular surfaces of broken meltglass. Note bright metallic inclusions in several vesicles.

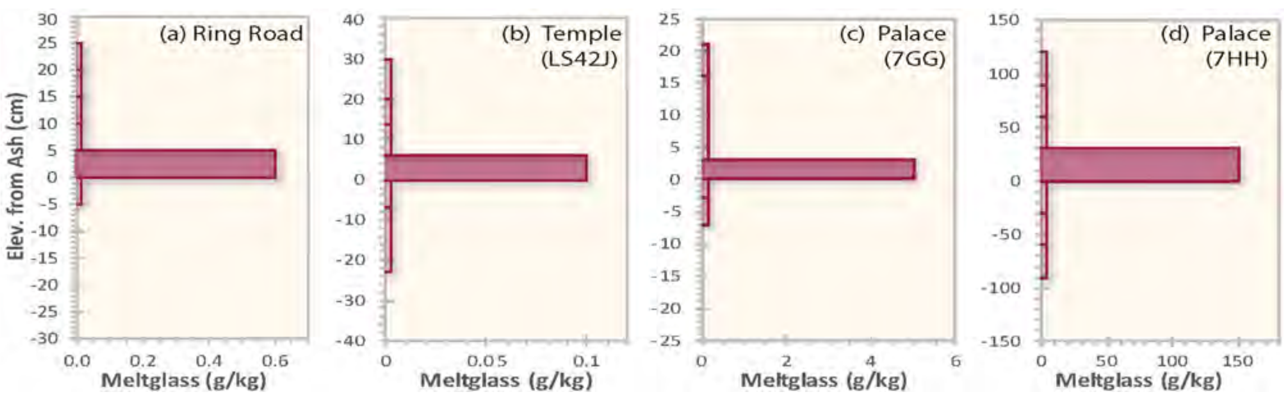

Figure 12: **Meltglass: melted pottery, mudbrick, and roofing material. (a-d)** Meltglass from 3 sites, the ring road, temple, and palace; no meltglass was found in the wadi, and none was found above or below the destruction layer at the other three sampling sites. Depths are in cm above or below the bottom of the destruction layer.

testing showed that the melted material would scratch glass but not quartz, indicating a Mohs hardness between 5.5 (glass) and 7 (quartz). Their hardness is substantially greater than typical sun-dried mudbrick (2-4 Mohs hardness).

The composition of the meltglass (collectively, melted mudbrick and roofing material) closely matched that of the melted pottery, dominantly composed of SiO_2 at 48.1 wt%; CaO at 17. 2 wt%; Al_2O_3 at 2.5 wt%; and C at 14.1 wt% (**SI Tables S4 and S5** [7]). Phosphate percentages in melted mudbrick varied from 6-16 wt%, and its presence can lower the melting point. The ternary phase diagram for the melted mudbrick showed a theoretical melting point between ~1300° to 1500°C (**SI Figure S3a** [7]), the same as the melted pottery.

Interpretation of Melted Mudbricks

Some minerals (e.g., calcite ($CaCO_3$) and soda ash (Na_2CO_3) present in the mudbricks and bulk sediment can act as fluxing agents to lower the equilibrium melting point. To investigate the fluxing effect at Abu Hureyra, Syria, Moore et al. [36] conducted heating experiments on Ca-Al-Si bulk sediment geochemically similar to the sediment at TeH. Laboratory temperatures were increased from ~1100°C to ~1850°C in increments of 50-150°C. Bulk sediment melted at ~1250°C, establishing a likely minimum melting point for TeH's melted mudbricks and sediment. However, the maximum exposure temperature was likely >1713°C, the melting point of quartz.

4.4 Melted roofing clay in the destruction debris

Melted clay material is associated with MB II roofs and upper-story floors at TeH, which were built using large wooden beams that spanned the mudbrick walls. These large beams were overlain by smaller wooden crossbeams, which were, in turn, covered with straw and leaves and topped with multiple layers of dried clay that were individually troweled

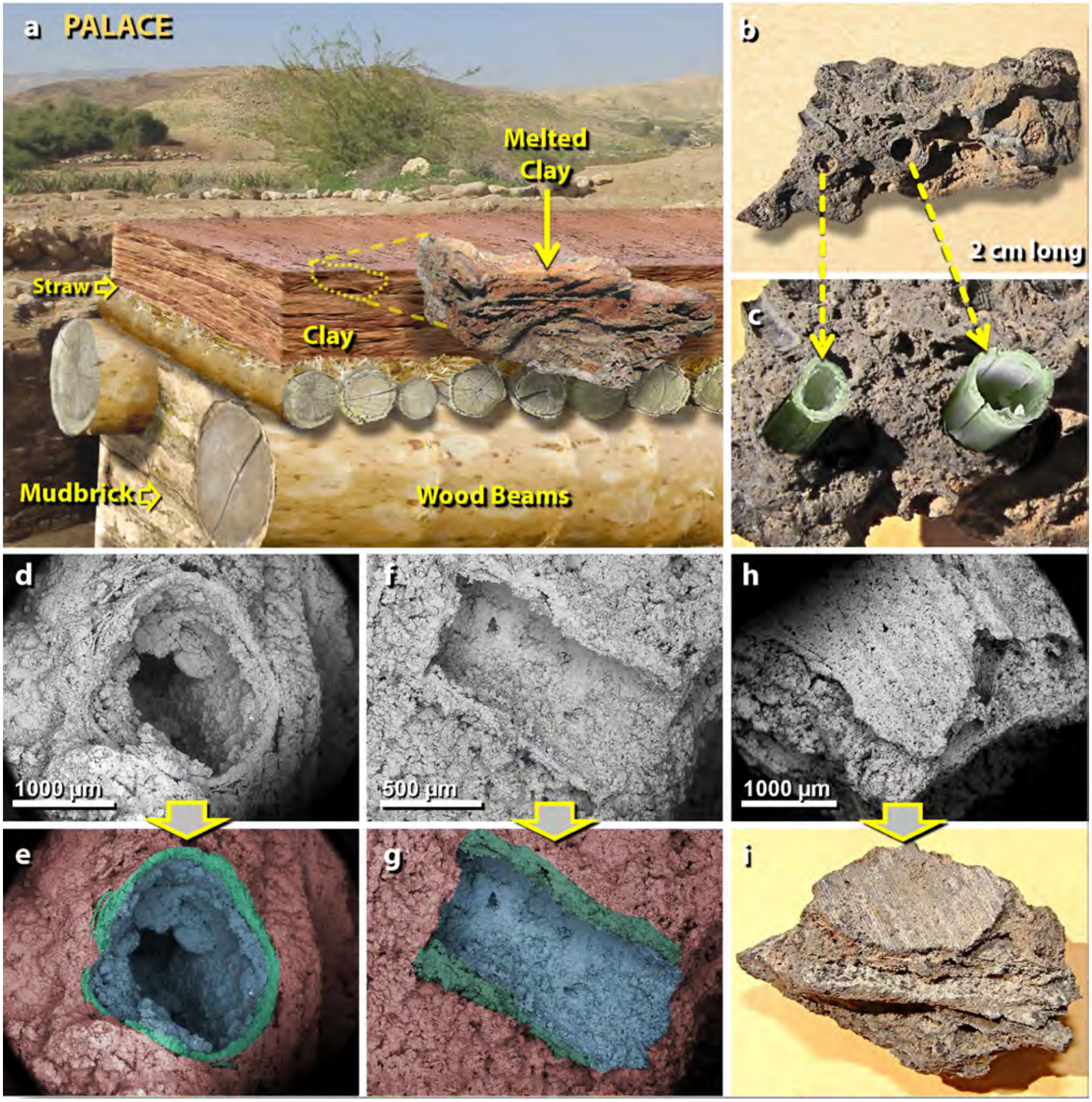

Figure 13: Melted palace roofing clay. (a) Artistic cutaway depiction of typical roof construction at TeH. The construction involved sequentially plastering multiple layers of clay (~10 cm or more in total thickness) over a bed of leaves and straw placed over wood beams. The "melted clay" inset at the middle right is a photo of melted roofing clay displaying heat-distorted layers of clay plaster. **(b)** A fragment of melted roofing clay exhibiting ~2-mm-diameter tubular holes left after the incineration of straw; **(c)** artistic depiction, re-creating protruding straw before burning; **(d)** The SEM image is the end-view of the hole left by burned straw embedded in roofing clay; **(e)** manually constructed EDS-based phase map of the same image, showing composition as determined by SEM-EDS; red represents melted clay matrix, green represents high-silica glass (60-90 wt% SiO_2) formed from melted silicified straw, and blue represents the silica-rich interior of the hole. **(f)** SEM image is the side-view of the imprint left by burned straw; **(g)** manually constructed EDS-based phase map of the same image, color-coded as in the previous example. **(h)** SEM image of leaf imprint into the clay roofing material, showing the ribbed structure of a leaf; **(i)** photomicrograph of the same object.

flat and smooth (Figure 13a). The melted roofing clay was associated with ash, charcoal, charred beams, and burned textiles, which suggests exposure to high-temperature fire. Most roofing clay displays imprints of the original roof construction material, e.g., straw, plant stems, and leaves (Figures 13 and 14). Typically, the depth of melting is ~1-5 mm. SEM analyses indicate that most imprints exhibit siliceous plant components, including phytoliths, parenchyma

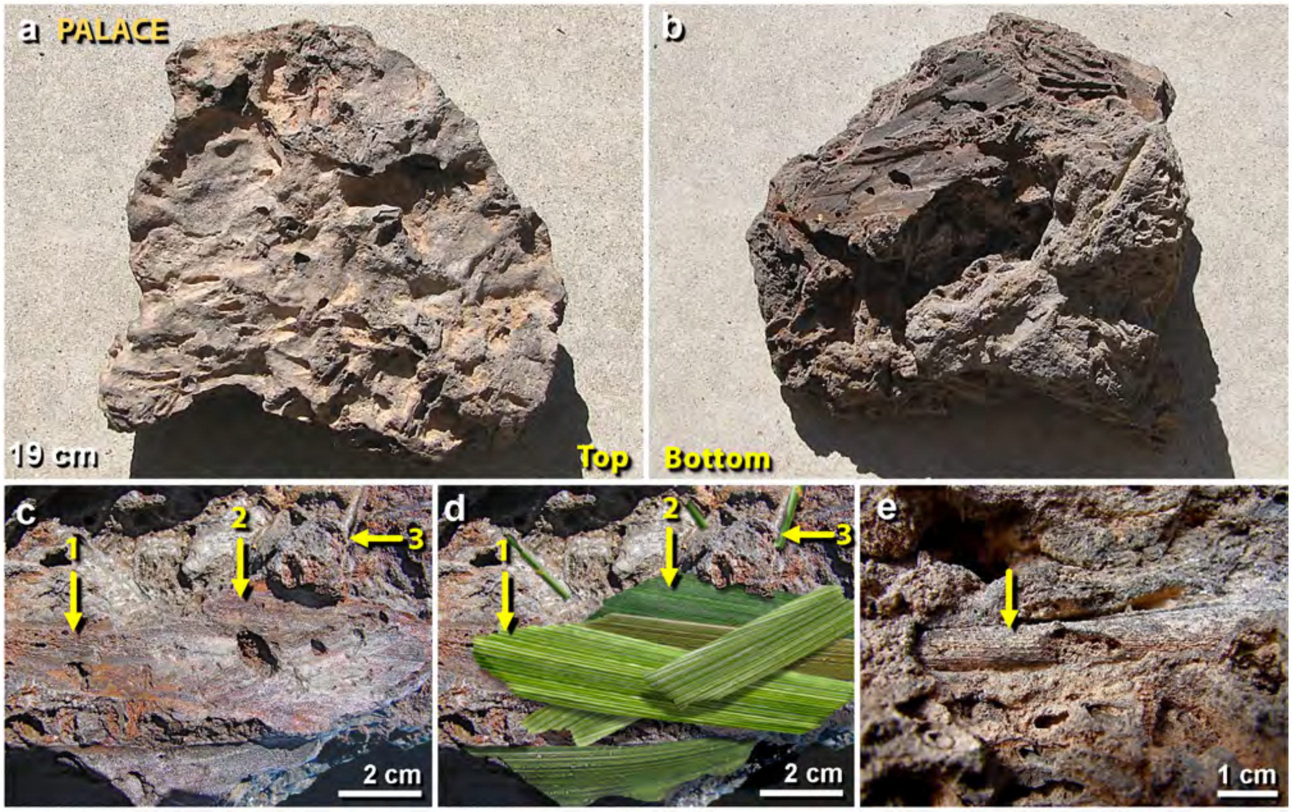

Figure 14: Plant imprints in melted roofing clay from the palace. (a) The upper surface of a 19-cm-wide piece of roofing clay, melted and distorted at high temperatures; **(b)** the lower surface of the same object, showing imprints of silicified plant material; **(c)** closeup of the lower surface with numbered yellow arrows pointing to ribbed imprints of leaves pressed into the bottom of roofing clay (#1 through #3); **(d)** artistic depiction, re-creating possible leaf structures before combustion; **(e)** yellow arrow points not to a plant imprint, but rather to a cylinder-like silica-rich pyromorph of plant stem embedded in roofing clay. The samples are from the destruction layer in the palace (Field UA, Square 7GG).

cells, stomata, and siliceous plant fibers, apparently fused into the roofing clay at high temperatures. Scratch testing indicated that the hardness of the plant-imprinted roofing clay was between 5.5 (glass) and 7.0 (quartz) on the Mohs scale. Their hardness is substantially greater than typical sun-dried mudbrick (2-4 Mohs hardness).

Interpretation of melted roofing clay

Exposure to high temperatures is inferred to have vaporized the water and carbon from the plant material and fused the silicified material and clay into hard vitrified masses. This process appears similar to that documented for proposed airburst/impact materials at Abu Hureyra, Syria [36], and Dakhleh Oasis, Egypt [50].

The clay imprints of siliceous plant material are inferred to be composed of biogenic hydrated silica ($SiO_2 \cdot H_2O$). Plants use dissolved silica from soils to produce Si-rich cell walls and connecting tissue, increasing the plants' rigidity, toughness, and herbivore resistance [51, 52]. This siliceous material can be freed from surrounding plant tissue by fire at ~450-550°C but does not melt at such low temperatures [53]. After combustion, these siliceous structures can retain their original morphologies [36]. Moore et al. [36] reported laboratory experiments with an oxygen/propylene torch in which temperatures of >1250°C were required to melt siliceous plant material embedded in Ca-Al-Si meltglass fully.

Summary of 4. High-temperature impact-related materials

Proxy Types:

- Melted ceramics, mudbrick, roofing clay
- Thermal gradients, vitrified inclusions
- Remanent magnetism

Analysis Methods:

- SEM-EDS, microscopy, thermal and magnetic testing

Key Findings:

- Glazed surfaces and vesicles show flash heating; melting is confined to the outer 2 mm.
- Heating >1400–1500°C confirmed; unmelted quartz implies brief exposure.
- Magnetism tests rule out lightning.
- Melted clays retain leaf imprints, fused phytoliths, and hardness consistent with vitrification.

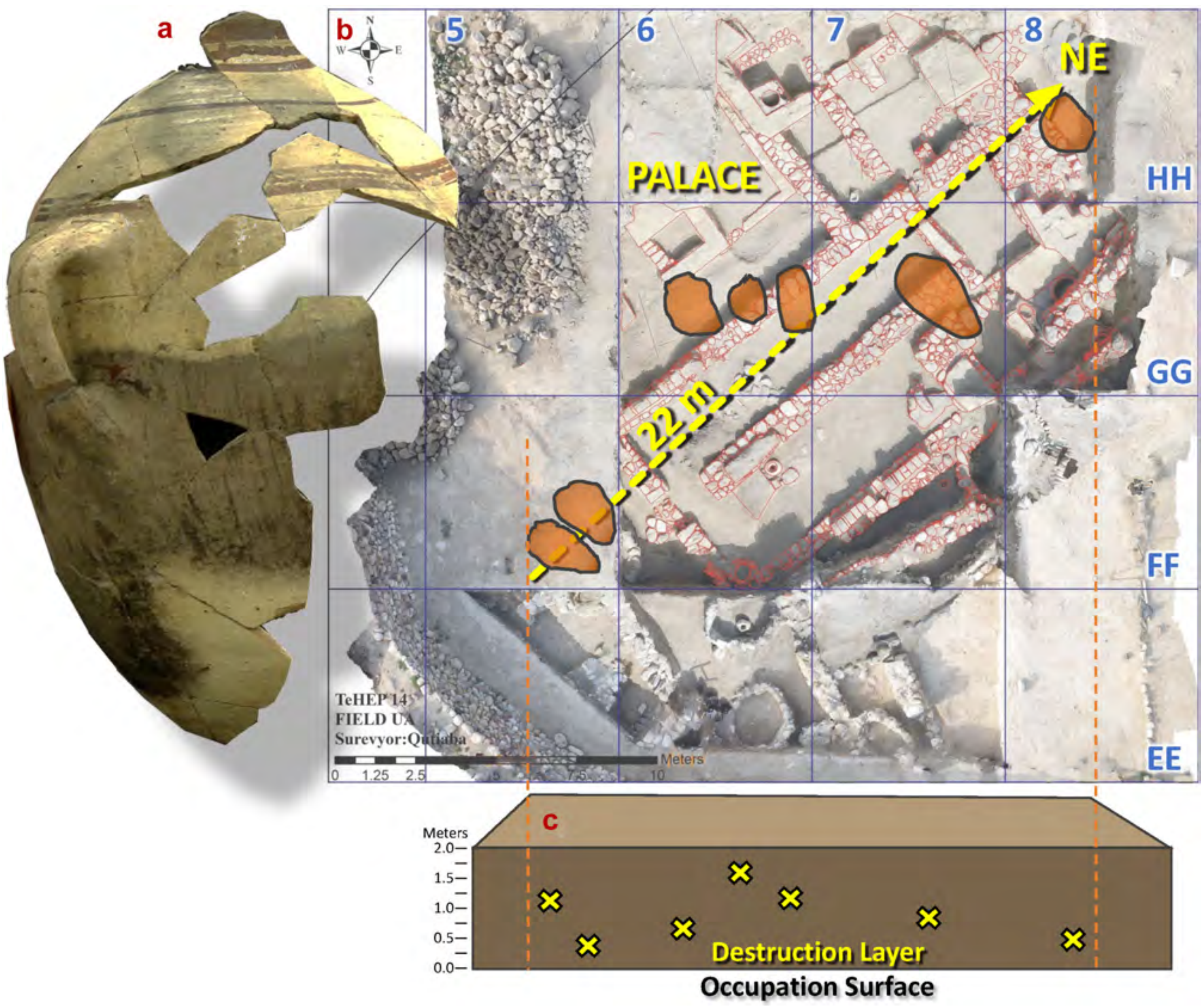

Figure 15: Directionality of potsherds from a single vessel. (a) Palace: a single distinctively decorated large vessel partially reconstructed from multiple potsherds. **(b)** An aerial view of the excavation site shows the locations of seven clusters of potsherds from the vessel, as shown in panel 'a.' The sherds were distributed ~22 m across six palace walls in multiple rooms. Also, the potsherds were found on top of some foundations, suggesting the walls no longer stood when the sherds were emplaced. **(c)** This panel represents a side view of the occupation surface. No potsherds from this single distinctively decorated vessel were found in contact with the occupation surface. Instead, all were "floating" ~0.25 to 1.75 m above the floor and wall foundations within the churned-up terminal destruction layer. Image and caption reproduced/adapted from Silvia et al. [2].

5. City-wide, SW-to-NE directionality of debris

5.1 Directional orientation of potsherd, charcoal, grains, and bones

The following section is reproduced/adapted from Silvia et al. [2]. Over 16 field seasons at TeH, extensive excavations were conducted across approximately 100 ~6 × 6-meter squares across the upper and lower tall. Bunch et al. [1] and Silvia et al. [2] identified linear directionality of potsherds, bones, charred grains, charcoal, plaster detritus, and blow-over deposits in multiple locations (Figures 15–18); however, they provided limited evidence to support this claim. Their studies attributed the observed directionality to high-velocity winds generated by an airburst event, with models estimating nearly supersonic wind speeds ranging from 255 m/s for a 60-meter asteroid to 330 m/s for a 75-meter asteroid. Their conclusions regarding directionality were drawn from a comprehensive analysis of 79 site photographs and drawings, along with ~100 field observations documented in archaeological Season Reports and the Ph.D. dissertation of co-author Dr. Silvia [6]. For further details, see Silvia et al.'s **Appendix, Oriented Materials, Table A2**.

Oriented trails of potsherds

Of the uniquely identifiable potsherds analyzed in this study, approximately 187 out of 191 (98%) are oriented in

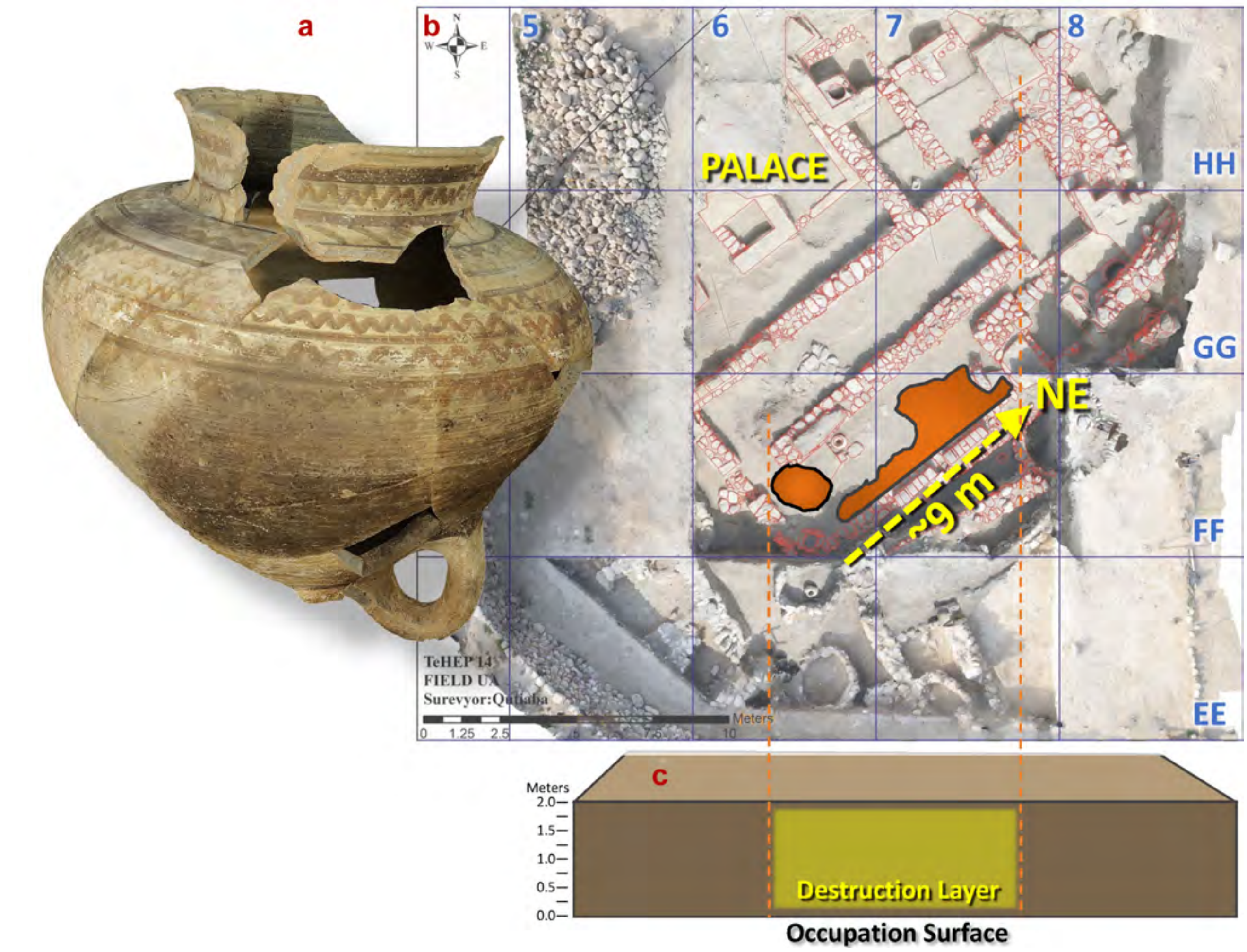

Figure 16: Directionality of potsherds from a single vessel. (a) Palace: ~12 reassembled sherds from a single distinctively decorated large vessel. **(b)** An aerial view of the excavation site shows the potsherds' locations, distributed across ~9 m from SW to NE. They were mixed with ~50 different vessels in three 6 × 6-m excavation squares and were intermingled with charcoal and carbonized grain. **(c)** This panel represents a side view of the occupation surface. No potsherds from this single distinctively decorated vessel were found in contact with the occupation surface on which they were initially placed. Instead, all were found "floating" randomly ~0.25 to 1.75 m above the floor within ~1.5 m of the 2-m-thick churned-up terminal destruction layer (yellow shaded area). Image and caption reproduced/adapted from Silvia et al. [2].

groups ranging from ~NNE to ENE, with an average direction of NE [1, 6]. Some clusters consist of potsherds from multiple vessels, while others originate from single vessels. Additional examples of directional potsherds can be found in Silvia et al.'s **Appendix, Figures A5–A10**. As shown below, widely dispersed potsherds from several distinctively decorated pots were narrowly spread over a distance of up to ~22 meters within the excavations, following an average SW-to-NE orientation (Figures 15 and 16). The specific site locations where directional evidence was observed are listed in Silvia et al.'s **Appendix, Oriented Materials, Table A2**.

Importantly, Bunch et al. [1] and Silvia et al. [2] found very few potsherds in direct contact with the original floor where they were almost certainly placed initially. Instead, they were suspended at varying depths of up to 2 m within a churned-up matrix of potsherds, broken and pulverized mudbricks, meltglass, melted pottery, microspherules, and charred building materials. All potsherds identifiable from single vessels exhibited a linear orientation, approximately SW to NE (range: ± 25°) (Figures 15 and 16). Only a few smaller intact vessels were recovered, likely preserved due to their small size or sheltered location. Among the broken vessels, it was rare to find all fragments within a single 6 × 6-meter excavated square; rather, sherds from the same shattered vessel were typically dispersed over distances exceeding 6 meters. As noted in Bunch et al. [1], this phenomenon was unique to the MBA terminal destruction layer and was absent from both older and younger stratigraphic layers at TeH and has not been reported at any other known site across the Middle East. This distribution pattern contrasts sharply with earthquake-related destruction, where vessels are typically shattered in situ and buried beneath collapsed walls and roofing material.

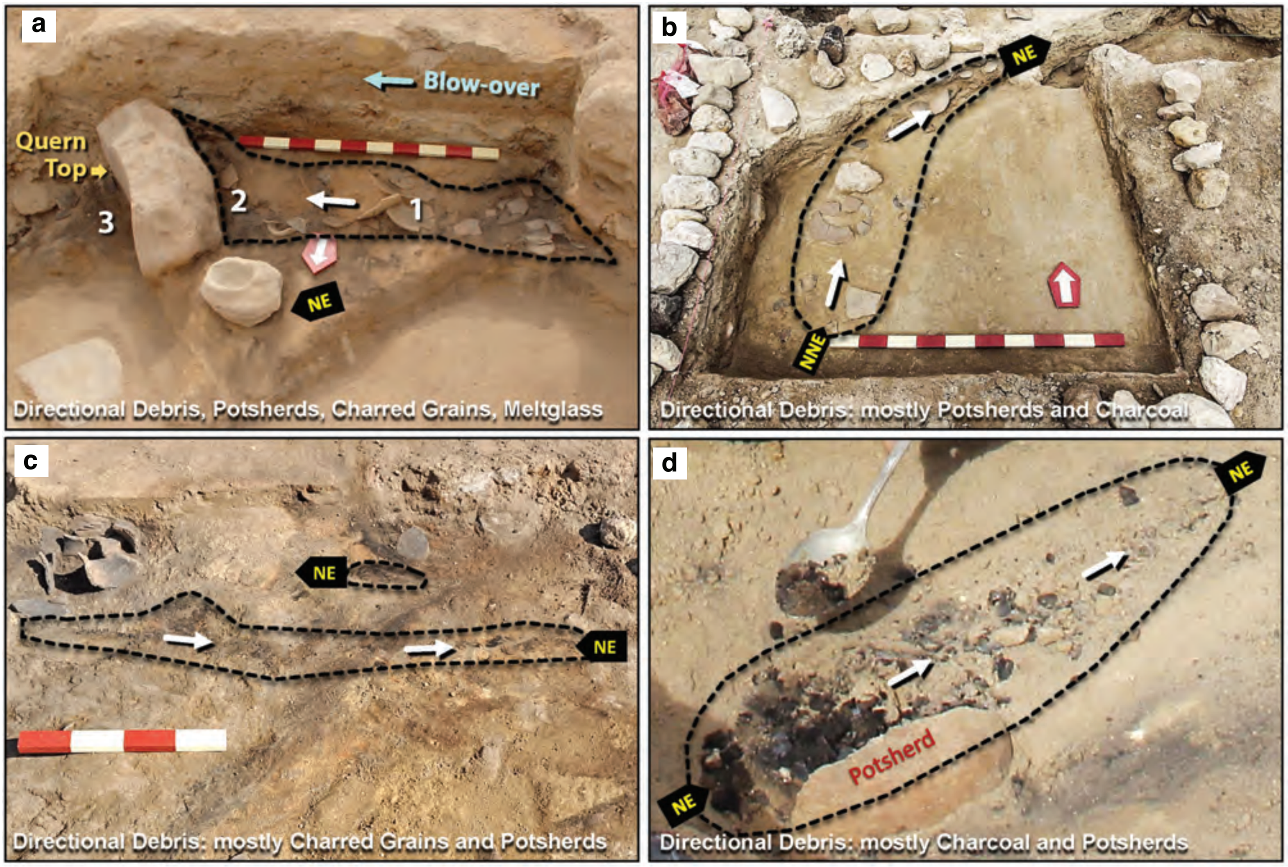

Figure 17: **The directionality of mudbricks, potsherds, charred grains, and charcoal.** Black dashed lines indicate the areas of interest. **(a)** 400-kg quern, at left in the photo, used for grinding grain while kneeling, is tipped over with the top towards the NE. Image view spans ~2.5 m. Area #1 shows broken pottery and meltglass piled along a sheared-off mudbrick wall; the direction of travel was from SW to NE (white arrow). The red arrow indicates north. Area #2 shows potsherds and meltglass piled against the bottom of the tipped-over quern. Area #3 on the NE side of the quern displays small amounts of charcoal, charred grains, ash, and mudbrick fragments but no potsherds, suggesting that the quern shielded the floor on its NE side. The area at the top labeled blow-over is evidence that strong winds sealed the quern with weakly laminated material, including pulverized mudbrick, charcoal, ash, and fragments of white building plaster. The draping of the blow-over indicates debris traveled from ~SW to NE, whether from strong impact-related winds or as fallback material from the dust-laden impact cloud. The scale stick is in 10-cm intervals. **(b)** Ring road: a trail of potsherds from the single pot that traveled ~1.2 m along an NNE-trending mudbrick wall and then, after striking an NE-trending wall, curved and continued along it. **(c)** Ring road: streaks of charred grains spanning up to 1.1 m (black dashed line with white arrows). **(d)** Palace: a SW-to-NE-trending streak of charcoal spilled out of a broken vessel (potsherd) and continued ~0.5 m to the NE. Image and caption reproduced/adapted from Silvia et al. [2].

Oriented grinding stone (quern), pottery, and charred grains

Within the palace's sealed, undisturbed MB II context, excavators uncovered a heavy saddle quern (weight: ~400 kg or 880#; dimensions: ~90 x 50 x 40 cm). Made of dense local stone and used for grinding grain while kneeling, the quern was found toppled from its dirt pedestal and tipped on its side on the floor of a food preparation area (Figure 17a). The geometric axis of the quern aligns with the SW-NE direction. Barley grains that had once been on top of the quern were found carbonized and strewn across the floor ~1 m to the NE between the overturned quern and the SW-facing wall, suggesting SW-to-NE movement (Figure 17a). Radiocarbon dating of the carbonized wood and grain on the floor confirms ~1650 BCE (~3600 ± 50 cal BP) as the date for the destruction event. Figure 17b shows potsherds from several broken vessels that traveled NNE until colliding with a sheared mudbrick wall, after which they continued ~1.2 m to the NE.

Oriented trails of charred grains and charcoal

Silvia et al. [2] reported that nearly every 6 × 6-m square excavated contained irregular elongated streaks of charred grains and charcoal, with an estimated 80% oriented NNE to ENE, averaging ~NE (Figure 17c, 17d). Additional examples of directional charred grains/charcoal are shown in Silvia et al.'s **Appendix, Figure A11 and A12**. This material is commonly visible on upper excavated surfaces and vertical side-wall surfaces.

The selected photographs below include top-down views of the ~NE-oriented potsherds, charred grains, and charcoal.

Boslough [54] attempted to refute the hypothesis of TeH's directionality by erroneously claiming he could determine directionality (i.e., wind direction) using photos of a two-dimensional trench wall, e.g., Figures 3, 6, and 18. Such a conclusion is impossible; wind direction can only be determined on-site by trained sedimentologists who examine the sediments in three dimensions, especially from the top down.

Evidence of directionality from SW to NE within buildings has been identified in ~100 excavated squares across the site (Figure 19). Directionality is indicated for up to six materials: (i) melted pottery, (ii) melted mudbricks, (iii) blow-over detritus (iv) general building material, (v) seeds and grains, and (vi) potsherds. Notably, all excavated squares, including the palace, temple, and ring road, display evidence of SW-NE-trending blow-over materials, primarily composed of churned-up deposits sealed by weakly laminated layers of pulverized mudbrick, ash, charcoal, and fragments of white plaster.

5.2 Criticism of directionality, blow-over layers, and high temperatures

Boslough [54] disputed the TeH directionality scenario and claimed that a shock wave or other airburst-related effects cannot produce a laminated blow-over layer. Contradicting that claim, previously published results about the 26-km-wide Ries crater by Pietrek et al. [55] reported the following impact-related effects [key phrases underlined]: "*finely laminated Tertiary clays, which are intensely plastically deformed*" that formed because the clay "*acted as lubricant for the ground hugging flow of crater derived breccias.*" Similarly, Buchner et al. [56] investigated Ries crater ejecta and reported that the following laminated features resulted from seismic waves from the impact event: "*convolute lamination and deformation in unsolidified sedimentary deposits are usually found in fine or silty sands.*" Furthermore, King et al. [57] investigated deposits from the K-Pg impact event and observed "*impactoclastic breccia*" that formed similarly to a large volcanic debris avalanche with "*evidence of early turbulent flow and a more conspicuous later stage of laminar flow.*" In addition, the Pelarda Formation in the Azuara impact crater in Spain displays thick, extensive impact ejecta exhibiting distinct laminations [58]. Moreover, excavations in the Chiemgau airburst/impact craters revealed laminated paleoliquefaction features resulting from impact-related seismicity [59]. Thus, the evidence from widely accepted impact craters/airbursts refutes Boslough's claim [54] that cosmic events cannot produce laminated deposits.

Boslough and Bruno [60] also asserted that Bunch et al.'s claims for shock wave velocities of 25 m/s (917 km/h) to 33 m/s (1200 km/h) at ~2000°C are not possible. However, they incorrectly assumed that Bunch et al.'s proposed TeH airburst wind speeds were the same magnitude as those of Tunguska. This assumption is incorrect; Bunch et al. [1] mentioned four times that the TeH airburst was "*larger than the airburst at Tunguska.*" In support of this, Bunch et al. provided two models of 12 and 23 Mt, each larger than the ~5 Mt proposed for Tunguska by Boslough and Crawford [61].

Boslough and Bruno [60] also claimed that the proposed TeH airburst could not have produced temperatures as high as 1000°C. However, Boslough enigmatically ignored his previous published results for similar airbursts. First, Boslough et al. [62] concluded that a large airburst in the Atacama Desert produced "*a supersonic vapor jet [>343 m/s] that exceeds silicate melting temperature [~1713°C],*" far higher than 1000°C. Furthermore, Boslough and Crawford modeled a 15-megaton low-altitude airburst in which "*the resulting fireball continues to descend rapidly through the atmosphere, driving a shock wave ahead of it as it moves downward at supersonic velocities,*" after which "*surface materials will be subjected to supersonic winds [343 m/s]*" and, as shown in their Fig. 8, surface temperatures reached 5800 K. That 15-megaton modeled airburst falls within the range of a 12- to 23-Mt airburst proposed by Bunch et al. [63] and Silvia et al. [2]

In addition, Boslough and Bruno [60] neglected to provide alternate explanations for the high-temperature melted minerals embedded into the surfaces of melted pottery, meltglass, and mudbrick (range >1000°C of 1064° to 2572°C; see Table 1). It is indisputable that airbursts can detonate just above Earth's surface and are capable of melting surficial sediments at >1000°C [3, 61, 64], making a near-surface airburst plausible at TeH.

In summary, Boslough and Bruno [60] maintained that the velocities, temperatures, and directionality reported in Bunch et al. are impossible for TeH. However, Boslough's previous contributions [61, 64] refute his own claims by reporting values equal to or exceeding the wind velocities and temperatures proposed in Bunch et al.

Interpretation of directionality

An inferred sequence of events that produced the destruction layer is shown in Figure 18. The following occurred over a brief span of seconds: a high-velocity, debris-entrained shock wave arrived from the SW, causing melted mudbrick, broken pottery, wall plaster, charred beams, and other interior debris to pile up against the SW-facing side of the wall; the shock wave demolished the mudbrick walls and blew the shattered remains to the NE along the base of the wall; the shock wave abraded (i.e., sand-blasted) the top surface of the wall, and deposited along its NE base a weakly laminated windblown or fallback layer of pulverized mudbrick, fragments of crushed building plaster, limestone spherules, ash, and charcoal, typically 20 to 30 cm thick. Altogether, the blast wave demolished the portions of walls and ramparts that extended higher than several courses of mudbrick, and blew the remains to the NE.

The ~2-m-thick destruction layer contained potsherds from thousands of pottery vessels, some displaying individually distinctive decorative patterns, facilitating their reassembly. Plotting the locations of sherds from individual vessels showed them to be oriented in an approximately SW-to-NE

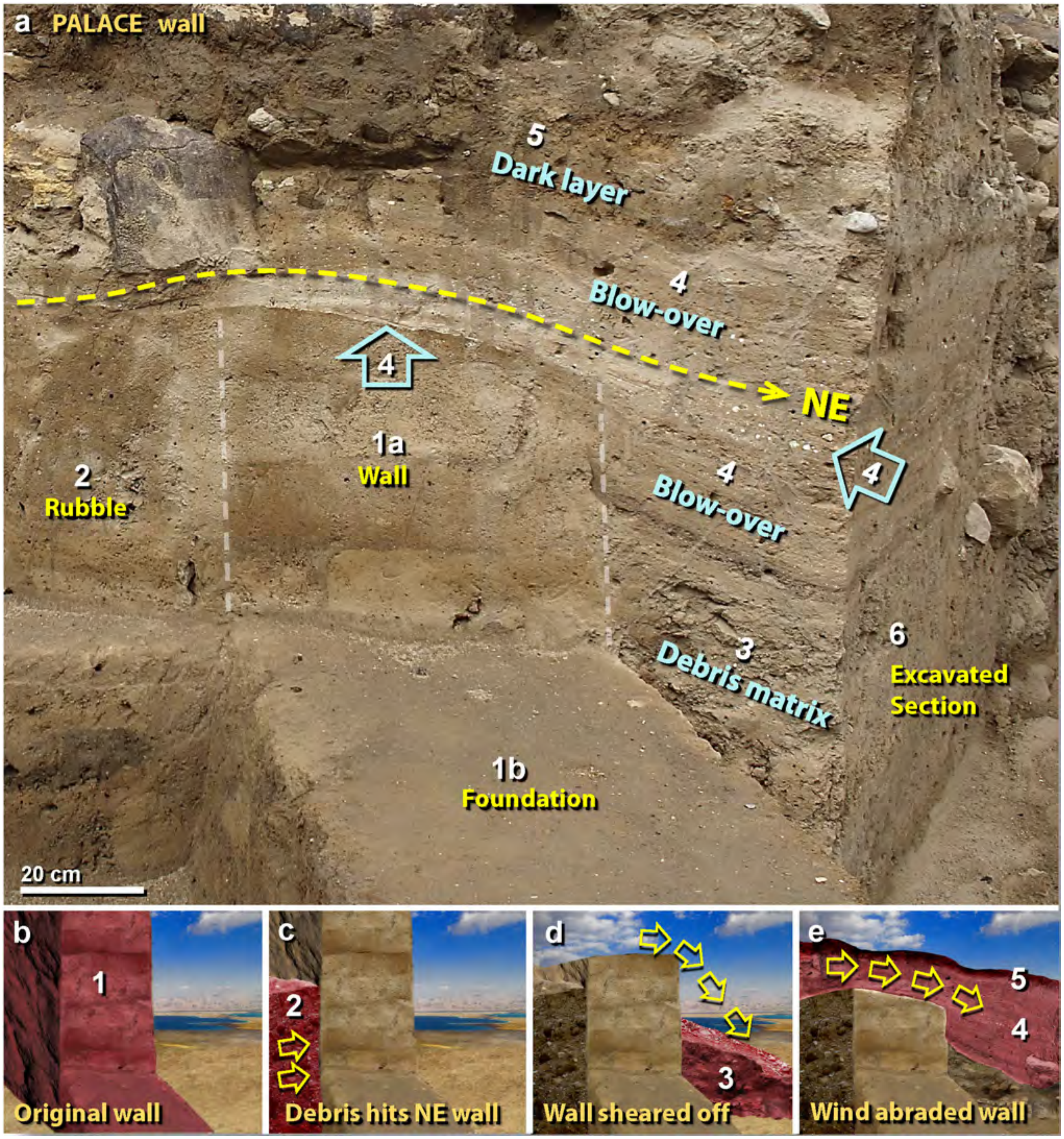

Figure 18: High-velocity effects. (a) Photo of an excavated section of the palace wall on the upper tall. In the center are the lower courses of the mudbrick wall (#1a, between white dashed lines) and foundation (#1b). The yellow dashed line and arrow indicate the wind direction of weakly laminated blow-over (blue arrow #4) to NE. Note the line of white fragments of broken plaster at the blue arrow (#4), where the curved wall top displays intense wind abrasion. It is outlined with small fragments of plaster and melted carbonate (limestone) spherules. At the right side of the image, #6 marks the limit of modern excavation. The sequence of wall destruction is illustrated in panels 'b' to 'e' below. **(b)** An artistic depiction, re-creating the pre-destruction mudbrick wall and foundation highlighted in red (#1). **(c)** Rubble in red (#2) was blown against the SW-facing side of the wall; the material mainly consists of pulverized mudbricks and shattered potsherds. **(d)** The wall section higher than several courses of mudbrick was demolished and blown to the NE, resulting in the deposition of debris matrix (#3) at the base of the wall. **(e)** High-velocity winds blew from SW to NE (arrows), severely abrading the top of the wall and burying it in debris. Winds produced the weakly laminated 'blow-over' (#4), containing small pulverized mudbricks, fragments of white wall plaster, and carbonate spherules stripped from the interior walls. The 'dark layer' (#5) on top mainly comprises charcoal, ash from city-wide fires, and fine post-destruction dust particles. Image and caption reproduced/adapted from Silvia et al. [2].

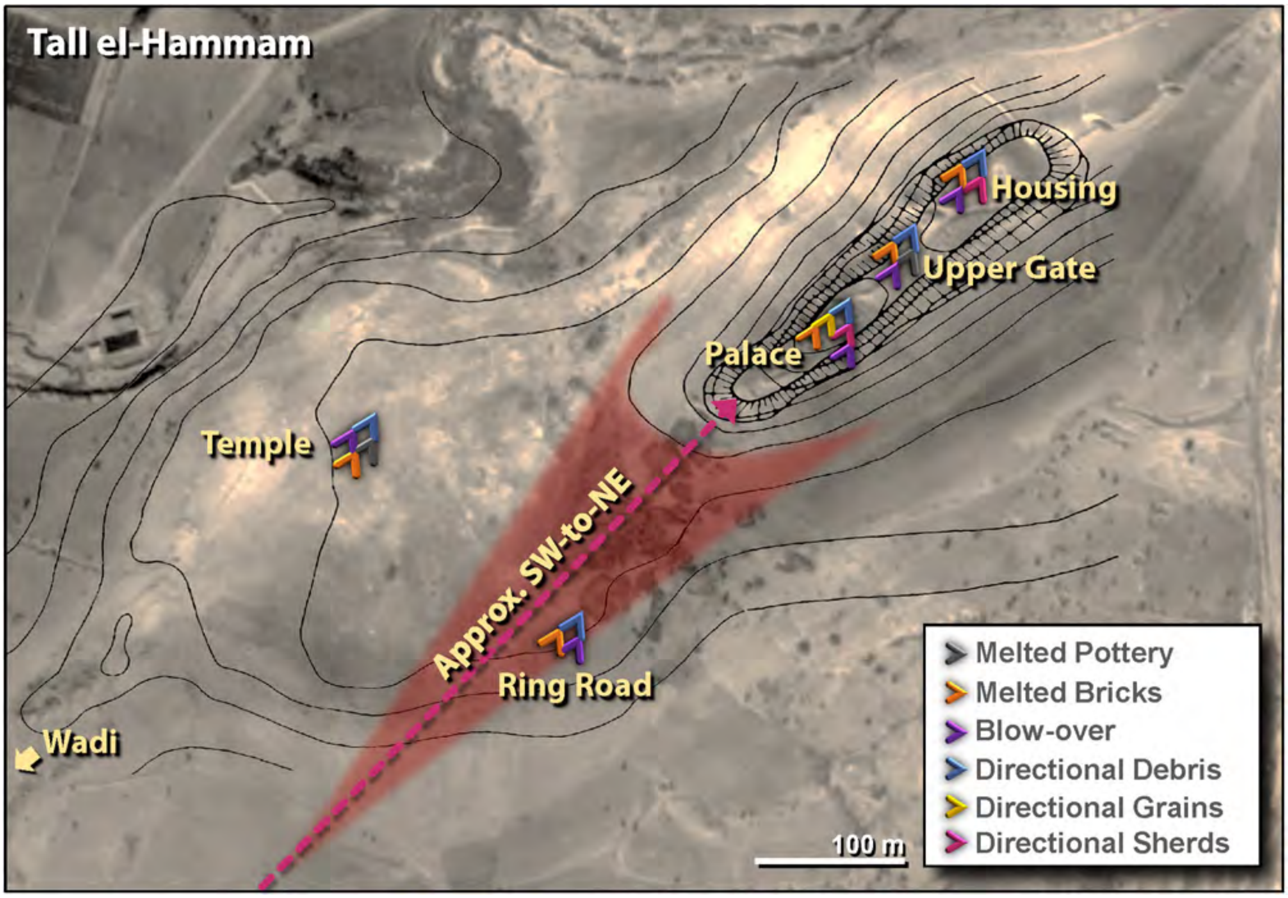

Figure 19: Directionality of debris across Tall el-Hammam. Color-coded arrows indicate the type and approximate direction of six categories of debris. A red dashed arrow highlights the inferred variation in the directionality of the airburst shock wave, moving from approximately SW to NE across excavations covering an area of ~58,000 m^2 (~480 m long by up to ~240 m wide). While the directions of most oriented materials fell within the red-shaded area, not all did. The conclusion supporting directionality is based on data compiled in Silvia et al. [2]: 32 photographs and drawings of NE-oriented potsherds; 8 photographs of 7 ~NE-oriented bones; 16 of charred grains and charcoal; 7 of plaster detritus; 4 of windblown "blow-over" deposits; and 12 captioned photographs and ~100 observations from archaeological Season Reports and the PhD dissertation of co-author, Dr. Silvia [6]. Image and caption reproduced/adapted from Bunch et al. [1] and Silvia et al. [2].

linear direction across the complex (Figure 19). The trails of sherds were intermixed with chaotically deposited debris, including mudbrick fragments, objects of daily life, carbonized wood beams, charred grain, bones, and limestone cobbles burned to a chalk-like consistency. Most of these materials were suspended within the destruction matrix above, not atop the Middle-Bronze-Age (MBA) floors.

This sequence of fallen walls, capped by blow-over layers, appears to have occurred nearly instantaneously because there is no evidence of erosion or passage of time between the top dark layer, the blow-over layers, and the underlying debris matrix. Following the destruction event, archeological evidence indicates that the city was only minimally rebuilt ~600 years later during the Iron Age. When rebuilding occurred, there was no evidence that later inhabitants recycled surviving mudbricks for rebuilding the city, and in any event, later structures are far too few to account for the massive number of missing mudbricks. Nearby cities were not rebuilt either, so no mudbricks from TeH could have been used for that purpose. Furthermore, the city foundations are sealed by pulverized mudbrick and charcoal that dates to ~1650 BCE throughout the city, indicating the destruction layer remained undisturbed for >3600 years until modern times. In summary, the evidence is consistent with the hypothesis that the city's mudbrick walls were pulverized by supersonic winds from a high-temperature event of cataclysmic proportions. Significantly, above the destruction layer, there is no evidence of extensive human re-occupation at TeH for centuries. Instead, gradual sediment erosion and redeposition buried the entire destruction layer. After that long hiatus, the city was only minimally rebuilt during the Iron Age and never returned to its former size and level of occupation.

Summary of 5. City-wide, SW-to-NE directionality of debris

Proxy Types:

- Oriented fragments (pottery, charcoal, bones)
- Blow-over laminations, tipped querns

Analysis Methods:

- Stratigraphic mapping, GIS-based trajectory modeling

Key Findings:

- ~98% of materials oriented SW-to-NE, aligned with an oblique airburst shock front.
- Single pots dispersed across 22 m, charred grain trails, and wall drapings indicate directed flow.
- Directionality is unique to the destruction layer.

6. Shock-metamorphic minerals in destruction debris

6.1 Shocked quartz grains with deformation features

The following section is reproduced/adapted from Silvia et al. [2]. Multiple studies have investigated various types of impact-related shock metamorphism in quartz, including planar deformation features (PDFs) [65–77] and planar fractures (PFs) [74, 77, 78]. Both types of lamellae are typically parallel, planar, less than a few microns wide, spaced a few microns apart, and crystallographically controlled. These lamellae are also commonly composed of amorphous silica [77], considered diagnostic of impact-cratering events [79].

In contrast, natural fractures in quartz and non-impact-related tectonic deformation lamellae (DLs) are typically non-parallel and non-planar. Most importantly, they display either hydrated amorphous silica or no silica at all, i.e., as open fractures [36, 67, 68, 70, 73, 74, 77, 80–85].

Some studies of cosmic impact structures have described another type of lamellae resulting from impact shock metamorphism and given them various names, including shock fractures [82, 86], vermicular microfractures (i.e., wormlike) [87–89], and shock extension fractures (SEFs) [87, 88, 90, 91]. These shock fractures are intergranular or intragranular cracks in quartz grains that are typically sub-parallel, sub-planar, greater than a few microns wide, spaced more than a few microns apart, not crystallographically controlled, and may or may not contain amorphous silica [76, 77, 85, 92–99]. Here, we follow previous studies [77, 85, 99, 100] and use the term "shock fractures" to denote microfractures in quartz produced by thermal and mechanical impact-related shock. Our study focused only on the subset of those shock fractures that contain non-hydrated amorphous silica, a term we use interchangeably with "*glass*."

6.2 Glass-filled shock fractures

Shock-metamorphic, glass-filled fractures differ from classical shock lamellae. Buchanan et al. [89] wrote "*Vermicular quartz [i.e., glass-filled, shock-fractured quartz], which apparently is composed of near-planar lamellae of silica glass in a host of crystalline quartz, suggests either formation by melting due to extremely high ambient temperatures (~1610°C) or by shock melting.*" Kieffer et al. [93] reported glass-filled shock-fractured quartz grains from Meteor Crater that they proposed resulted from a process called "*jetting*," in which molten quartz is injected under high pressure into shock-generated fractures in the grains. Wakita et al. [101] also observed that during the early stages of an impact, molten material might be jetted when the impactor contacts target rocks. Similarly, Ernstson [94, 97, 102] observed that target rocks and grains may fracture from thermal shock and spallation (i.e., tensile fracturing), which occurs "*where the expanding compressive shock front superimposes with the tensile rarefaction waves starting from reflection at the free surface of the impacted target.*" [97]. Under these conditions, the stress on quartz grains from the rarefaction wave exceeds their tensile strength and, thus, produces fractures. If the shock pressures and temperatures are sufficient to melt or vaporize the target material, silica vapor or melt can be injected into the fractures.

6.3 Previous investigations of shock-fractured quartz

One previous shocked-quartz study focused on the Trinity atomic airburst and Meteor Crater [77]. Two other studies focused on the airburst event at the Younger Dryas boundary (YDB) at Abu Hureyra, Syria [100] and three sites in South Carolina, Maryland, and New Jersey along the Eastern Seaboard of the USA [99]. All three studies presented evidence and a protocol for identifying glass-filled, shock-fractured quartz associated with airbursts. Their key conclusion is that quartz fractures filled with melted silica strongly indicate shock metamorphism at pressures approximately >1 GPa (= ~10,197 kg/cm^2), whether from an airburst or a typical crater-forming impact.

6.4 Methods used to identify shocked quartz

Bunch et al. [1] and Hermes et al. [77] cited multiple studies concluding that glass-filled lamellae in quartz grains are evidence of impact-related shock metamorphism. Thus, a crucial portion of Silvia et al. [2] involved identifying those quartz fractures filled with melted silica, and they reported that all the quartz grains investigated contained amorphous silica within their fractures. To reach that conclusion, Silvia et al. [2] used the following 11 techniques:

1. **EPI-illumination microscopy (EPI)** shows whether a fracture is filled but does not show whether the material is amorphous.
2. **Optical transmission microscopy (OPT)** uses crossed polarizers to determine whether parts of a quartz grain are isotropic (i.e., they remain dark during rotation) and are likely to be amorphous.
3. **The universal stage** was used in shocked quartz investigations to measure the orientations of microscopic shock-induced structures.
4. **Scanning electron microscopy (SEM)** can determine whether fractures are filled but does not determine the material's composition.
5. **Energy dispersive spectroscopy (EDS)** can determine the composition of any material filling the fractures,

e.g., amorphous silica, hydrated silica, other minerals, or polishing compounds.

6. **Focused ion beam milling (FIB)** was used to create thin slices of quartz grains for use in the TEM to investigate crystallinity.
7. **Transmission electron microscopy (TEM)** was used to determine whether fractures are filled with material and which areas are amorphous.
8. **Scanning transmission electron microscopy (STEM)** was used to determine whether fractures are filled with material.
9. **Selected area diffraction (SAD), fast-Fourier transform (FFT), and inverse fast-Fourier transform (IFFT)** are TEM techniques used to generate diffraction patterns that show which parts of a quartz grain are amorphous.
10. **Cathodoluminescence (CL)** was used to determine which parts of a quartz grain are crystalline or amorphous. Non-luminescent (black) areas indicate the presence of amorphous silica.
11. **Electron backscatter diffraction (EBSD)** was used to determine which parts of a quartz grain are amorphous and the degree to which the crystalline lattice has been damaged by shock.

6.5 Identification of shocked and shock-fractured quartz

Our collective studies (Bunch et al. [1], Silvia et al. [2], and this study) explored the characteristics of shocked quartz and glass-filled quartz fractures initially observed by Bunch et al. in the terminal destruction layer in the palace and temple. See Table 2 for characteristic details. Importantly, we also investigated whether the characteristics of these fractured quartz grains differ from those of classically shocked quartz. Abundant additional evidence is re-published in Figures 20–25 below. The results showed that an average of ~1 in 800 TeH quartz grains (n = 7 crystallites in 5 grains) display shock lamellae, ranging in thickness from <1-2 µm with an inter-lamellar spacing of ~1 to 10 µm with most lamellae in the 2-5-µm spacing range. Most shock lamellae are discontinuous for all grains and do not cross intra-grain boundaries. Most lamellae appear parallel to sub-parallel, but some are straight, and others appear curved, all of which have been reported at known impact sites, such as Meteor Crater, AZ [106]. In contrast, tectonic lamellae, i.e., ones that develop from slow strain along fault lines, are lattice dislocations that do not display open, glass-filled fractures [70, 107], allowing for differentiation from impact-shocked quartz. One example from TeH is shown in **SI Figure S6** [7].

6.6 Criticisms of TeH shocked quartz

Jaret and Harris [108] contended that Bunch et al. [1] did not follow well-established techniques and failed to provide convincing evidence of classically shocked quartz at TeH. To the contrary, Bunch et al. [1] used three analytical techniques that are standard for identifying shocked quartz: SEM, cathodoluminescence, and the universal stage, with the latter widely considered the most definitive technique for identifying shocked quartz [72, 104, 109–111]. Other techniques are sometimes used but were unavailable to Bunch et al. during the 2020-2023 pandemic. Subsequently, Silvia et al. [2] expanded on Bunch et al.'s analyses to explore the formation of classical, high-pressure shocked quartz and glass-filled, shock-fractured quartz, a form of low-shock metamorphosis. That study presented new evidence acquired using ten analytical techniques, as listed below.

Interpretation of TeH shocked quartz

Bunch et al. [1] and Silvia et al. [2] investigated three layers each from the palace and temple: one sample each from within, immediately above, and immediately below the terminal destruction layer. They observed glass-filled, shock-fractured quartz only in the terminal destruction layer, suggesting that a high-pressure, high-temperature event occurred when that layer was deposited around 3600 years ago.

The shocked TeH quartz grains are inferred to have resulted from low-grade shock metamorphism during the impact event, but we also considered other processes that can produce lamellae in quartz.

(i) **Lightning**: shock lamellae can form during lightning strikes. However, unlike impact-related shock lamellae found across the grains' interior, these only form within a few microns of the grain edge. Lightning-produced lamellae also are more closely spaced (<0.33 µm) and do not form along the (0001) plane [112], as some do at TeH. These three characteristics are unlike those observed at TeH and eliminate lightning as a likely source of shocked TeH quartz grains.

(ii) **Tectonism**: non-impact deformation lamellae can be produced by tectonically-induced pressures associated with faults, such as the Rift Zone near TeH. However, such lamellae are not oriented along the (0001) plane [105, 107]; they commonly vary by ±10-30°. Tectonic forces produce slow-strain deformation that creates lamellae with the appearance of twisted ribbons but do not contain amorphous quartz [68, 107]. SEM analyses of HF-etched grains allow for unambiguous visual distinction between glass-filled PDFs and glass-free tectonic lamellae, which are not visible on the surface of sectioned grains [68, 107]. In addition, tectonic lamellae often appear blue in CL imagery and never black [107]. This result eliminates tectonism as the source of the lamellae in all TeH quartz grains based on this criterion.

Multiple investigations [77, 85, 99, 100] observed that shocked and shock-fractured quartz could be definitively differentiated from tectonically-shocked grains in several ways. **a)** Unlike in tectonic grains, the lamellae in the impact-shocked grains are crystallographically

Table 2: Features of shocked quartz.

Deformation of quartz grains	Origin		
Features	**TeH #**	**Craters**	**Tectonics**
Lamellae width, 1-2 μm	7	Y	no
Lamellae spacing, 2-10 μm	7	Y	no
Lamellae are mostly parallel	7	Y	no
Lamellae can be sub-parallel	7	Y	Y
Lamellae can be decorated	7	Y	Y
Lamellae parallel to *c* axis	2	Y	no
Amorphous quartz in lamellae	7	Y	no
Some lamellae are healed	7	Y	no
Assymetry; lamellae indurated	7	Y	no
Lamellae visible in SEM and epi	7	Y	no
Crystallographically correct	7	Y	no
Grains show mosaicism	5	Y	no
Grains show undulose extinction	2	Y	no
Feather features	1	Y	no
Black cathodoluminescence	7	Y	no
Red cathodoluminescence	7	Y	Y
Blue cathodoluminescence	no	no	Y

Features found in shocked quartz from known impact craters ('Craters') compared to those from TeH and those in tectonically deformed quartz grains ('Tectonics'). 'TeH #' represents the number of observed TeH shocked grains. The TeH grains match all 17 features of known impact-shocked material, whereas tectonically shocked grains match only 2 of 17 features, conclusively demonstrating that TeH grains are not tectonic.

aligned. **b)** Impact-shocked lamellae are visible in SEM imaging and with epi-illumination using optical microscopy, indicating the presence of amorphous quartz. **c)** Impact-shocked lamellae are often non-luminescent (black) under CL imaging. **d)** Shock-fractured quartz grains commonly display open lamellae, i.e., with gaps between the crystalline quartz sidewalls filled with non-hydrated melted silica. These two characteristics are never observed in tectonic quartz, where fractures are crystalline dislocations, not melted silica. Thus, the TeH shocked and shock-fractured quartz grains are not tectonic in origin and, instead, are consistent with similar quartz grains previously reported in touch-down airbursts [85, 99, 100]. However, they differ from classically shocked quartz grains produced in typical cratering impacts [77], mainly because the fractures typically are sub-parallel and sub-planar, as observed in airbursts [99, 100].

(iii) **Authigenesis:** Silvia et al. [2] also considered whether the amorphous silica within the fractures might be hydrated silica ($SiO_2{\cdot}H_2O$), a common mineral that forms when dissolved quartz is deposited within grain fractures. To investigate this possibility, they analyzed the silica in all fractured grains and determined that none is composed of hydrated silica. The melted silica they observed has stoichiometric EDS ratios for Si:O (~47:53 wt%) consistent with melted quartz and inconsistent with hydrated silica, which typically contains ≥60 wt% oxygen. Thus, a high-temperature, high-velocity airburst event best explains the melted quartz observed in some fractured quartz grains from TeH.

(iv) **Anthropogenesis**: shock lamellae in quartz can be produced artificially under laboratory conditions. Most such lamellae are oriented 45° to the *c*-axis, but some are parallel. This mechanism does not apply to TeH, where the sample deposits are deeply buried and sealed from potential modern contamination.

(v) **Nuclear detonations:** shock lamellae can form in aboveground and underground atomic bomb blasts [113], but, of course, no nuclear detonations have occurred at TeH.

(vi) **Impact events**: shocked quartz is traditionally accepted as an indicator of a hard impact on Earth's surface, and so another possibility is a crater-forming impact, either at 1650 BCE or during a much older event. However, no shocked quartz grains were found above or below the destruction layer in the palace or the temple, making it likely that they date to 1650 BCE and unlikely to result from an older or younger impact event. No contemporary crater has yet been identified, but a hypothetical crater of only a few tens of meters in diameter could have been created. If so, such a small crater may have been rapidly buried by wind action and/or overbank flooding from the Jordan River and, thus, no longer be visible.

(vii) **Airbursts**: finally, the most likely scenario is that the shock lamellae resulted from exposure to high pressures and high temperatures during a super-Tunguska-like cosmic airburst. In addition, when incoming bolides detonate at altitude, they can burst into numerous meters-wide fragments that strike the ground to form small transient craters, generating enough energy to create shocked quartz.

Based on the evidence, we conclude that shocked TeH quartz grains were ejected from ground zero (either under the airburst or in a crater) as distal ejecta and diluted by much higher numbers of non-shocked detrital grains. These shocked grains are a mixture of low-grade impact-related sub-planar microfractures, planar features (PFs), feather features (FFs), and planar deformation features (PDFs), most likely formed at ~1 to 10 GPa (10 k to 100 k standard atmospheres). Most shocked TeH grains have discontinuous lamellae partially healed due to simultaneous exposure to high pressures and temperatures. We collectively infer that this shock metamorphism occurred during one or more small crater-forming impacts or airbursts w34ithin ~5-10 km of the city.

Summary of 6. Shock-metamorphic minerals in destruction debris

Proxy Types:

- Shocked quartz grains with PDFs, PFs, nPFs, and glass-filled fractures

Analysis Methods:

- SEM, TEM, EBSD, FIB, optical microscopy

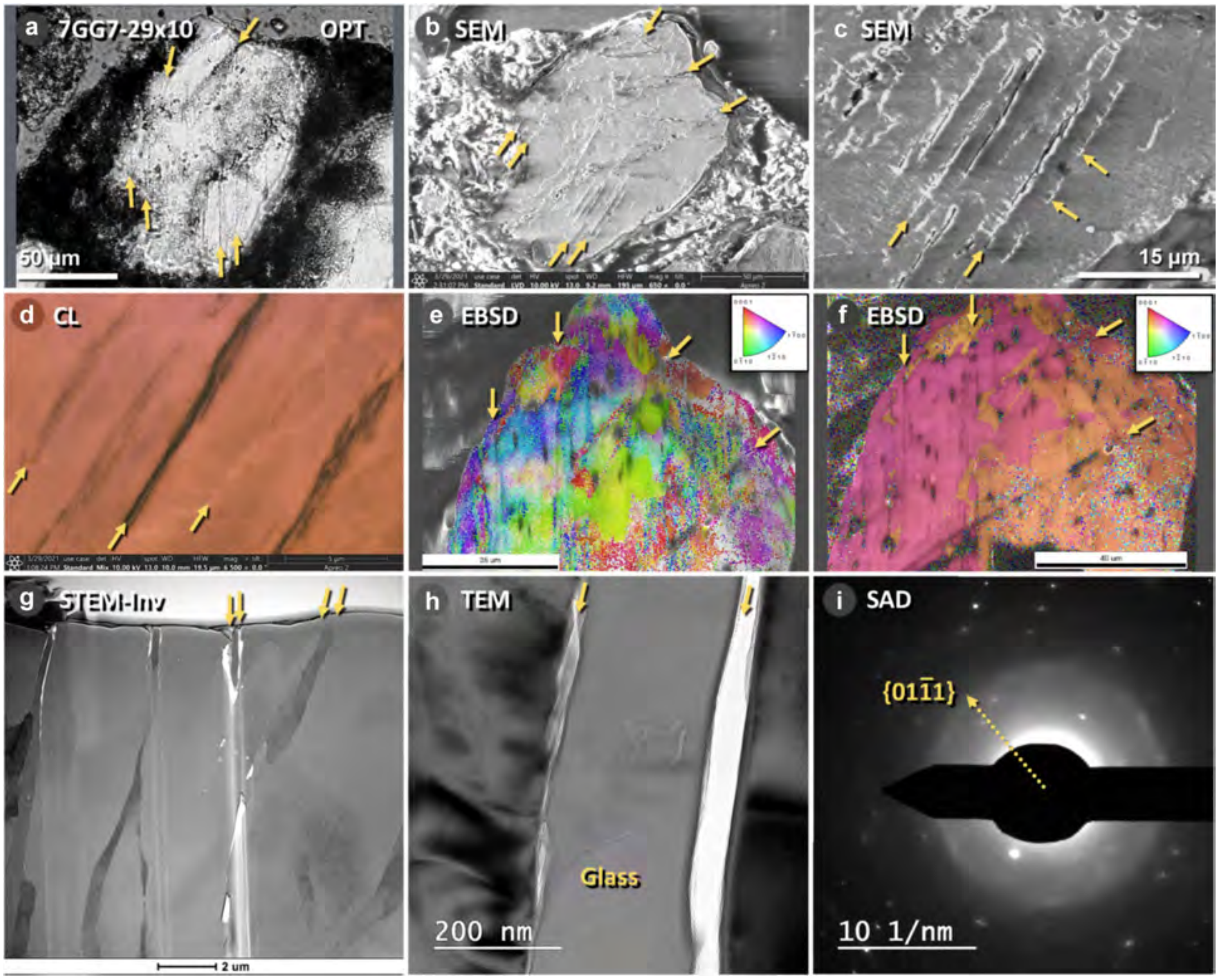

Figure 20: Shock-fractured quartz grain from the palace. All images are from grain 7GG7-29 × 10**. (a)** Cross-polarized optical photomicrograph of the shock-fractured quartz grain. Yellow arrows indicate visible shock-fractured lamellae in this and the following panels. Three sets of differently oriented lamellae are apparent. Amorphous silica remains dark during rotation under crossed polars. **(b)** SEM image of the same quartz grain. **(c)** Close-up SEM image showing two sets of lamellae. Note the short feather-like lamellae, indicative of low-pressure shock-fractured quartz [1, 103]. **(d)** Cathodoluminescence (CL) image showing oriented lamellae. Dark (non-luminescent) linear features represent fractures filled with melted silica (glass), an indicator of shock metamorphism [77, 100]. **(e)** Electron backscatter diffraction (EBSD) image. Dark linear features, marked by arrows, indicate lamellae filled with melted silica. The range of colors represents minor crystalline lattice dislocations caused by shock metamorphic damage to the grain [77, 100]. The legend of color-coded Miller-Bravais indices is at the upper right. **(f)** EBSD image of the same grain, where the two colors represent Dauphine twinning, commonly observed in shock-fractured quartz grains [77, 100]. **(g)** Scanning-transmission electron microscope (STEM) image (inverted color). Darker features at the arrows are sometimes bounded by lighter borders, representing sub-parallel and sub-planar shock lamellae [77, 100]. Note that glass-filled fractures are non-planar and non-parallel, unlike classical shock lamellae, and, therefore, cannot be indexed accurately with a universal stage. **(h)** Transmission electron microscope (TEM) close-up image showing a medium-gray lamella infilled with melted silica (glass) and bounded by open fractures (light-colored bands) and crystalline matrix (darker areas to left and right). **(I)** The selected area diffraction (SAD) pattern was acquired from the central region in panel 'h.' The bright diffuse ring indicates the presence of melted silica within an area that includes crystalline quartz, indicated by bright spots. The outer border of the diffuse halo corresponds to the {0 1 $\bar{1}$ 1} diffraction line of quartz. Panels A-D are reproduced/adapted from Bunch et al. [1] and panels E-I are from Silvia et al. [2], usable under Creative Commons, CC by 4.0 (http://creativecommons.org/licenses/by/4.0/).

Key Findings:

- Quartz grains show 2–10 GPa PDFs, not found in control samples.
- TEM and EBSD confirm crystal deformation typical of impacts.
- Features resemble shock from atomic and meteoritic explosions.

7. Shocked and shock-fractured quartz grains from the tunguska airburst

This section was reproduced/adapted from Kletetschka et al. [3] To assess the similarities/differences of TeH shocked quartz with that from the known airburst, we compared the TeH results to those reported by Kletetschka

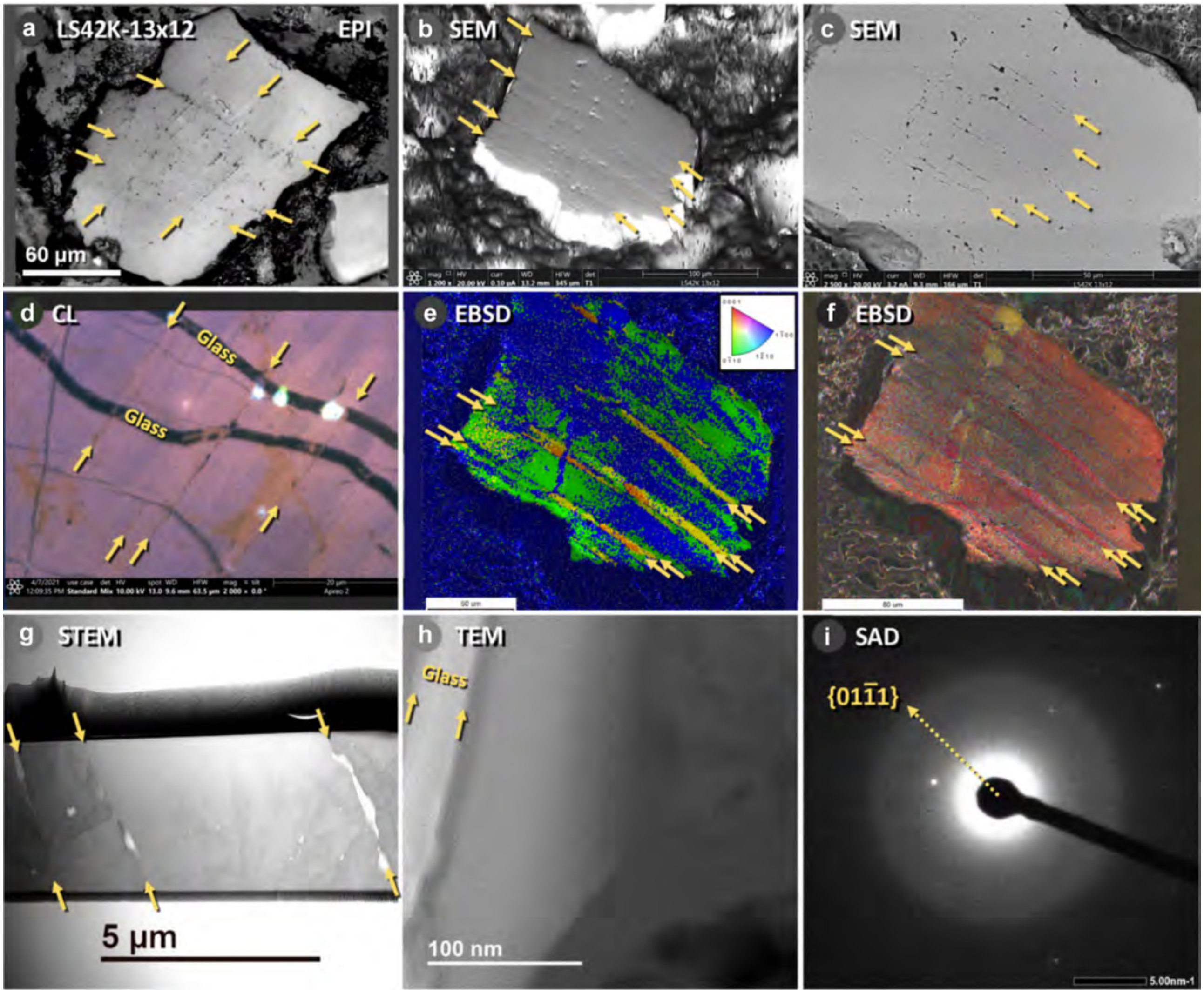

Figure 21: Shock-fractured quartz grain from the temple complex. All images are from grain LS42K-13 × 12. **(a)** Epi-illuminated photomicrograph of shock-fractured quartz grain. Yellow arrows indicate visible shock-fractured lamellae here and in the following panels. Two sets of differently oriented lamellae are apparent. **(b)** EBSD-SEM image of the quartz grain. **(c)** Close-up SEM image of lamellae, indicative of shock-fractured quartz [1, 103]. **(d)** Cathodoluminescence (CL) image displaying oriented lamellae. Darker linear features represent open fractures filled with melted silica (glass), an indicator of shock metamorphism [77, 100]. **(e)** Electron backscatter diffraction (EBSD) image. Linear features at arrows indicate twinned lamellae infilled with melted silica. The wide range of colors represents crystalline lattice dislocations caused by shock metamorphic damage to the grain [77, 100]. The alternating colors represent Dauphine twinning, commonly observed in shock-fractured quartz grains [77, 100]. **(f)** Another EBSD image similar to panel 'e.' **(g)** Scanning-transmission electron microscope (STEM) image (inverted color). The darker features at the arrows, bounded in some cases by light borders, represent sub-parallel, sub-planar shock lamellae [77, 100]. Because some glass-filled fractures are non-planar and non-parallel, unlike classical shock lamellae, they cannot be indexed accurately with a universal stage. When present, the PDFs and PFs were indexed. **(h)** A close-up transmission electron microscope (TEM) image shows a lamella at arrows filled with melted quartz (glass). **(i)** This selected area diffraction (SAD) image was acquired in the region in panel 'h.' The bright diffuse ring indicates the presence of melted silica within an area that includes crystalline quartz, indicated by bright spots. The outer border of the diffuse halo corresponds to the $\{0\,1\,\bar{1}\,1\}$ diffraction line of quartz. Panels 'A' and 'D' are reproduced/adapted from Bunch et al. [1] and all other panels are from Silvia et al. [2], usable under Creative Commons, CC by 4.0 (http://creativecommons.org/licenses/by/4.0/).

et al. [3] and Bunch et al. [1] The Tunguska airburst [114] was estimated at ~5 to 30 megatons of TNT equivalent at an altitude of 5-15 km. In addition, Bunch et al. [1] and Kletetschka et al. [3] considered whether the evidence indicates that the TeH airburst was more powerful than the one at Tunguska.

In a previous study, shocked quartz was reported at Tunguska a few miles from ground zero [115] but has been disputed as being from an earlier impact event [116]. A previous hypothesis explains how shock lamellae might form in a cosmic airburst like Tunguska. Kletetschka et al. [117] proposed that when unconsolidated surface sediments

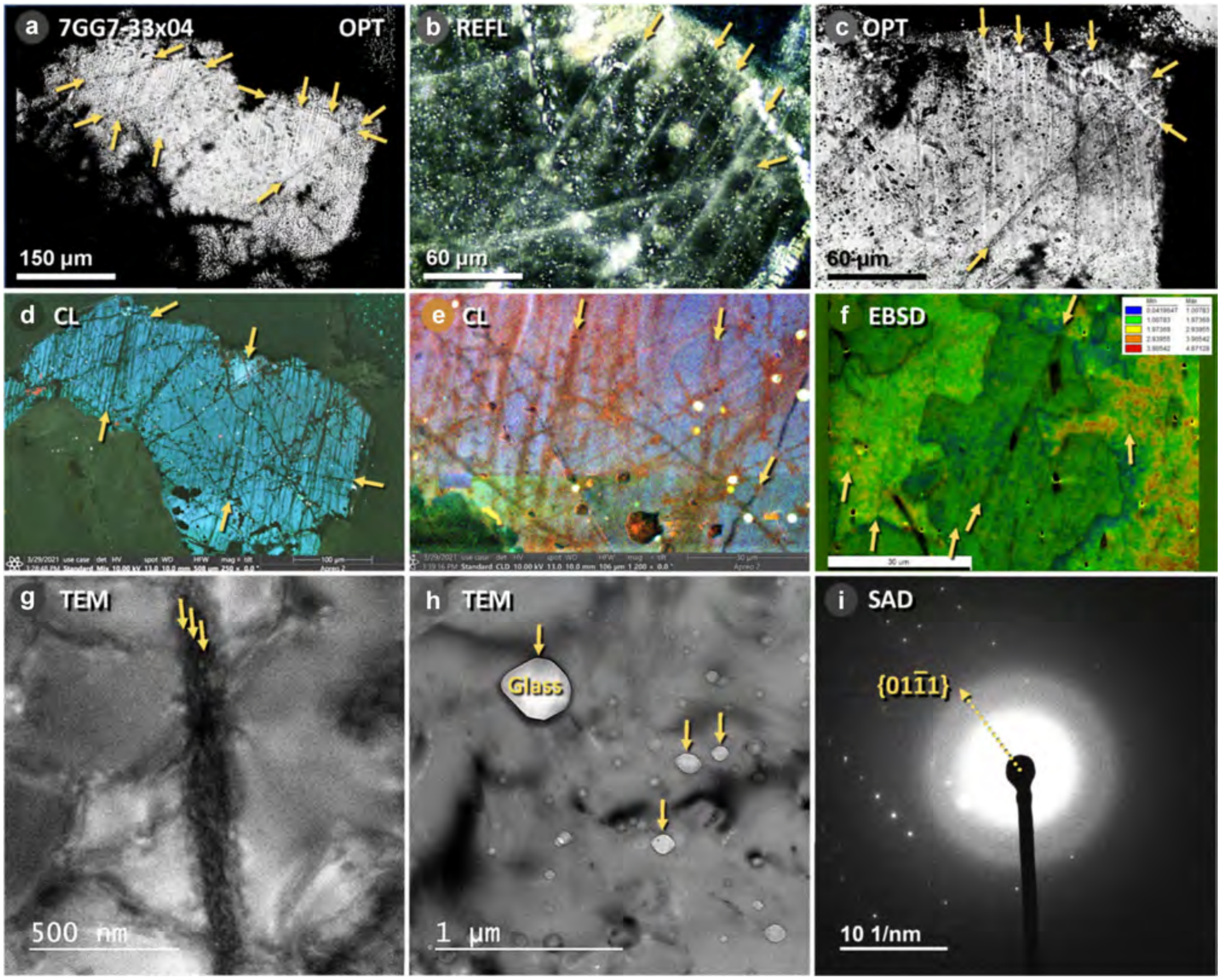

Figure 22: **Shock-fractured quartz grain from the palace.** All images are from grain 7GG7-33 × 04**. (a)** Cross-polarized optical photomicrograph of shock-fractured quartz grain. Yellow arrows indicate visible shock-fractured lamellae here and in the following panels. Three sets of differently oriented lamellae are visible. **(b)** Reflected-light close-up photomicrograph showing visible lamellae. **(c)** Close-up cross-polarized optical photomicrograph showing three sets of shock-fractured lamellae. **(d)** Cathodoluminescence (CL) image showing oriented lamellae. TEM imaging below confirms that some black linear features represent open fractures, while others contain melted silica (glass), an indicator of thermal or mechanical shock metamorphism [77, 100]. **(e)** Another CL image also displays red and dark linear features indicative of melted silica [77, 100]. **(f)** Electron backscatter diffraction (EBSD) image. Linear features at arrows indicate lamellae infilled with melted silica. The range of colors represents crystalline lattice dislocations caused by shock metamorphic damage to the grain [77, 100]. Dark green represents minimal damage, ranging to red, indicating substantial lattice damage. **(g)** TEM image. Multiple dark linear features at the arrows represent sub-parallel and sub-planar shock lamellae [77, 100]. **(h)** A close-up transmission electron microscope (TEM) image shows numerous vesicles infilled with melted quartz (glass). **(i)** This selected area diffraction (SAD) image was acquired in the region in panel 'h.' The bright diffuse ring indicates the presence of melted silica within the large vesicle, surrounded by crystalline quartz, indicated by the bright spots. The outer border of the diffuse halo corresponds to the {0 1 $\bar{1}$ 1} diffraction line of quartz. Panel 'd' is reproduced/adapted from Bunch et al. [1] and all others are reproduced/adapted from Silvia et al. [2].

containing quartz grains are struck by the atmospheric shock wave from an airburst, shock lamellae develop if the velocity exceeds 7 km/s, the elastic limit of quartz.

Bunch et al. [1] and Kletetschka et al. [3] searched for potential shock lamellae in thin-sectioned quartz grains (10 grains in 25 g = 400/kg, or 10 in ~4,000 quartz grains), similar to the results for TeH. A few shocked quartz grains appear to have been ejected from ground zero and mixed with numerous unshocked detrital grains. As with impact-related PDFs, the lamellae commonly appear as one or more sets that are closely spaced (2-10 µm), narrow (<2 µm), and range from curved to straight and parallel to subparallel (Figures 26–29). The lamellae in grains from Tunguska match the features of impact-shocked quartz (Table 2).

Kletetschka et al.'s analyses of grain #07 × 12 reveal lamellae along specific crystalline planes (Figures 26, 27), with both crystalline quartz and amorphous silica present (Figures 28, 29).

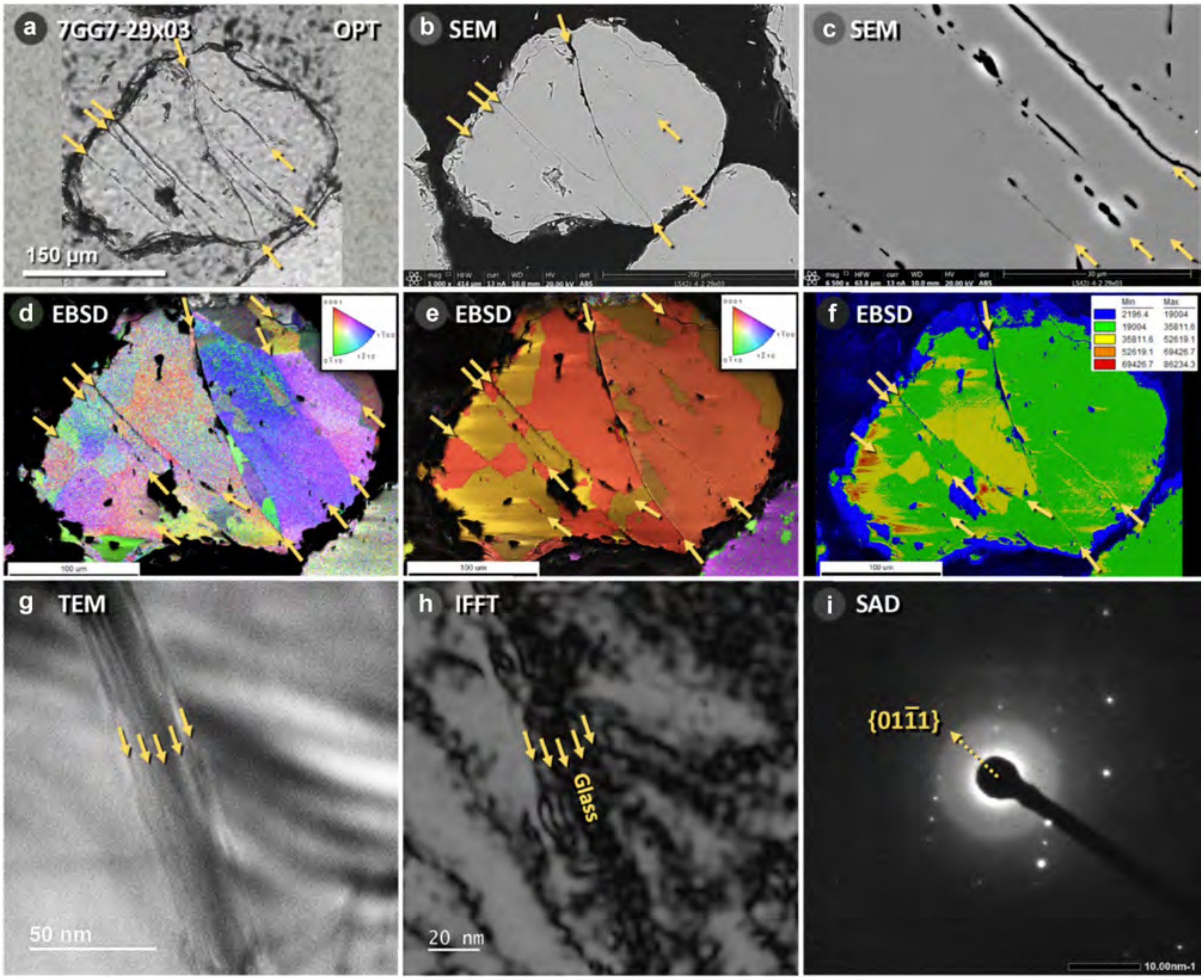

Figure 23: **Shock-fractured quartz grain from the palace.** All images are from grain 7GG7-29 × 03. **(a)** Cross-polarized optical photomicrograph of shock-fractured quartz grain. Yellow arrows indicate visible shock-fractured lamellae and PFs here and in the following panels. One set of lamellae is visible. **(b)** Scanning electron microscope (SEM) image of the same grain. **(c)** Close-up SEM image showing shock-fractured lamellae. Note that some glass-filled fractures are non-planar and non-parallel, unlike classical shock lamellae, and, therefore, cannot be indexed with a universal stage. When present, the PDFs and PFs were indexed. **(d)** Electron backscatter diffraction (EBSD) image. Linear features at arrows indicate lamellae infilled with melted silica (glass). The range of colors represents crystalline lattice dislocations caused by shock metamorphic damage to the grain [77, 100]. **(e)** Another EBSD image where the two colors indicate the presence of Dauphine twinning, an indicator of shock metamorphism [77, 100]. **(f)** EBSD image. The range of colors represents crystalline lattice dislocations caused by shock metamorphic damage to the grain [77, 100]. Green represents minimal damage, ranging to red, signifying high damage. **(g)** Transmission electron microscope (TEM) image. Multiple dark linear features at the arrows represent sub-parallel and sub-planar shock lamellae [77, 100]. **(h)** Inverse Fast Fourier transform (IFFT) image. Dark areas represent substantial grain damage, indicative of melted silica (glass); light gray areas represent minimal to no damage to the crystalline lattice. **(i)** This selected area diffraction (SAD) image was acquired in the region in panel 'h.' The bright diffuse ring indicates the presence of melted silica within the large vesicle, surrounded by crystalline quartz, indicated by the bright spots. The outer border of the diffuse halo corresponds to the {0 1 $\bar{1}$ 1} diffraction line of quartz. All images and captions are reproduced/adapted from Silvia et al. [2].

Implications of shocked quartz at Tunguska

Quartz grains in Tunguska's surface sediments typically are only minimally shocked, often with only one set of lamellae, indicating low-shock conditions. This shocked quartz shares similar characteristics at TeH, suggesting similar formation conditions. However, the shocked grains at Tall el-Hammam commonly display multiple sets of lamellae and, therefore, are inferred to have formed under much more energetic shock conditions, suggesting a more powerful airburst at TeH than at Tunguska.

Summary of 7. Shocked quartz from the tunguska airburst

Proxy Types:

- Quartz grains from Tunguska

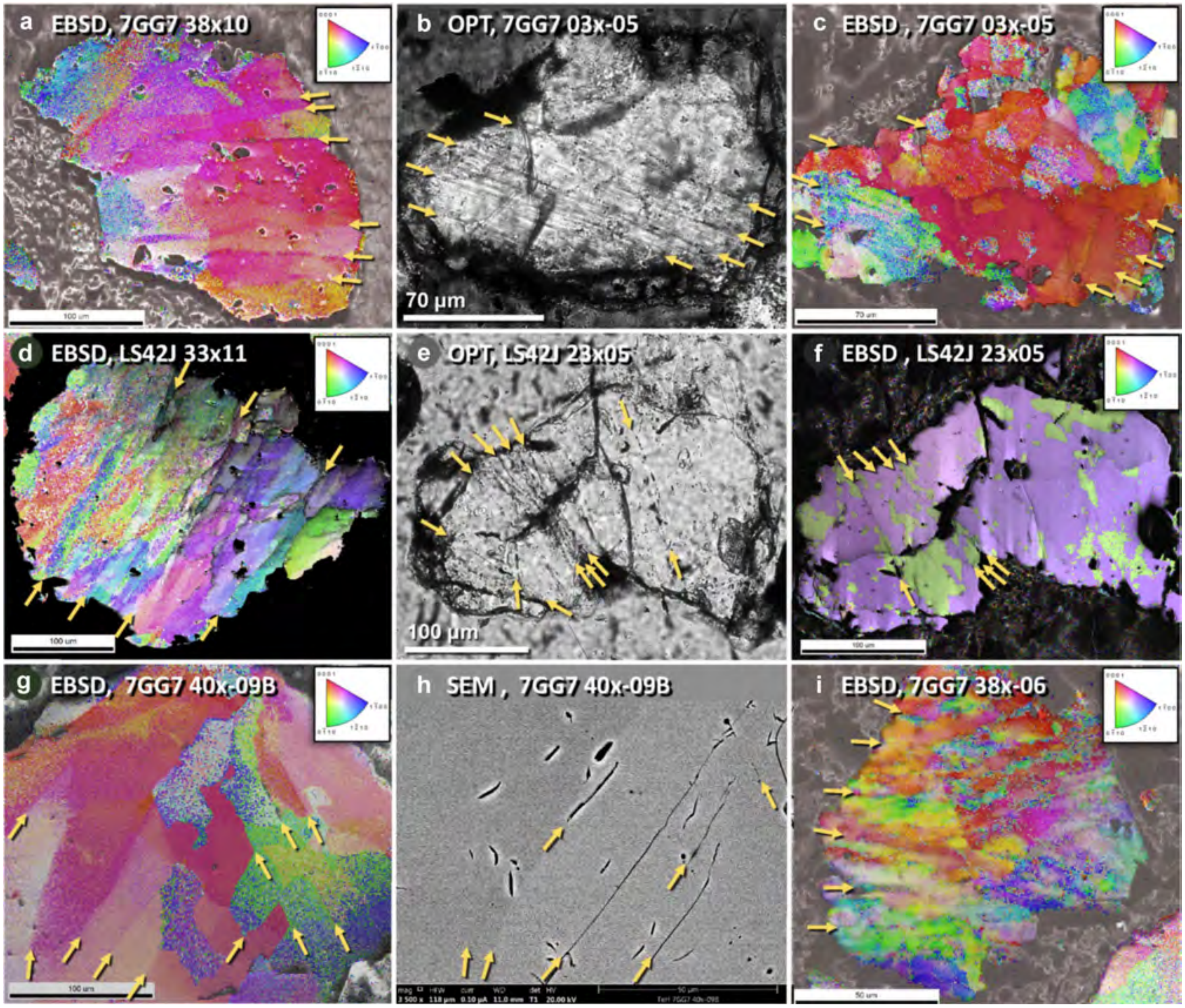

Figure 24: Multiple shock-fractured quartz grains from the palace and temple complex. (a) Electron backscatter diffraction (EBSD) image of a quartz grain 7GG7 38 × 10. Linear features at arrows indicate lamellae infilled with melted silica (glass). The range of colors represents high-pressure crystalline lattice damage [77, 100]. **(b)** Cross-polarized optical photomicrograph of shock-fractured quartz grain 7GG7 38 × –05 from the palace with one set of shock-fractured lamellae. **(c)** EBSD image of the same grain as in panel 'b' shows one set of shock-fractured lamellae. **(d)** EBSD image of quartz grain LS42J 33 × 11 from the temple complex shows one set of shock-fractured lamellae. **(e)** Cross-polarized optical photomicrograph of shock-fractured quartz grain LS42J 23 × 05 from the temple complex, showing several sets of shock-fractured lamellae. **(f)** EBSD image of the same grain in panel 'e' with two colors representing the presence of Dauphine twinning, often an indicator of shock metamorphism [77, 100]. **(g)** EBSD image of quartz grain 7GG7 40 × –09B from the palace, with a range of colors representing crystalline lattice dislocations caused by shock metamorphic damage to the grain [77, 100]. **(h)** Close-up SEM image of the same grain as in panel 'g' with multiple dark linear features at the arrows representing sub-parallel, sub-planar shock lamellae [77, 100]. **(i)** EBSD image of quartz grain 7GG7 38 × –06 from the palace shows two lamellae sets. The range of colors represents crystalline lattice dislocations caused by shock metamorphic damage to the grain [77, 100]. Images and captions are reproduced/adapted from Silvia et al. [2].

Analysis Methods:
- SEM, TEM, EBSD

Key Findings:
- Tunguska grains match TeH in PDFs and fractures.
- Supports similarity between Tunguska and TeH events.
- Number of PDFs suggests that TeH was more powerful than Tunguska.

8. High-temperature impact-related melted materials

8.1 Melted quartz grains in destruction debris

Crystalline quartz melts between 1670°C and 1713°C, and because quartz is pervasive and easily identified, melted quartz grains serve as a critical temperature indicator. At TeH, we observed that quartz grains found on broken,

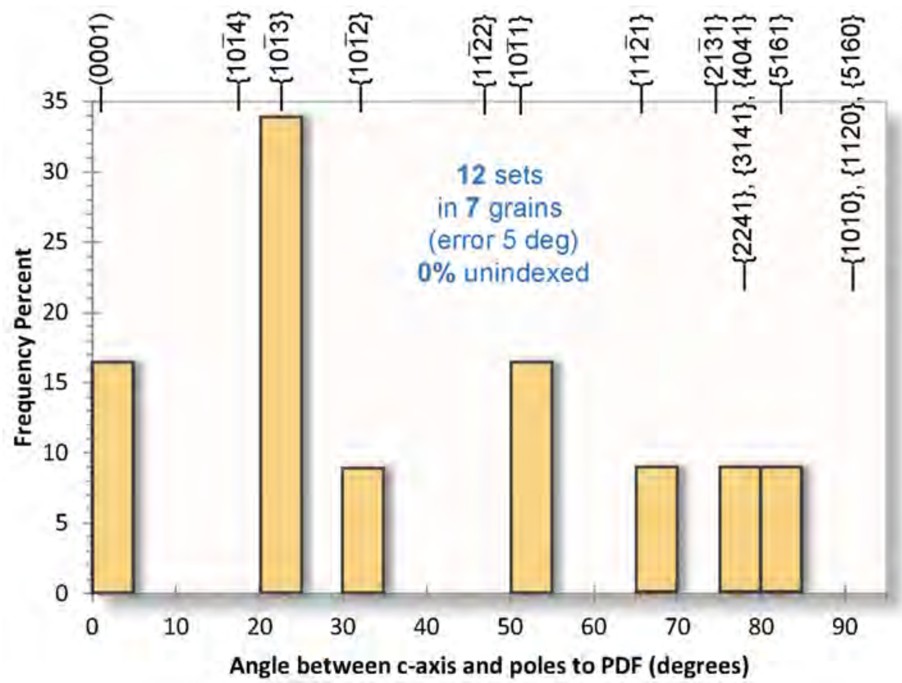

Figure 25: Crystallographic orientations of shock lamellae in quartz grains from Tall el-Hammam. Seven quartz grains from the destruction layer at TeH exhibit twelve sets of planar deformation features (shock lamellae), each aligned with known crystallographic planes. The angles of all lamellae, in degrees relative to the grain's *c*-axis, were successfully measured (indexed) using a universal stage, indicating they formed along preferred orientations typical of high-pressure shock metamorphism. The crystallographic axes were plotted with the ANIE indexing program and compared to known axes of quartz [104]. The discrete clustering of lamellae orientations in 5-degree bins is typical of those previously reported in crater-forming impacts/airbursts [77, 85, 99, 100, 104, 105], and thus, reinforces our interpretation that these are diagnostic features of a high-energy cosmic airburst. Figure reproduced from Silvia et al. [2].

unmelted surfaces of potsherds were unmelted, indicating exposure to low temperatures. On the other hand, most quartz grains on the outer surfaces of pottery, mudbricks, and roofing clay exhibited some degree of melting, and unmelted quartz grains were rare. Melted quartz grains were observed on melted pottery and mudbricks with an estimated density of 1 per 5 mm^2.

Melted quartz grains at TeH exhibit a wide range of morphologies. Some show evidence of partial melting that only melted grain edges (Figures 30, 31). Others displayed nearly complete melting with diffusion into the melted Ca-Al-Si matrix of pottery or mudbrick (Figure 30). Some melted quartz grains exhibit vesiculation caused by outgassing (Figures 30, 31), suggesting that those temperatures rose to greater than or equal to quartz's melting point of ~2230°C, at which the quartz begins to dissociate.

An SEM-EDS elemental map of one melted grain showed that the quartz had begun to dissociate into elemental Si (Figure 30b). Another grain (Figure 31c–31e) displayed flow marks consistent with exposure to temperatures well above 1713°C where the viscosity of quartz falls low enough for it to begin to flow. Another SEM-EDS analysis confirmed that one agglutinated mass of material is 100 wt% SiO_2 (Figure 31f and 31g), suggesting that this polycrystalline quartz grain shattered, partially melted, and fused together.

Interpretation of melted quartz

Moore et al. [36] reported that during heating experiments, many quartz grains <50-µm-wide exhibited partial melting at as low as 1300°C, but larger grains >50-µm-wide remained visually unaltered up to ~1700°C. By 1850°C, all quartz grains had fully melted. These experiments established a particle-size dependency and confirmed the melting point for >50-µm-wide TeH quartz grains between ~1700-1850°C. Melted >50-µm-wide quartz grains on the surfaces of melted pottery and mudbrick from the TeH destruction layer indicate exposure to unusually high temperatures >1700°C.

Previously, Thy et al. [118] proposed that glass at Abu Hureyra did not form during a cosmic impact but formed in biomass slag resulting from thatched hut fires. However, Thy et al. did not determine whether high-temperature melted grains existed in the biomass slag. To test that claim, Moore et al. [36] analyzed biomass slag from Africa provided by Thy and found only low-temperature melted grains with melting points of ~1200°C, consistent with a temperature range for biomass slag of 1155-1290°C, as reported by Thy et al. [119].

Upon testing the purported impact glass from Abu Hureyra, Moore et al. [36] discovered high-temperature mineral grains that melt from 1713° to >2000°C, as found

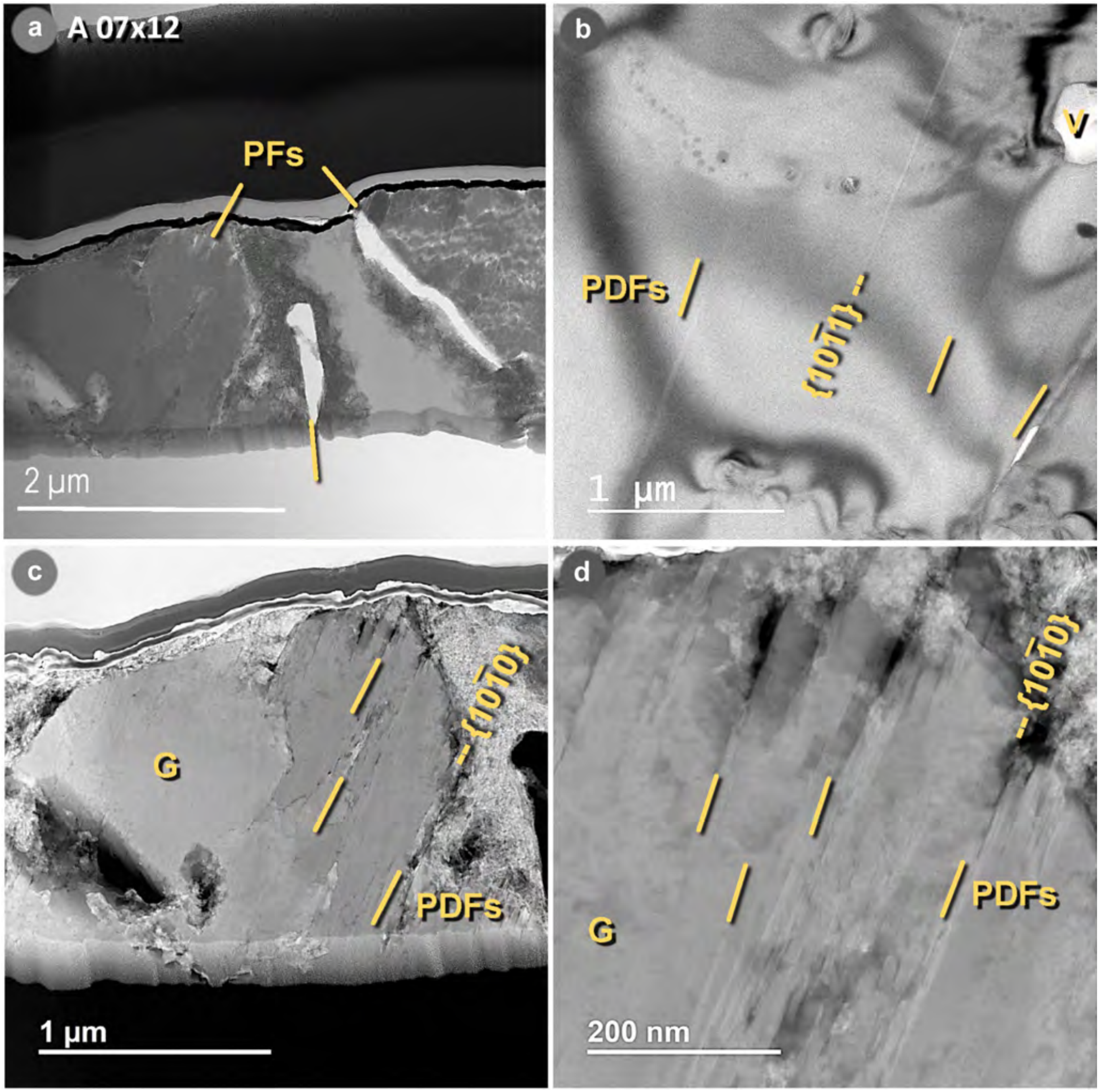

Figure 26: **Transmission Electron Microscopy revealing shock-fracturing in a Tunguska quartz grain (#07 × 12).** All panels are HRTEM brightfield images. "PFs" identify planar fractures; "PDFs" mark planar deformation features; "G" marks areas of glass, as determined by SAD; and "V" marks vesicles. **(a)** Low-resolution image of most of the FIB foil showing two large, glass-filled fractures. **(b)**, **(c)**, and **(d)** High-resolution TEM images showing multiple lamellae (yellow lines) oriented to the {1 0 $\bar{1}$ 0} and {1 0 $\bar{1}$ 1} crystallographic planes of quartz, as determined by measurements with selected area diffraction (SAD). All images and captions are reproduced/adapted from Kletetschka et al. [3].

in TeH glass. These test results suggest that the melted glass from Abu Hureyra was exposed to higher temperatures than those associated with fires in thatched huts. Because of the presence of high-temperature minerals at TeH, we conclude that, as at Abu Hureyra, the meltglass could not have formed simply by burning thatched huts or wood-roofed, mudbrick buildings.

8.2 Melted Fe- and Si-rich spherules in the destruction layer

The presence of melted spherulitic objects (i.e., "spherules") has commonly been used to help identify and investigate high-temperature airburst/impact events in the sedimentary record [36, 63, 120–129]. Although these objects are referred to here as "spherules," they display many other

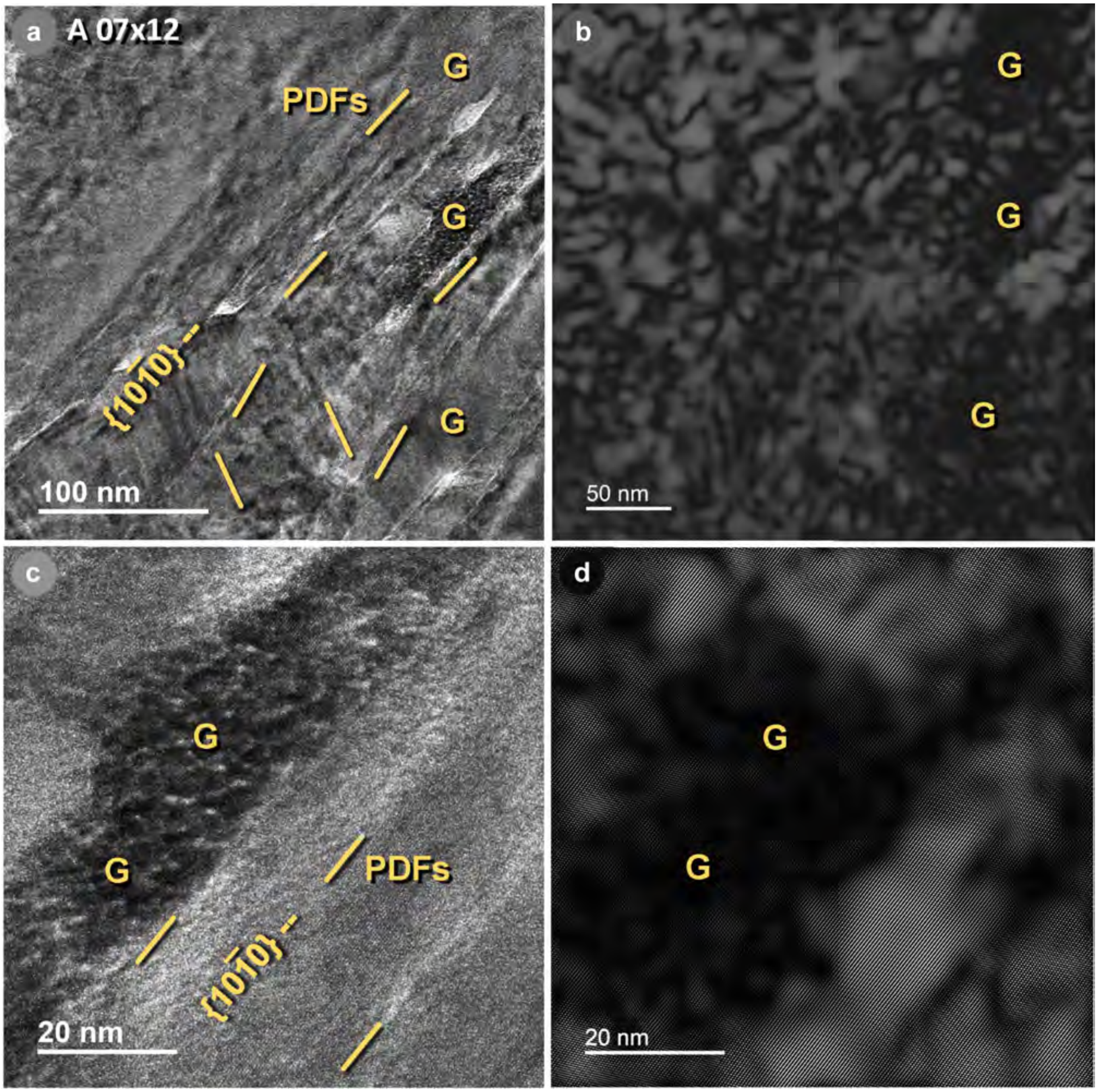

Figure 27: Tunguska Transmission Electron Microscopy of shock-fractured quartz grain (#07 × 12). "PDFs" mark planar deformation features, and "G" marks areas of glass, as determined by SAD. **(a)** and **(c)** High-resolution TEM images of grain areas with mixed amorphous silica at "G," showing multiple lamellae (yellow lines) oriented to the 1 0 $\bar{1}$ 0} crystallographic plane of quartz (yellow lines), as determined by SAD. **(b)** and **(d)** Corresponding inverse fast Fourier transform (IFFT) images showing lighter-colored areas with crystalline lattice. The darker-colored regions with amorphous or heavily damaged silica are marked as "G." The image and caption are reproduced/adapted from Kletetschka et al. [3].

impact-related morphologies, including rounded, sub-rounded, ovate, oblate, elongated, teardrop, dumbbell, and/or broken forms. Optical microscopy and SEM-EDS are commonly used to identify and analyze spherules and the processes by which they are formed. Care is needed to conclusively distinguish high-temperature spherules produced by cosmic impacts from other superficially similar forms. Other objects frequently occurring in sediments include anthropogenic spherules (typically from modern coal-fired power plants), authigenic framboids (**SI Figure S7** [7]), rounded detrital magnetite, and volcanic spherules, which can be differentiated from impact spherules using SEM-EDS.

Spherules in TeH sediment were investigated from stratigraphic sequences that include the MB II destruction layer at four locations: palace, temple, ring road, and wadi. Figure 32 shows spherule abundances in #/kg of sediment

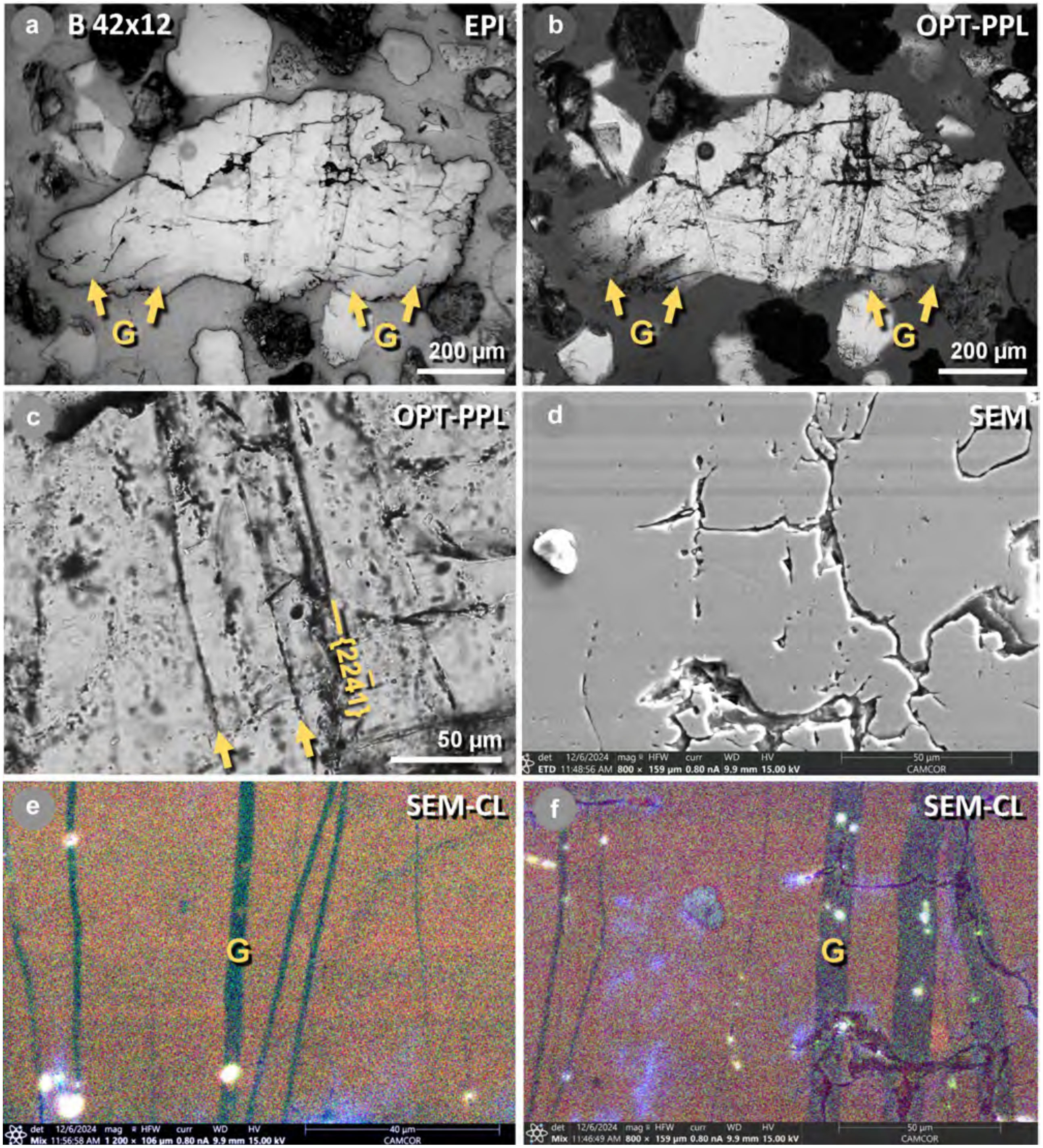

Figure 28: Tunguska Optical, Scanning electron microscopy (SEM), and cathodoluminescence (SEM-CL) images. Grain #42 × 12. **(a)** Epi-illuminated optical image and **(b)** optical plane-polarized image (OPT-PPL) of ~1030-µm-diameter quartz grain. "G" marks darker gray areas indicative of melted silica that is isotropic under crossed polars. **(c)** OPT-PPL image showing planar fractures (PFs) oriented to the {2 2 $\bar{4}$ 1} plane. **(d)** SEM image of glass-filled fractures. **(e-f)** SEM-CL images with reddish coloring indicating crystalline quartz. "G" marks non-luminescent areas (black), indicating fully melted silica along sub-planar lamellae. All images and captions are reproduced/adapted from Kletetschka et al. [3].

by sampling location. Five discontinuous samples from the wadi spanned 170 cm, ranging from 10-cm thick for the destruction layer up to 20 cm thick for other samples; the MB II destruction layer at this location contained 2780 spherules/kg with none in samples from different levels (Figure 32a, **SI Table S3** [7]). Notably, when melted mudbrick from the ring road was being mounted for SEM analysis, numerous loose spherules were observed within

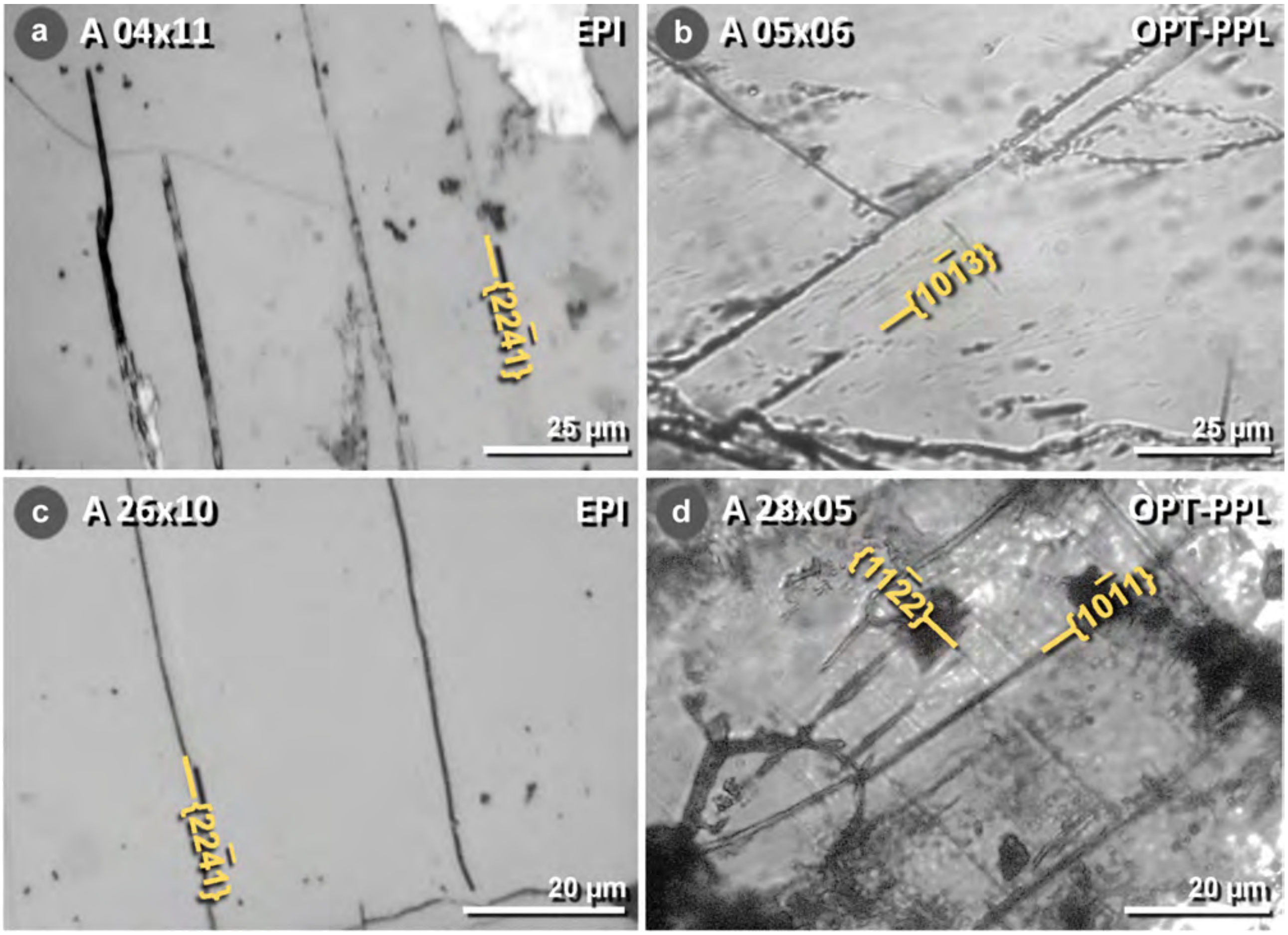

Figure 29: Quartz grains displaying planar fractures (PFs). (a-d) Epi-illuminated and plane-polarized optical images of glass-filled planar fractures (PFs) in selected quartz grains. Image and caption are reproduced/adapted from Kletetschka et al. [3].

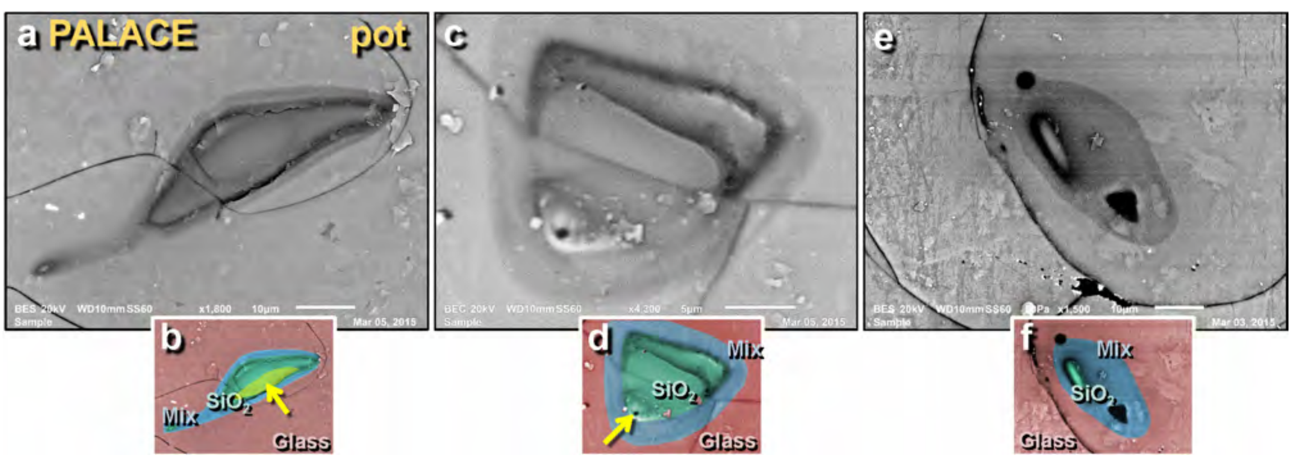

Figure 30: SEM images of melted quartz grains on melted potsherd from the palace. (a) Highly melted quartz grain from the upper surface of melted pottery; shows flow lines of molten quartz in darker 'neck' at upper right; **(b)** manually constructed EDS-based phase map showing 100% quartz grain (green) embedded in Ca-Al-Si matrix of melted pottery (red); blue marks mixing zone between SiO_2 and matrix at approximately >1713°C, the melting point of quartz. The yellow arrow points to an area depleted in oxygen, indicating a high-temperature transformation to elemental Si mixed with melted SiO_2. **(c)** Highly melted quartz grain; **(d)** manually constructed EDS-based phase map showing diffusion/mixing zone in blue with an arrow pointing to bubbles, indicating outgassing as grain reached temperatures above its melting point. **(e)** Quartz grain that has almost completely melted; **(f)** manually constructed EDS-based phase map showing the small remnant of a melted quartz grain (green) with a wide mixing zone (blue).

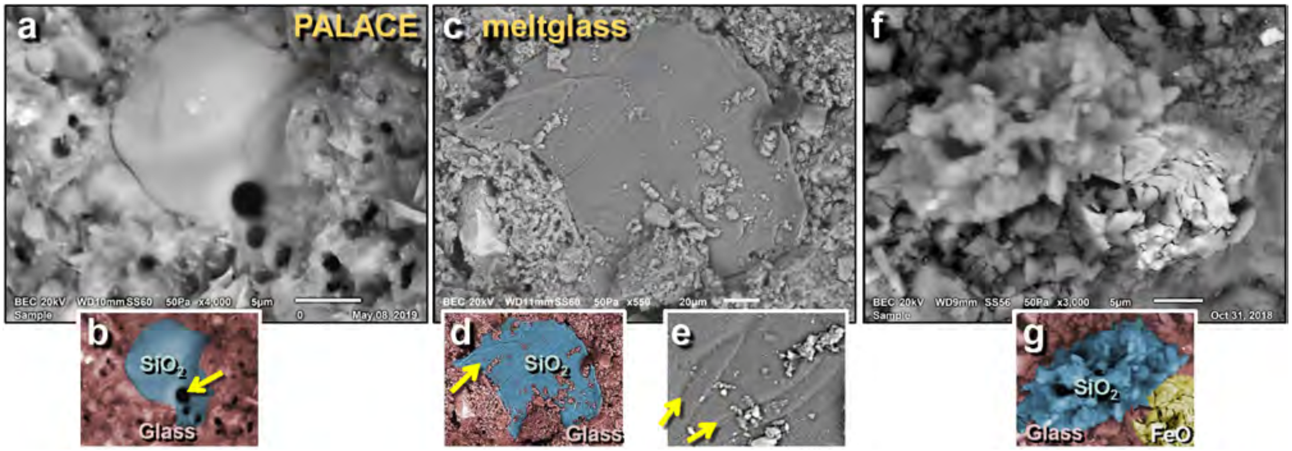

Figure 31: SEM images of melted quartz grains on melted mudbrick from the palace. (a) Highly melted quartz grain; **(b)** manually constructed EDS-based phase map indicates center is pure SiO_2 surrounded by melted mudbrick. The arrow points to a vesicle, indicating outgassing as grain temperature rose above ~1713°C, the melting point of quartz. **(c)** A flattened quartz grain's surface shows flow marks toward the upper right. Temperatures much higher than 1713°C are required to lower the viscosity enough for quartz flow sufficiently. **(d)** Manually constructed EDS-based phase map with an arrow pointing to vesicles indicating outgassing at high temperatures. **(e)** Close-up of grain in panel 'c' showing flow marks (schlieren) at arrows. **(f)** Shattered, melted quartz splattered onto mudbrick meltglass; **(g)** manually constructed EDS-based phase map indicating that the blue area is SiO_2; the yellow area is a shattered, thermally altered Fe-oxide grain.

vesicles of the sample, confirming a close association between the spherules and meltglass. Six contiguous samples from the ring road (Field LA, Square 28M) spanned 30 cm with all 5 cm thick; the MB II destruction layer at this location contains 2150 spherules/kg with none detected in younger or older samples (Figure 32b). For the temple (Field LS, Square 42J), five continuous samples spanned 43 cm and ranged in thickness from 6 to 16 cm; the MB II layer contained ~2345 Fe- and Si-rich spherules/kg with 782/kg in the sample immediately below and none at other levels (Figure 32c). For the palace (Field UA, Square 7GG), the sequence spanned 28 cm with five contiguous samples of sediment ranging from 3-cm thick for the MB II destruction layer to 13-cm thick for some outlying samples. In the palace, 310 spherules/kg (Figure 32d) were observed in the destruction layer, and none were found in samples above or below this layer. At all four locations, the peaks in high-temperature spherule abundances occur in the MB II destruction layer dating to ~1650 BCE.

SEM images of spherules are shown in Figures 33–35, and compositions are listed in **SI Table S4** [7]. The average spherule diameter was 40.5 µm, ranging from 7 to 72 µm. The dominant minerals were Fe oxides averaging 40.2 wt%, with a range of up to 84.1 wt%; elemental Fe, with a range of up to 80.3 wt%; SiO_2 averaging 20.9 wt%, ranging from 1.0 to 45.2 wt%; Al_2O_3 averaging 7.8 wt% with a range of up to 15.6 wt%; and TiO_2 averaging 7.1 wt% with a range of up to 53.1 wt%. Fourteen spherules had compositions >48 wt% of oxidized Fe, elemental Fe, and TiO_2; five contained <48 wt% Fe and Ti; and two had >75 wt% Fe with no Ti. Eight of the 23 spherules analyzed contained detectable levels of Ti at up to 53.1 wt%.

Two unusual spherules from the palace contain anomalously high percentages of rare-earth elements (REEs) at >37 wt% of combined lanthanum (La) and cerium (Ce) (Figure 34), as determined by preliminary measurements using SEM-EDS. Minor oxides account for the rest of the spherules' bulk composition (**SI Table S1** [7]).

One 54-µm-wide sectioned spherule contains titanium sulfide (TiS) with a melting point of ~1780°C. TiS, known as wassonite, was first identified in meteorites (Figure 35) and has been reported in impact-related material in the United States [63], Syria [36], Chile [130], and Germany [95]. Although TiS sometimes occurs as an exsolution product forming fine networks in magnetite and ilmenite and can be of terrestrial origin, an impact-related origin is the only plausible explanation here because of the spherulitic nature of the object.

One unusual piece of 167-µm-wide Ca-Al-Si meltglass contains nearly two dozen iron oxide spherules on its surface (Figure 36). The meltglass contains a completely melted quartz grain as part of the matrix (Figure 36b). Most of the spherules appear to have been flattened or crushed by collision with the meltglass while they were still partially molten (Figure 36c).

Interpretation of spherules and meltglass

Melted materials from non-impact-related combustion have been reported in multiple studies. Consequently, we investigated whether Ca-, Fe-, and Si-rich spherules and meltglass (mudbrick, pottery, plaster, and roofing clay) may have formed normally rather than from a cosmic impact event. For example, (i) glassy spherules and meltglass are known to form when carbon-rich biomass smolders below

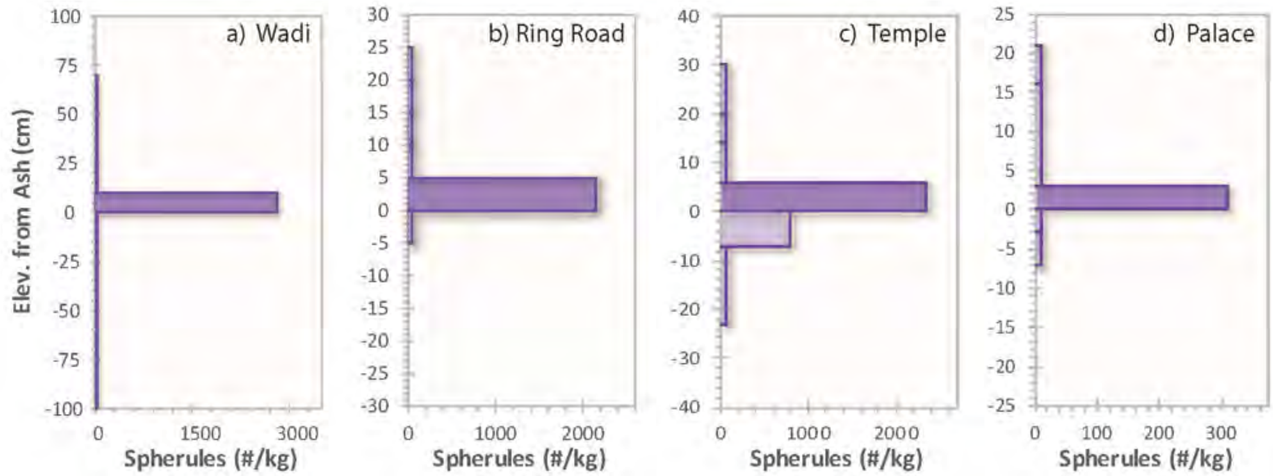

Figure 32: Spherule abundances. (a-d). Number per kg for Fe- and S-rich spherules from 4 locations. Depths are in cm above or below the bottom of the destruction layer.

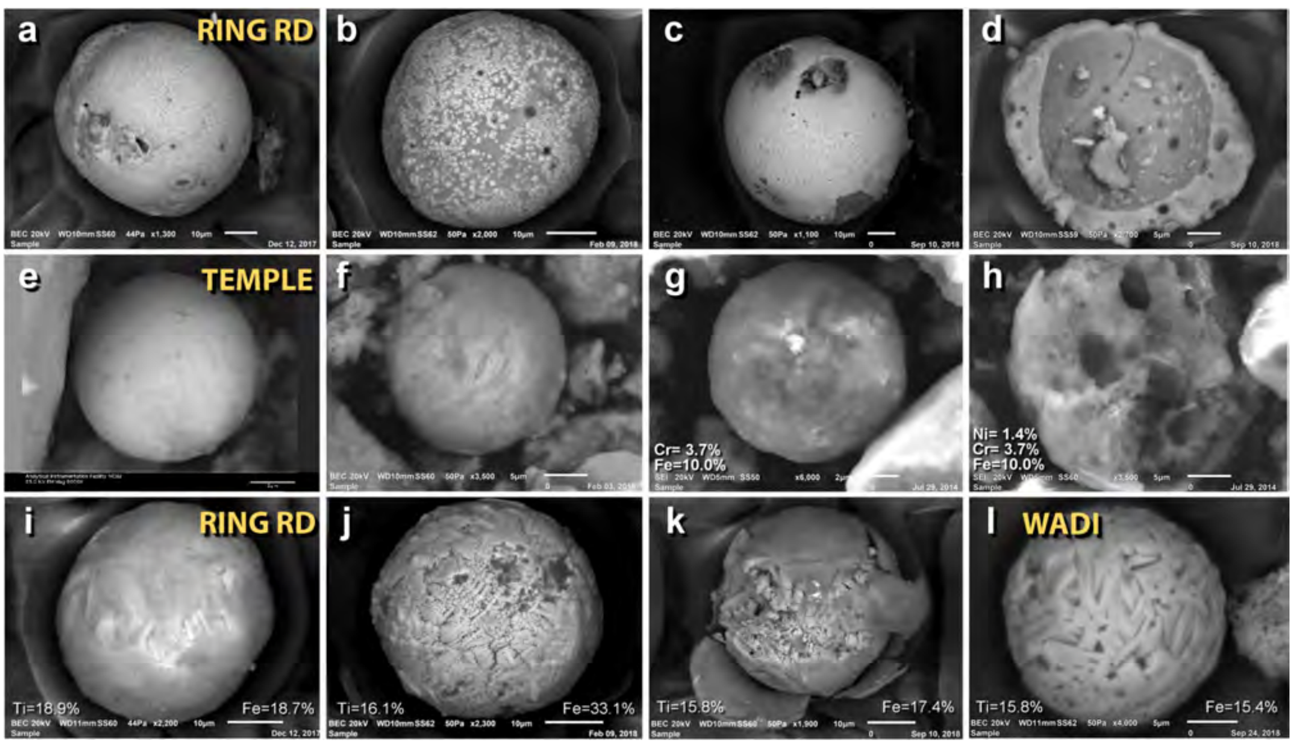

Figure 33: SEM images of mostly silica-rich spherules from TeH. (a-d) Representative spherules from the ring road on the lower tall. **SEM images of iron-rich spherules. (e-f)** Fe-rich spherules from the temple complex. **(g)** temple spherule containing ~3.7 wt% Cr. **(h)** Broken, vesicular spherule from temple containing 1.4 wt% Ni and 3.7 wt% Cr. **SEM images of titanium-rich spherules.** Ti content ranges from 18.9 to 1.2 wt%, averaging 10.7 wt%. **(i-k)** Spherules from the ring road. **(l)** Spherule from the wadi site.

ground at ~1000° to 1300°C, such as in midden mounds [119], buried peat deposits [131], underground coal seams [132], burned haystacks [133], and in large bonfires, such as at the Native American site at Cahokia, Illinois, in the USA [134]. (ii) Also, ancient fortifications (hillforts) in Scotland and Sweden, dating from ~1000 BCE to 1400 AD, display artificially vitrified walls that melted at temperatures of ~850° to 1000°C [135]. (iii) Partially vitrified pottery and meltglass derived from the melting of wattle and daub (thatch and clay) with estimated temperatures of ~1000°C have been reported in burned houses of the Trypillia culture in Ukraine [136, 137]. (iv) Vitrified mudbricks and pottery

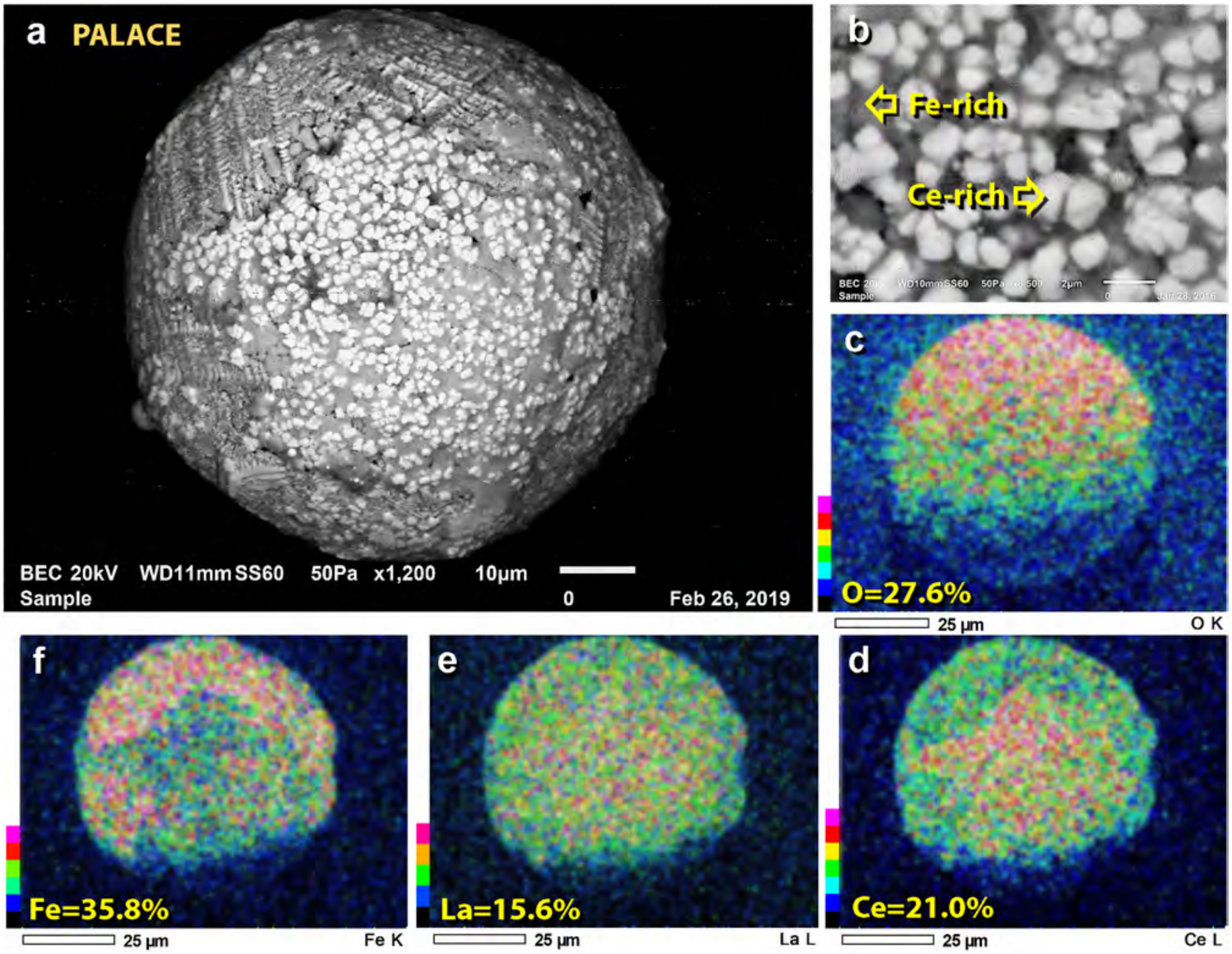

Figure 34: **SEM image of rare-earth (REE) spherule. (a)** REE-rich 72-µm-wide spherule from the palace, dominantly composed of Fe, La, Ce, and O. **(b)** Close-up of REE blebs found on the spherule. **(c-f)** SEM-EDS elemental maps showing composition. La = 15.6 wt% and Ce = 21.0 wt%. Ce is enriched over Fe and La in the middle part of the spherule, as seen in panels 'd' through 'f.'

that melted at <1100°C have been reported at Sardis, Turkey, dating to the seventh and sixth centuries BCE [138]; in the northern Jordan Valley at an Early-Bronze-Age site called Tell Abu al-Kharaz [139]; and at Early-Bronze-Age Tell Chuera in Syria [140]. All these sites describe melting temperatures ranging from ~850° to 1300°C.

In another example of meltglass, vitrified bricks at Tell Leilan in Syria, dating to ~2850 to 2200 BCE, are estimated by Weiss [141] to have melted at ~1200°C, and he attributed high-calcium spherules to low-temperature combustion of thatch roofing materials [142]. However, thatch has low calcium content, leading Courty [143] to propose that this material formed from melted lime-based plaster during an airburst/impact at Tell Leilan ~550 years before the destruction of TeH. Courty [143] reported aluminosilicate spherules with unusual high-temperature elemental nickel (melting point: ~1455°C); complex vesicular glass particles that contain terrestrially rare unoxidized nickel inclusions; and both single and multiple calcite spherules (melting point = 1500°C, as measured by experiments in this contribution).

However, there is a definitive difference between the melted TeH materials and other non-impact melting: high-temperature minerals are embedded in meltglass at TeH, but none are present at these other sites (except for Tell Leilan). Moore et al.36 investigated biomass glass from midden mounds in Africa to explore this difference and found no high-temperature minerals. For this contribution, we used SEM-EDS to examine aluminosilicate meltglass from an underground peat fire in South Carolina, USA; meltglass in coal-fired fly ash from New Jersey, USA; and mining slag from a copper mine in Arizona, USA. All these non-TeH meltglass examples display unmelted quartz and contain no other high-temperature melted grains, consistent with low-temperature melting at <1300°C.

At the sites with non-impact meltglass, estimated temperatures were consistently less than 1300°C, too low to melt

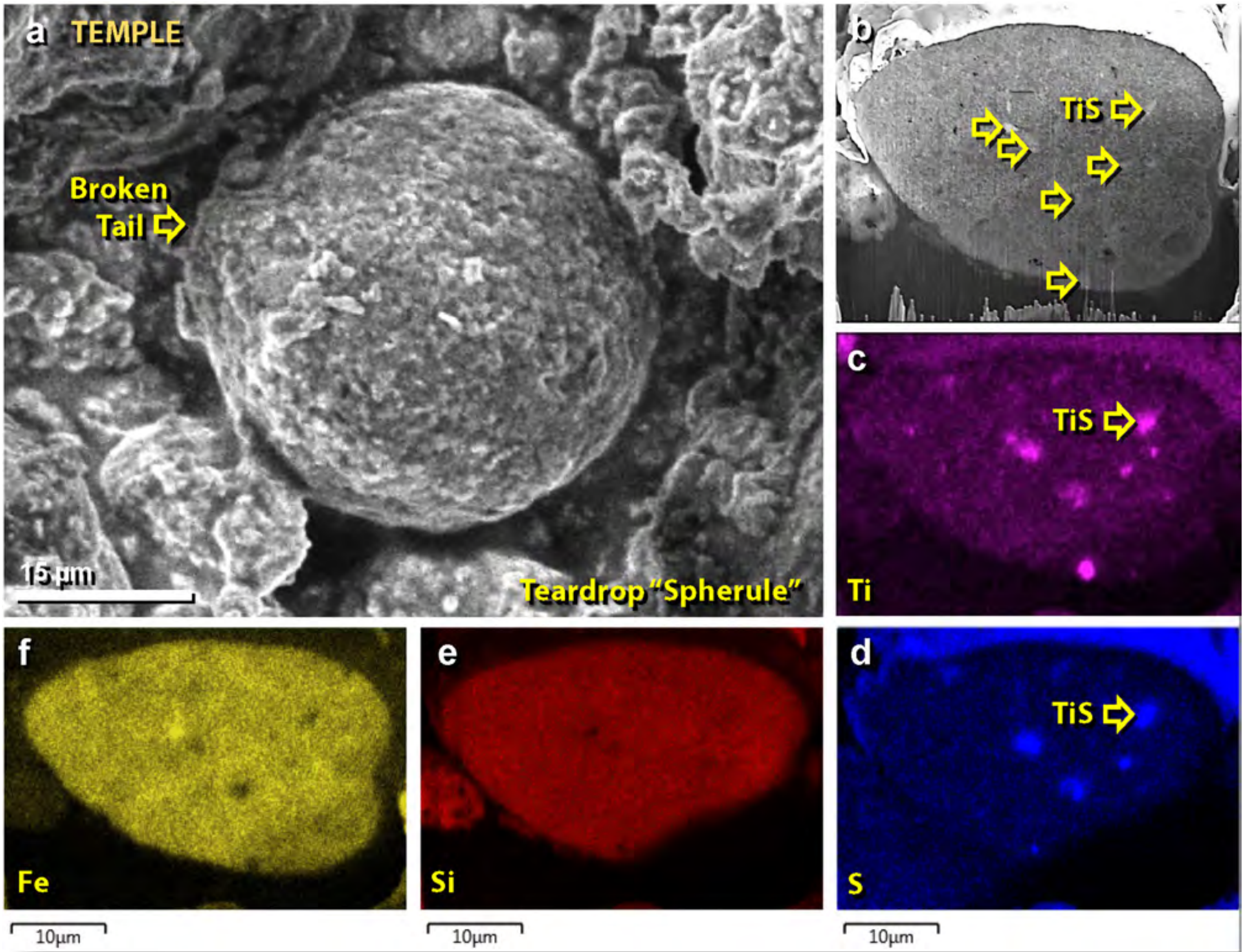

Figure 35: SEM images of a spherule mainly composed of Fe and Si. (a) Fe-Ti-rich 54-µm-wide spherule from the palace. The spherule displays a protrusion to the left, suggesting aerodynamic shaping when molten, after which the tail detached. **(b)** A focused ion beam (FIB) was used to section the spherule, revealing inclusions of wassonite or titanium sulfide (TiS; yellow arrows) that are lighter colored than the matrix. **(c-f)** Color-coded SEM-EDS elemental maps showing the distribution of Ti, S, Si, and Fe and the location of the TiS grains. The spherule is dominantly composed of Fe and Si, with minor amounts of Ti and S found in TiS inclusions.

magnetite into Fe-rich spherules, e.g., with compositions of >97% wt% FeO, as are found at TeH. Nor can these low temperatures produce meltglass and spherules embedded with melted zircon (melting point = 1687°C), chromite (2190°C), quartz (1713°C), platinum (1768°C), and iridium (2466°C). Moore et al. [36] confirmed that melting these high-temperature minerals requires minimum temperatures of ~1500° to 2500°C.

This evidence demonstrates that although the matrix of the spherules and meltglass at TeH likely experienced incipient melting at temperatures lower than ~1300°C, this value represents only the minimum temperature of exposure because the high-temperature minerals embedded in them do not melt at such low temperatures. Instead, the spherules and meltglass at TeH must have reached temperatures greater than ~1300°C, most likely involving brief exposure to ambient temperatures of ~2500°C, the melting point of iridium. These temperatures far exceed those characteristic of city fires and other types of biomass burning. In summary, this evidence is consistent with very high temperatures known during cosmic impacts but inconsistent with other known natural causes.

8.3 Melted calcium carbonate spherules and plaster in the destruction layer

In sediments of the destruction layer, we observed amber-to-off-white-colored spherules (Figure 37) at high concentrations of ~240,000/kg in the palace, ~420/kg in the temple, ~60/kg on the ring road, and ~910/kg in the wadi (**SI Table S2** [7]). In all four profiles, the spherules peak in the destruction layer with few to none above or below. Peak abundances of calcium carbonate spherules are closely associated with peak abundances of plaster fragments, which are the same color. By far the most spherules (~250× more) occurred in the destruction layer of the palace, where excavations showed that nearly every room and ceiling was surfaced with off-white lime-based plaster. Excavators uncovered high-quality lime plaster fragments still adhering to mudbricks inside the MB II palace complex, and in one palace room, we uncovered fragments of melted plaster (Figure 37e). In contrast, lime plaster was very rarely used in buildings on the lower tall, including those near the temple.

To explore a potential connection between plaster and spherules, we performed SEM-EDS on samples of the palace plaster. Comparison of SEM-EDS analyses shows that the plaster composition has a >96% similarity to the spherule composition: $CaCO_3$ = 71.4 wt% in plaster vs. 68.7 wt% in the spherules; elemental C = 23.6 vs. 26.3 wt%; SiO_2 = 2.4 vs. 1.8 wt%; MgO = 1.7 vs. 2.0 wt%; and SO_3 = 0.94 vs. 1.2 wt%. The high carbon percentage and low sulfur content indicate that the plaster was made from calcium carbonate, not gypsum ($CaSO_4{\cdot}2H_2O$). SEM imaging revealed that the plaster contains small plant parts, commonly used in plaster as a binder, and is likely the source of the high abundance of elemental C in the plaster. Inspection showed no evidence of

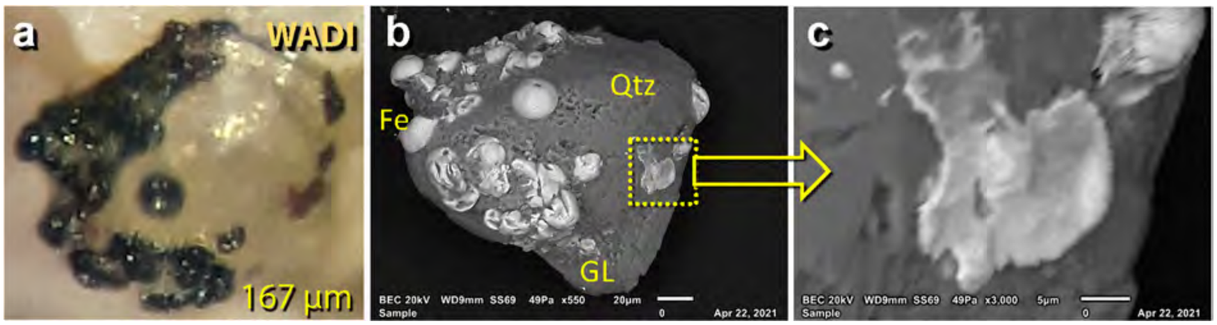

Figure 36: Fe-rich spherules embedded in meltglass. (a) Optical photomicrograph of a 167-µm-wide piece of meltglass with embedded Fe-rich spherules. **(b)** SEM image of the same grain as in panel 'a.' Melted quartz grain (Qtz) is embedded in the Ca-Al-Si-rich matrix, which has the same composition as melted mudbrick. **(c)** The SEM close-up image of the boxed area and panel 'b' shows a splattered Fe-rich spherule.

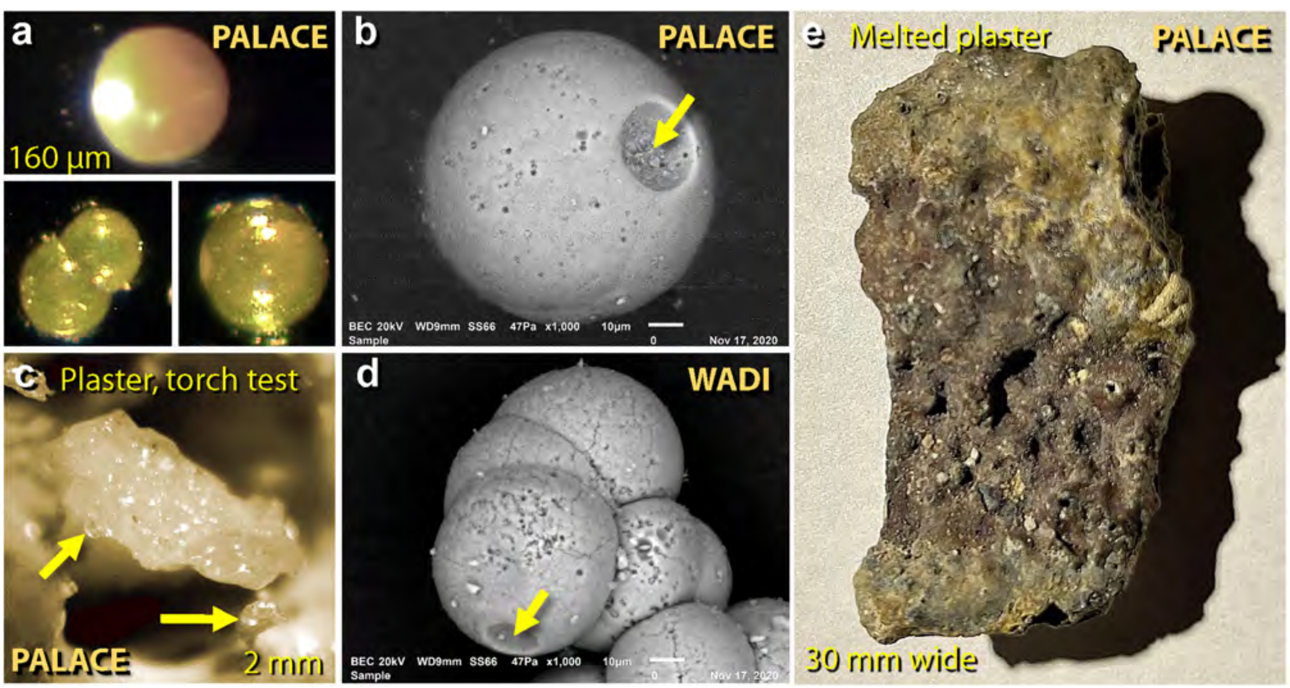

Figure 37: Images of calcium carbonate spherules and melted plaster from TeH. (a) Photomicrographs of translucent, amber-colored $CaCO_3$ spherules from the destruction layer in the palace. **(b)** SEM image of 83-µm carbonate spherule with impact or outgassing crater at arrow. **(c)** Photomicrograph of ~2-mm-wide piece of partially melted palace plaster from oxygen/propylene torch test, showing incipient melting at 1500°C. Arrows point to hemispheric droplets emerging as spherules. **(d)** A 142-µm cluster of 8 carbonate spherules with apparent impact or outgassing crater at arrow. **(e)** 64 × 30 mm piece of melted plaster that broke off the palace wall and became melted. It is composed only of calcium, carbon, and oxygen.

microfossils, such as coccoliths, brachiopods, and foraminifera. The morphology of the spherules indicates that they are not authigenic or biological in origin.

Interpretation of carbonate plaster and spherules

One of the earliest known uses of $CaCO_3$-based plaster was in ~6750 BCE at Ayn Ghazal, ~35 km from TeH in modern-day Amman, Jordan [144]. At that site, multi-purpose lime plaster was used to make statues and figurines and to coat the interior walls of buildings. Because the production of lime-based plaster occurred at least 3000 years before TeH was destroyed, the inhabitants of TeH undoubtedly were familiar with the process. Typically, lime powder was produced in ancient times by stacking wood/combustibles interspersed with limestone rocks and then setting the stack on fire. The temperatures of ~800-1100°C were required to transform the stones into crumbly chalk, which was then mixed with water to make hydrated lime and plastered onto mudbrick walls [144].

At TeH, fragments of $CaCO_3$-based plaster are intermixed in covarying abundances, with CaCO3-based spherules having both compositions matching within 96%. This similarity suggests that the carbonate spherules are derived from the plaster. We infer that the high-temperature blast wave from the impact event stripped some plaster from the interior walls of the palace and melted some into spherules. However, it is not easy to directly melt $CaCO_3$, which gives off CO_2 at high temperatures and decomposes into lime powder. We investigated this cycle in a heating experiment with an oxygen/propylene torch and found that we could decompose the plaster at ~1500°C, the upper limit of the heating test, and begin incipient melting of the plaster. The heated plaster produced emergent droplets at that temperature but did not transform into free spherules (**SI Text S2** [7]).

Similar spherules have been reported from Meteor Crater, where spherules up to ~200 µm in diameter are composed entirely of $CaCO_3$ formed from a cosmic impact into limestone [145, 146]. One of several possible hypotheses for TeH is that during the impact event, the limestone plaster converted to CaO with an equilibrium melting point of 2572°C. However, it is highly likely that airborne contaminants, such as sodium and water vapor, reacted with the CaO and significantly lowered the melting point, allowing spherule formation at ≥1500°C.

The proposed chemical sequence of events of plaster formation and the later impact are as follows:

1. Limestone was heated to ~800-1100°C, decomposing to quicklime:

$$CaCO_3 \rightarrow CaO + CO_2$$

2. Quicklime was mixed with water to make a wet plaster:

$$CaO + H_2O \rightarrow Ca(OH)_2$$

3. The plaster hardened and slowly absorbed CO_2 to revert to $CaCO_3$:

$$Ca(OH)_2 + CO_2 \rightarrow H_2O + CaCO_3$$

----

4. The high-temperature impact event melted some plaster into spherules:

$$CaCO_3 \rightarrow CaO \text{ (spherules)} + CO_2 \text{ (>1500°C)}$$

5. CaO spherules slowly absorbed CO_2 to revert to $CaCO_3$:

$$Ca + CO_2 \rightarrow CaCO_3 \text{ (as spherules)}$$

8.4 Melted zircon grains in the destruction layer

To more accurately determine the maximum temperatures of the destruction layer, we used SEM-EDS to comprehensively investigate melted minerals on the outer surfaces of melted pottery and mudbricks. We searched for and analyzed zircon (melting point: ~1687°C), chromite (~2190°C), and quartz (~1713°C) [36].

Melted zircons in pottery and mudbricks were observed (Figure 38) at an estimated density of 1 per 20 mm^2. On highly melted surfaces, nearly all zircons showed some degree of melting. In contrast, almost all zircons found on broken interior surfaces were unmelted (Figure 38d), except those within ~1 mm of melted surfaces. This observation implies that the temperature of the surrounding atmosphere was higher than the internal temperatures of the melting objects. Unmelted potsherds displayed only unmelted minerals.

The melted zircons in TeH materials exhibit a wide range of morphologies. Most showed evidence of sufficient melting to alter or destroy the original distinctive, euhedral shape of the grains. Also, the grains were often decorated with vesicles associated with fractures (Figure 38a, 38c).

Stoichiometric zircon contains 67.2 wt% and 32.8 wt% ZrO_2 and SiO_2, respectively, but in several TeH samples, we observed a reduction in the SiO_2 concentration due to a loss of oxygen due to the dissociation of SiO_2. This alteration occurred at 1676°C, slightly below zircon's melting point of 1687°C [147]. This zircon dissociation leads to varying ZrO_2:SiO_2 ratios and the formation of distinctive granular textures of pure ZrO_2, also known as baddeleyite [148] (Figures 38–40). With increasing time at temperature, zircon will eventually convert partially or wholly to ZrO_2. Nearly all zircons observed on the surfaces of melted materials were either melted or showed some conversion to baddeleyite. We observed one zircon grain (Figure 40d and 40e) displaying granular ZrO_2 associated with three phases that span a wide range of SiO_2 concentrations, likely formed at temperatures above 1687°C. This extreme temperature and competing loss of SiO over an inferred duration of

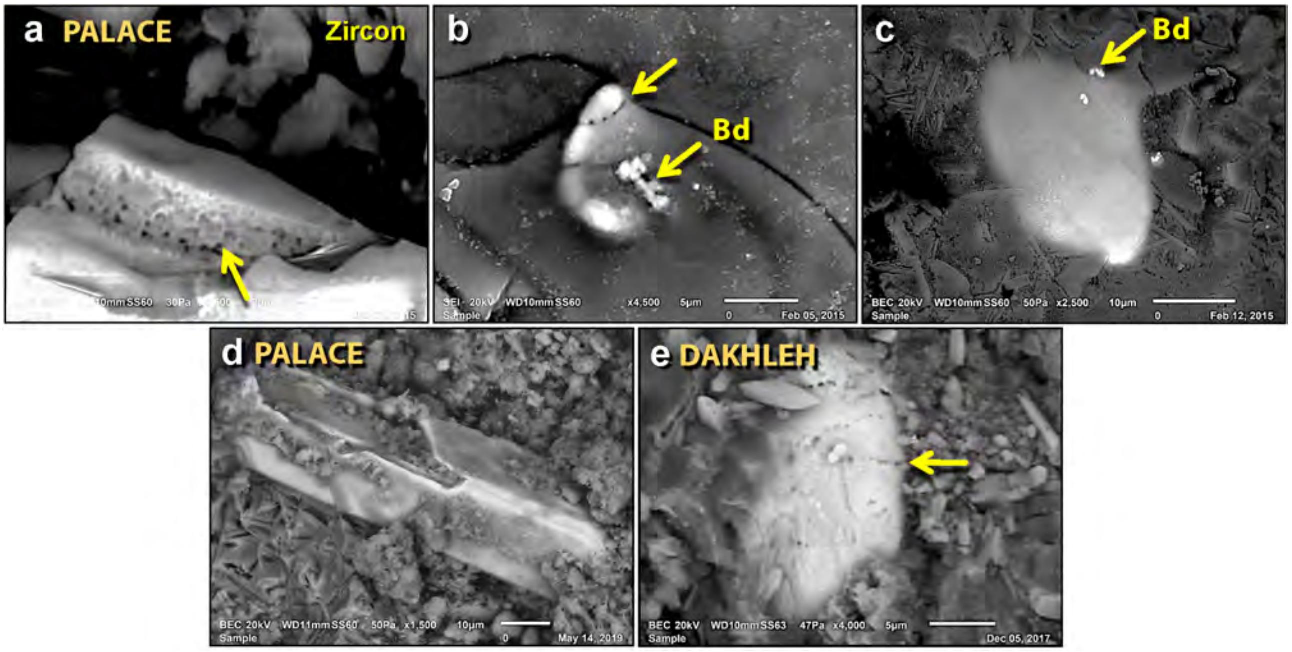

Figure 38: **SEM images of melted zircon grains.** **(a)** Melted TeH zircon grain with bubbles at yellow arrow due to high-temperature dissociation and/or entrapped porosity. **(b)** Melted TeH zircon grain decorated with bubbles along the fracture line at the upper arrow; arrows labeled "Bd" point to bright granular baddeleyite, ZrO_2, formed during the high-temperature dissociation of zircon. **(c)** Almost entirely melted TeH zircon grain mixed into the Ca-Al-Si matrix. **(d)** A typical unmelted zircon grain from TeH with straight, euhedral edges. Grain shows cracks on the top surface from possible thermal or mechanical damage. **(e)** For comparison, from cosmic airburst/impact at Dakhleh Oasis in Egypt: melted zircon decorated with lines of bubbles (arrow).

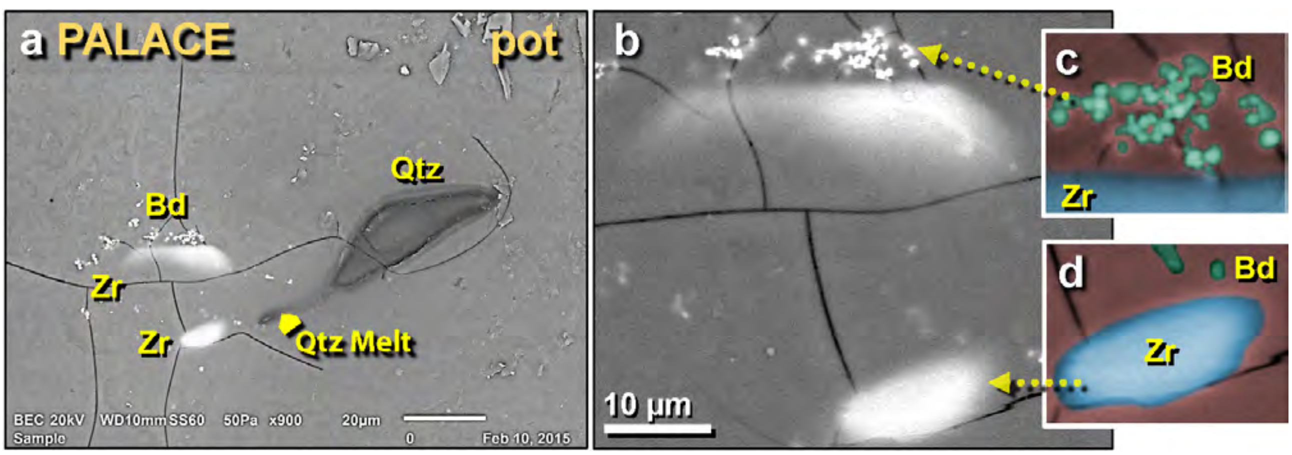

Figure 39: **SEM images of other melted zircon grains in palace potsherd.** **(a)** Two melted zircon grains adjacent to a previously discussed melted quartz grain; **(b)** close-up of same zircon grains; **(c)** manually constructed EDS-based phase map showing baddeleyite grains in green. The blue area represents melted zircon, while the red background represents the Ca-Al-Si matrix of the melted pottery. **(d)** Manually constructed EDS-based phase map of zircon grain showing small baddeleyite grains in green at the top.

only several seconds led to complex microstructures, where grains melted, outgassed, and diffused into the surrounding matrix.

Interpretation of melted Zircon

Zircon grains have a theoretical equilibrium melting point of ~1687°C. Under laboratory heating [36], zircon grains showed no detectable alteration in shape at ~1300°C but displayed incipient melting of grain edges and dissociation to baddeleyite beginning at ~1400°C with increasing dissociation to 1500°C [36]. Most zircon grains <50 µm completely melted at a temperature of ~1500°C, while at ~1700°C, the shapes of zircon grains >120 µm were still recognizable but displayed considerable melting [36]. These experiments establish a lower melting range for TeH zircon grains of ~1400° to 1500°C.

Patterson [149] showed that zircon dissociation becomes favorable above 1538°C and particles between 1 µm and 100 µm in size melted and dissociated when passing through a plasma, forming spherules with various amounts of SiO_2 glass containing ZrO_2 crystallites ranging in size from 5 nm to 1 µm. Most zircon crystals were monoclinic, but tetragonal ZrO_2 was observed for the smaller crystallite sizes. Residence times were 100 ms, and the specific ZrO_2 to SiO_2 ratio within each spherule depended on the particle's time at temperature [150].

Bohor et al. [148] presented images of impact-shocked zircons from the K-Pg impact event at 66 Ma that are morphologically indistinguishable from those at TeH. Decorated zircon grains are uncommon in nature but commonly associated with cosmic impact events, as evidenced by partially melted zircon from the known airburst/impact at Dakhleh Oasis, Egypt (Figure 38e). The presence of bubbles indicates that temperatures reached at least 1676°C, where the zircon began to dissociate and outgas. Similar dissociated zircon grains have also been found in tektite glass and distal fallback ejecta (deposited from hot vapor clouds). Granular baddeleyite-zircon has been found in the ~150-km-wide K-Pg impact crater [151] and the 28-km-wide Mistatin Lake crater in Canada [151]. The dissociation of zircon requires high temperatures of ~1676°C [148], implying that TeH was exposed to similar extreme conditions.

8.5 Melted chromite grains in the destruction debris

Examples of melted chromite, another mineral that melts at high temperatures, were also observed. Thermally-altered chromite grains were observed in melted palace materials, including pottery, mudbricks, and roofing clay. Their estimated density was 1 per 100 mm^2, making them rarer than melted zircon grains. The morphologies of chromite grains range from thermally altered (Figure 41a) to fully melted (Figure 41b). One chromite grain from the palace displays unusual octahedral cleavage or shock-induced planar fractures (Figure 41b). The typical chemical composition for chromite is 25.0 wt% Fe, 28.6 wt% O, and 46.5 wt% Cr, although the Cr content can vary from low values to ~68 wt%. SEM images reveal that, as chromite grains melted, some Cr-rich molten material migrated into and mixed with the host melt, causing increased Cr and Fe and the corresponding depletion of Si. The ratio of Cr to Fe in chromite affects its equilibrium melting point, which varies from ~1590°C for a negligible amount of Cr up to ~2265°C for ~46.5 wt% Cr as in chromite or chromian magnetite ($(Fe)Cr_2O_4$), placing the melting point of TeH chromite at close to 2265°C.

Interpretation of melted Chromite

Chromite grains theoretically melt at ~2190°C. Moore et al. [36] reported the results of heating experiments in which chromite grains in bulk sediment showed almost no thermal alteration up to ~1500°C (**SI Figure S8** [7]). At temperatures of ~1600°C and ~1700°C, the shapes of chromite grains were intact but exhibited limited melting of grain edges. These results establish a range of ~1600° to 1700°C for melting chromite grains.

Because chromite typically does not exhibit cleavage, the grain exhibiting this feature is highly unusual. Its origin is unclear, but there are several possibilities. The cleavage may have resulted from exsolution while cooling in the source magma. Alternately, the lamellae may have resulted from mechanical shock during a cosmic impact, under the same conditions that produced the shocked quartz, as Chen et al. [152] reported for meteorites shocked at pressures of ~12 GPa. Or they may have been formed by thermal shock, i.e., rapid thermal loading followed by rapid quenching. This latter suggestion is supported by the observation that the outside glass coating on the potsherd does not exhibit any quench crystals, implying that the cooling progressed rapidly from liquid to solid (glass). The lack of quench crystals is rare in terrestrial events except for some varieties of obsidian but common in melted material produced by atomic detonations (trinitite), lightning strikes (fulgurites), and cosmic airburst/impacts (meltglass) [63]. More investigations are needed to determine the origin of the shocked chromite.

8.6 Nuggets of Ir, Pt, Ru, Ni, Ag, Au, Cr, and Cu in meltglass

Using SEM-EDS, Bunch et al. investigated abundances and potential origins (terrestrial versus extraterrestrial) of platinum-group elements (PGEs) embedded in TeH meltglass, in addition to Ni, Au, and Ag. Samples studied include these melted materials: pottery (n = 3), mudbrick (n = 6), roofing clay (n = 1), and lime-based building plaster (n = 1). On the surfaces of all four types of meltglass, we observed melted metal-rich nuggets and irregularly shaped metallic splatter, some with high concentrations of PGEs (ruthenium (Ru), rhodium (Rh), palladium (Pd), osmium (Os), iridium (Ir), and platinum (Pt)) and some nuggets enriched in silver (Ag), gold (Au), chromium (Cr), copper (Cu), and nickel (Ni) and no PGEs (Figures 42–44). Importantly, these metal-rich nuggets were observed only on the top surfaces of meltglass, not inside vesicles or broken interior surfaces.

Using SEM-EDS, Bunch et al. identified variable concentrations and assemblages of PGEs. The metallic particles appear to have melted at high temperatures based on the minimum melting points of the elements: iridium at 2466°C, platinum = 1768°C, and ruthenium = 2334°C, indicating a temperature range of between approximately 1768° and 2466°C. Our investigations also identified two PGE groups, one with nuggets in which Pt dominates Fe and the other with metallic splatter in which Fe dominates Pt.

Pt-dominant nuggets. Bunch et al. conducted 21 measurements on Pt-dominant TeH nuggets on meltglass (Figure 42a–42c). The nuggets average ~5 µm in length (range: 1 to

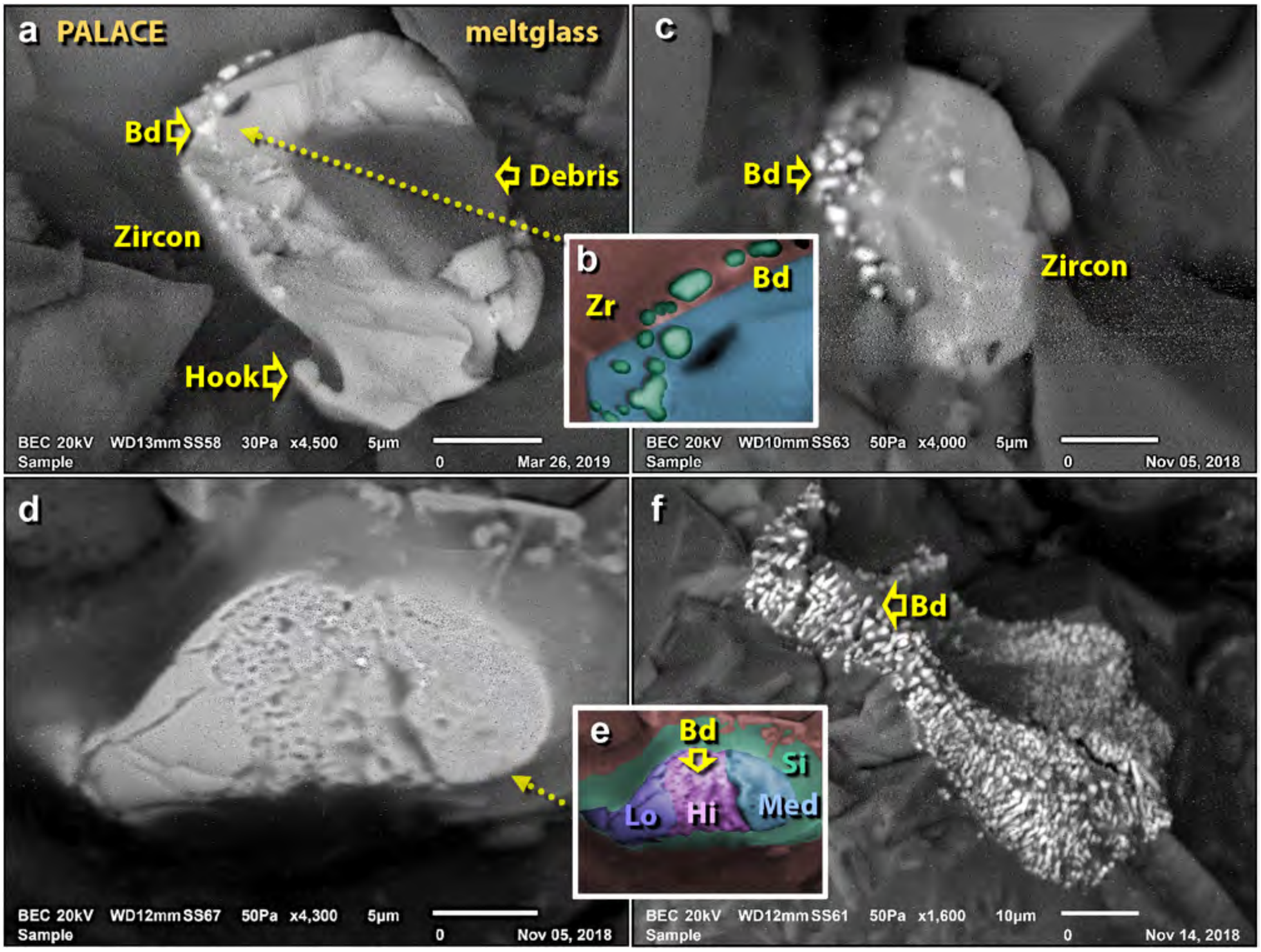

Figure 40: SEM images of melted zircon grains in mudbrick meltglass from the palace. (a) Thermally distorted zircon grain with a hook-like feature that resulted from the flow of molten material at >1687°C; the darker area represents unrelated debris on top of zircon. **(b)** Manually constructed EDS-based phase map showing baddeleyite grains (Bd = ZrO_2) in green, zircon in blue, and melted mudbrick in red. **(c)** Zircon grain shows limited thermal alteration, yet sufficient to cause dissociation into bright baddeleyite grains at ~1676°C. **(d)** Zircon grain exhibits three phases of thermal alteration, as shown in detail in **(e)**, where a manually constructed EDS-based phase map demonstrates that high temperatures caused bubbling in the center band of zircon (purple = high), producing sub-micron-sized grains of baddeleyite (e.g., at arrow). Medium temperatures caused zircon to melt and flow (blue = low), and lower temperatures at the left end of the grain produced thermal cracks (medium blue = medium). The green area marks the high-Si diffusion zone resulting from the dissociation of zircon. **(f)** Zircon grain from TeH has been fully converted to granular baddeleyite.

12 µm) with an estimated concentration of 1 nugget per 10 mm^2. For these nuggets, Fe concentrations average 1.0 wt%, Ir = 6.0 wt%, and Pt = 44.9 wt% (**SI Tables S6 and S7** [7]). The presence of PGEs was confirmed by two SEM-EDS instruments that verified the accurate identification of PGEs through analyses of several blanks that showed no PGE content. Some concentrations are low (<1 wt%) with high uncertainties (±100 wt%), and elemental concentrations greater than 10 wt% have certainties of approximately ±10 wt%, making these results preliminary and indicating the need for further analyses. However, despite high uncertainties, the two instruments' relative elemental relationships of Fe>Pt or Pt>Fe were consistent.

To determine the source of TeH nuggets and splatter, we constructed ternary diagrams (Figure 44). Terrestrial PGE nuggets are commonly found in ore bodies that, when eroded, can become concentrated in riverine placer deposits, including those of the Jordan River floodplain. To compare Fe-Ir-Pt relationships among the TeH nuggets, we compiled data from nearby placer deposits in Greece [153], Turkey [154, 155], and Iraq [156], along with distant placers in Russia [157–159], Canada [160], and Alaska, USA [161, 162]. Compiling 109 Pt-dominant placer nuggets indicates that the average Fe concentration is 8.2 wt%, Ir = 2.9 wt%, and Pt = 80.3 wt%. For the Ir-dominant placer nuggets (n = 104), Fe = 0.4 wt%, Ir = 47.8 wt%, and Pt = 5.3 wt% (**SI Tables S6 and S7** [7]). The ternary diagrams reveal that the values for Pt-dominant TeH nuggets overlap with Pt-dominant terrestrial placer nuggets, but the Fe-dominant splatter is dissimilar (Figure 44a).

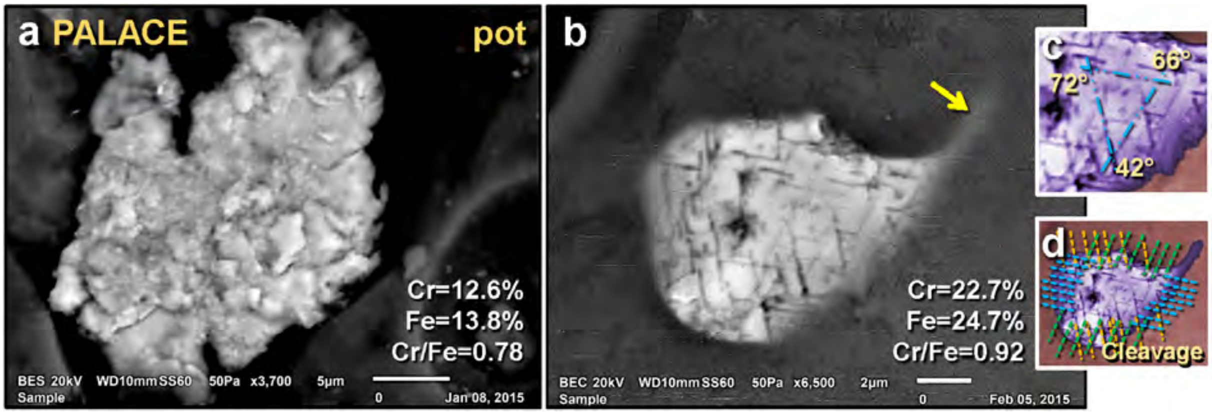

Figure 41: SEM images of melted chromite grains found on a melted potsherd from the palace. (a) Shattered, polycrystalline chromite grain that appears to have become agglutinated while molten. **(b)** Melted chromite grain, displaying cleavage (lamellae) suggestive of thermal and/or mechanical shock metamorphism at ~12 GPa; **(c)** close-up image showing angles between three sets of crystalline cleavage; **(d)** manually constructed EDS-based phase map showing chromite (purple) embedded in Ca-Al-Si matrix. The lines mark three sets of cleavage extending across the entire grain. A melt tail merging with the matrix is observed to trail off to the upper right of the grain at the arrow.

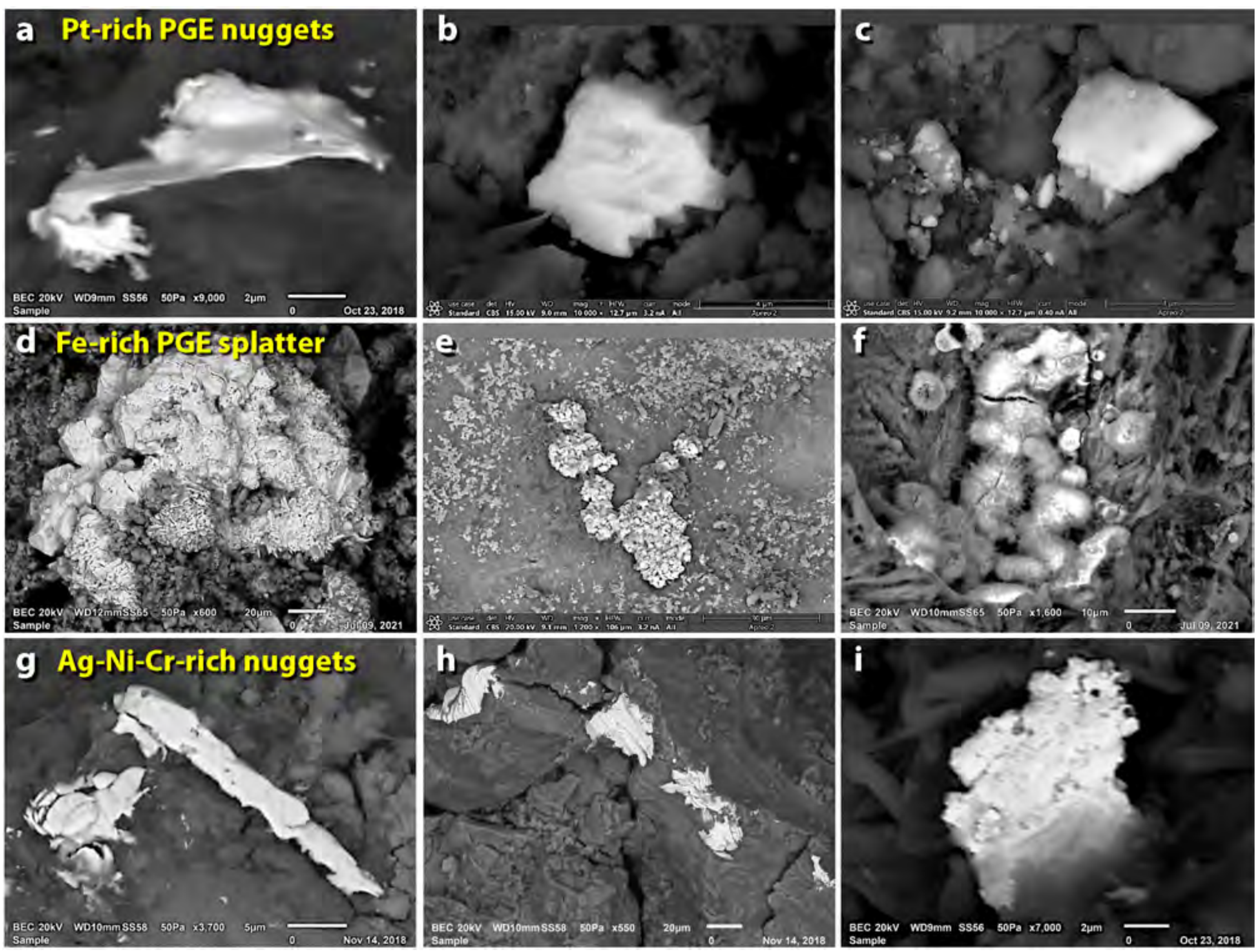

Figure 42: SEM images of nuggets of melted metals in mudbrick meltglass from the palace. (a-c) Pt-dominant TeH nuggets enriched in ruthenium (Ru), rhodium (Rh), palladium (Pd), osmium (Os), iridium (Ir), and platinum (Pt). **(d-f)** Fe-dominant TeH splatter is also enriched in PGEs. **(g-i)** Nuggets enriched in varying percentages and combinations of nickel (Ni), chromium (Cr), copper (Cu), and silver (Ag).

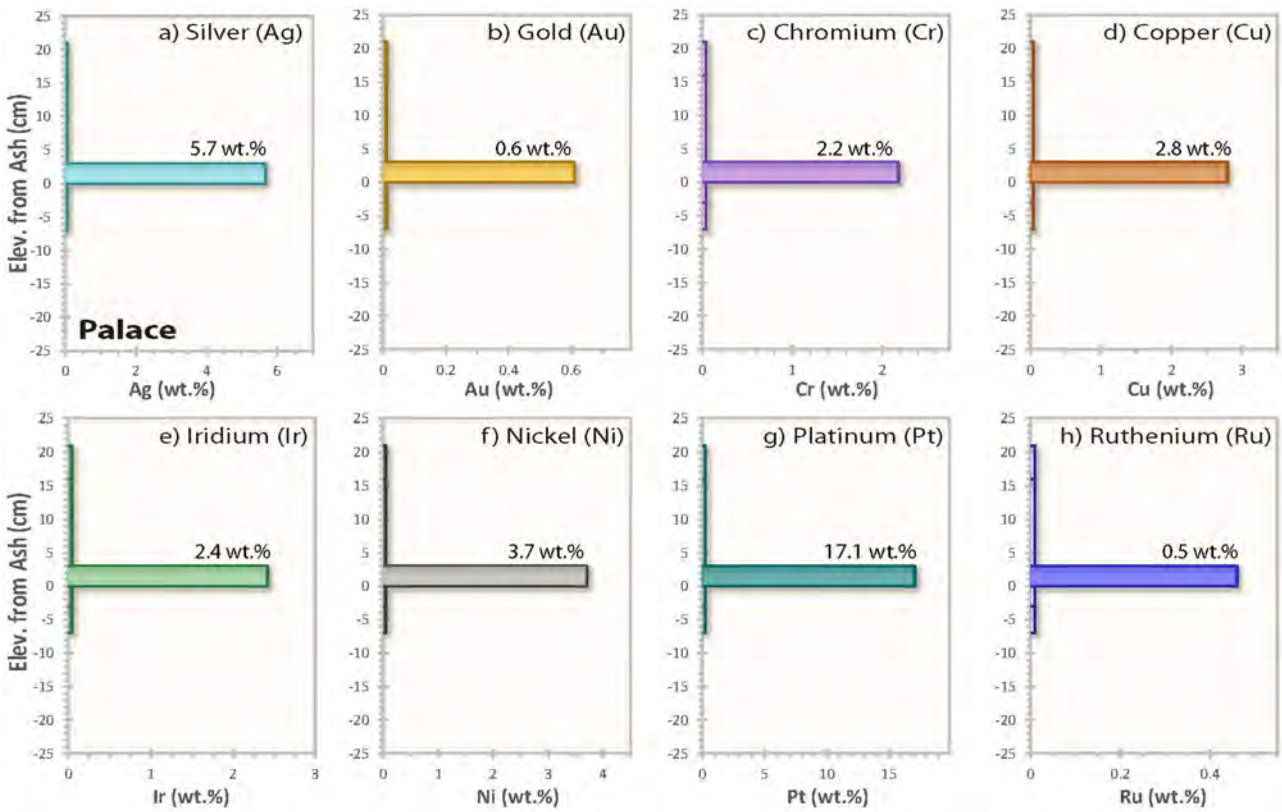

Figure 43: Average composition of selected metal-rich nuggets from the palace. (a-h) Silver (Ag), gold (Au), chromium (Cr), copper (Cu), iridium (Ir), nickel (Ni), platinum (Pt), and ruthenium (Ru), showing wt% in selected nuggets from the destruction layer of the palace (7GG).

Fe-dominant splatter. We made eight measurements on the TeH Fe-dominant PGE splatter (Figure 42d–42f). The metal-rich areas average ~318 µm in length (range: 20-825 µm) with an estimated concentration of 1 per mm^2, 100× more common than the TeH nuggets. Average concentrations are Fe = 17.5 wt%, Ir = 4.7 wt%, and Pt = 1.5 wt%.

We explored a potential extraterrestrial origin by constructing ternary diagrams to compare TeH Fe-dominant splatter with known meteorites and comets (Figure 44b, 44c). We compiled data for 164 nuggets extracted from carbonaceous chondritic meteorites (e.g., Allende, Murchison, Leoville, and Adelaide) [163–166], seafloor cosmic spherules [167, 168], iron meteorites [166, 169], Comet Wild 2 [170], and cometary dust particles [170]. For average weight percentages, see **SI Tables S6 and S7** [7]. The Fe-dominant TeH splatter (Figure 44b) closely matches nuggets from carbonaceous chondrites and cosmic spherules but is a weak match for most iron meteorites (Figure 44c). In addition, the TeH nuggets are similar to four cometary particles, two of which were collected during the Stardust flyby mission of Comet Wild 2 in 2004 [170]. For average weight percentages, see **SI Tables S6 and S7** [7].

To further explore an extraterrestrial connection for TeH Fe-dominant splatter, we compiled wt% data for TeH PGEs (Rh, Ru, Pd, Os, Ir, and Pt) and normalized them to CI chondrites using values from Anders and Grevasse [171]. We compared those values to CI-normalized nuggets in carbonaceous chondrites, including CV-type chondrites (e.g., Allende) and CM types (e.g., Murchison) [163, 164, 166, 172–175], seafloor cosmic spherules [168], micrometeorites [167], and iron meteorites [166, 169]. These results are shown in Figure 44d.

The TeH Fe-dominant splatter closely matches all types of extraterrestrial material with a similar pattern among all data sets: Pd has the lowest normalized values, and Os and/or Ir have the highest, closely followed by Pt. The TeH splatter was also compared to the CI-normalized wt% of bulk meteoritic material from CV- and CM-type chondrites (Figure 44d). The composition of TeH splatter shows poor correlation with bulk chondritic materials, although the splatter is an excellent geochemical match with the PGE nuggets inside them. In summary, the CI normalization of PGEs suggests an extraterrestrial origin for the Fe-dominant TeH splatter, just as the ternary diagrams suggest an extraterrestrial source. The correspondence of these two independent results suggests that this study's quantification of PGEs is sufficiently accurate.

Another unusually abundant element, Mo, is associated with Fe-dominant splatter but not Pt-dominant nuggets.

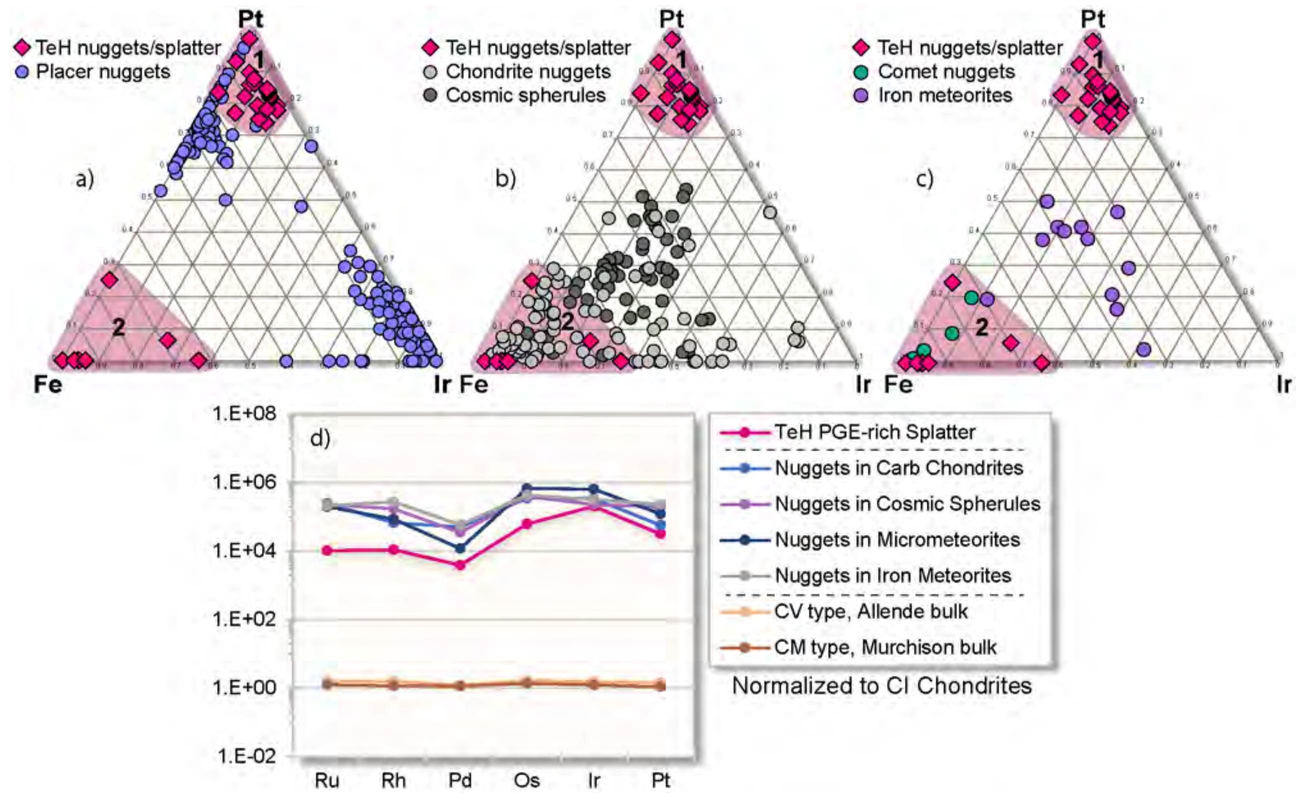

Figure 44: Ternary diagrams for PGE-rich grains. Comparison of Fe-Ir-Pt ratios of PGE-rich nuggets fused into the surfaces of TeH meltglass. There are two populations of TeH nuggets (red diamonds): Pt-dominant at #1 (top) and Fe-dominant at #2 (bottom left). **(a)** TeH Pt-dominant nugget group #1 (red diamonds) overlaps Pt-dominant but not Ir-dominant nuggets (blue circles) from placers and ophiolite deposits in Greece, Turkey, Iraq, Russia, Canada, and the USA. The Fe-dominant TeH nugget group #2 is geochemically dissimilar to all known placer nuggets, suggesting that these nuggets are not placer-derived. **(b)** TeH nuggets (red diamonds) compared to nuggets in carbonaceous chondrites (light gray circles) and nuggets in cosmic spherules (dark gray circles). Pt-dominant TeH nuggets in group #1 are a poor match, but Fe-dominant TeH splatter is an excellent match with chondritic meteorites and cosmic spherules, suggesting that they may be extraterrestrial in origin and that the impactor may have been a chondrite. **(c)** TeH nuggets (red diamonds) are a poor match for most nuggets in iron meteorites (purple circles) but an excellent match for nuggets found in comets (green circles). These data suggest that Fe-dominant PGE nuggets at TeH may have originated from cometary material. **(d)** Semi-log comparison of PGEs ruthenium (Ru), rhodium (Rh), palladium (Pd), osmium (Os), iridium (Ir), and platinum (Pt), normalized to CI chondrites. TeH Fe-dominant splatter (red line) is an excellent match for PGE nuggets in carbonaceous chondrites (blue line), cosmic spherules (purple line), micrometeorites (dark blue line), and iron meteorites (gray line). In contrast, TeH PGE nuggets are a poor match for bulk material from CI-normalized CV-type chondrites (e.g., Allende; orange line) and CM-type chondrites (e.g., Murchison; brown line).

Mo averages 0.3 wt%, with up to 1.1 wt% detected in Fe-dominant splatter, but none were detected in TeH Pt-dominant nuggets. Mo is not reported in terrestrial placer nuggets and occurs in low concentrations (less than ~0.02 wt%) in iron meteorites. In contrast, Mo is reported at high concentrations in PGE nuggets from carbonaceous chondrites (~11.5 wt%), cosmic spherules (0.6 wt%), and cometary material (5.8 wt%). Thus, the Mo content of the TeH splatter appears dissimilar to terrestrial material but overlaps values of known cosmic material, suggesting an extraterrestrial origin.

Based on the volume and weight of the meltglass, we estimate that the extraterrestrial-like metallic TeH Fe-dominant splatter represents <1 wt% of the total mass of the meltglass. This low concentration is typical of low impactor content in impact ejecta (<1 wt%) [101].

Ag, Au, Cr, Cu, and Ni in TeH nuggets. We also investigated nuggets that lack PGEs. The geochemistry of these nuggets shows two distinct populations, one Ni-dominant and one Fe-dominant (Figure 42g–42i). Twelve measurements of TeH samples show enrichments in Ag averaging 5.7 wt%, Au = 0.6 wt%, Cr = 2.2 wt%, Cu = 2.8 wt%, and Ni = 3.7 wt%. All particles appear to have been melted at high temperatures: silver at ~961°C, gold at 1064°C, chromium at 1907°C, copper at 1085°C, and nickel at 1455°C.

Ternary diagrams for Cr, Fe, and Ni show that some TeH nuggets exhibit chemical similarities to mineral deposits in Greece, Turkey, and Oman, suggesting that some nuggets are of terrestrial origin. However, other TeH nuggets are chemically similar to materials found in iron meteorites, chondrites, achondrites, and comets (**SI Figure S9** [7]). Compared to meteoritic material, the Ni-dominant group roughly corresponds to measurements from sulfide inclusions in chondrites [176], and the Fe-dominant group overlaps both chondritic sulfide inclusions and metal-rich grains from Comet Wild 2 [177]. These results suggest that a small fraction (<1 wt%) of the Cr- and Ni-rich dust found embedded in TeH meltglass is of extraterrestrial origin, most likely ejected from an airburst/impact of either a meteorite or a comet.

Interpretation of PGE nuggets

Notably, the PGE-rich nuggets and splatter were observed embedded only on melted surfaces of the TeH meltglass but not inside the vesicles or within the meltglass. This observation suggests that the nuggets and splatter were not contained in the original sedimentary matrix but were fused onto the TeH glass while still molten. Geochemical analyses suggest a dual origin. The Pt-dominant nuggets do not match known extraterrestrial material and instead appear to be of terrestrial origin, possibly from placer deposits and regional mines. It is unclear exactly how they became embedded onto but not inside TeH meltglass, but one possibility is that they were buried initially as river-laid, PGE-rich placer deposits. If so, we propose that they were ejected during the impact event and distributed across the molten glass by the impact blast wave. Another possibility is that they derive from jewelry and raw precious metals in the palace complex that were pulverized and dispersed during the high-velocity destruction of the palace.

In contrast, the Fe-dominant nuggets fused into the surfaces of TeH meltglass closely match the composition of nuggets from chondritic meteorites, cosmic spherules, and comets, consistent with an extraterrestrial origin. The data suggest that a carbonaceous chondrite or a comet detonated in the air near TeH, pulverized PGE-rich nuggets within the bolide, accreted terrestrial placer nuggets, and dusted both terrestrial and extraterrestrial material across the surfaces of molten mudbricks, pottery, and building plaster at low concentrations of <1 wt%.

8.7 Platinum, iridium, and palladium in the destruction layer

For TeH bulk sediment, neutron activation analyses show Pt abundance peaks in the destruction layer of all profiles tested (Figure 45a–45d) at ~2× to 8× an average crustal abundance of 0.5 ppb. Sedimentary Ir was below detection at <0.1 ppb for the palace, temple, and ring road but unusually high in the wadi, where values peaked at 1.0 ppb, ~50× larger than a crustal abundance of 0.02 ppb (**SI Table S3** [7]). Also, Pt/Pd ratios in bulk sediment from the destruction layers are anomalously higher than background layers by ~4× to 14× (Figure 45e–45h).

Interpretation of Platinum, Iridium, and Palladium

Abundances of Pt, Ir, and the Pt/Pd ratios all peak in sediment at or near the top of the destruction layer, suggesting an influx of those elements at 1650 BCE, most likely from both extraterrestrial and terrestrial sources. Sedimentary concentrations of Ir only peaked in the wadi samples and were not detectable at the other three sites for unknown reasons.

8.8 Meltglass vesicles lined with metal-rich minerals

The interior portions of many melted pieces of mudbrick, roofing clay, and pottery are highly vesicular. The walls of these vesicles nearly always display an array of metal-rich crystals (Figure 46). These include elemental iron and iron oxides, labeled as FeO, but are oxidized as hematite (Fe_2O_3) with a melting point of ~1565°C; magnetite (Fe_3O_4) that melts at ~1590°C; and/or elemental iron (Fe) melting at ~1538°C (Figure 46a, 46b, 46d, 46f, 46g). Also observed on vesicle walls were crystals of Fe phosphide (Fe_2P) that melt at ~1100°C (Figure 46c, 46g), manganese oxide (MnO) at ~1945°C (Figure 46d), calcium phosphate ($Ca_3(PO_4)_2$) at ~1670°C (Figure 46e), and calcium silicate ($CaSiO_2$) at ~2130°C (Figure 46e).

Interpretation of minerals in vesicles

In some cases, these mineral crystals appear to have crystallized from the molten matrix as it solidified. In other cases, it seems that they plated onto the vesicle surface, suggesting that they may have condensed through vapor deposition from the high-temperature, mineral-saturated atmosphere within the vesicle.

8.9 Melted iron and titanium in the destruction layer

SEM inspection of the palace mudbrick meltglass revealed partially melted grains of magnetite (Fe_3O_4) with a melting point of ~1590°C (Figure 47a, 47b) and titanomagnetite ($TiFe_2O_4$) with a melting point of ~1550°C (Figure 47c, 47d). The latter is an oxyspinel commonly occurring as discrete grains or an exsolution product within magnetite. The chemical composition of magnetite at equilibrium is 72.36 wt% Fe and 27.64 wt% O. Titanomagnetite is 21.42 wt% Ti, 49.96 wt% Fe, and 28.63 wt% O. SEM-EDS analysis confirms similar compositions for the observed TeH grains.

Interpretation of melted Iron and Titanium

These grains display bubble-rich features that are commonly associated with grain fractures. There are several possibilities. (i) Approximately 20% of the time, magnetite grains are reported to be naturally overprinted by porous magnetite as a precipitation product, creating a bubble-like texture [178]. (ii) Alternatively, these features may be textures caused by differential dissolution [179, 180]. (iii) The grains may have been exposed to temperatures equal to or greater than their melting point, causing the outgassing of volatiles or the rapid reduction of iron oxides. Because of the morphological

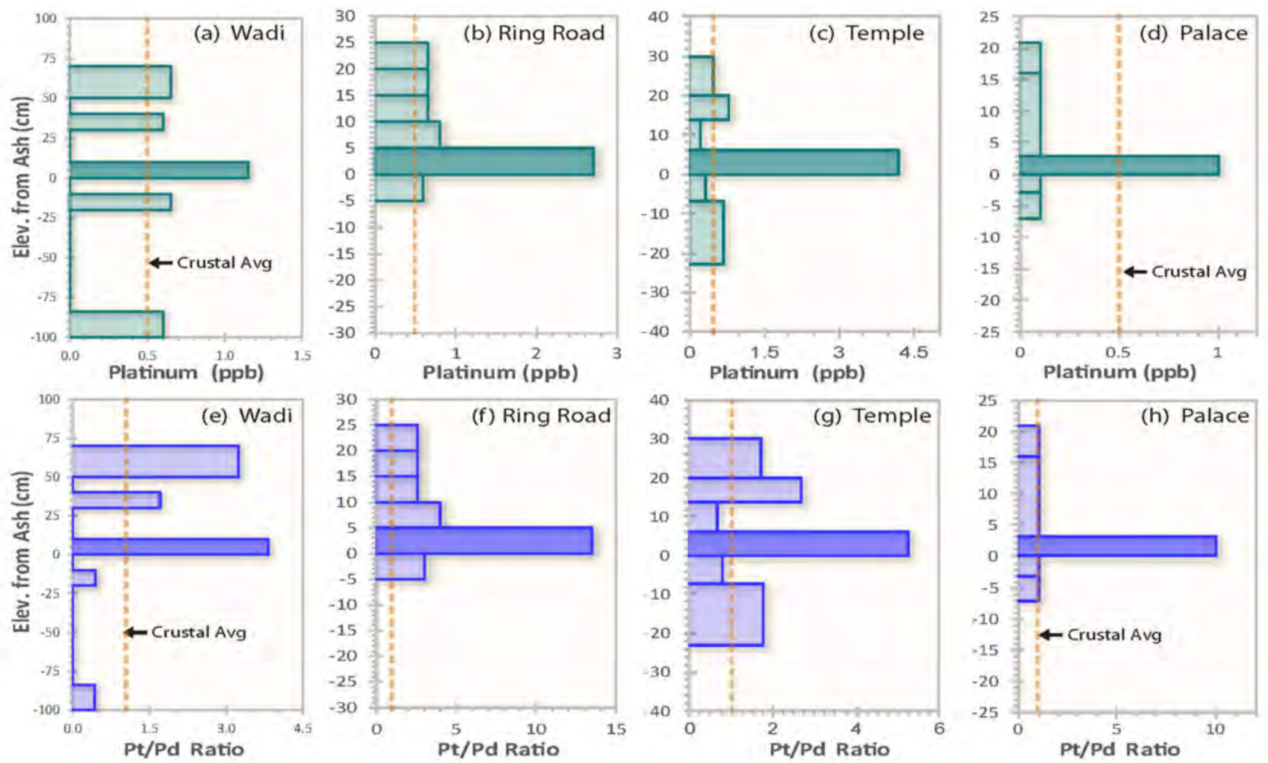

Figure 45: Plots for sedimentary Platinum and Palladium. (a-d). Platinum (Pt) concentrations. **(e-h).** Platinum/palladium ratios (Pt/Pd). Depths are in cm above or below the bottom of the destruction layer. Sample locations are labeled. Crustal abundance values (orange dashed lines) are ~0.5 ppb for Pt.

dissimilarity of TeH grains to published examples of grains altered by precipitation and dissolution, we infer that these grains were altered by exposure to high temperatures.

8.10 Melted iron sulfide and iron phosphide in the destruction layer

Sulfide and phosphide grains were found attached to the walls of the vesicles within the mudbrick meltglass. SEM-EDS analyses of palace mudbrick meltglass identified melted Fe sulfide (FeS), also known as troilite (Figures 48, 49), with a composition of 63.53 wt% Fe and 36.47 wt% S and a melting point of ~1194°C. Commonly associated with the Fe sulfide, Fe phosphide (Fe_2P; Figure 48b, 48e) is a nickel-poor variety of barringerite, a mineral first identified at Meteor Crater in Arizona. Another variant of Fe phosphide, Fe_3P, was also identified in melted mudbrick from the palace. Both phosphide variants melt at ~1100°C. Fe phosphide is common in meteorites, but although terrestrially rare, Fe_2P is found in pyrometamorphic rocks, such as those in the Hatrurim Formation in nearby Israel [181]. Britvin et al. [181] reported that the local Fe phosphide displays averages for Fe at 76.4 wt% and P at 21.4 wt%, with small amounts of Ni, Co, and Cr at 2.2 wt%. The composition of Fe phosphide found at TeH is comparable, averaging 78.3 wt% Fe and 21.7 wt% P. However, unlike those Fe_2P grains from Israel, the TeH grains lack detectable Ni, Co, and Cr.

Interpretation of Iron sulfide and Iron phosphide

Visual inspection indicated that the sulfide and phosphide grains were attached to the inner surfaces of vesicles and, therefore, most likely formed by vapor deposition at >1100°C rather than by crystallization from the melted matrix. Troilite (FeS) is very rare terrestrially but common in meteoritic material [63, 182]. Harris et al. [182] reported finding inclusions of troilite (FeS) as meteoritic clasts in Chilean meltglass proposed to have derived from a cosmic airburst that left meltglass on the surface along a 19-km-long stretch of the Atacama Desert approximately 12,800 years ago. At that site, troilite is typically found lining the walls of vesicles in the meltglass, as is the case for TeH meltglass.

8.11 Melted calcium phosphide in the destruction layer

SEM-EDS analyses also show that vesicles in melted mudbrick from the palace contain calcium phosphide (Ca_3P_2) (Figure 50). This mineral has a stoichiometric composition of ~66.0 wt% Ca and ~34.0 wt% P and melts at ~1600°C (Table 1). Unlike Fe sulfide and Fe phosphide discussed above, which appear to have formed by vapor deposition, these examples most likely crystallized from the molten Ca-Al-Si matrix material.

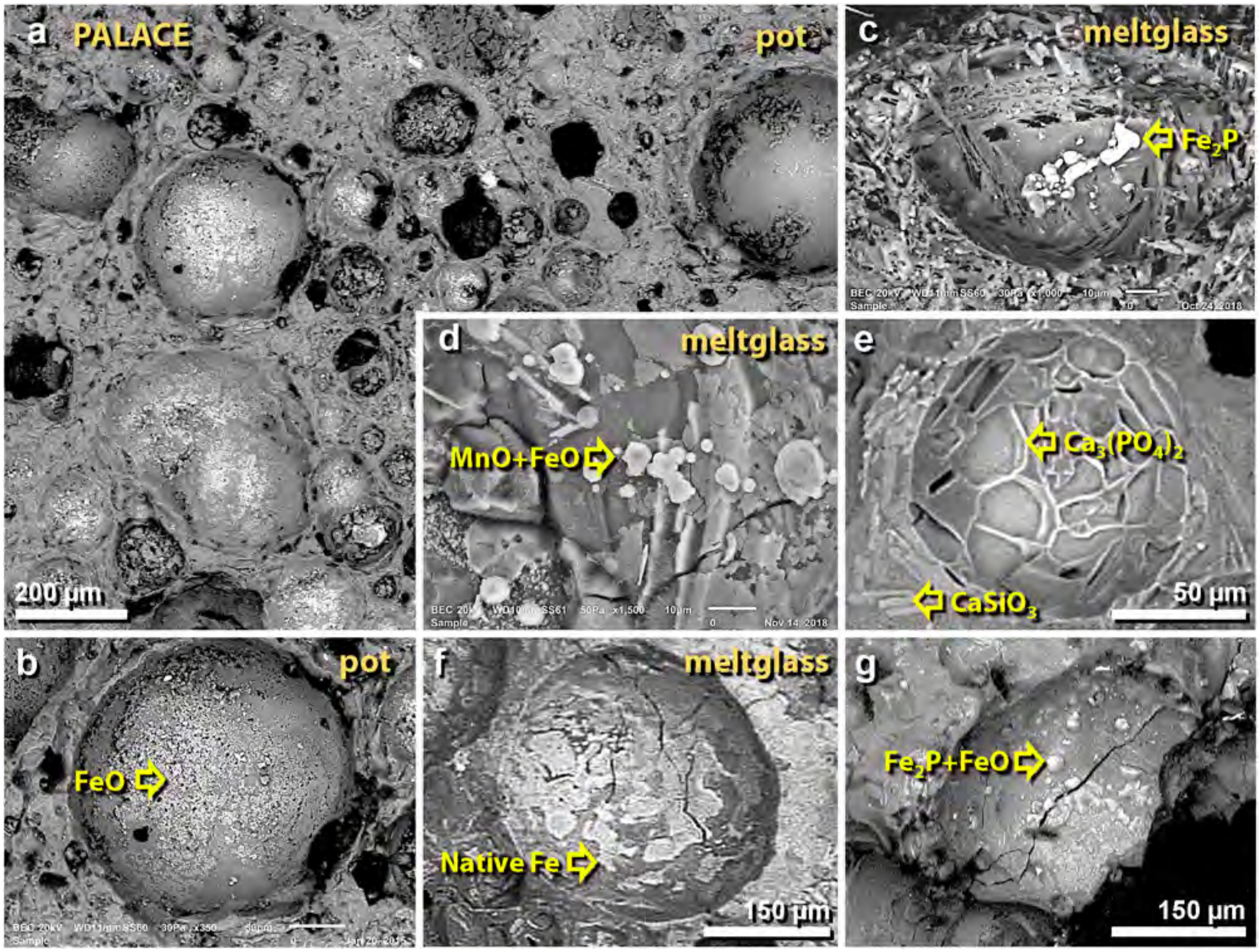

Figure 46: SEM images of gas vesicles in melted material from the palace. (a-b) Vesicles in melted pottery are lined with crystals of iron and iron oxide (elemental Fe, Fe_2O_3, and/or Fe_3O_4). **(c-g)** Vesicles in melted mudbrick and roofing clay often are lined with a variety of crystals, including elemental Fe, iron oxide, Fe phosphide (Fe_2P), manganese oxide (MnO), calcium phosphate ($Ca_3(PO_4)_2$), and calcium silicate ($CaSiO_3$). These crystals are consistent with vapor deposition at high temperatures.

8.12 Melted calcium silicate (wollastonite) in the destruction layer

SEM-EDS analyses of palace mudbrick meltglass (Figure 51a, 51b) and melted pottery (Figure 51c) reveal the presence of Ca silicate, also known as wollastonite ($CaSiO_3$), with a composition of 48.3 wt% CaO and 51.7 wt% SiO_2 and a melting point ~1540°C (Table 1). These crystals are mostly found on broken surfaces of the matrix but are sometimes observed inside vesicles. Unlike Fe sulfide and Fe phosphide above, which appear to have formed by vapor deposition, these crystals appear to have condensed from the molten matrix as it cooled.

Summary of 8. High-temperature impact-related melted materials

Proxy Types:

- Melted spherules (Fe, Si, Ca)
- Melted chromite, zircon
- Melted metal-rich nuggets (Ir, Pt, Ni, Au, Ag)
- Meltglass with metallic linings

Analysis Methods:

- SEM, TEM, EDS, neutron activation, elemental mapping

Key Findings:

- Spherules and nuggets embedded in glass require >2000°C.
- Recrystallized chromite/zircon confirms extreme heating.
- Enriched Ir-Pt-Pd signals match known impact layers.

9. Human bones in the destruction layer

9.1 Bones in the upper tall at TeH

If the MB II destruction event at TeH was of sufficient magnitude and abruptness to be fatal for human inhabitants, as the evidence indicates, human remains should exist in the MB II layer. Indeed, human skeletal remains of sufficient

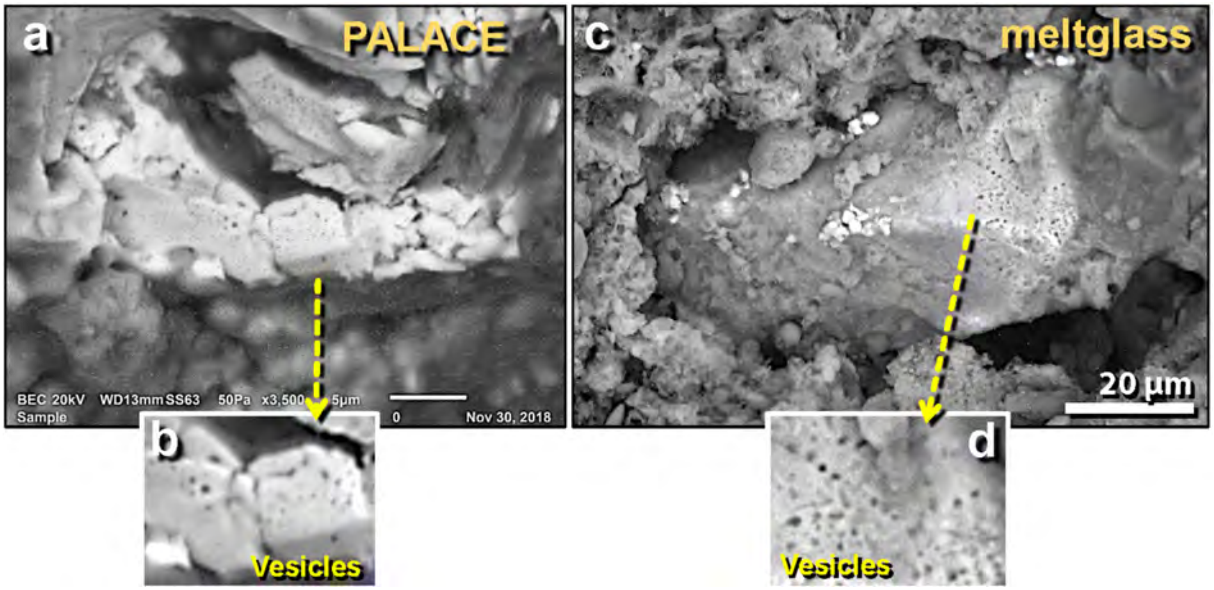

Figure 47: SEM images of melted iron and titanomagnetite in mudbrick meltglass from the palace. (a) Shattered Fe grain containing <0.1 wt% oxygen as determined by SEM-EDS; **(b)** close-up showing surface porosity. **(c)** Titanomagnetite grain showing surface porosity; **(d)** close-up showing aligned porosity possibly along former grain boundaries. The cause of the porosity is uncertain, but because these grains are associated with other high-temperature melted minerals, we propose that this porosity resulted from exposure to high temperatures.

size to be positively identified were found on the upper ring road that encircled the upper tall between the MB II defensive fortification wall and the outer wall of the MB II palace. Two human skulls were found about 20 cm apart (Figure 52a, 52b), adjacent to a portion of a pelvis and a likely arm bone fragment. One skull was missing the mandible, and the right orbit was crushed about 50%. The second skull fragment consisted only of the upper dentition and the lower half of the right orbit. Only two or three rib fragments were found, and no other long bones were recovered. The forensic evidence suggests that the two bodies may have been decapitated, dismembered, and disarticulated. The record indicates that most of the bones had been shattered into small pieces and mixed into a matrix of pulverized mudbricks. It is impossible to determine whether the small bones are from humans or small mammals, but their proximity to identifiable human bones makes it most likely that they are human. If so, only ~10% of the combined original bone mass of both humans is present as observable fragments within a 75-cm radius from the skulls. The remaining 90% of the two skeletons are missing and assumed to have been destroyed and/or located further away in the sediment matrix.

These skeletons were found on the roadway around the upper tall, where the road was 3-4 m wide. The top of the nearby rampart was several meters wide. The remains were found about four meters below the modern surface, well-sealed and undisturbed beneath archaeological sterile strata. The bodies had been rapidly entombed by pulverized mudbrick containing abundant ash and charcoal. No weapons were found associated with the skeletons or evidence of damage by weapons, and neither body showed any indication of exposure to scavengers. Although humans can be mortally affected by earthquakes, volcanism, and warfare, these bone characteristics, both individually and collectively, show no evidence that such events caused these human deaths. Furthermore, even though these bones were closely associated with large charcoal fragments, the bones lacked evidence of direct exposure to fire. Radiocarbon ages of the surrounding charcoal (~1650 BCE) are contemporary with those elsewhere in the destruction event.

We also searched and found human bone fragments in palace bulk sediments, ~15 m away from the skeletons on the ring road. Some palace bone fragments were found with meltglass fused to them (Figure 53), indicating a close association between the high-temperature event and the bones. We quantified bone abundances in the sediment using a >1.2 mm screen (#12 ASTM sieve). The destruction layer contained ~19 bone fragments per kilogram, weighing 3.2 g/kg. The largest bone was ~2.1 cm long × 0.8 cm wide (average size of bones = 0.6 × 0.2 cm). No other bone fragments were observed in nine different samples, three above the destruction layer and six below. After excavating nearly 100 squares (0.36 hectares or ~1% of the site), researchers have found ~10 partial human skeletons out of an estimated city population of ~8,000 people [6]. However, dozens to hundreds of broken and disarticulated bone fragments were found in each of the 100 squares, but these were too small to be conclusively identified as human or animal.

9.2 Bones in the lower tall at TeH

During Season 6 [15], excavations were conducted in two 6-by-6-meter squares along the ring road of the lower tall.

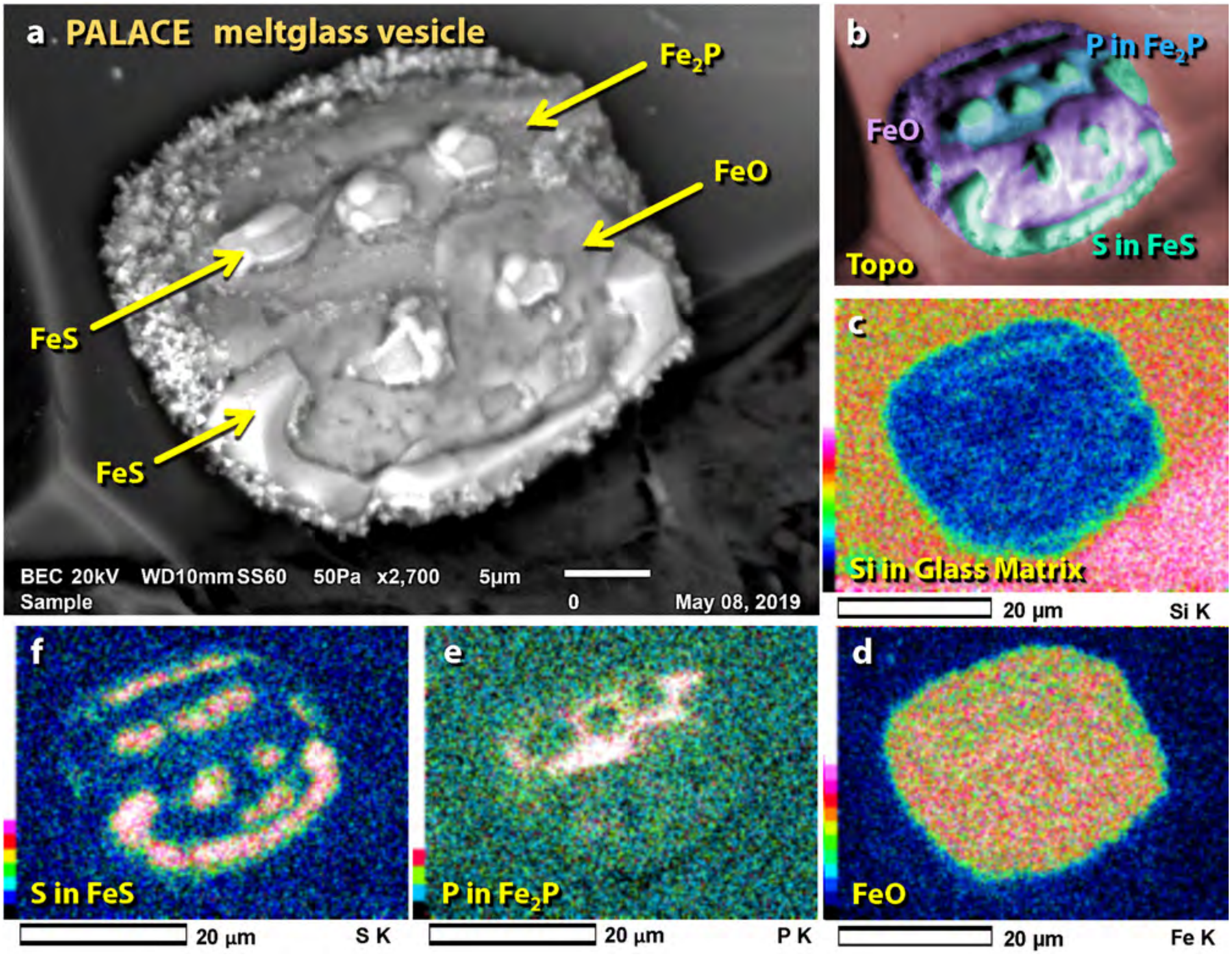

Figure 48: SEM images of Fe-S-P-enriched nugget in vesicle of mudbrick meltglass from the palace. (a) Chemically complex nugget inside a vesicle; contains Fe, S, and P. **(b)** Manually constructed EDS-based phase map showing that nugget is dominantly composed of Fe oxides, S as FeS, and P as Fe_2P. **(c-f)** SEM-EDS elemental maps show the variable composition of nuggets.

Both squares revealed a significant abundance of disarticulated and fragmented human skeletal remains in the MB II destruction layer [15] (Figure 52c). In one square, three partially intact skeletons were found. All bones observed were embedded in a loose debris matrix composed of pulverized mudbrick, ash, and charcoal (Figure 52c). There are no indications of intentional burial, scavenging, accidental death, violence, or battle damage.

Two osteologists examined the bones of two adults and one child [15]. Disarticulation of the skeletons was generally severe, and only leg bones were preserved for the adult skeletons. For one skeleton, ~10 cm of the ends of both femurs showed evidence of charring. The remaining skeleton was represented by many fragmented bones found in the surrounding matrix. Metatarsal bones were abnormally hyper-extended (i.e., joints were over-stretched), and the proximal phalanges were hyper-flexed at almost 90 degrees to the metatarsals. The right knee joint of one skeleton also was hyper-extended [15]. The legs were hyper-flexed backward in a nearby child's skeleton, and the knee joints were disarticulated. Another skeleton was found buried in a crouching position with the hands raised to the face, a posture commonly adopted for protecting the head, as occurred during the volcanic eruption at Pompeii [184].

Bones were also found in another square, ~6 meters south of the square containing the skeletons. This square contained ~100 bones/kg with an average length of 5.0 mm (range: 0.5 mm to 4.7 cm) and an average width of 1.0 mm (range: 0.5 to 5.0 mm). The largest was a small rib bone (4 by 47 mm) from a human infant or a small mammal. The bone fragments weighed ~6.0 g/kg.

We also observed a 3.5-mm-long charred bone splashed with meltglass (Figure 54). In one case, molten sediment had partially melted the bone, mixed with it, flowed, and cooled in place. Previous experiments by Moore et al. [36] suggest that such melting occurs at ≥1500°C. These bones also were

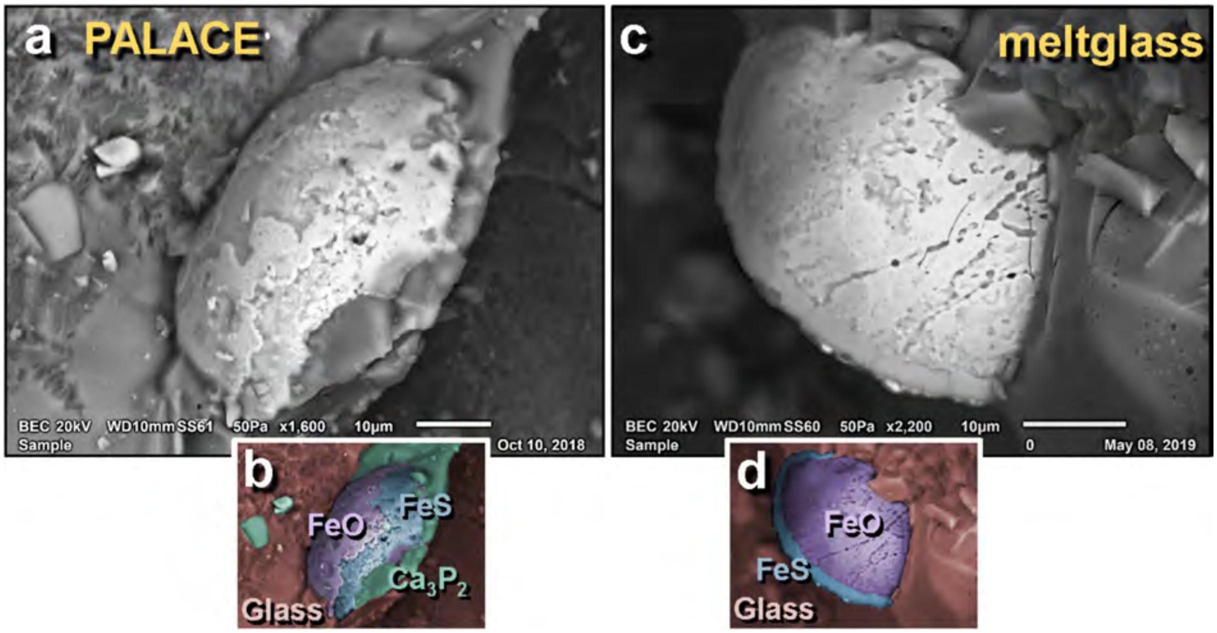

Figure 49: **SEM images of Fe-S-Ca-P-rich grains in mudbrick meltglass from the palace. (a)** Melted Fe-rich grain is chemically complex, containing Fe, S, Ca, and P. **(b)** Manually constructed EDS-based phase map marking areas of Fe oxides (purple, labeled as FeO), FeS (blue), and Ca_3P_2, calcium phosphide (green). **(c)** High-temperature melted Fe-rich grain; **(d)** manually constructed EDS-based phase map showing the area that is predominantly Fe oxide, bordered by a thin rim of FeS.

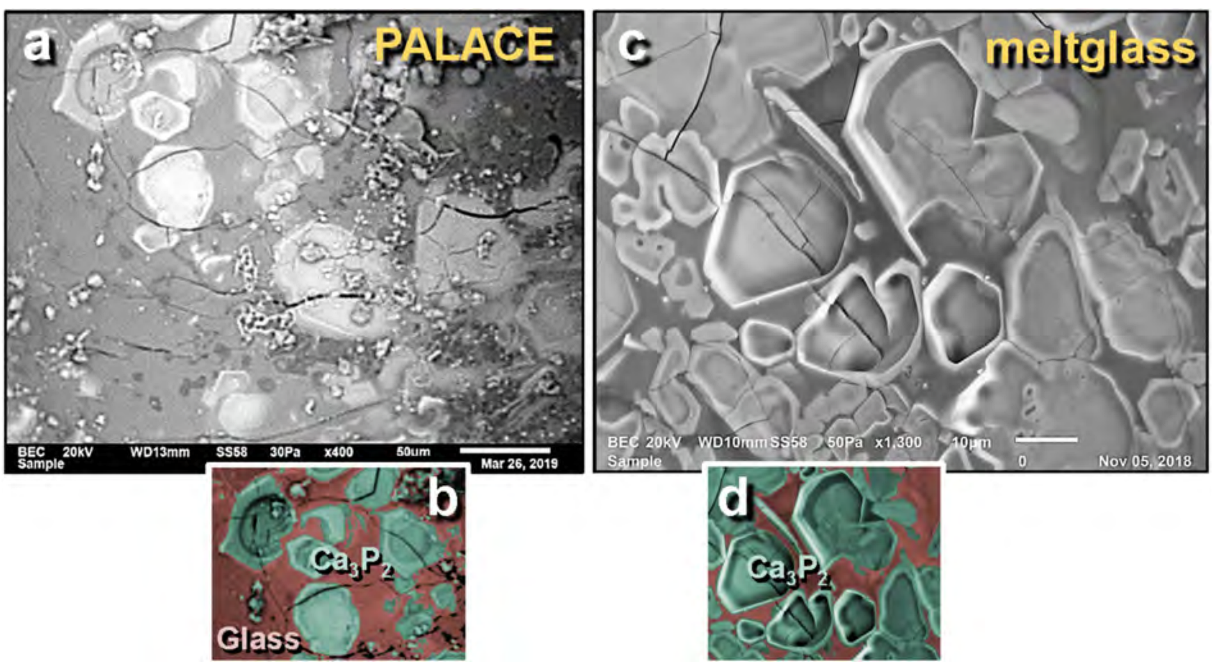

Figure 50: **SEM images of calcium phosphide crystals in vesicles of mudbrick meltglass from the palace. (a)** and **(c)** Crystals of calcium phosphide, Ca_3P_2, lining the inside wall of meltglass vesicles; **(b)** and **(d)** manually constructed EDS-based phase map of Ca_3P_2 (green) crystals embedded in typical Ca-Al-Si melted matrix.

associated with geochemical anomalies. The rib bone is visibly salt-encrusted, measured by SEM-EDS at ~46 wt% NaCl, and the NaCl content of the attached sediment was very high at ~54 wt% (Figure 54a). Anomalously high concentrations of salt were found only associated with the bones and sediment in the destruction layer at 1650 BCE, and not in

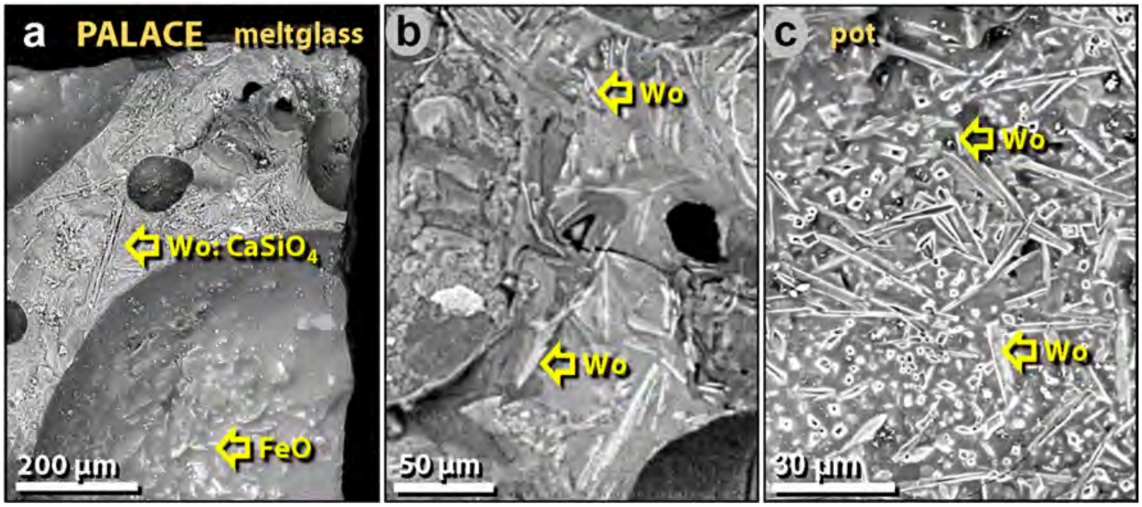

Figure 51: SEM images of wollastonite crystals in palace melted pottery and mudbricks. (a) Spindle-like wollastonite crystals ($CaSiO_4$) on the broken face of mudbrick meltglass. Iron oxide crystals line the vesicle. **(b)** Wollastonite crystal within the meltglass matrix. **(c)** Wollastonite crystals within a vesicle of melted pottery.

strata above or below, indicating an unusual influx of salt at that time. The rib bone also exhibits several nuggets of silver and tin oxide (SnO_2) (Figure 54b), with morphologies suggesting that they splashed onto the bone and sediment while molten. Ag melts at ≥961°C and SnO_2 at ≥1630°C, although Sn melts at ~232°C. The melted tin and silver nuggets are also similar to those observed on the surface of melted mudbricks in the palace that were found fused to meltglass in the temple complex (Figure 54c) and observed splashed across loose sediment (Figure 54d).

Interpretation of human bones

A medical doctor (co-author T.W.) inspected the human bones and concluded that the injuries occurred perimortem, including damage to the eye socket of one skull. We propose that the individuals represented by the bones were violently torn apart by a powerful airburst/impact, leaving only a few hand and foot bones still articulated and unbroken. It would not be possible to duplicate these injuries and disperse the bones found in this layer by warfare or accidental falls from a great height, e.g., from the top of the adjacent rampart. Although tornadoes (max winds of ~512 km/h or ~318 mph) can cause bone breakage, organ damage, and disarticulation (**SI Text S3** [7]), they are exceedingly rare in Jordan or Israel and typically low intensity. In any event, no known tornado has been shown to burn bones and break them into small fragments.

The most severe injuries to human bodies result from the impact of airborne high-velocity objects, such as during explosions and tornadoes (**SI Text S3** [7]). In addition, the ground-hugging blast wave from an airburst/impact would be laden with high-velocity missiles, including sand, gravel, pulverized mudbrick, plaster fragments, potsherds, broken branches, and shattered timbers. At tornado-force wind velocities and extremely high ambient temperatures, these missiles would be capable of incinerating/stripping flesh and crushing bones. Current evidence suggests that the human mortality rate at TeH was very high; most likely, none of the ~8,000 inhabitants survived.

Based on the distribution of human bones on the upper and lower tall, we propose that the force of a high-temperature, debris-laden, high-velocity blast wave from an airburst/impact (i) incinerated and flayed their exposed flesh, (i) decapitated and dismembered some individuals, (iii) shattered their bones into mostly cm-sized fragments, (iv) scattered their bones across several meters, (v) buried the bones in the destruction layer, and (vi) charred or disintegrated any bones that were still exposed.

Although man-made explosives and atomic bombs can account for an extreme range of damage to humans, they can be ruled out because of the age of the site. In addition, warfare, accidents, and tornadoes can be eliminated because they are incapable of causing the observed severe skeletal damage at TeH. The circumstances and condition of the human bones and fragments suggest that at the moment of death, these individuals were going about everyday activities inside the palace, on the upper ring road, and/or on the rampart above the road, where they were struck by a high-temperature thermal pulse, followed by a hyper-velocity blast wave from a catastrophic cosmic airburst, a super-Tunguska event, most likely larger than the airburst at Tunguska, Siberia in 1908, where ~500 reindeer and several herders within the blast radius suffered severe burns and were killed, but sustained no disarticulation [185].

Summary of 9. Human bones in the destruction layer

Proxy Types:

- Disarticulated, fragmented, and scorched bones

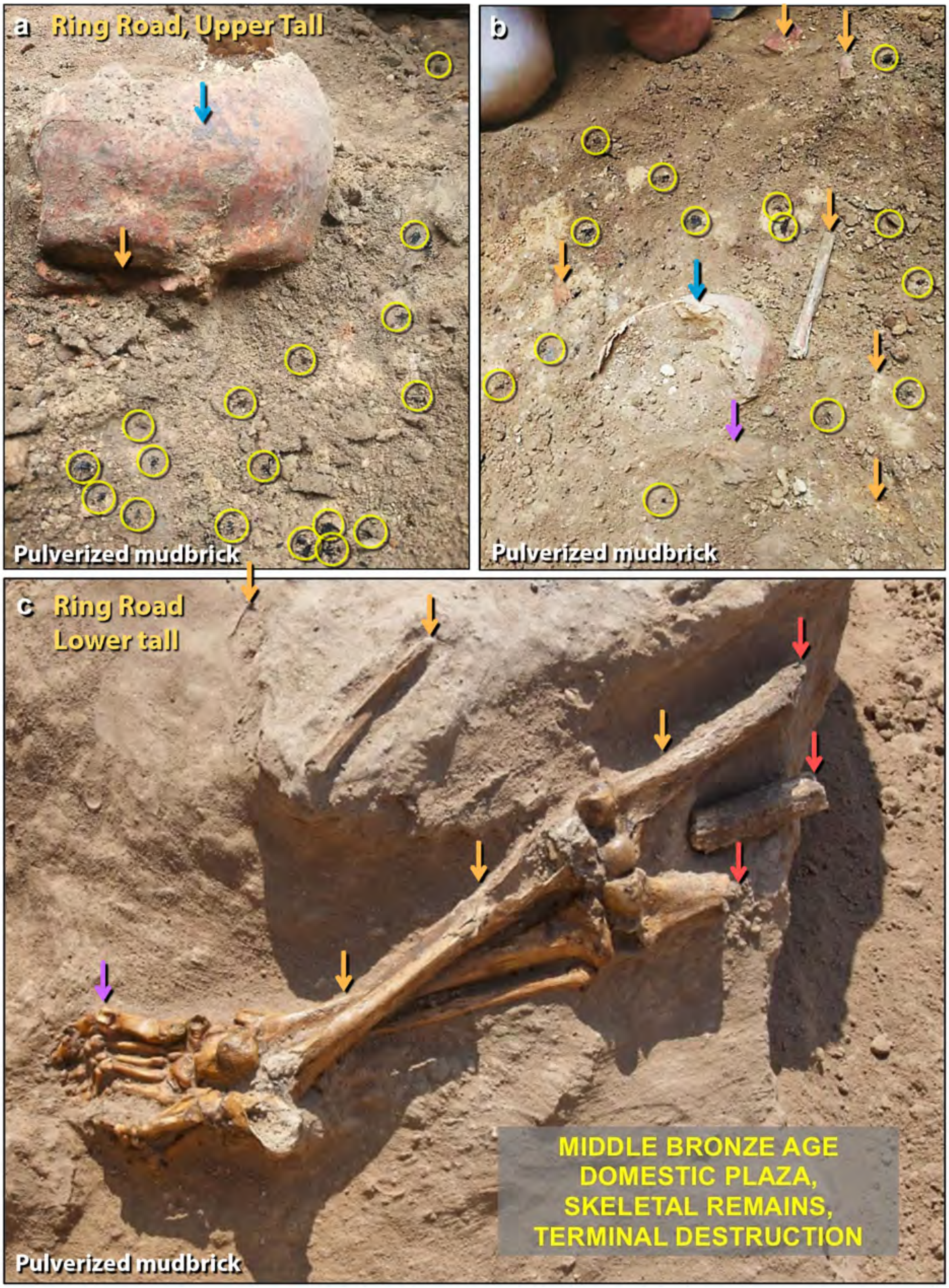

Figure 52: **Human bones in the destruction layer. (a)** Photo of a disarticulated skull found near the palace on the ring road around the upper tall. The right eye socket has been crushed (orange arrow). The skull is embedded in pulverized mudbrick containing numerous charcoal fragments (yellow circles) and is stained with ash commonly found in the destruction layer (blue arrow). The orange tint of the skull suggests it was exposed to temperatures >200°C [183]. **(b)** Rear view of the same skull in panel 'a' (blue arrow) near the second skull (purple arrow)

and numerous disarticulated, fragmented human bones (orange arrows). Charcoal fragments at yellow circles. **(c)** The lower torso is from the ring road of the lower tall (orange arrows) and other disarticulated bones. Bones show evidence of being burned (red arrows); the rest of the skeleton is dismembered and disarticulated. Hyper-flexed toes (purple arrow) are consistent with either perimortem or postmortem exposure to high temperatures.

Analysis Methods:

- Osteological and spatial analysis

Key Findings:

- Fragmentation and burning patterns indicate explosive trauma.
- The lack of burials suggests body disintegration consistent with airburst effects.

10. Anomalously high salt concentrations and environmental aftermath

10.1 Salt enrichment in the destruction layer sediments

Early general observations at TeH indicated that anomalously high salt concentrations mark the destruction layer. For example, where the carbon-rich, potentially fertile destruction layer is exposed on the surface of the lower tall, it is unsuitable for agriculture until the salts are leached using local spring water. Some areas of the lower tall have never been farmed, and the MB II surface exposed at ground level turns white with salt crystals following rainfall. For most excavated squares, the newly exposed MB II surface from each day's archeological excavation produced an obvious white salt crust overnight as humidity leached salt to the surface. Also, we observed that the newly exposed mud/ash mortar between mudbricks hardened after exposure because of salt crystals and that many pottery sherds and some bones from the destruction layer were encrusted with large salt crystals.

We also discovered melted salt crystals in the destruction layer. For example, some palace meltglass displayed blebs of non-crystalline, melted potassium chloride (KCl; Figure 55), with a melting point of ~772°C and a boiling point of 1420°C. KCl is stoichiometrically composed of ~52.4 wt% K and 47.6 wt% Cl. We also identified melted sodium chloride, NaCl (Figure 55c, 55d), with a melting point of 801°C and a boiling point of 1465°C. NaCl is composed of ~39.3 wt% Na and ~60.7 wt% Cl. Even though both of these salts melt at low temperatures and alone are not definitive indicators of a cosmic impact, they appear non-crystalline and are fused into the meltglass, indicating exposure to temperatures sufficient to melt sediment (>1200°C). Also, the blebs display vesicles from outgassing, suggesting that they may have exceeded their melting points.

Using SEM-EDS analysis, six other samples of melted mudbrick from the palace were found to average ~4.4 wt%

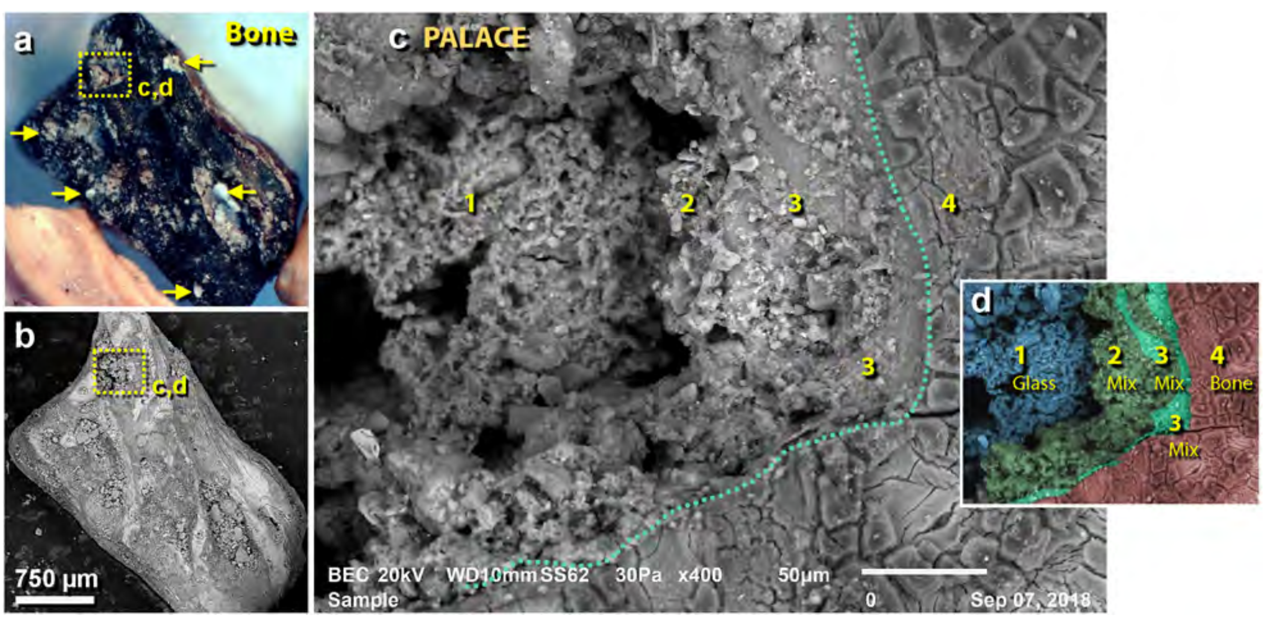

Figure 53: Bone fragment splattered with meltglass in the destruction layer. (a) 3.5-mm-long charred bone from the palace. The yellow boxed area indicates an area of melted glass on bone, as shown in panels 'c' and 'd.' Yellow arrows point to other areas with meltglass fused to the bone. **(b)** SEM image of bone in panel 'a.' **(c)** SEM close-up image of boxed area in panel 'a.' Green arrows mark the glass-to-bone boundary, as shown in panel 'd.' #1 represents unmelted Ca-Al-Si-rich sediment with no bone component; #2 and #3 represent partially melted sediment mixed with melted bone (hydroxyapatite); #4 presents charred bone. **(d)** Colorized SEM image of panel 'c' showing gradation of bone-and-sediment mixing based on multiple SEM-EDS analyses.

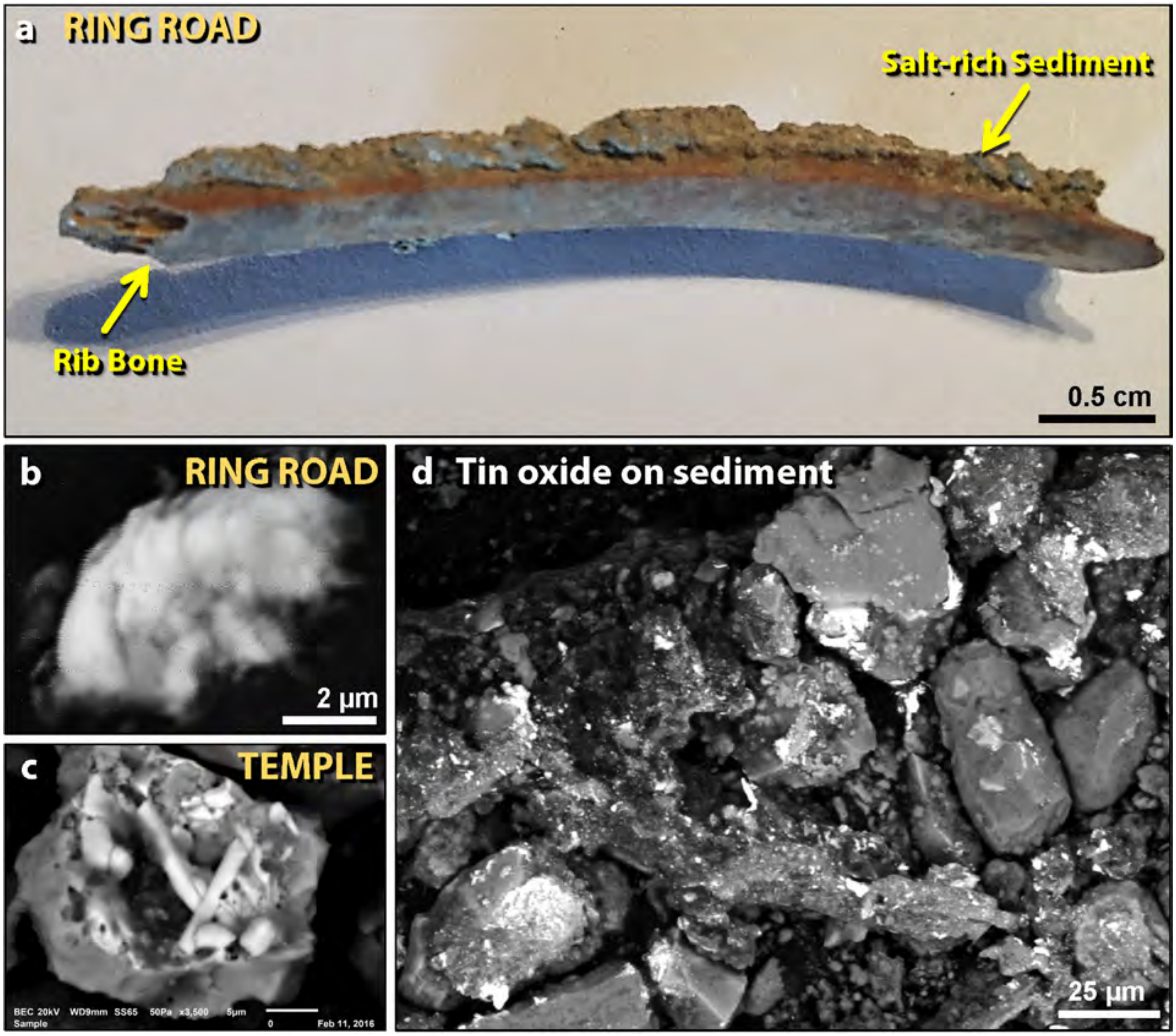

Figure 54: Bone associated with salt and melted tin oxide (SnO_2). (a) Photomicrograph of 4.7 cm-long human or mammal rib bone from the ring road on the lower tall. NaCl is present at high concentrations in the sediment (~54 wt%) and on the bone (~46 wt%). (b) Tin oxide particle (SnO_2) appears to have collided with sediment on the bone while molten, possibly as unoxidized tin. The melting point of SnO_2 is ~1630°C, but unoxidized tin melts at ~232°C. **(c)** A similar tin oxide particle from the temple, ~150 from the lower ring road sampling site. Particles are fused into meltglass. (d) Tin oxide splashed onto sediment around the bone in panel 'a'.

NaCl (range: 2.0 to 9.1 wt%), and one sample of pottery from the palace contains ~17.5 wt% NaCl at its surface. For two samples from the temple, SEM-EDS analyses showed that some melted mudbrick includes an average of ~2.0 wt% NaCl with associated sediment containing ~54 wt% NaCl. Activation Laboratories in Canada used neutron activation analyses to determine salt content in samples from within, above, and below the MB II destruction layer from the palace and temple. The results showed a peak concentration of ~5.5 wt% salt plus sulfate in the MB II layer, tapering off to about half or less above and below this layer. We also directly measured the salinity of these same samples, with the destruction layer containing ~4 wt% salt in the palace and ~3.9 wt% in the temple (Figure 56). In both palace and temple areas, the salt content of two sediment samples above and two below the destruction layer exhibited values below detection at <1 wt%. The ring road displayed values of ~3 wt% in the destruction layer (Figure 56) but also had high values above and below, possibly due to the erosion of salt-rich sediment onto the road.

10.2 Soil sterilization and long-term abandonment in the Jordan Valley

Numerous lines of evidence reveal the sudden, catastrophic destruction of TeH at ~1650 BCE [6]. At the same time, archaeologists excavating nearby sites noted what they termed the "Late Bronze Age Gap" [6, 16, 186], during which ~16 cities/towns, including TeH, and >100 smaller

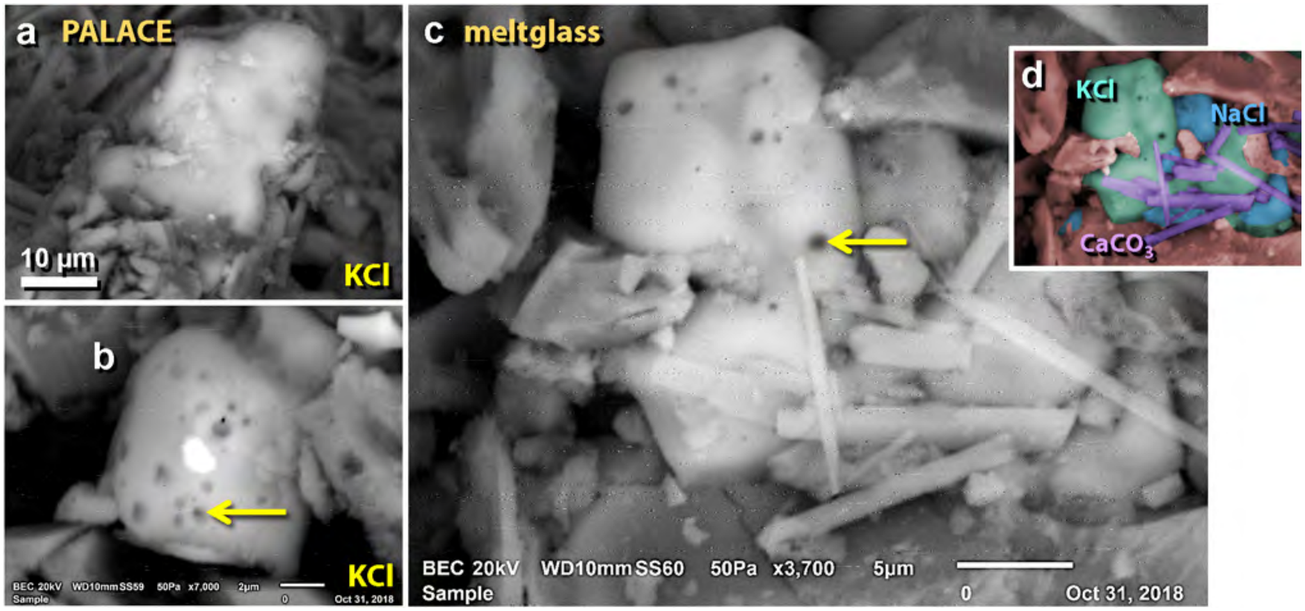

Figure 55: SEM images of melted potassium and sodium salt grains. (a-b) Potassium chloride (KCl) grains melted into the surface of the palace mudbrick meltglass. **(c)** Melted NaCl and KCl grains. Bubbles (yellow arrow) suggest that the salt grains exceeded their melting points. **(d)** Manually constructed EDS-based phase map of panel 'c,' showing potassium chloride (KCl; green), sodium chloride (NaCl; blue), and spindle-like calcium carbonate crystals ($CaCO_3$; purple).

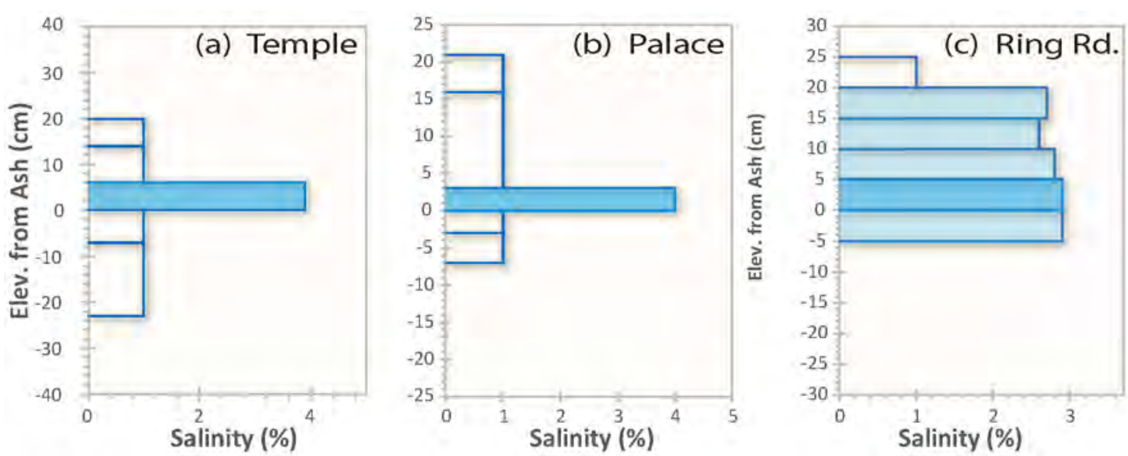

Figure 56: Salinity in TeH Sediment. (a-c) Percentage of salinity for three sites: temple, palace, and ring road. The wadi site had <1% salt content in all samples. Open bars mean below detection (<1%).

villages [187–189] were abandoned across the 30-km-wide lower Jordan Valley. This abandonment continued throughout the Late Bronze Age and most of the early Iron Age. Population levels are estimated to have plummeted from ~45,000-60,000 people to only a few hundred nomadic tribespeople inhabiting the area following this destruction event [6]. For TeH, the occupation gap is >600 years [6]. The archaeological record indicates a gap of approximately 300 years in the Jericho area in the southwestern Jordan Valley. For Tall Nimrin, about 5 km north of TeH, there is a post-MBA occupation gap of ~500 years [41, 186, 190], and in addition, excavators found remains of destroyed MB II walls. No walls were taller than ~2 m, or 10 courses of mudbricks [41, 186, 190], and all were on the north side of the tall, similar to 10-course-high TeH wall remnants that appear shielded from the proposed impact.

This multi-century abandonment is particularly puzzling, given that this area contains the most fertile agricultural land within a radius of hundreds of kilometers across Jordan, Israel, and Palestine. The destruction was so remarkable and pervasive that the ensuing name of the area became Abel, meaning "the mourning grounds" (specifically, to mourn because of a calamity) [13]. Consequently, this does not appear to have been a typical disaster that occasionally

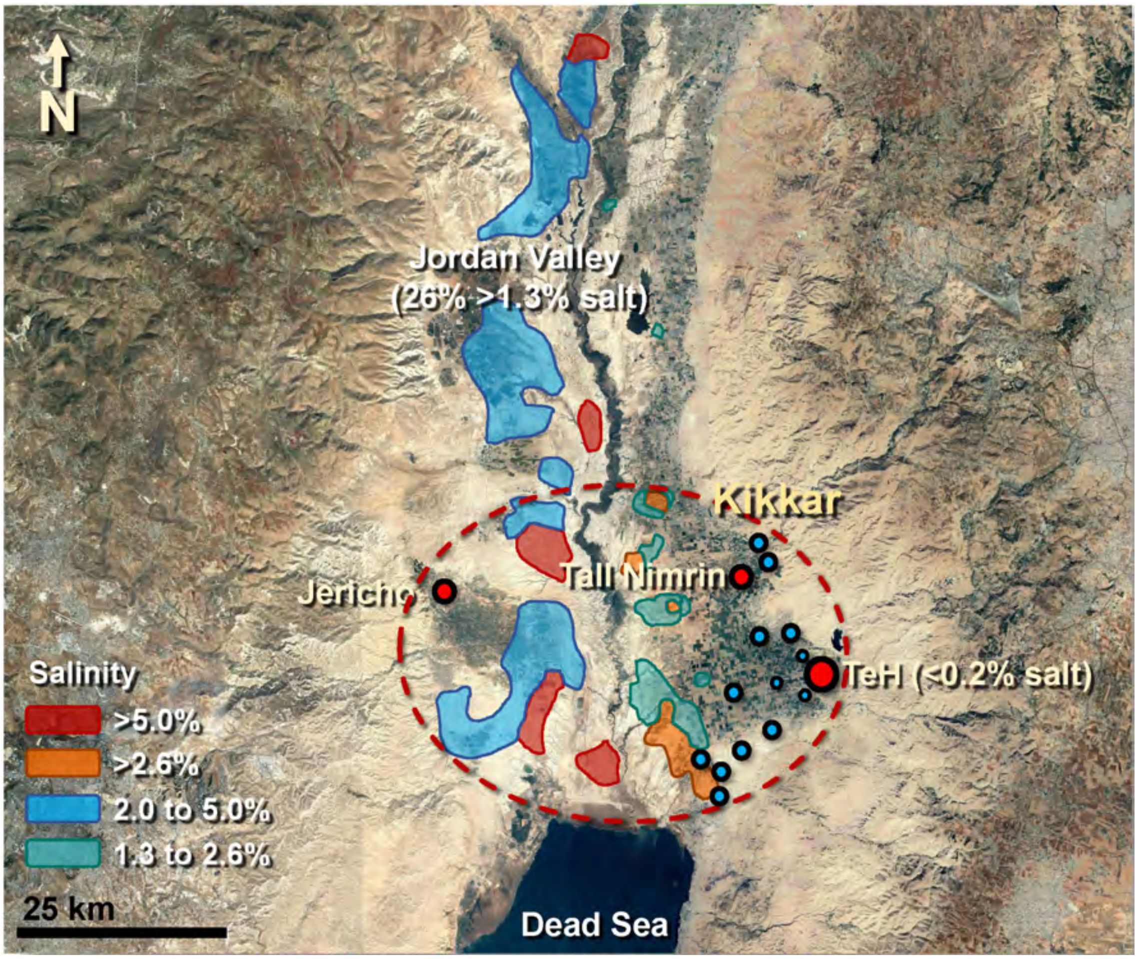

Figure 57: **Salt and the 16 Cities of the Plain.** Covering ~26% of the southern Jordan Valley, the colorized areas mark modern-day salinity concentrations of ≥1.3%, considered lethal for many domestic food crops. TeH (largest red dot) was the principal city in the area; Tall Nimrin is the next largest, with smaller towns in blue. The dashed red oval indicates the extent of the Kikkar, known as the "disk of the Jordan." All 16 major settled sites and >100 villages in the southern Jordan Valley appear to have been abandoned at ~1650 BCE (3600 cal BP). Jericho was minimally resettled ~300 years after the destruction event. Tall Nimrin was resettled ~500 years later, and TeH was reoccupied ~600 years later. Source of base image: "The Southern Jordan Valley." 35° 51.254 N, 35° 33.092 E. Google Earth; Maxar Technologies; CNES/Airbus. Imagery date: 10/29/2020; accessed: 4/4/2021. Permissions: https://about.google/brand-resource-center/products-and-services/geo-guidelines/ Modified by the authors using Adobe Photoshop CC2014 (adobe.com/products/photoshop.html).

occurs due to warfare and earthquakes; instead, it seems to have been a regional civilization-ending catastrophe that depopulated more than 500 km^2 of the southern Jordan Valley for 3 to 7 centuries [6].

So, what could have caused the long-term abandonment of the entire lower Jordan Valley with its fertile agricultural land? One potential clue is that the destruction layers in both the palace on the upper tall and the temple on the lower tall contain salts at average concentrations of ~4%, ranging up to 54 wt%, while conversely, salt concentrations above and below the destruction layers are undetectable at <1 wt%. In modern times, the surface sediments around TeH are non-saline at <0.2% salt [191] (Figure 57). Elsewhere in the Kikkar, or southern Jordan Valley, ~26% of the area has salinity levels ≥1.3 wt% with some parts >5 wt% [191–193] (Figure 57).

According to the US Department of Agriculture (USDA), wheat will not germinate if the soil salt content is >1.3 wt%, and barley will not germinate at >1.8 wt% [194, 195]. These are the two primary cereal grains of the Ancient Near East. Thus, if the unusually high concentrations of salt recorded at TeH were similar throughout much of the southern Jordan Valley, no crops could have been grown until, with time, the salt had leached out of the soil. Accomplishing the desalination of the soils would have taken hundreds of years, based on typical farming practices.

Although the precise origin of the peaks in salinity at TeH is unknown, we speculate that an impact into or an airburst above high-salinity surface sediments (26% of land in the southern Jordan Valley at >1.3% salinity) and/or above the Dead Sea (with ~34 wt% salt content) may have distributed hypersaline water across the lower Jordan Valley. If so, this influx of salt may have substantially increased the salinity of surface sediments within the city and surrounding fields. Any blast survivors would have been unable to grow crops and would have been forced to abandon the area. After ~600 years, the high salt concentrations sufficiently leached out of the salt-contaminated soil to allow the return of agriculture.

Summary of 10. High salt concentrations and environmental aftermath

Proxy Types:

- Salts (~4 wt%) in soils
- Post-destruction site abandonment

Analysis Methods:

- Geochemical assays, stratigraphy, land-use history

Key Findings:

- Salt is likely derived from vaporized Dead Sea brines.
- Agriculture ceased for ~600 years due to hypersaline soil conditions.

11. Coeval destruction and burning of Jericho

By ~1650 BCE, Tell es-Sultan, proposed as the biblical Jericho, reached its maximum extent [196] at ~7 hectares [197], or about one-fifth the size of TeH, located ~22 km to the east. Jericho was the most prosperous city in the area and the third largest after TeH and Tall Nimrin. For that time, it had state-of-the-art defenses with thick walls and a massive stone revetment [198].

Then suddenly, the city suffered violent destruction and a fierce conflagration at the end of MB II at the same time as TeH [39]. An early site excavator, Kenyon, wrote, "*The destruction was complete. Walls and floors were blackened or reddened by fire, and every room was filled with fallen bricks, timbers, and household utensils; in most of the rooms, the fallen debris was heavily burnt* [40]."

During the destruction event, a massive stone MBA defensive tower toppled and burned [39], leaving a thick layer of broken mudbricks, fire-cracked rocks, broken pottery, and burned fragments of wooden beams [39]. Along the base of a massive curving stone defensive wall adjoining the tower, a 7-to-10-m-wide destruction layer contains a thick accumulation of ash, charcoal, and carbonized wooden beams, covered by huge stones, broken mudbricks, and rubble [199]. Marchetti et al. [39], another key group of site excavators, noted that the ash was white, suggesting high-temperature combustion. However, excavators found no high-temperature materials, such as melted mudbricks or pottery, suggesting temperatures of less than ~1200°C [36], the melting point of local sediment.

Near the tower was a series of storerooms gutted by fire and filled with broken storage jars and carbonized grains strewn across the floors [39, 196, 200]. Almost no complete vessels were found; instead, broken potsherds were suspended throughout the destruction matrix at different elevations [39]. In addition, human remains were found mixed within the debris layer, and almost all the bones were burned, disarticulated, and shattered into small fragments [39]. The excavators noted that their colors indicate exposure to high temperatures [39].

Kenyon reported that the massive MBA eastern wall, which faced toward TeH, collapsed, and some destruction debris cascaded down the steep slope adjoining the city walls [201]. She also concluded that the collapse of the eastward-facing fortifications had taken place before the walls were affected by fire [40]. Kenyon uncovered a thick deposit of Iron Age material overlying the crumbled defensive walls, but LBA material was missing [37]. Instead, up to one meter of culturally sterile sediment lay atop the MBA destruction layer in places, leading Kenyon to conclude that for hundreds of years after the destruction of Jericho, the city lay abandoned [198].

Interpretation of the destruction of Jericho

The destruction of Jericho was not unusual. Cities in the Jordan Valley have a long history of episodic destructions by earthquakes and warfare [196, 201, 202]. However, Kenyon found no conclusive evidence of either at ~1650 BCE [196], and no known major area earthquakes occurred between ~1800 and 1560 BCE [203]. In previous destruction episodes, the inhabitants rebuilt immediately, but this time, Jericho was inexplicably abandoned for centuries [198].

The causes of the destruction of Jericho are unclear. Notably, its age is 1653 ± 18 BCE (range: 1670 to 1626 BCE), making it statistically coeval with the destruction of TeH at 1661 ± 20 BCE (range: 1686 to 1632 BCE) (Figure 58**; SI Tables S8, S9** [7]). One possibility is that Jericho's destruction resulted from the high-temperature thermal pulse and high-velocity blast wave of a cosmic airburst that first struck TeH and then Jericho, where it collapsed the fortified walls and burned the city, located ~22 km to the west of TeH. This burning is consistent with Tunguska, where Svetsov [204, 205] showed that the radiation energy from the Tunguska explosion was sufficient to set fires within a diameter of ~20 km. Thus, for TeH, the minimum destruction distance is ~22 km, similar to that of the Tunguska airburst in 1908 [114, 204–206].

Summary of 11. Coeval destruction of Jericho

Proxy Types:

- Burned ruins, pottery

Analysis Methods:

- Excavation, radiocarbon dating

Key Findings:

- Jericho destruction ~1650 BCE, coinciding with TeH.
- A similar absence of warfare evidence supports regional catastrophe.

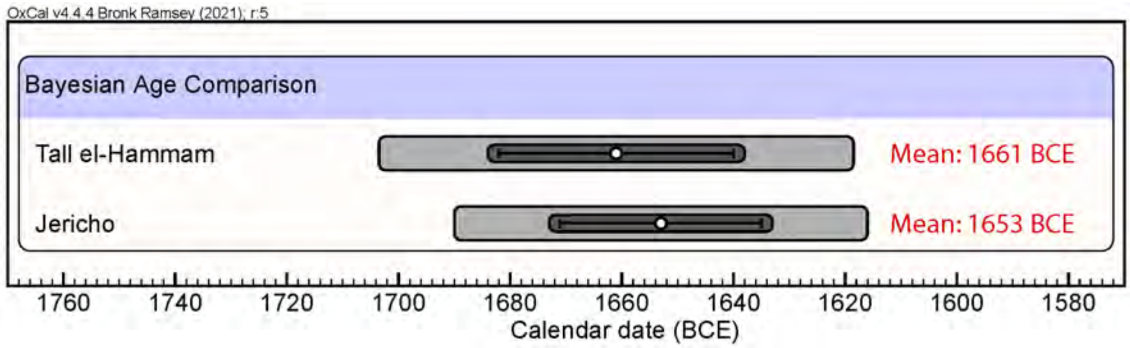

Figure 58: **Comparison of Dates of MBA Destruction of Jericho and TeH.** Bayesian calculation shows essentially identical age ranges at 68% Confidence Interval for the destruction layers of the two cities. For TeH, the range is 1686 to 1632 BCE (1661 ± 21 BCE), and for Jericho, 1670-1626 years BCE (1653 ± 18 BCE), for a common overlap of 38 years, making them statistically coeval.

12. Potential causes of the destruction of TeH

Here, we consider nine processes that potentially could account for some or all of the wide-ranging observations and evidence related to the destruction of TeH and nearby cities/villages. Table 3 lists the potential matches for 12 lines of evidence for each possibility. Using this evidence, we summarize which process best explains the observed evidence at TeH.

12.1 Natural disasters: floods, sandstorms, tornadoes

These natural disasters account for only 5 of 12 characteristics, such as moving around potsherds, bones, and city debris. However, they are unable to account for widespread burning, the melting of various materials, and for shocked quartz.

12.2 Earthquakes

This possibility matches only 3 of 12. Earthquakes can cause fires but cannot explain most of the high-temperature melted materials, peaks in PGEs, and shocked quartz. Although earthquakes potentially can explain the directionality of the debris, all previous earthquakes left debris at TeH in the N/S orientation, aligned parallel to the Dead Sea rift, rather than in the observed SW/NE direction. In any event, no known major earthquakes occurred in the area from ~1800 to 1560 BCE [203]. The only two earthquakes known to have caused significant damage at TeH occurred in ~2100 BCE (>6.8 magnitude) and 3300 BCE (>6.0 magnitude). After both of these disasters, the inhabitants of TeH rebuilt the city [6].

12.3 Humans activities

This possibility matches only 5 of 12 lines of evidence. These activities include glass-making; smelting gold, silver, and copper; and fashioning metals into jewelry and artifacts. During the MBA, copper smelting only reached temperatures of ~1100°C [207], and glass-making reached ~1100°C [207]. Maximum temperatures achievable during MBA pottery-making were <1050°C [119], making this activity incapable of melting pottery and mudbrick at >1400°C. Also, this activity cannot melt zircon, quartz, and chromite grains at >1500°C and cannot produce peak concentrations in Pt, Ir, Ni, Cr, or shocked quartz. These temperatures are too low to melt chromite, quartz, or zircon grains at >1500°C, and pressures are too low to shock quartz. Downward contamination of materials from modern human activities can be eliminated because most TeH meltglass is buried 2 m or more beneath archaeologically sterile layers.

12.4 Normal city fires/wildfires/midden fres

This possibility matches only 5 of 12 lines. Besides the MB II destruction layer, several other non-MBA charcoal-rich strata were observed in the sedimentary record, indicating extensive TeH city fires at different times. However, none of those contain melted pottery, melted mudbricks, or any other high-temperature proxies. For comparison, after the Great Fire of London in 1666, several types of thermally altered objects were found, including partially melted clay bricks, potsherds, and window glass [208], but none show a degree of melting comparable to that at TeH. For a modern comparison, the firebombing of Dresden, Germany, during World War II produced updrafts of ~275 km/h, and yet, maximum temperatures were no higher than ~1000°C [209], which is high enough to soften but not melt glass, and too low to melt elemental iron at ~1538°C. Typical non-impact fires cannot account for abundance peaks in Pt, Ir, Ni, and Cr, as well as the melting of zircon, quartz, and chromite or the production of shock metamorphism in quartz.

Biomass glass or slag is sometimes found in midden piles of prehistoric settlements in Africa with estimated formation temperatures of 1155-1290°C [119], and this process can produce vesicular meltglass and Si-rich spherules. However, Moore et al. [36] investigated examples of this biomass glass and found that temperatures did not rise high enough to melt zircon, chromite, or quartz. Furthermore, midden fires cannot produce abundance peaks in Pt, Ir, Ni, and Cr or shock metamorphism in quartz.

Table 3: Potential explanations for the destruction characteristics observed at Tall el-Hammam.

Characteristics	Flood	Sandstorm	Tornado	Earthquake	Humans	City fire	Fire/eruption	Warfare	Lightning	Crater	Airburst
Pottery suspended above floor	Y	Y	Y	--	--	--	--	--	--	Y	Y
Potsherds across multiple rooms	Y	Y	Y	--	--	--	--	--	--	Y	Y
Bones suspended above floor	Y	Y	Y	--	--	--	--	--	--	Y	Y
Debris moved atop foundations	Y	Y	Y	--	--	--	--	--	--	Y	Y
Directionality of pottery, bones	Y	Y	Y	--	--	--	--	--	--	Y	Y
Citywide burning	--	--	--	Y	Y	Y	Y	Y	Y	Y	Y
Ash/charcoal deposition	--	--	--	Y	Y	Y	Y	Y	Y	Y	Y
Bones burned	--	--	--	Y	Y	Y	Y	Y	Y	Y	Y
Melted pottery, mudbricks, plaster	--	--	--	--	Y	Y	Y	Y	Y	Y	Y
Melted Si-Fe-Ca microspherules	--	--	--	--	Y	Y	Y	Y	Y	Y	Y
Melted chromite, zircon, quartz	--	--	--	--	--	--	--	--	Y	Y	Y
Shock-fractured quartz	--	--	--	--	--	--	--	--	Y	Y	Y
# compared to Impact	**5 of 12**	**5 of 12**	**5 of 12**	**3 of 12**	**5 of 12**	**5 of 12**	**5 of 12**	**5 of 12**	**7 of 12**	**12 of 12**	**12 of 12**
% compared to Impact	**42%**	**42%**	**42%**	**25%**	**42%**	**42%**	**42%**	**42%**	**58%**	**100%**	**100%**

"Humans" refers to human activities, such as smelting and pottery-making. "Fire/eruption" refers to volcanism.

12.5 Volcanic eruptions/fires

This possibility matches 5 of 12. Temperatures of typical magmas range from 700 °C to 1300 °C, although temperatures of komatiite magmas may occasionally reach 1600°C [210]. These temperatures could account for the melted zircon but are too low to melt or mechanically shock grains of quartz [211]. Also, volcanism has never been shown to produce high-iron spherules, such as those found at the [63, 126, 129].

One of the largest volcanic eruptions known in the last 10,000 years occurred at ~1663-1599 BCE (3613-3549 cal BP) [212], centered in the eastern Mediterranean on Thera, a Greek island now known as Santorini. The explosion generated a massive tsunami that is proposed to have reached the island of Crete 110 km away and triggered the collapse of the Minoan culture, which evidence suggests was closely related to the culture at TeH [14, 16]. Approximately 60 km^3 of volcanic ash and pumice were ejected during this eruption [213], and this debris buried the MBA town of Akrotiri on the island of Thera. Related tephra deposits have also been found in Turkey and Israel, and a thin (~1 mm) layer may have reached Jordan, including TeH [213]. However, this massive volcanic explosion was too distant from TeH (>1000 km) to have caused its destruction, and also, it is dated 40-100 years younger than the destruction and abandonment of TeH. We searched for but found no evidence at TeH of volcanic tephra, ash, pumice, or lava in any sedimentary profile, indicating that no severe contemporary eruptions occurred near TeH at ~1650 BCE.

12.6 Warfare

This option matches only 5 of 12. We considered whether ancient sieges could have led to city fires in the TeH destruction layer. However, only one arrowhead and no spear points or swords were associated with any of the skeletons in the ruins. During ancient warfare, conquered cities were commonly demolished and replaced by the invading army's culture and religion, but there is no evidence of warfare in the destruction layer at TeH. In any event, ancient warfare cannot explain melted high-temperature minerals, peaks in PGEs, and shocked quartz. For modern warfare, the detonation of military explosives can theoretically produce most of the evidence, but the TeH melted material comes from deeply buried strata sealed by Iron Age occupations unaffected by modern explosives. Modern defensive artillery revetments, excavated during the 1967 Middle Eastern war, were not coincident with the archaeological excavations that produced the evidence.

12.7 Lightning

This possibility matches 7 of 12. Temperatures in lightning strikes can exceed 4000°C, which is hot enough to boil zircon. Lightning strikes can also produce shocked quartz grains, which are confined to the outer 0.33 µm of quartz grains and do not propagate into the interior, unlike the shocked grains found at TeH [112]. Furthermore, low values for remanent magnetism indicate that lightning could not have produced the TeH melted material tested. Also, lightning would not account for high-velocity winds, the directionality of debris, and the rapid destruction of buildings and walls spanning a distance of ~400 meters across the tall.

12.8 Crater-forming cosmic impact

This option is one of the only two that matches 12 of 12 observations. Although a hard impact potentially accounts for all of the evidence, this mechanism seems somewhat unlikely because there is currently no known crater in the area. However, although improbable, a crater with a diameter of less than a few hundred meters may be buried in the Jordan River floodplain or hidden underwater at the northern end of the Dead Sea. The Jordan Valley has been subject to massive seasonal floods for over 3000 years, sufficient time for fluvial deposition to conceal a small crater. Alternately, an aerial burst of a bolide can produce a "shotgun blast" of small objects that can reach the ground and create small craters that range in diameter from a few meters to a few tens of meters. Wind and water action could readily and rapidly erase any surface evidence of such craters, especially in this area of rapid sediment deposition in the active floodplain of the lower Jordan Valley. The evidence at TeH matches that of crater-forming impacts, except for the lack of a crater.

12.9 Cosmic airburst

This option is one of only two that match 12 of 12 lines of evidence, and both possibilities are cosmic impact events. Overall, one or multiple super-Tunguska-sized airbursts by a comet or meteorite seems most likely to account for the wide-ranging suite of observed evidence for the destruction of TeH (Table 3). In the future, searching for proxies across the Jordan Valley at various distances from TeH would be helpful. Any discernible pattern would help locate ground zero, where proxy concentrations would be the largest. We know from archeological evidence that 16 cities/towns and >100 villages across the southern Jordan Valley were abandoned at this time, but not if their walls were destroyed or if high-temperature, high-pressure proxies were present at those sites. Because airburst/impact proxies fall off exponentially with distance from ground zero, the distribution would help determine the event's intensity.

It is worth speculating that a remarkable catastrophe, such as the destruction of TeH by a cosmic object, may have generated an oral tradition that, after being passed down through many generations, became the source of the written story of Genesis. The description in Genesis of the destruction of an urban center in the Dead Sea area is consistent with having been an eyewitness account of a cosmic airburst, e.g., (i) stones fell from the sky; (ii) fire came down; (iii) thick smoke rose from the fires; (iv) a major city was devastated; (v) inhabitants were killed; and (vi) area crops were destroyed. If our hypothesis is correct, the destruction of TeH is the second oldest known incident of impact-related destruction of a human settlement, after Abu Hureyra in Syria ~12,800 years ago [36, 214, 215].

Summary of 12. Potential causes of TeH destruction

Scenarios Tested:
- Natural events, warfare, human activities, fires, earthquakes, volcanoes, lightning, impact, airburst

Analysis Methods:
- Comparative forensic analysis

Key Findings:
- There is no evidence of natural disasters, warfare, fire, or tectonic motion.
- Only cosmic airburst explains combined high-T, shock, and blast indicators.

13. Investigation of other airbursts

13.1. Comparison of TeH to trinity atomic detonation

In 1945, the first atomic bomb test, called Trinity, took place at the Alamogordo Bombing Range near Socorro, New Mexico. The bomb exploded in the atmosphere atop a 30-m tower, making the detonation an airburst in which the explosive yield equaled ~22 kilotons of TNT equivalent [216, 217]. This atomic blast was several orders of magnitude less powerful than the Tunguska cosmic airburst in 1908 in Siberia, estimated at ~3-30 megatons of TNT equivalent at an altitude of 5-10 km [218]. The Trinity fireball had a maximum fireball temperature of ~300,000°C [217] and an average plume temperature of ~8,000°C [113, 219], hotter than the sun's surface (>5500°C) and several times brighter [63]. After ~3 seconds, the plume temperatures fell to ~1713°C [217], the melting point of quartz.

The Trinity explosion formed a shallow crater ~1.4 m deep and ~80 m in diameter and ejected molten surface sediment that fell back as green glass, commonly called trinitite. This nuclear-melted green glass was found on the ground surface for a diameter of ~400 m, along with a high abundance of green glass spherules both macroscopic (0.1 to 5 mm) and microscopic (microns to tens of microns), the latter having been found as far as 2 km from ground zero. Bunch et al. [63] reported high-temperature melted minerals in trinitite, indicating ground temperatures of >2200°C, consistent with reported conditions [217].

Even though an atomic bomb blast is not applicable because of the absence of nuclear explosions in the area, an atomic blast produces a wide range of melt products that are morphologically indistinguishable from the melted material found at TeH (Figure 59). These include shocked quartz [113]; melted and decorated zircon grains (Figure 59a, 59b);

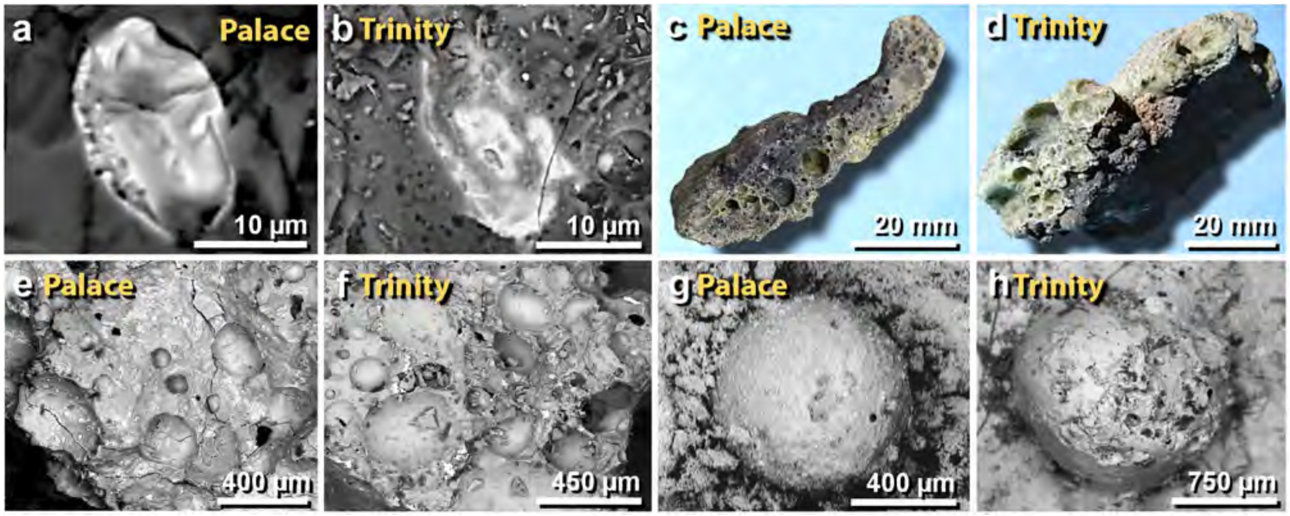

Figure 59: Comparison of melted materials from TeH with those from the Trinity atomic bomb test. (a-b) SEM images compare a melted, decorated zircon embedded in mudbrick meltglass from the palace with material similar to Trinity. **(c-d)** Photomicrographs compare a melted potsherd from the palace with similar-looking meltglass from Trinity. **(e-f)** The melted zircons in panels 'a' and 'b' were found in highly vesicular glass like these from the palace and the Trinity site, respectively. **(g-h)** SEM images of a spherule fused onto mudbrick meltglass from the palace and a spherule embedded into trinitite from the Trinity atomic test.

globules of melted material (Figure 59c, 59d); meltglass containing large vesicles lined with Fe-rich crystals that were likely deposited by vapor deposition (Figure 59e, 59f); spherules embedded in a meltglass matrix (Figure 59g, 59h). Also, atomic detonations can replicate the physical destruction of buildings, human lethality, and the incineration of a city, as occurred in World War II.

13.2. Comparison of TeH to Tunguska cosmic airburst

On June 30, 1908, a cosmic airburst occurred over Tunguska, Russia, in a remote part of Siberia. The bolide has been variously estimated as a low-density rocky asteroid or a small comet 50-80 m in diameter [114, 205]. The blast yield is estimated at ~3-30 megatons of TNT equivalent with a burst altitude of ~5-10 km. The airburst generated a pressure wave that toppled or snapped approximately 80 million trees by one estimate [220] across ~2000 km^2 in a radial pattern away from ground zero [114, 205, 221]. The fallen trees partially burned across an area of ~200 km^2 with a radius of ~8 km. Estimated wind velocities were ~40-70 m/s (144-250 km/h), greater than an EF-3 tornado [222]. Tunguska's blast pressure not only toppled trees but also pressed the tree fluids from the bark into the pre-existing tree rings of the surviving trees [223]. The Tunguska airburst deposited high-temperature melted spherules [114, 206], meltglass [206, 224, 225], diamonds [226, 227], shocked quartz [115, 228], and iridium [229]. All these impact-related proxies have also been observed at TeH.

The temperature of the Tunguska fireball is unknown but estimated to have been >10,000°C [230]. The airburst initially ignited ~200 km^2 of the forest before spreading to consume ~500 km^2 of forest [205]. A similar but much smaller airburst occurred over Chelyabinsk, Russia, on February 15, 2013, with a yield of ~500 kilotons of TNT equivalent with a burst altitude of 12 km.

Even though the Tunguska area was sparsely inhabited, the blast killed ~3 of the ~30 people who were within or near the zone of fallen trees. Some of the injured survivors remained unconscious for hours to days [185]. Nearly everyone experienced severe burns within an eight-km radius of ground zero across an area covering ~200 km^2. Also, as many as 500 reindeer were killed by the blast, and hundreds more were severely burned [185]. Based on this evidence, we collectively propose that the airburst that destroyed TeH at ~1650 BCE was larger than that at Tunguska.

To compare Tunguska to an airburst at TeH, we superimposed the ~2000 km^2 area of fallen trees at Tunguska over the Dead Sea area at an exact comparative scale (Figure 60). The Tunguska footprint would cover about one-third of the north end of the Dead Sea and most of the plain of the Jordan Valley, including TeH, Jericho, and other MB II cities. This map suggests that if a super-Tunguska-scale cosmic event occurred over the Jordan Valley, the detonation and ensuing blast wave would have been energetic enough to have caused widespread destruction, contradicting Boslough and Bruno [60] and Boslough [54].

13.3 Other large airburst events

Numerous airbursts have been recorded across Europe during the Holocene, suggesting that airbursts are far more common (recurring every few hundred to a thousand years) than generally considered [77, 85]. If so, a relatively recent airburst at TeH is statistically plausible. Previous studies concluded

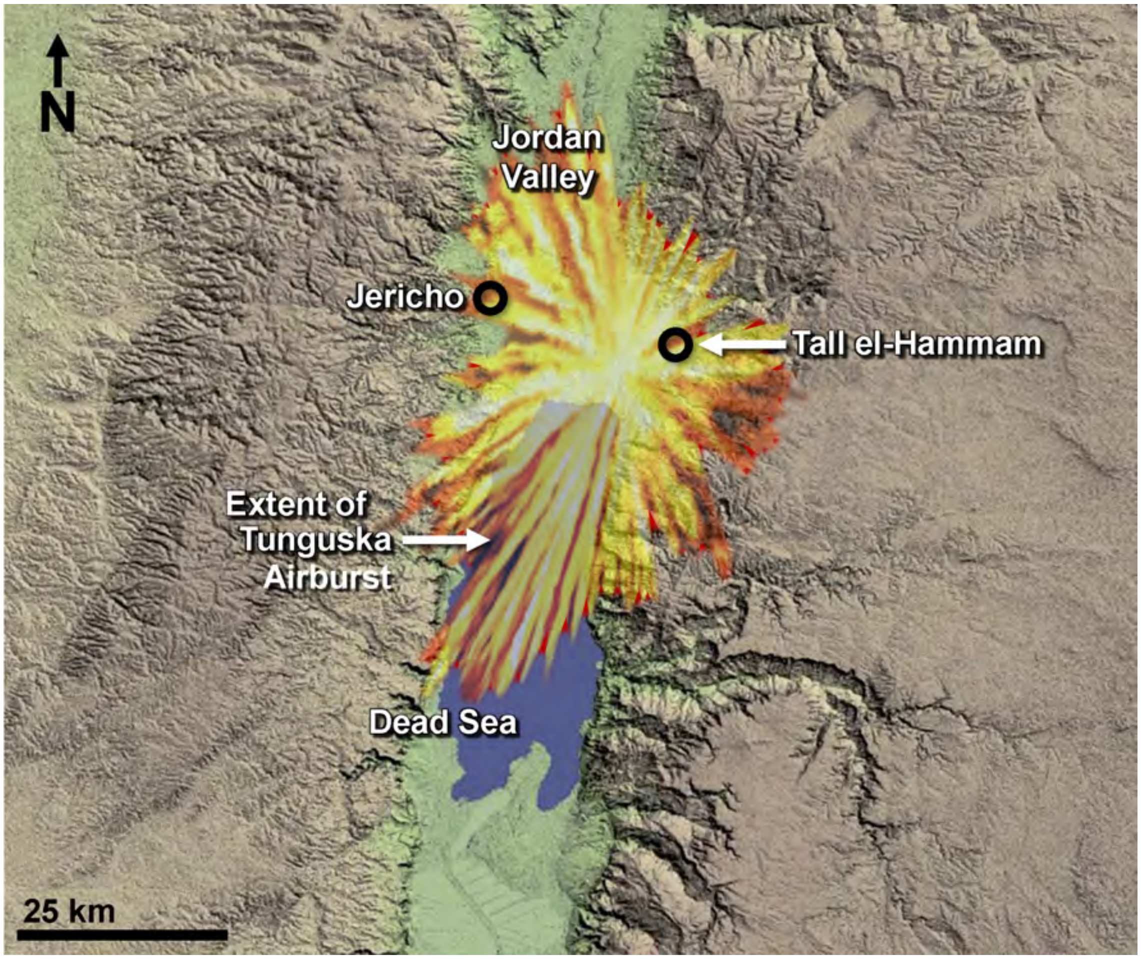

Figure 60: The extent of the cosmic airburst at Tunguska, Siberia (1908), superimposed on the Dead Sea area. The Tunguska blast was ~75 km wide N-S, affecting 2,200 km^2. This accurately scaled image shows that a cosmic airburst similar in energy to the one at Tunguska could cover a large segment of the Dead Sea and the Jordan Valley. Note that this overlay is for comparison only; the location, orientation, direction of travel, entry direction, and size of the proposed TeH impact is unknown but estimated to have been larger than that at TeH. Source of base image: Shuttle Radar Topography Mission (SRTM) SRTMGL1 DEM of the Jordan Valley from February 2000 was obtained from https://earthexplorer.usgs.gov/ maintained by the USGS/Earth Resources Observation and Science (EROS) Center, Sioux Falls, South Dakota, accessed on 4/4/2021. The authors modified this image using Adobe Photoshop CC2014 (adobe.com/products/photoshop.html).

that although airbursts mainly vaporize the bolide, fragments commonly reach the ground surface, and the kinetic energy of the airburst vapor jet may be high enough to produce shallow craters [85, 231, 232], along with shocked quartz, meltglass, microspherules, breccia, and other impact-related proxies, as reported at TeH.

The following are some proposed examples of low-altitude Type 2 airbursts that caused extensive damage to Earth's surface: (i) Chrudim/Pardubice in the Czech Republic [233, 234], (ii) Nalbach/Saarlouis in Germany [235–237]. (iii) Chiemgau in Germany [32, 76, 95, 96, 238–244], (iv) Niederrhein in Germany [245], (v) Franconia in Germany [246], (vi) Sachsendorf Bay in Germany [247], (vii) seven possibly related strewn fields across about half of the Czech Republic [234], (viii) a 6400-year-old strewn field in Finland [248], (ix) the Luzice melt rock and megabreccia outcrops, proposed as evidence of a low-altitude airburst [249], (x) the 20-km-diameter Kolesovice airburst crater in the Czech Republic [250], (xi) a 2600-year old strewn field in Kansas [251], (xii) a 1600-year-old airburst in Ohio that destroyed several Native American villages [252], (xiii) a 5000-year-old airburst by an iron meteorite in Poland [253], (xiv) a ~12,500-year-old strewn field in the Atacama Desert of Chile [130, 254, 255], (xv) multiple airbursts on four continents 12,800 years ago by the Younger Dryas impact event [36, 63, 98, 100, 120, 123, 124, 126, 127, 129, 221, 256–265], (xvi) a large airburst at the Dakhleh Oasis in Egypt ~145,000 years ago [50, 182, 266], (xvii) two near-surface airbursts in Antarctica, one ~430,000 years old and a second one ~2.3 Myr old [232, 267], and (xiii) an airburst in the Libyan Desert ~29 million years ago [268].

Summary of 13. Investigation of other airbursts

Comparisons:

- Trinity (1945), Tunguska (1908), Abu Hureyra (YDB at 12,800 cal BP)

Key Findings:

- TeH signatures closely match known airburst and nuclear markers.
- Reinforces super-Tunguska-style event at TeH.

14. Modeling of a super-Tunguska airburst near TeH

14.1 The earth impact effects program (EIEP)

Bunch et al. [1] explored some parameters of two hypothetical airbursts that might produce the evidence observed at TeH. They used EIEP, or Impact Calculator, created by impact experts J. Melosh, R. Marcus, and G. Collins [269], a web-based tool designed to estimate the regional environmental consequences of an impact event on Earth, such as ejecta distribution, ground shaking, atmospheric blast waves, and thermal effects. The results presented in **SI Tables S10 and S11** [7] are just two of many possible scenarios with significant uncertainties [269].

According to the Impact Calculator, a stony meteorite descending at a 45° incidence angle would explode above a sedimentary surface ~5 km southwest of TeH. Bunch et al. considered two possible impactor diameters of 60 and 75 m, providing bounds for the most likely impact scenario. An object larger than approximately 80 m would typically excavate a significant crater nearly a km in diameter, which seems unlikely since no craters are currently known in the Jordan Valley. At the low end of the impactor size range, a 60-meter object would detonate at an altitude of 4.7 km with a yield of ~12 MT, producing 917 km/h (570 mph) windspeeds 5 km away at TeH (**SI Table S10** [7]). At the high end of the range, a 75-meter diameter object would detonate at an altitude of 1.3 km with a yield of ~23 MT, producing 1200-km/h (740 mph) windspeeds 5 km away at TeH, far greater than the largest Category-5 tornado ever recorded (~512 km/h = 318 mph) with a theoretical peak overpressure of ~2.5 bars (35 psi). Such wind speeds and pressures are greater than the tensile strength for adobe-style mudbricks of 0.12 MPa (17 psi) and flexural strengths of 0.17 MPa (25 psi) [270–273], exceeding the pressure needed to demolish and pulverize mudbrick walls. Those pressures even exceed the destruction limits of modern buildings of reinforced concrete. Pressures of only ~0.14 MPa (20 psi) result in a >99% human fatality rate. In addition, the Tunguska airburst produced a seismic shock of ~5.0 on the Richter scale, and an impact-related earthquake of similar magnitude at TeH would have caused severe damage to the city's mudbrick walls. No single, large crater would form for both size impactors, but multiple large-to-small fragments would likely hit the surface, possibly forming small, shallow craters that may have been filled over time by wind and water. These calculations demonstrate that 12- to 23-megaton super-Tunguska-like airbursts can theoretically account for all the evidence observed at TeH.

At Jericho, ~15 km from the center of the 75-m airburst, Category-3 hurricane wind velocities would have reached 216 km/h (134 mph) (**SI Table S11** [7]). For the 60-m impactor, windspeeds would have reached 237 km/h (147 mph), equivalent to an EF-3 tornado and powerful enough to shear and collapse mudbrick walls [271]. This wind speed is consistent with the estimated range of Tunguska wind velocities of ~40-70 m/s (144-250 km/h), equivalent to EF-3 through EF-5 tornadoes [222].

14.2 Hydrocode airburst model for Tall el-Hammam (Autodyn)

The following section is reproduced/adapted from Silvia et al. [2] To estimate the airburst effects of a hypothetical impactor near TeH, Silvia et al. produced a hydrocode computer model of the proposed event.

Hydrocode modeling is commonly used for impact simulations [85, 222, 231, 269, 274–279], and specifically, Autodyn-2D, a hydrocode program from Ansys, Inc., has seen widespread use [222, 280–292]. In the current study, Silvia et al. first modeled the TeH airburst using the Earth Impact Effects Program (EIEP) developed by Marcus et al. [293] and Collins et al. [269, 278] Second, Silvia et al. input the EIEP results into Autodyn-2D (Ansys, Inc.), a hydrocode software program commonly used for modeling high-velocity airbursts and impacts [222, 231, 269, 274–291]. For more information, see **Appendix, Autodyn modeling, Appendix, Testing the accuracy of modeling, Appendix, Previous modeling of airbursts** below.

The temperatures modeled in this study are not fully quantitative because of the inherent difficulties in accurately determining extreme temperatures under highly chaotic conditions. The Autodyn program can account for the kinetic energy, strain energy, and contact energy but does not calculate how some parameters affect temperature (e.g., plasma chemistry/physics and thermal radiation), potentially leading to modeled temperatures that are too high. Thus, Autodyn's calculated temperatures presented here should be considered semiquantitative. Nevertheless, the calculations demonstrate that a Tunguska-scale airburst of as little as ~4 Mt under a specific set of impact parameters can theoretically account for all the evidence observed at TeH, including high temperatures.

Silvia et al. [2] used the following modeling parameters in Autodyn: 55-m-wide asteroid, airburst energy: 3.68 Mt, entry velocity: 11 km/s, density: 2920 kg/m^3; entry angle: 90°; initial breakup height: 47.9 km; burst height: 653 m. The touch-down airburst produces an airburst with a TNT-equivalent energy of 3.68 megatons, equaling more than 160 Hiroshima-sized nuclear bombs. Silvia et al. modeled values

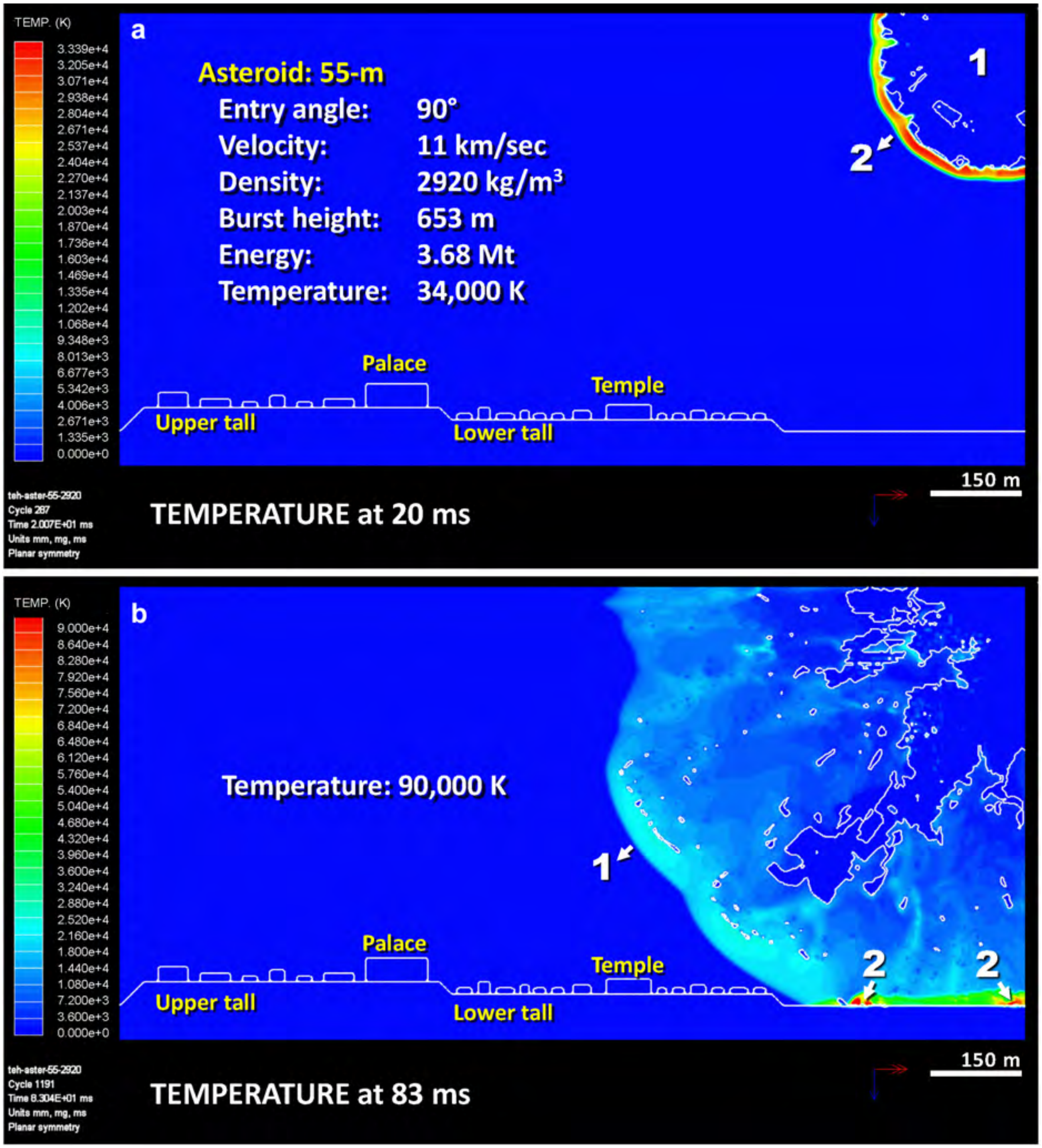

Figure 61: Modeled airburst at 20 ms. (a) Within the airburst, the semiquantitative temperature is >34,000 K **(#1);** pressure reaches ~30 GPa (≥300,000 kg/cm^2), and the shock wave velocity is ~18 km/s **(#2)**. Several possibilities might explain the lack of vaporization at high temperatures. (i) A large proportion of the bolide is vaporized, but the temperatures are so transient (<2 s) that there is insufficient time for the complete melting of all bolide fragments. (ii) Some fragments are pushed out at the leading edge of the high-temperature wave and, therefore, are not exposed to the highest temperatures. (iii) Some fragments travel within the near-vacuum (#2 in panel 'a') behind the shock front and are protected from the highest temperatures. **(b) (#1)** The airburst radius expands to ~700 m. **(#2)** At the ground surface, semiquantitative temperatures (total energy, including thermal and radiant) exceed ~95,000 K [294, 295], sufficient to produce meltglass and spherules from the condensation of melted and vaporized matter. The shock speed reaches ~16 km/s, far higher than that formed by any terrestrial mechanism. For comparison, the most powerful known tornadoes have wind speeds of ~0.16 km/s, 1000 times slower than that modeled here. Field of view = 1500 m wide × 750 m high. Images and captions are reproduced/adapted from Silvia et al. [2].

for pressure, semiquantitative temperature, shock speed, bulk material failure, and visual materials reproduced in Figures 61 and 62.

Note that the illustrated buildings are for representational purposes only and are not accurately positioned. The scale of the occupation mound (comprising the upper and lower

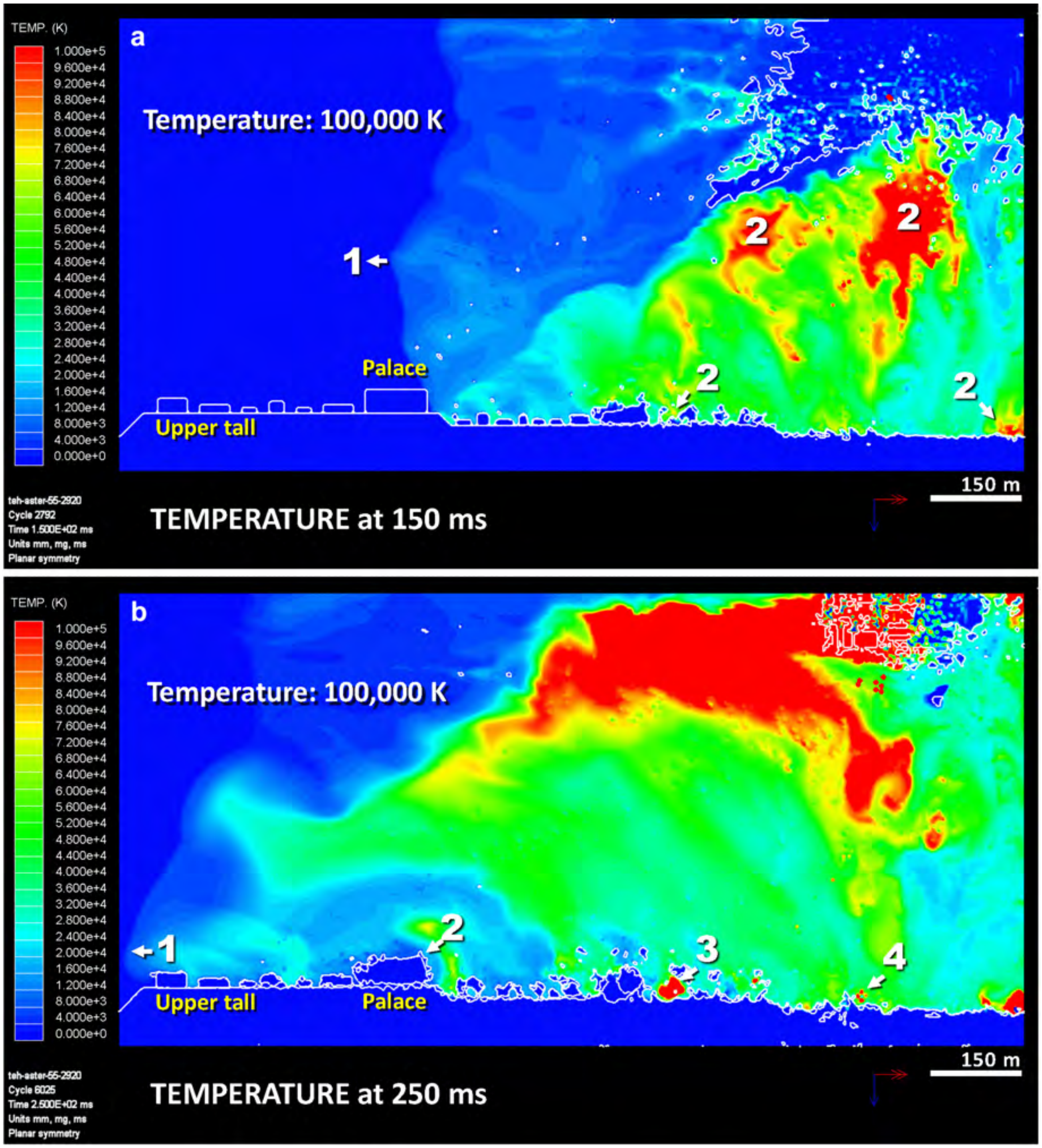

Figure 62: **Modeled airburst at 121 ms. (a) (#1)** The airburst radius expands to 1090 m. Shock speeds reach up to 15 km/s. **(#2)** Semiquantitative temperatures in portions of the reflection wave exceed ~95,000 K [294, 295] at the ground surface and in the atmosphere. **(b) (#1)** The airburst radius widens to nearly 1500 m wide after 250 ms. **(#2)** The side of the palace facing the airburst is subjected to temperatures briefly exceeding 70,000 K. **(#3)** Portions of the lower tall experience temperatures exceeding ~95,000 K for only a few ms [294, 295]. **(#4)** Impact craters SW of the lower tall also experience temperatures of >95,000 K [294, 295]. Images and captions are reproduced/adapted from Silvia et al. [2].

tall) is approximately accurate horizontally but vertically exaggerated about two times for better visibility. The temple, palace, and other structures are also vertically exaggerated about two times.

Interpretation of airburst modeling

Regarding modeling limitations, the EIEP and Autodyn models have high uncertainties, given that airbursts are highly complex events with multiple variables that are difficult to model. Despite these limitations, such models are widely used to explore and better understand airburst conditions. The parameters used for modeling the airburst at TeH are only one set of numerous conceivable scenarios. Using these diameters of impactors (55, 60, 75 m) does not imply that these parameters accurately describe what happened at TeH around 3600 years ago; instead, it is just one set of

Table 4: Key findings from the results sections categorized according to proxy types analyzed, the analytical methods used, and the principal conclusions drawn. The table facilitates cross-comparison of interdisciplinary datasets used to support the hypothesis of a cosmic airburst at Tall el-Hammam.

Results section	Proxy types	Analytical methods	Key findings
1. Stratigraphy of Tall el-Hammam	Sedimentary layers (debris matrix, blow-over, dark layer), melted materials (mudbrick, pottery, roofing clay)	Stratigraphic profiling, elevation mapping, sediment sampling, visual analysis	Three distinct layers; widespread debris matrix and charcoal-rich dark layer; unique to MB II; lack of erosion implies rapid deposition
2. Dating of the Destruction Layer	Carbonized wood, seeds, grains, collagen, pottery styles	Radiocarbon dating with OxCal Bayesian modeling, pottery seriation	Destruction dated to 1650 ± 50 BCE; consistent with pottery seriation; short-lived organics improve accuracy
3. Evidence of Widespread Burning and Extreme Temperatures	Melted materials, soot, charcoal, DLC	LOI, TOC/soot analysis, SEM, TEM, DSC-TGA	Charcoal-rich debris matrix; soot/TOC ratio ~76%; 74% of elements melted ≥1300°C; DLC peaks at ~3 ppm
4. High-Temperature Impact-Related Materials	Melted ceramics, mudbrick, roofing clay, magnetic signatures	SEM-EDS, microscopy, thermal and magnetic testing, heating experiments	Vesicular glassy surfaces; melting >1400°C; quartz unmelted; lightning ruled out; vitrified leaf imprints
5. SW-to-NE Directionality of Debris	Oriented potsherds, grains, charcoal, bones, blow-over layers	Spatial distribution mapping, excavation photography, orientation analysis	Consistent SW-to-NE debris dispersion; not earthquake-like; evidence of high-velocity directional blast
6. Shock-Metamorphic Minerals in Destruction Debris	Shocked quartz grains, glass-filled fractures	OPT, SEM-EDS, EBSD, TEM, diffraction techniques	Presence of planar deformation features and shock lamellae in quartz; multi-GPa pressures indicated; glass-filled shock fractures documented
7. Shocked Quartz Grains from Tunguska	Tunguska quartz grains	SEM-EDS, petrography, diffraction comparison	Similar shock features in TeH and Tunguska quartz; supports a cosmic airburst analog
8. High-Temperature Impact-Related Melted Materials	Meltglass, spherules, elemental nuggets, melt inclusions	SEM-EDS, TEM, phase diagrams, melting point analysis	Widespread meltglass with embedded metals and silicates; melting >1700°C; composition consistent with impact-derived high temperatures
9. Human Bones in the Destruction Layer	Skeletal remains, bone fragments	Excavation context analysis, orientation and disarticulation assessment	Highly disarticulated, fragmented bones; some exploded skulls; suggests rapid high-energy trauma
10. High Salt Concentrations and Environmental Aftermath	Salt content in sediments	Gravimetric analysis, stratigraphic mapping	~4 wt% salt in destruction layer; inferred origin from Dead Sea salts; long-term soil sterilization and regional abandonment for centuries
11. Coeval Destruction and Burning of Jericho	Charcoal layers, pottery styles	Comparative stratigraphy, seriation, radiocarbon dating	Jericho shows synchronous burning at ~1650 BCE; no evidence of warfare; consistent with TeH destruction
12. Evaluation of Potential Causes	All previously described proxies	Elimination-based comparative analysis	Natural fires, warfare, volcanism, and lightning ruled out; only cosmic airburst explains the evidence
13. Investigation of Other Airbursts	Comparative site data (Tunguska, Trinity)	Analog comparison, physical and mineralogical parallels	TeH destruction aligns with effects from Tunguska and Trinity tests; unique suite of features replicated in impact and airburst events
14. Modeling of a Super-Tunguska Airburst	Simulated impact effects	Hydrocode modeling (Autodyn), Earth Impact Effects Program (EIEP)	Model predicts high-velocity jet, surface melting, and shock wave; closely matches field observations at TeH

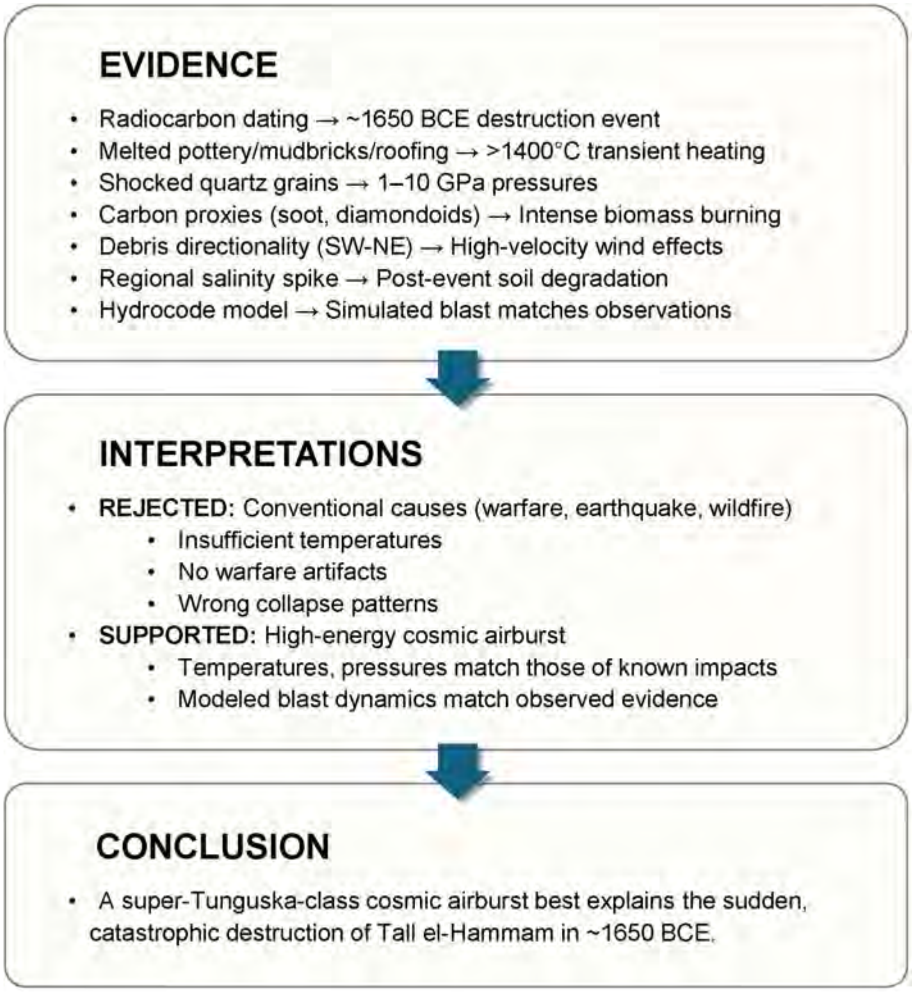

Figure 63: **Visual Flowchart.** To aid in synthesizing the complex, multidisciplinary data presented in this study, we provide a summary flowchart that directly links the key proxies, analytical methods, and findings to their broader interpretations. This schematic representation highlights the logical progression from field observations and laboratory analyses to the rejection of conventional hypotheses and the acceptance of a cosmic airburst as the most plausible explanation for the destruction of Tall el-Hammam. By visually organizing the evidence and its implications, this framework underscores the robust, converging lines of support for a high-energy, low-altitude cosmic event around 1650 BCE.

circumstances under which the city's destruction could have occurred.

Based on atomic testing and Tunguska, the fireball of all sizes of modeled impactors is estimated to have expanded to ~1 km in diameter [296] and reached temperatures exceeding 300,000°C in the center [217], many times higher than the surface of the sun (5500°C). The impactors would have emitted an intense thermal pulse (>45 cal/cm^2) at the speed of light, providing enough heat to melt silicate and other materials [205, 217]. Temperatures would have remained higher than the melting point of quartz (1713°C) for >25 seconds [217], sufficient to produce meltglass. As the high-temperature (≥1713°C) shock wave propagated outward for a few seconds, it provided sufficient heat to melt the surfaces of mudbricks, pottery, roofing clay, and plaster [276, 277].

The physical evidence from TeH suggests that ground temperatures briefly rose above 1850°C, setting flammable materials on fire. These temperatures are far above ~150°C, which is considered lethal for humans, leading to a nearly 100% fatality rate of exposed humans [273]. In summary, the impact models that range from ~4 to 23 megatons presented in **SI Tables S10 and S11** [7] are consistent with the observed evidence at TeH.

Comparing TeH to the Tunguska airburst, we collectively conclude that the damage at TeH was greater than that at Tunguska in 1908. A supercomputer-generated model of a hypothetical 15-megaton airburst at Tunguska (within the range of 12-23 Mt modeled here) was developed at Sandia National Laboratories by Boslough [277]. He wrote that when a bolide explodes in the atmosphere, a high-temperature, supersonic jet of ionized gases and impactor fragments reaches Earth's surface at high velocity, can excavate unconsolidated sediment, and expands radially outward. Surface temperatures rise higher than the melting points of silica-rich materials, and the surge's radial velocity can exceed the speed of sound (343 m/s or 1,225 km/h). Radiative and convective heating can transform surface and excavated materials into meltglass [61]. Svetsov [205] computer-modeled the airburst of an 80-m-wide impactor and found that radiative fluxes from the blast were sufficiently high to melt ~0.5 cm of surface sediment at >1700°C for ~20 seconds. This closely matches the half-centimeter-thick melting of mudbricks, pottery, and roofing clay observed TeH, making a hypothetical super-Tunguska airburst plausible. Even though the 15-Mt Sandia computer model has large uncertainties, the modeled scenario accounts for all the evidence, including the destruction of thick mudbrick walls at TeH and Jericho (Table 2).

The tests of the modeled results produced by West et al. [85] with Autodyn for Trinity and the EIEP for the airbursts at Tunguska and Chelyabinsk (**Appendix, Tunguska, Table A3, and Appendix, Chelyabinsk, Table A4** in West et al. [85]) are reasonably close to actual values. These results provide confidence that our model for an airburst at TeH is also reasonably accurate.

Summary of 14. Modeling a super-tunguska airburst near TeH

Methods:

- Earth Impact Effects Program (EIEP), Autodyn simulations

Key Findings:

- Best-fit: 55–75 m bolide, 4–6 km/s, Type II airburst.
- Simulated effects align with TeH evidence: fireball, shock, thermal flux.
- The model supports an airburst destroying the city.

Summary of analytical results for all proxies

Table 4 below lists the Section Title, Proxy Types, Analytical Methods, and Key Findings for each of the Results sections presented above. Figure 63 is a flowchart that links this contribution's key proxies, analytical methods, and findings.

Conclusions

Extensive archaeological and geochemical analyses support the hypothesis that around 1650 BCE, Tall el-Hammam, a major urban center in the southern Jordan Valley, was destroyed by a cosmic airburst event of super-Tunguska magnitude. The ~1.5-meter-thick destruction layer across the site preserves compelling evidence of extreme high-temperature and high-pressure conditions, including shocked quartz, vesicular and melted construction materials, diamond-like carbon, soot, Fe–Si-rich microspherules, and $CaCO_3$ spherules derived from molten plaster. These proxies are diagnostic of intense shock metamorphism and thermal exposure exceeding 2000°C.

Field evidence, including the leveling of >12 meters of the palace complex and a massive mudbrick rampart, as well as widespread disarticulated skeletal remains, suggests a catastrophic, high-energy event consistent with a supersonic shock wave. The SW-to-NE debris dispersal pattern further supports a directed blast, modeled effectively by hydrocode simulations of a Type-II "touchdown" airburst. Vaporization of local Dead Sea brines or sedimentary salt layers is consistent with anomalous salt concentrations (~4 wt%) within the destruction matrix, resulting in hypersaline soils that likely led to a ~300–600-year-long regional abandonment.

Alternative hypotheses, including fires, earthquakes, volcanism, lightning, anthropogenic activities, and warfare, were systematically evaluated and rejected as sole or combined causes due to their inability to replicate the full suite of observed damage features. In contrast, the cosmic airburst model explains the directionality of debris, high-temperature melt phenomena, and shock metamorphism in a single, integrated scenario.

This event likely had profound cultural and environmental impacts across the region, including the collapse of regional settlements and agriculture. It is plausible that oral traditions recording this catastrophe were eventually incorporated into the written biblical narrative describing the destruction of Sodom.

The Tall el-Hammam event represents the second oldest known case of a human settlement destroyed by a cosmic impact/airburst after Abu Hureyra, Syria (~12,800 years ago). Although the probability of such super-Tunguska-scale airbursts is low on human timescales (estimated global recurrence intervals of 200–1000 years), their capacity to annihilate entire cities highlights a severe, ongoing threat to modern civilization. This study emphasizes the need for continued research into impact proxies across the Jordan Valley and beyond to characterize better the frequency, scale, and consequences of cosmic airbursts in human history.

Acknowledgments

We thank seven reviewers whose comments/suggestions substantially improved the manuscript. We gratefully acknowledge the invaluable assistance of the senior staff of the Tall el-Hammam Excavation Project, directed by co-author Steven Collins: Assistant Director Gary A. Byers, and Assistant Director Carrol M. Kobs. Additionally, we thank Daniel Galassini, Michael Luddeni, Brandy Forrest, James Barber, and Sultan Madi. We also thank Metin Ozen and Chris Cowan of Ozen Engineering, Inc. for their assistance with Autodyn. We are also grateful for the help of Gary Chandler and Nelia Dunbar, researchers in the Materials and Metallurgical Engineering Lab at New Mexico Tech, Socorro, NM, who contributed SEM and microprobe data, respectively. We thank Allison Sikes at Eurofins EAG Laboratories for the DSC-TGA measurements and microscopy on the pottery samples. We thank Thomas Whyte, Department of

Anthropology, Appalachian State University, for helping identify some bones. REH obtained Trinitite from the Trinity site with permission from the White Sands Missile Range Public Affairs Office. We thank the Institute of Geology, Czech Academy of Science of the Czech Republic for access to the paleomagnetic laboratory instruments in Pruhonice, Czech Republic. We also gratefully acknowledge using the CAMCOR facilities at the University of Oregon. We also recognize David Kimbel (deceased) of the Comet Research Group for grain-size analyses. We gratefully acknowledge some of the co-authors of the initial version of this publication: James H. Wittke, Dale Bachelor, David Burleigh, Joel Kathan, Siddhartha Mitra, Mark C.L. Patterson, Edward C. Swindel, and Kurt Langworthy. In particular, we sincerely appreciate Eugene Jhong and Brian Muraresku through the Athanatos Foundation, whose interest and support helped make this research possible.

Data availability

All supporting data are included in this manuscript.

Collective author contributions (including Bunch et al. [63] and Silvia et al. [2])

All authors reviewed and approved the manuscript. Conceived aspects of the project: P.J.S., M.A.L., T.E.B., R.E.H., W.S.W., G.K., M.C.L.P., S.M., C.R.M., K.L., J.P.K., A.W. Contributed parts of the manuscript and Supporting Information: P.J.S., M.A.L., T.E.B., J.H.W., T.D.B., R.E.H., W.S.W., G.K., S.M., C.R.M., J.P.K., A.W. Directed/performed fieldwork: P.J.S., M.A.L., R.E.H., G.K., E.C.S., T.W., G.A.H. Directed/performed analytical research: P.J.S., M.A.L., T.E.B., A.V.A., T.D.B., R.E.H., C.M., D.B., W.S.W., J.K., G.K., M.C.L.P., S.M., C.R.M., K.L., J.P.K., A.W. All co-authors contributed field data, samples, instrumental data, data interpretations, and/or relevant sections to the Supplemental Information. AI (ChatGPT) was used to improve the readability of this manuscript.

Competing interests

The authors declare no competing interests.

Funding

GK's support came from the Czech Science Foundation projects 20-08294 S, Ministry of Education, Youth and Sports LTAUSA 19141, and institutional support RVO 67985831. The study was further funded through generous grants from Eugene Jhong and Brian Muraresku through the Athanatos Foundation to the Comet Research Group (CRG), the University of California Santa Barbara, the University of South Carolina (USC), and the South Carolina Institute for Archaeology and Anthropology (SCIAA), University of South Carolina, primarily. We also thank the thousands of donors and members of the Comet Research Group (grant TeH-2012) who have been crucial in making this research possible.

References

[1] Bunch, T.E.; LeCompte, M.A.; Adedeji, A.V.; Wittke, J.H.; Burleigh, T.D.; Hermes, R.E.; Mooney, C.; Batchelor, D.; Wolbach, W.S.; Kathan, J.; et al. [Retracted] A Tunguska Sized Airburst Destroyed Tall el-Hammam a Middle Bronze Age City in the Jordan Valley Near the Dead Sea. *Sci. Rep.* **2021**, *11*, 18632, doi: 10.1038/s41598.021.97778.3.

[2] Silvia, P.J.; Collins, S.; LeCompte, M.A.; Costa, L.; Howard, G.A.; Kennett, J.P.; Moore, C.R.; Kletetschka, G.; Victor Adedeji, A.; Hermes, R.E.; et al. Modeling how a Powerful Airburst Destroyed Tall el-Hammam, a Middle Bronze Age City Near the Dead Sea. *Airburs. Crater. Imp.* **2024**, *2*, 1–52, doi: 10.14293/ACI.2024.0005.

[3] Kletetschka, G.; Takac, M.; Smrcinova, L.; Kavkova, R.; Abbott, D.; LeCompte, M.A.; Moore, C.R.; Kennett, J.P.; Adedeji, V.; Witwer, T.; et al. New Evidence of High-Temperature, High-Pressure Processes at the Site of the 1908 Tunguska Event: Implications for Impact and Airburst Phenomena. *Airburs. Crater. Imp.* **2025**, *3*, 20250001, doi: 10.14293/ACI.2025.0001.

[4] Dev777. Tall el-Hammam Overlooking the Jordan Valley 2007. Available online: https://commons.wikimedia.org/wiki/File:Tall_el-Hammam_overlooking_the_Jordan_Valley_2007.jpg (ed Licensed under https://creativecommons.org/licenses/by-sa/4.0/deed.en) (Wikipedia.com, 2007). (accessed April 2025).

[5] Collins, S.; Kobs, C.M.; Luddeni, M.C. *The Tall al-Hammam Excavations, Volume 1: An Introduction to Tall al-Hammam: Seven Seasons (2005–2011) of Ceramics and Eight Seasons (2005–2012) of Artifacts from Tall al-Hammam*; Penn State Press, 2015.

[6] Silvia, P.J. *The Middle Bronze Age Civilization-Ending Destruction of the Middle Ghor.* PhD thesis, Trinity Southwest University, 2015.

[7] Bunch, T.E.; LeCompte, M.A.; Victor Adedeji, A.; Wittke, J.H.; David Burleigh, T.; Hermes, R.E.; Mooney, C.; Batchelor, D.; Wolbach, W.S.; Kathan, J.; et al. A Tunguska Sized Airburst Destroyed Tall el-Hammam a Middle Bronze Age City in the Jordan Valley Near the Dead Sea. *Sci. Rep.* **2021**, *11*, 18632, doi: 10.1038/s41598.021.97778.3.

[8] Collins, S.; Byers, G.A.; Kobs, C.M. *The Tall al-Hammam Excavation Project, Season Fourteen 2019 Report: Excavation, Interpretations, and Insights*, Department of Antiquities of Jordan: Amman, Jordan, 2019.

[9] Collins, S.; Byers, G.A.; Kobs, C.M. *The Tall al-Ḥammām Excavation Project, Season Ten 2015 Report: Excavation, Interpretations, and Insights*, Department of Antiquities of Jordan: Amman, Jordan, 2015.

[10] Collins, S.; Byers, G.A.; Kobs, C.M. *The Tall al-Ḥammām Excavation Project, Season Eleven 2016 Report: Excavation, Interpretations, and Insights*, Department of Antiquities of Jordan: Amman, Jordan, 2016.

[11] Collins, S.; Byers, G.A.; Kobs, C.M. *The Tall al-Ḥammām Excavation Project, Season Twelve 2017 Report: Excavation, Interpretations, and Insights*, Department of Antiquities of Jordan: Amman, Jordan, 2017.

[12] Collins, S.; Byers, G.A.; Kobs, C.M. *The Tall al-Ḥammām Excavation Project, Season Thirteen 2018 Report: Excavation, Interpretations, and Insights*, Department of Antiquities of Jordan: Amman, Jordan, 2018.

[13] Collins, S. Tall el-Hammam Is Sodom: Billington's Heshbon Identification Suffers from Numerous Fatal Flaws. *Bib. Res. Bull.* **2012**, *XII*.

[14] Collins, S. *The Search for Sodom & Gomorrah*, Trinity Southwest University Press, 2006.

[15] Collins, S.; Aljarrah, H. *Tall el-Hammam Season Six, 2011: Excavation, Survey, Interpretations and Insights*, Department of Antiquities of Jordan: Amman, Jordan, 2011.

[16] Collins, S.; Byers, G.A.; Kobs, C.M.; Silvia, P.J. *Tall el-Hammam Season Nine, 2014: Excavation, Survey, Interpretations and Insights*. Department of Antiquities of Jordan: Amman, Jordan, 2014.

[17] Collins, S.; Byers, G.A.; Luddeni, M.C.; Moore, J.W. The Tall el-Hammam Excavation Project, Season Activity Report, Season Two: 2006/2007 Excavation, Exploration, and Survey. *Ann. Dept. Antiq. Jor.* **2007**, *VII*.

[18] Collins, S.; Eylayyan, Y.; Byers, G.A.; Kobs, C.M. *Tall el-Hammam Season Seven, 2012: Excavation, Survey, Interpretations and Insights*, Department of Antiquities of Jordan: Amman, Jordan, 2012.

[19] Collins, S.; Hamdan, G.A.; Byers, G.A.; Haroun, J.; Aljarrah, H.; Luddeni, M.C.; McAllister, S.; Abu-Shmais, A.; Dasougi, Q. *The Tall el-Hammam Excavation Project, Season Activity Report, Season Five: 2010 Excavation, Exploration, and Survey*, Department of Antiquities of Jordan: Amman, Jordan, 2010.

[20] Collins, S.; Hamdan, G.A.; Haroun, J.; Aljarrah, H.; Luddeni, M.C.; McAllister, S.; Dasougi, Q.; Abu-Shmais, A.; Graves, D. *The Tall el-Hammam Excavation Project, Season Activity Report, Season Four: 2009 Excavation, Exploration, and Survey*. Department of Antiquities of Jordan: Amman, Jordan, 2009.

[21] Collins, S.; Hamdan, K.; Byers, G.A.; McAllister, S.; Haroun, J.; Luddeni, M.C.; Massara, G.K.; Al-Jarrah, H.; Mullins, R.A.; Dasougi, Q. Tall al-Hammam: Preliminary Report on Four Seasons of Excavation (2006-2009). *Ann. Dept. Antiq. Jor.* **2009**, *53*, 385–414.

[22] Collins, S.; Kobs, C.M.; Byers, G.A. *The Tall al-Hammam Excavation Project, Season Fifteen 2020 Report: Excavation, Interpretations, and Insights*, Department of Antiquities of Jordan: Amman, Jordan, 2020.

[23] Collins, S.; Tarawneh, K.; Byers, G.A.; Kobs, C.M. *Tall el-Hammam Season Eight, 2013: Excavation, Survey, Interpretations and Insights*, Department of Antiquities of Jordan: Amman, Jordan, 2013.

[24] Bronk Ramsey, C. Bayesian Analysis of Radiocarbon Dates. *Radiocarbon* **2009**, *51*, 337–360.

[25] Bronk Ramsey, C. Probability and Dating. *Radiocarbon* **1997**, *40*, 461–474.

[26] Reimer, P.J.; Austin, W.E.N.; Bard, E.; Bayliss, A.; Blackwell, P.G.; Ramsey, C.B.; Butzin, M.; Cheng, H.; Edwards, R.L.; Friedrich, M.; et al. The IntCal20 Northern Hemisphere Radiocarbon Age Calibration Curve (0–55 cal kBP). *Radiocarbon* **2020**, *62*, 725–757, doi: 10.1017/rdc.2020.41.

[27] Telford, R.J.; Heegaard, E.; Birks, H.J.B. All Age–depth Models are Wrong: But How Badly? *Quat. Sci. Rev.* **2004**, *23*, 1–5.

[28] Kennett, J.P.; Kennett, D.J.; Culleton, B.J.; Aura Tortosa, J.E.; Bischoff, J.L.; Bunch, T.E.; Daniel, I.R.; Erlandson, J.M.; Ferraro, D.; Firestone, R.B.; et al. Bayesian Chronological Analyses Consistent with Synchronous Age of 12,835-12,735 Cal B.P. for Younger Dryas Boundary on Four Continents. *Proc. Natl. Acad. Sci. U. S. A.* **2015**, *112*, E4344–4353, doi: 10.1073/pnas.1507146112.

[29] Carlisle, D.B.; Braman, D.R. Nanometre-size diamonds in the Cretaceous/Tertiary boundary clay of Alberta. *Nature* **1991**, *352*, 708–709, doi: 10.1038/352708a0.

[30] Hough, R.M.; Gilmour, I.; Pillinger, C.T. Carbon Isotope Study of Impact Diamonds in Chicxulub Ejecta at Cretaceous-Tertiary Boundary Sites in Mexico and the Western Interior of the United States. In *Large Meteorite Impacts and Planetary Evolution II, Special Paper*; Dressler, B.O., Sharpton, V.L., Ed.; 1999; Volume 339, pp. 215–222.

[31] Kinzie, C.R.; Que Hee, S.S.; Stich, A.; Tague, K.A.; Mercer, C.; Razink, J.J.; Kennett, D.J.; DeCarli, P.S.; Bunch, T.E.; Wittke, J.H.; et al. Nanodiamond-rich Layer Across Three Continents Consistent with Major Cosmic Impact at 12,800 Cal BP. *J. Geol.* **2014**, *122*, 475–506.

[32] Shumilova, T.G.; Isaenko S.I.; Ulyashev, V.V.; Makeev, B.A.; Rappenglück, M.A.; Veligzhanin, A.A.; Ernstson, K. Enigmatic Glass-Like Carbon from the Alpine Foreland, Southeast Germany: A Natural Carbonization Process. *Acta Geol. Sin.-Eng Edition* **2018**, *92*, 2179–2200, doi: 10.1111/1755.6724.13722.

[33] Schoell, M.; Carlson, R.M. Diamondoids and Oil are Not Forever. *Nature* **1999**, *399*, 15–16.

[34] Bruce, L.F.; Kopylova, M.G.; Longo, M.; Ryder, J.; Dobrzhinetskaya, L.F. Luminescence of Diamonds from Metamorphic Rocks. *Am. Min.* **2011**, *96*, 14–22, doi: 10.2138/am.2011.3467.

[35] De Araujo, P.L.B.; Mansoori, G.A.; De Araujo, E.S. Diamondoids: Occurrence in Fossil Fuels, Applications in Petroleum Exploration and Fouling in Petroleum Production. A Review Paper. *Int. J. Oil Gas Coal Technol.* **2012**, *5*, 316–367.

[36] Moore, A.M.T.; Kennett, J.P.; Napier, W.M.; Bunch, T.E.; Weaver, J.C.; LeCompte, M.; Adedeji, A.V.; Hackley, P.; Kletetschka, G.; Hermes, R.E.; Wittke, J.H.; et al. Evidence of Cosmic Impact at Abu Hureyra, Syria at the Younger Dryas Onset (~12.8 ka): High-temperature melting at >2200 °C. *Sci. Rep.* **2020**, *10*, 4185, doi: 10.1038/s41598.020.60867.w.

[37] Kenyon, K.M. Excavations at Jericho, 1952. *Palest. Explor. Quart.* **1952**, *84*, 62–82.

[38] Nigro, L. *The Italian-Palestinian Expedition to tell es-Sultan, Ancient Jericho (1997–2015): Archaeology and Valorisation of Material and Immaterial Heritage 175–214*, Oxford, Archaeopress, 2020.

[39] Marchetti, N. *A Century of Excavations on the Spring Hill at Tell es-Sultan, Ancient Jericho: A Reconstruction of its Stratigraphy*, University of Rome; Palestinian Dept. of Antiquities, 2000.

[40] Kenyon, K.M. *Excavations at Jericho/Vol. 3, The Architecture and Stratigraphy of the Tell Plates*, Brit. School of Archeology in Jerusalem, 1981.

[41] Flanagan, J.W.; McCreery, D.W.; Yāsīn, H.A.N.; Kehrberg, I. Tall Nimrin: Preliminary Report on the 1995 Excavation and Geological Survey. *Ann. Dept. Antiq. Jor.* **1996**, *40*, 271–292.

[42] Omotoyinbo, J.A.; Oluwole, O. Working Properties of Some Selected Refractory Clay Deposits in South Western Nigeria. *J. Min. Mater. Charact. Eng*. **2008**, *7*(3), 233–245, doi: 10.4236/jmmce.2008.73018.

[43] Haccuria, E.; Crivits, T.; Hayes, P.C.; Jak, E. Selected Phase Equilibria Studies in the Al2O3–CaO–SiO2 System. *J. Am. Ceram. Soc.* **2016**, *99*, 691–704.

[44] Kletetschka, G.; Wieczorek, M.A. Fundamental Relations of Mineral Specific Magnetic Carriers for Paleointensity Determination. *Phys. Earth Planet. Inter.* **2017**, *272*, 44–49.

[45] Klokočník, J.; Kostelecký, J.; Bezděk, A.; Cílek, V.; Kletetschka, G.; Staňková, H. Support for two subglacial impact craters in northwest Greenland from Earth gravity model EIGEN 6C4 and other data. *Tectonophysics* **2020**, *780*, 228396, doi: 10.1016/j.tecto.2020.228396.

[46] Kletetschka, G.; Kohout, T.; Wasilewski, P.J. Magnetic Remanence in the Murchison Meteorite. *Meteorit. Planet. Sci.* **2003**, *38*, 399–405.

[47] Kletetschka, G.; Ocampo Uria, A.; Zila, V.; Elbra, T. Electric Discharge Evidence Found in a New Class of Material in the Chicxulub Ejecta. *Sci. Rep.* **2020**, *10*, 9035, doi: 10.1038/s41598.020.65974.2.

[48] Kletetschka, G.; Vondrák, D.; Hruba, J.; Prochazka, V.; Nabelek, L.; Svitavská-Svobodová, H.; Bobek, P.; Horicka, Z.; Kadlec, J.; Takac, M.; et al. Cosmic-Impact Event in Lake Sediments from Central Europe Postdates the Laacher See Eruption and Marks Onset of the Younger Dryas. *J. Geol.* **2018**, *126*, 561–575.

[49] Wasilewski, P.; Kletetschka, G. Lodestone: Natures Only Permanent Magnet-What it is and How it Gets Charged. *Geophys Res. Lett.* **1999**, *26*, 2275–2278.

[50] Osinski, G.R.; Kieniewicz, J.; Smith, J.R.; Boslough, M.B.E.; Eccleston, M.; Schwarcz, H.P.; Kleindienst, M.R.; Haldemann, A.F.C.; Churcher, C.S. The Dakhleh Glass: Product of an Impact

Airburst or Cratering Event in the Western Desert of Egypt? *Meteorit. Planet. Sci.* **2008**, *43*, 2089–2106, doi: 10.1111/j.1945.5100.2008.tb00663.x.

[51] Piperno, D.R. *Phytoliths: A Comprehensive Guide for Archaeologists and Paleoecologists*, AltaMira Press, 2006; p. 248.

[52] Yost, C. *Phytolith Analysis of Feature Fill Samples from the el Dornajo Site, Ecuador*, Paleo Research Institute Golden, Colorado, 2008; p. 17.

[53] Humphreys, G.S.; Shakesby, R.A.; Doerr, S.H.; Blake, W.H.; Wallbrink, P. Hart, D.M. Some Effects of Fire on the Regolith. In *Advances in Regolith*, Roach, I.C., Ed.; CRC LEME, 2008; pp. 216–220.

[54] Boslough, M. *Comments on Tall el-Hammam*, PubPeer.org, 2025. https://pubpeer.org/ (accessed April 2025).

[55] Pietrek, A.; Kenkmann, T.; Jung, D. Bunte Breccia Revisited: The Distribution and Source of Water in the Ejecta of Ries Crater Germany. In *46th Annual Lunar and Planetary Science Conference*, 2015; p. 1534.

[56] Buchner, E.; Sach, V.J.; Schmieder, M. Ries Impact Deposits in the North Alpine Foreland Basin of Germany as a Terrestrial Analog Site for Impact-produced Seismites and Sand Spikes on Planet Mars. *AIMS Geosciences* **2025**, *11*, 68–90, doi: 10.3934/geosci.2025005.

[57] King Jr D.T.; Petruny, L.W. Stratigraphy and Sedimentology of Coarse Impactoclastic Breccia Units Within the Cretaceous-Tertiary Boundary Section, Albion Island, Belize. In *Impact Markers in the Stratigraphic Record*, Springer, 2003; pp. 203–227.

[58] Claudin, F.; Ernstson, K.; Monninger, W. *New Approach to an Old Debate: The Pelarda Formation Meteorite Impact Ejecta*, Azuara Structure: Iberian Chain, NE Spain, 2019.

[59] Ernstson, K.; Mayer, W.; Neumair, A.; Sudhaus, D. The Sinkhole Enigma in the Alpine Foreland, Southeast Germany: Evidence of Impact-induced Rock Liquefaction Processes. *Central Eur. J. Geosci.* **2011**, *3*, 385–397.

[60] Boslough, M.; Bruno, A. Misunderstandings About the Tunguska Event, Shock Wave Physics, and Airbursts have Resulted in Misinterpretations of Evidence at Tall el-Hammam. *Sci. Rep.* **2025**, *15*, 13869.

[61] Boslough, M.; Crawford, D.A. Low-altitude Airbursts and the Impact Threat. *Int. J. Impact. Eng.* **2008**, *35*, 1441–1448.

[62] Boslough, M.; Schultz, P.H.; Harris, R.S. Hypervelocity Airburst Shower Formation of the Pica Glass. *13th Planetary Crater Consortium Meeting, 10–12 August, 2022 in Boulder, Colorado and Virtually*, LPI Contributions, 2022; Volume 2702, p. 2021.

[63] Bunch, T.E.; Hermes, R.E.; Moore, A.M.; Kennett, D.J.; Weaver, J.C.; Wittke, J.H.; DeCarli, P.S.; Bischoff, J.L.; Hillman, G.C.; Howard, G.A.; et al. Very High-temperature Impact Melt Products as Evidence for Cosmic Airbursts and Impacts 12,900 Years Ago. *Proc. Natl. Acad Sci. U. S. A.* **2012**, *109*, E1903–1912, doi: 10.1073/pnas.1204453109.

[64] Boslough, M. Airburst Modeling. In *Handbook of Cosmic Hazards and Planetary Defense*, 2014; pp. 1–24, doi: 10.1007/978.3.319.02847.7_56.1.

[65] Goltrant, O.; Cordier, P.; Doukhan, J.-C. Planar Deformation Features in Shocked Quartz; A Transmission Electron Microscopy Investigation. *Earth Planet. Sci. Lett.* **1991**, *106*, 103–115.

[66] Christie, J.; Ardell, A. Substructures of Deformation Lamellae in Quartz. *Geology* **1974**, *2*, 405–408, doi: 10.1130/0091-7613(1974)2<405:SODLIQ>2.0.CO;2.

[67] Bohor, B.; Fisler, D.; Gratz, A.J. Distinguishing Between Shock and Tectonic Lamellae with the SEM. In *Lunar and Planetary Science Conference*, 1995; Volume 26, p. 145.

[68] Gratz, A.J.; Fisler, D.K.; Bohor, B.F. Distinguishing Shocked from Tectonically Deformed Quartz by the use of the SEM and Chemical Etching. *Earth Planet. Sci. Lett.* **1996**, *142*, 513–521.

[69] Gratz, A.J.; Tyburczy, J.; Christie, J.; Ahrens, T.; Pongratz, P. Shock Metamorphism of Deformed Quartz. *Phys. Chem. Minerals* **1988**, *16*, 221–233.

[70] Hamers, M.; Drury, M. Scanning Electron Microscope-cathodoluminescence (SEM-CL) Imaging of Planar Deformation Features and Tectonic Deformation Lamellae in Quartz. *Meteorit. Planet. Sci.* **2011**, *46*, 1814–1831.

[71] Stöffler, D.; Gault, D.; Wedekind, J.; Polkowski, G. Experimental Hypervelocity Impact Into Quartz Sand: Distribution and Shock Metamorphism of Ejecta. *J. Geophys. Res.* **1975**, *80*, 4062–4077.

[72] Stöffler, D.; Langenhorst, F. Shock Metamorphism of Quartz in Nature and Experiment: I. Basic Observation and Theory. *Meteoritics* **1994**, *29*, 155–181.

[73] Vernooij, M.G.; Langenhorst, F. Experimental Reproduction of Tectonic Deformation Lamellae in Quartz and Comparison to Shock-induced Planar Deformation Features. *Meteorit. Planet. Sci.* **2005**, *40*, 1353–1361, doi: 10.1111/j.1945.5100.2005.tb00406.x.

[74] French, B.M.; Koeberl, C. The Convincing Identification of Terrestrial Meteorite Impact Structures: What Works, What Doesn't, and Why. *Earth Sci. Rev.* **2010**, *98*, 123–170, doi: 10.1016/j.earscirev.2009.10.009.

[75] Langenhorst, F. Shock Metamorphism of Some Minerals: Basic Introduction and Microstructural Observations. *Bull. Czech Geol. Surv.* **2002**, *77*, 265–282.

[76] Ernstson, K.; Mayer, W.; Neumair, A.; Rappenglück, B.; Sudhaus, D. The Chiemgau crater strewn field: Evidence of a Holocene large impact event in Southeast Bavaria, Germany. *J. Sib. Fed.* **2010**, *3*, 72–103.

[77] Hermes, R.E.; Wenk, H.-R.; Kennett, J.P.; Bunch, T.E.; Moore, C.R.; LeCompte, M.A.; Kletetschka, G.; Adedeji, A.V.; Langworthy, K.; Razink, J.; et al. Microstructures in Shocked Quartz: Linking Nuclear Airbursts and Meteorite Impacts. *Airburs. Crater. Imp.* **2023**, *1*, 1–40.

[78] Ferriere, L.; Osinski, G.R. Shock Metamorphism. In *Impact Cratering: Processes and Products*, Osinski, G.R., Pierazzo, E., Ed.; John Wiley & Sons, 2012; pp. 106–124.

[79] French, B.M. *Traces of Catastrophe: A Handbook of Shock-Metamorphic Effects in Terrestrial Meteorite Impact Structures*, Lunar and Planetary Institute, 1998; p. 120.

[80] Christie, J.M.; Griggs, D.T.; Carter, N.L. Experimental Evidence of Basal Slip in Quartz. *J. Geol.* **1964**, *72*, 734–756.

[81] Christie, J.M.; Raleigh, C.B. The Origin of Deformation Lamellae in Quartz. *Am. J. Sci.* **1959**, *257*, 385–407, doi: 10.2475/ajs.257.6.385.

[82] Gratz, A. Deformation in Laboratory-shocked Quartz. *J. Non-Cryst. Solids* **1984**, *67*, 543–558.

[83] McLaren, A.; Retchford, J.; Griggs, D.; Christie, J. Transmission Electron Microscope Study of Brazil Twins and Dislocations Experimentally Produced in Natural Quartz. *Phys. Stat. Solidi (B)* **1967**, *19*, 631–644.

[84] McLaren, A.; Turner, R.; Boland, J.; Hobbs, B. Dislocation Structure of the Deformation Lamellae in Synthetic Quartz; A Study by Electron and Optical Microscopy. *Contrib. Mineral. Petrol.* **1970**, *29*, 104–115.

[85] West, A.; Young, M.D.; Costa, L.; Kennett, J.P.; Moore, C.R.; LeCompte, M.A.; Kletetschka, G.; Hermes, R.E. Modeling Airbursts by Comets, Asteroids, and Nuclear Detonations: Shock Metamorphism, Meltglass, and Microspherules. *Airburs. Crater. Imp.* **2024**, *2*, 1–30.

[86] Kowitz, A.; Güldemeister, N.; Schmitt, R.T.; Reimold, W.U.; Wünnemann, K.; Holzwarth, A. Revision and Recalibration of Existing Shock Classifications for Quartzose Rocks Using Low-shock Pressure (2.5-20 GPa) Recovery Experiments and Mesoscale Numerical Modeling. *Meteorit. Planet. Sci.* **2016**, *51*, 1741–1761, doi: 10.1111/maps.12712.

[87] Kowitz, A.; Schmitt, R.T.; Uwe Reimold, W.; Hornemann, U. The first MEMIN Shock Recovery Experiments at Low Shock Pressure (5–12.5 GPa) with Dry, Porous Sandstone. *Meteorit. Planet. Sci.* **2013**, *48*, 99–114.

[88] Reimold, W.U.; Koeberl, C. Impact Structures in Africa: A Review. *J. Afr. Earth Sci.* **2014**, *93*, 57–175, doi: 10.1016/j.jafrearsci.2014.01.008.

[89] Buchanan, P.; Reimold, W. Planar Deformation Features and Impact Glass in Inclusions From the Vredefort Granophyre, South Africa. *Meteorit. Planet. Sci.* **2002**, *37*, 807–822, doi: 10.1111/j.1945.5100.2002.tb00857.x.

[90] Koeberl, C.; Reimold, W.U.; Cooper, G.; Cowan, D.; Vincent, P.M. Aorounga and Gweni Fada Impact Structures, Chad: Remote Sensing, Petrography, and Geochemistry of Target Rocks. *Meteorit. Planet. Sci.* **2005**, *40*, 1455–1471.

[91] Reimold, W.U.; Crósta, A.P.; Hasch, M.; Kowitz, A.; Hauser, N.; Sanchez, J.P.; Simões, L.S.A.; de Oliveira, G.J.; Zaag, P.T. Shock Deformation Confirms the Impact Origin for the Cerro do Jarau, Rio Grande do Sul, Brazil, Structure. *Meteorit. Planet. Sci.* **2019**, *54*, 2384–2397, doi: 10.1111/maps.13233.

[92] Kieffer, S.W. Shock Metamorphism of the Coconino Sandstone at Meteor Crater, Arizona. *J. Geophys. Res.* **1971**, *76*, 5449–5473, doi: 10.1029/JB076i023p05449.

[93] Kieffer, S.W.; Phakey, P.P.; Christie, J.M. Shock processes in Porous Quartzite: Transmission Electron Microscope Observations and Theory. *Contrib. Mineral. Petrol.* **1976**, *59*, 41–93, doi: 10.1007/BF00375110.

[94] Ernstson, K. *Shock Metamorphism.* 2020. Available online: http://www.impact-structures.com/shock-metamorphism-page/. (accessed April 2025).

[95] Ernstson, K.; Bauer, F.; Hiltl, M. A Prominent Iron Silicides Strewn Field and Its Relation to the Bronze Age/Iron Age Chiemgau Meteorite Impact Event (Germany). *Earth Sci.* **2023**, *12*, 26–40.

[96] Ernstson, K.; Sideris, C.; Liritzis, I.; Neumair, A. The Chiemgau Meteorite Impact Signature of the Stöttham Archaeological Site (Southeast Germany). *Mediterr. Archaeol. Archaeom.* **2012**, *12*, 249–259.

[97] Ernstson, K. *Meteorite Impact Spallation: From Mega- to Micro-scale*. 2014. Available online: http://www.impact-structures.com/impact-educational/meteorite-impact-spallation-from-mega-to-micro-scale/ (accessed April 2025).

[98] Moore, A.M.T.; Kennett, J.P.; Napier, W.M.; Bunch, T.E.; Weaver, J.C.; LeCompte, M.A.; Adedeji, A.V.; Kletetschka, G.; Hermes, R.E.; Wittke, J.H.; et al. Abu Hureyra, Syria, Part 2: Additional Evidence Supporting the Catastrophic Destruction of this Prehistoric Village by a Cosmic Airburst ~12,800 Years Ago. *Airburs. Crater. Imp.* **2023**, *1*, 1–36. doi: 10.14293/ACI.2023.0002.

[99] Moore, C.R.; LeCompte, M.A.; Kennett, J.P.; Brooks, M.J.; Firestone, R.B.; Ivester, A.H.; Ferguson, T.A.; Lane, C.S.; Duernberger, K.A.; Feathers, J.K.; et al. Platinum, Shock-fractured Quartz, Microspherules, and Meltglass Widely Distributed in Eastern USA at the Younger Dryas onset (12.8 ka). *Airburs. Crater. Imp.* **2024**, *2*, 1–31.

[100] Moore, A.M.T.; Kennett, J.P.; LeCompte, M.A.; Moore, C.R.; Li, Y.-Q.; Kletetschka, G.; Langworthy, K.; Razink, J.J.; Brogden, V.; van Devener, B.; et al. Abu Hureyra, Syria, Part 1: Shock-fractured Quartz Grains Support 12,800-year-old Cosmic Airburst at the Younger Dryas Onset. *Airburs. Crater. Imp.* **2023**, *1*, 1–28, doi: 10.14293/ACI.2023.0003.

[101] Wakita, S.; Johnson, B.C.; Denton, C.A.; Davison, T.M. Jetting During Oblique Impacts of Spherical Impactors. *Icarus* **2021**, *360*, 114365.

[102] Ernstson, K. Evidence of Meteorite Impact-induced Thermal Shock in Quartz. In *Modern Problems of Theoretical, Experimental and Applied Mineralogy, Yushkin Readings*, 2020; pp. 361–362.

[103] Poelchau, M.; Kenkmann, T. Feather Features: A Low-Shock-pressure Indicator in Quartz. *J. Geophys. Res. Solid Earth* **2011**, *116*.

[104] Huber, M.S.; Ferrière, L.; Losiak, A.; Koeberl, C. ANIE: A Mathematical Algorithm for Automated Indexing of Planar Deformation Features in Quartz Grains. *Meteorit. Planet. Sci.* **2011**, *46*, 1418–1424, doi: 10.1111/j.1945.5100.2011.01234.x.

[105] Voorn, M. *A New Way to Confirm Meteorite Impact Produced Planar Features in Quartz: Combining Universal Stage and Electron Backscatter Diffraction techniques*; 2010.

[106] Bunch, T.E. A Study of Shock-induced Microstructures and Solid State Transformations of Several Minerals from Explosion Craters, Ph.D Thesis. University of Pittsburgh, 1966.

[107] Hamers, M.F. *Identifying Shock Microstructures in Quartz from Terrestrial Impacts: New Scanning Electron Microscopy Methods*; UU Department of Earth Sciences, 2013.

[108] Jaret, S.J.; Scott Harris, R. No Mineralogic or Geochemical Evidence of Impact at Tall el-Hammam, a Middle Bronze Age City in the Jordan Valley near the Dead Sea. *Sci. Rep.* **2022**, *12*, 5189, doi: 10.1038/s41598.022.08216.x.

[109] Ferrière, L.; Alwmark, C.; Holm-Alwmark, S.; Leroux, H.; Koeberl, C. Finding, Characterization, and Significance of Shocked Quartz Grains. In *81st Annual Meeting of the Meteoritical Society*, 2018; Volume 81, pp. 6274.

[110] Koeberl, C. The Geochemistry and Cosmochemistry of Impacts. In *Treatise on Geochemistry: Planets, Asteroids, Comets and the Solar System*, Holland, H., Turekian, K., Eds.; Elsevier, 2014; Volume 2, pp. 73–118, doi: 10.1016/B978.0.08.095975.7.00130.3.

[111] Koeberl, C. The Geochemistry and Cosmochemistry of Impacts. *Treatise Geochem.* **2003**, *1*, 739–791.

[112] Gieré, R.; Wimmenauer, W.; Müller-Sigmund, H.; Wirth, R.; Lumpkin, G.R.; Smith, K.L. Lightning-induced Shock Lamellae in Quartz. *Am. Min.* **2015**, *100*, 1645–1648, doi: 10.2138/am.2015.5218.

[113] Eby, G.N.; Charnley, N.; Pirrie, D.; Hermes, R.; Smoliga, J.A.; Rollinson, G. Trinitite Redux: Mineralogy and Petrology. *Am. Min.* **2015**, *100*, 427–441, doi: 10.2138/am.2015.4921.

[114] Florenskiy, K. Preliminary Results from the 1961 Combined Tunguska Meteorite Expedition *Meteoritica* **1965**, *XXIII*, 3–37.

[115] Vannucchi, P.; Morgan, J.P.; Della Lunga, D.; Andronicos, C.L.; Morgan, W.J. Direct Evidence of Ancient Shock Metamorphism at the Site of the 1908 Tunguska Event. *Earth Planet. Sci. Lett.* **2015**, *409*, 168–174.

[116] Poelchau, M. A Look at Unindexed PDFs: How High Should the Value Be for Shocked Rocks? In *Lunar and Planetary Science Conference*, 2015; 2473.

[117] Kletetschka, G.; Kavkova, R.; Ucar, H. Plasma Shielding Removes Prior Magnetization Record from Impacted Rocks Near Santa Fe, New Mexico. *Sci. Rep.* **2021**, *11*, 22466, doi: 10.1038/s41598.021.01451.8.

[118] Thy, P.; Willcox, G.; Barfod, G.H.; Fuller, D.Q. Anthropogenic Origin of Siliceous Scoria Droplets from Pleistocene and Holocene Archaeological Sites in Northern Syria. *J. Archaeol. Sci.* **2015**, *54*, 193–209.

[119] Thy, P.; Segobye, A.K.; Ming, D.W. Implications of Prehistoric Glassy Biomass Slag from East-Central Botswana. *J. Archaeol. Sci.* **1995**, *22*, 629–637.

[120] Firestone, R.B., West, A.; Kennett, J. P.; Becker, L.; Bunch, T.E.; Revay, Z.S.; Schultz, P.H.; Belgya, T.; Kennett, D.J.; Erlandson, J. M.; et al. Evidence for an Extraterrestrial Impact 12,900 Years Ago that Contributed to the Megafaunal Extinctions and the Younger Dryas Cooling. *Proc. Natl. Acad Sci. U. S. A.* **2007**, *104*, 16016–16021, doi: 10.1073/pnas.0706977104.

[121] Firestone, R.B.; West, A.; Revay, Z.; Hagstrum, J.T.; Belgya, T.; Que Hee, S.S.; Smith, A.R. Analysis of the Younger Dryas Impact Layer. *J. Siberian Fed. Univ.* **2010**, *1*, 30–62.

[122] Hagstrum, J.T.; Firestone, R.B.; West, A.; Weaver, J.C.; Bunch, T.E. Impact-related Microspherules in Late Pleistocene Alaskan and Yukon "Muck" Deposits Signify Recurrent Episodes of Catastrophic Emplacement. *Sci. Rep.* **2017**, *7*, 16620, doi: 10.1038/s41598.017.16958.2.

[123] Israde-Alcantara, I.; Bischoff, J.L.; Domínguez-Vázquez, G.; Li, H.C.; DeCarli, P.S.; Bunch, T.E.; Wittke, J.H.; Weaver, J.C.; Firestone, R.B.; West, A.; et al. Evidence from Central Mexico Supporting the Younger Dryas Extraterrestrial Impact Hypothesis. *Proc. Natl. Acad Sci. U. S. A.* **2012**, *109*, E738–E747, doi: 10.1073/pnas.1110614109.

[124] LeCompte, M.A.; Goodyear, A.C.; Demitroff, M.N.; Batchelor, D.; Vogel, E.K.; Mooney, C.; Rock, B.N.; Seidel, A.W. Independent Evaluation of Conflicting Microspherule Results from Different Investigations of the Younger Dryas Impact Hypothesis. *Proc. Natl. Acad Sci. U. S. A.* **2012**, *109*, E2960–E2969, doi: 10.1073/pnas.1208603109.

[125] LeCompte, M.A.; West, A.; Andedeji, A.V.; Demitroff, M.; Witwer, T.; Langenburg. R.A. The Bowser Road Mastodon and the Younger Dryas Impact Hypothesis, Appendix 3. In *The Archaeological Recovery of the Bowser Road Mastodon, Orange County NY*, Gramly, R.M., Ed.; Persimmon Press, 2017.

[126] Pino, M.; Abarzúa, A.M.; Astorga, G.; Martel-Cea, A.; Cossio-Montecinos, N.; Navarro, R.X.; Lira, M.P.; Labarca, R.; LeCompte, M.A.; Adedeji, V.; et al. Sedimentary Record from Patagonia, Southern Chile Supports Cosmic-impact Triggering of Biomass Burning, Climate Change, and Megafaunal Extinctions at 12.8 ka. *Sci. Rep.* **2019**, *9*, 4413, doi: 10.1038/s41598.018.38089.y.

[127] Teller, J.; Boyd, M.; LeCompte, M.; Kennett, J.; West, A.; Telka, A.; Diaz, A.; Adedeji, V.; Batchelor, D.; Mooney, C.; et al. A Multi-proxy Study of Changing Environmental Conditions in a Younger Dryas Sequence in Southwestern Manitoba, Canada, and Evidence for an Extraterrestrial Event. *Quat. Res*. **2020**, *93*, 60–87, doi: 10.1017/qua.2019.46.

[128] Wu, Y.; Sharma, M.; LeCompte, M.A.; Demitroff, M.N.; Landis, J.D. Origin and Provenance of Spherules and Magnetic Grains at the Younger Dryas Boundary. *Proc. Natl. Acad Sci. U. S. A.* **2013**, *110*, E3557–E3566, doi: 10.1073/pnas.1304059110.

[129] Wittke, J.H.; Weaver, J.C.; Bunch, T.E.; Kennett, J.P.; Kennett, D.J.; Moore, A.M.; Hillman, G.C.; Tankersley, K.B.; Goodyear, A.C.; Moore, C.R.; et al. Evidence for Deposition of 10 Million Tonnes of Impact Spherules Across Four Continents 12,800 y Ago. *Proc. Natl. Acad Sci. U. S. A.* **2013**, *110*, E2088–E2097, doi: 10.1073/pnas.1301760110.

[130] Harris, R.; Schultz, P. Are Ti-Rich Particles in Late Pleistocene Sediments from Patagonia Distal Ejecta from an Atacama Airburst? In *Lunar and Planetary Science Conference*, 2019; p 2526.

[131] Baker, G.A. *Tektites*, National Museum of Victoria, 1959.

[132] Sharygin, V.; Sokol, E.; Belakovskii, D. Fayalite-sekaninaite Paralava from the Ravat Coal Fire (Central TAJIKISTAN). *Russ. Geol. Geophys.* **2009**, *50*, 703–721.

[133] Baker, G. Micro-forms of Hay-silica Glass and of Volcanic Glass. *Mineral. Mag. J. Mineral. Soc.* **1968**, *36*, 1012–1023.

[134] Pauketat, T.R.; Kelly, L.S.; Fritz, G.J.; Lopinot, N.H.; Elias, S.; Hargrave, E. The Residues of Feasting and Public Ritual at Early Cahokia. *Am. Antiq.* **2002**, *67*, 257–279.

[135] Friend, C.; Dye, J.; Fowler, M. New Field and Geochemical Evidence from Vitrified Forts in South Morar and Moidart, NW Scotland: Further Insight Into Melting and the Process of Vitrification. *J. Archaeol. Sci.* **2007**, *34*, 1685–1701.

[136] Johnston, S.; Diachenko, A.; Gaydarska, B.; Nebbia, M.; Voke, P.; Bondar, K.; Litkevych, V.; Chapman, J. The Experimental Building, Burning and Excavation of a Two-storey Trypillia House. *PAST (Newsletter of the Prehistoric Society)* **2018**, *89*, 13–15.

[137] Orton, D.C.; Nottingham, J.; Rainsford-Betts, G.; Hosking, K.; Millard, A.R. Animal Bones [from Nebelivka]. In *Early Urbanism in Europe*, Bisserka, G., Ed.; De Gruyter Open Ltd., 2020; pp 383–404.

[138] Dever, W.G. *Preliminary Excavation Reports: Sardis, Idalion, and Tell El-Handaquq North*; American Schools of Oriental Research, 1996; Volume 53.

[139] Bikai, P.M.; Egan, V. Archaeology in Jordan. *Am. J. Archaeol.* **1996**, *100*, 507–535.

[140] Yates, C.J.C. *Beyond the Mound: Locating Complexity in Northern Mesopotamia During the "Second Urban Revolution"*; Boston University, 2014.

[141] Senior, L.M. *Time and Technological Change: Ceramic Production, Labor, and Economic Transformation in a Third Millennium Complex Society (Tell Leilan, Syria)*; The University of Arizona, 1998.

[142] Weiss, H.; Eidem, J.; Guilderson, T.; Kasten, U.; Larsen, T.; Mori, L.; Ristvet, L.; Rova, E.; Wetterstrom, W. Revising the Contours of History at Tell Leilan. *Ann. Archeol. Arabes Syrie.* **2002**, *45*, 59.

[143] Courty, M.-A. The Soil Record of an Exceptional Event at 4000 B.P. in the Middle East. In *Natural Catastrophes During Bronze Age Civilisations: Archaeological, Geological, Astronomical and Cultural Perspectives*, 1998; p 93.

[144] Grissom, C.A. Conservation of Neolithic Lime Plaster Statues from 'Ain Ghazal. *Stud. Conserv.* **2013**, *41*, 70–75, doi: 10.1179/sic.1996.41.Supplement.1.70.

[145] Osinski, G.; Bunch, T.; Wittke, J. Evidence for the Shock Melting of Carbonates from Meteor Crater, Arizona. *Meteorit. Planet. Sci. Suppl.* **2003**, *38*, 5070.

[146] Osinski, G.; Bunch, T.; Wittke, J. Impact Melt Generation at Meteor Crater, Arizona: Implications for Impacts into Volatile-rich Target Rocks. *Meteorit. Planet. Sci. Suppl.* **2007**, *42*, 5110.

[147] Butterman, W.C.; Foster, W.R. Zircon Stability and the Zr02-Si02 Phase Diagram. *Am. Mineral. J. Earth Planet. Materials* **1967**, *52*, 880–885.

[148] Bohor, B.; Betterton, W.; Krogh, T. Impact-shocked Zircons: Discovery of Shock-induced Textures Reflecting Increasing Degrees of Shock Metamorphism. *Earth Planet. Sci. Lett.* **1993**, *119*, 419–424.

[149] Patterson, M.C.L. *Development of a Coalesced Arc Plasma Reactor for Minerals Processing*; University of Cambridge, 1986.

[150] Rochow, E.G. *The Chemistry of Silicon: Pergamon International Library of Science, Technology, Engineering and Social Studies*; Elsevier, 2013; Volume 9.

[151] Glass, B.P.; Simonson, B.M. Mesozoic Spherule/Impact Ejecta Layers. In *Distal Impact Ejecta Layers;* Springer, 2013; pp. 245–320.

[152] Chen, M.; Shu, J.; Mao, H.K.; Xie, X.; Hemley, R.J. Natural Occurrence and Synthesis of Two New Postspinel Polymorphs of Chromite. *Proc. Natl. Acad Sci. U. S. A.* **2003**, *100*, 14651–14654, doi: 10.1073/pnas.2136599100.

[153] Economou-Eliopoulos, M.; Eliopoulos, D.G.; Tsoupas, G. On the Diversity of the PGE Content in Chromitites Hosted in Ophiolites and in Porphyry-Cu Systems: Controlling Factors. *Ore Geol. Rev.* **2017**, *88*, 156–173.

[154] Cabri, L.J.; Harris, D.C.; Weiser, T.W. Mineralogy and Distribution of Platinum-group Mineral (PGM) Placer Deposits of the World. *Explor. Min. Geol.* **1996**, *2*, 73–167.

[155] Uysal, I. Platinum-Group Minerals (PGM) and other Solid Inclusions in the Elbistan-Kahramanmaraş Mantle-hosted Ophiolitic Chromitites, South-eastern Turkey: Their Petrogenetic Significance. *Turk. J. Earth Sci.* **2008**, *17*, 729–740.

[156] Jansen, M.; Aulbach, S.; Hauptmann, A.; Höfer, H.E.; Klein, S.; Krüger, M.; Zettler, R.L. Platinum Group Placer Minerals in Ancient Gold Artifacts–Geochemistry and Osmium Isotopes of Inclusions in Early Bronze Age Gold from Ur/Mesopotamia. *J. Archaeol. Sci.* **2016**, *68*, 12–23, doi: 10.1016/j.jas.2016.02.004.

[157] Tolstykh, N.D.; Sidorov, E.G.; Laajoki, K.V.; Krivenko, A.P.; Podlipskiy, M. The Association of Platinum-group Minerals in Placers of the Pustaya River, Kamchatka, Russia. *Can. Mineral.* **2000**, *38*, 1251–1264.

[158] Okrugin, A. Mineral Parageneses and the Origin of Isoferroplatinum Nuggets from the Ignali Placer Deposit. *Geol. Ore Depos*. **2004**, *43*(3), 268–280.

[159] Zaccarini, F.; Pushkarev, E.; Garuti, G.; Krause, J.; Dvornik, G.P.; Stanley, C.; Bindi, L. Platinum-group Minerals (PGM) Nuggets from Alluvial-Eluvial Placer Deposits in the Concentrically Zoned Mafic-ultramafic Uktus Complex (Central Urals, Russia). *Eur. J. Mineral.* **2013**, *25*, 519–531, doi: 10.1127/0935.1221/2013/0025.2296.

[160] Barkov, A.; Martin, R.; Fleet, M.; Nixon, G.; Levson, V. New Data on Associations of Platinum-group Minerals in Placer Deposits of British Columbia, Canada. *Mineral. Petrol.* **2008**, *92*, 9–29.

[161] Tolstykh, N.D.; Foley, J.Y.; Sidorov, E.G.; Laajoki, K.V. Composition of the Platinum-group Minerals in the Salmon River Placer Deposit, Goodnews Bay, Alaska. *Can. Mineral.* **2002**, *40*, 463–471.

[162] Fedortchouk, Y.; LeBarge, W.B.; Barkov, A.Y.; Fedele, L.; Bodnar, R.J. Major-and Trace-element Composition of Platinum Group Minerals and Their Inclusions from Several Yukon Placers. *Yukon Explor. Geol*. **2009**, 185–196.

[163] Harries, D.; Berg, T.; Langenhorst, F.; Palme, H. Structural Clues to the Origin of Refractory Metal Alloys as Condensates of the Solar Nebula. *Meteorit. Planet. Sci.* **2012**, *47*, 2148–2159.

[164] Daly, L.; Bland, P.A.; Dyl, K.A.; Forman, L.V.; Evans, K.A.; Trimby, P.W.; Moody, S.; Yang, L.; Liu, H.; Ringer, S.P.; et al. In Situ Analysis of Refractory Metal Nuggets in Carbonaceous Chondrites. *Geochim. Cosmochim. Acta* **2017**, *216*, 61–81, doi: 10.1016/j.gca.2016.11.030.

[165] Schwander, D. *Extraktion und Nanoanalytische Charakterisierung Refraktärer Nanometallpartikel Frühester Solarer Materie und Synthese Metallischer Nanopartikel aus Dotierten Ca-Mg-Al-Si-Schmelzen*; Universitäts Bibliothek Mainz, 2014, doi:http://doi.org/10.25358/openscience-2859.

[166] Bonté, P.; Jehanno, C.; Maurette, M.; Brownlee, D. Platinum Metals and Microstructure in Magnetic Deep Sea Cosmic Spherules. *J. Geophys. Res. Solid Earth* **1987**, *92*, E641–E648.

[167] Rudraswami, N.; Parashar, K.; Shyam Prasad, M. Micrometer-and Nanometer-sized Platinum Group Nuggets in Micrometeorites from Deep-sea Sediments of the Indian Ocean. *Meteorit. Planet. Sci.* **2011**, *46*, 470–491.

[168] Rudraswami, N.G.; Shyam Prasad, M.; Plane, J.M.C.; Berg, T.; Feng, W.; Balgar, S. Refractory Metal Nuggets in Different Types of Cosmic Spherules. *Geochim. Cosmochim. Acta* **2014**, *131*, 247–266.

[169] Brownlee, D.; Bates, B.; Wheelock, M. Extraterrestrial Platinum Group Nuggets in Deep-sea Sediments. *Nature* **1984**, *309*, 693–695.

[170] Joswiak, D.; Brownlee, D.; Nguyen, A.; Messenger, S. Refractory Materials in Comet Samples. *Meteorit. Planet. Sci.* **2017**, *52*, 1612–1648.

[171] Anders, E.; Grevesse, N. Abundances of the Elements: Meteoritic and Solar. *Geochim. Cosmochim. Acta* **1989**, *53*, 197–214.

[172] Berg, T.; Maul, J.; Schönhense, G.; Marosits, E.; Hoppe, P.; Ott, U.; Palme, H. Direct Evidence for Condensation in the Early Solar System and Implications for Nebular Cooling Rates. *Astrophys. J. Lett.* **2009**, *702*, L172.

[173] Palme, H.; Hutcheon, I.; Spettel, B. Composition and Origin of Refractory-metal-rich Assemblages in a Ca, Al-rich Allende Inclusion. *Geochim. Cosmochim. Acta* **1994**, *58*, 495–513.

[174] Schwander, D.; Berg, T.; Harries, D.; Schönhense, G.; Ott, U. Composition and Clues to the Origin of Refractory Metal Nuggets Extracted from Chondritic Meteorites. *Meteorit. Planet. Sci.* **2014**, *49*, 1888–1901.

[175] Wark, D.; Lovering, J. Refractory/platinum Metal Grains in Allende Calcium-aluminium-rich Clasts (CARC's): Possible Exotic Presolar Material? In *Lunar and Planetary Science Conference*; 1976; Volume 7.

[176] Nazarov, M.A.; Kurat, G.; Brandstaetter, F.; Ntaflos, T.; Chaussidon, M.; Hoppe, P. Phosphorus-bearing Sulfides and their Associations in CM Chondrites. *Petrology* **2009**, *17*, 101–123.

[177] Flynn, G.J.; Bleuet, P.; Borg, J.; Bradley, J.P.; Brenker, F.E.; Brennan, S.; Bridges, J.; Brownlee, D.E.; Bullock, E.S.; Burghammer, M.; et al. Elemental Compositions of Comet 81P/Wild 2 Samples Collected by Stardust. *Science* **2006**, *314*, 1731–1735, doi: 10.1126/science.1136141.

[178] Makvandi, S.; Beaudoin, G.; McClenaghan, B.M.; Layton-Matthews, D. The Surface Texture and Morphology of Magnetite from the Izok Lake Volcanogenic Massive Sulfide Deposit and Local Glacial Sediments, Nunavut, Canada: Application to Mineral Exploration. *J. Geochem. Exp.* **2015**, *150*, 84–103.

[179] Knipping, J.L.; Bilenker, L.D.; Simon, A.C.; Reich, M.; Barra, F.; Deditius, A.P.; Wälle, M.; Heinrich, C.A.; Holtz, F.; Munizaga, R. Trace Elements in Magnetite from Massive Iron Oxide-apatite Deposits Indicate a Combined Formation by Igneous and Magmatic-hydrothermal Processes. *Geochim. Cosmochim. Acta* **2015**, *171*, 15–38.

[180] Knipping, J.L.; Fiege, A.; Simon, A.C.; Oeser, M.; Reich, M.; Bilenker, L.D. In-situ Iron Isotope Analyses Reveal Igneous and Magmatic-hydrothermal Growth of Magnetite at the Los Colorados Kiruna-type Iron Oxide-apatite Deposit, Chile. *Am. Mineral.* **2019**, *104*, 471–484, doi: 10.2138/am.2019.6623.

[181] Britvin, S.; Murashko, M.; Vapnik, E.; Polekhovsky, Y.S.; Krivovichev, S. Barringerite Fe 2 P from Pyrometamorphic Rocks of the Hatrurim Formation, Israel. *Geol. Ore Depos.* **2017**, *59*, 619–625.

[182] Harris, R.; Schultz, P. Evidence of Multiple Cometary Airbursts During the Pleistocene from Pica (Chile), Dakhleh (Egypt), and Edeowie (Australia) Glasses. In *Lunar and Planetary Science Conference*, 2020; pp. 2229.

[183] Rubio, L.; Díaz-Vico, R.; Smith-Fernández, I.; Smith-Fernández, A.; Suárez, J.; Martin-de-Las-Heras, S.; Santos, I. Spectrophotometric Color Measurement to Assess Temperature of Exposure in Cortical and Medullar Heated Human Bones: A Preliminary Study. *Diagnostics (Basel)* **2020**, *10*, 979, doi: 10.3390/diagnostics10110979.

[184] Knüsel, C.J. Crouching in Fear: Terms of Engagement for Funerary Remains. *J. Soc. Archaeol.* **2014**, *14*, 26–58, doi: 10.1177/1469605313518869.

[185] Jenniskens, P.; Popova, O.P.; Glazachev, D.O.; Podobnaya, E.D.; Kartashova, A.P. Tunguska Eyewitness Accounts, Injuries, and Casualties. *Icarus* **2019**, *327*, 4–18, doi: 10.1016/j.icarus.2019.01.001.

[186] Flanagan, J.W.; McCreery, D.W. First Preliminary Report of the 1989 Tell Nimrin Project. *Annu. Dept. Antiquit. Jordan* **1990**, *34*, 131–152.

[187] Ibrahim, M.; Sauer, J.A.; Yassine, K. The East Jordan Valley Survey 1976 (Part two). In *Archaeology of Jordan: Essays and Reports*, University of Jordan: Amman, 1988; pp. 189–207.

[188] Ibrahim, M.A.; Sauer, J.A.; Yassine, K. The East Jordan Valley Survey, 1975. *Bull. Am. Sch. Orient. Res.* **1976**, *222*, 41–66.

[189] Yassine, K. *Tell Nimrin: An Archaeological Exploration*, University of Jordan, 2011.

[190] Flanagan, J.W.; McCreery, D.W.; Yassine, K.N. Preliminary Report of the 1990 Excavation at Tell Nimrin. *Annu. Dept. Antiq. Jordan* **1992**, *36*, 89–111.

[191] Al-Rifaee, M.K. Jordan Valley. In *Salinity Management Workshop for the CGIAR Research Program on Water, Land, and Ecosystem (WLE)*, 2013.

[192] Ammari, T.G.; Tahhan, R.; AbubakeR, S.; Al-Zu'bi, Y.; Tahboub, A.; Ta'any, R.; Abu-Romman, S.; Al-Manaseer, N.; Stietiya, M.H. Soil Salinity Changes in the Jordan Valley Potentially Threaten Sustainable Irrigated Agriculture. *Pedosphere* **2013**, *23*, 376–384.

[193] Singer, A. Saline and Alkaline Soils in Israel. In *The Soils of Israel*, 2007; pp. 231–248.

[194] Ayers, R.S.; Westcot, D.W. *Water Quality for Agriculture*, Food and Agriculture Organization of the United Nations Rome, 1985; Volume 29.

[195] USDA. *Crop Tolerance and Yield Potential of Selected Crops as Influenced by Irrigation Water Salinity (ECw) or Soil Salinity (ECe)*, USDA: Washington, DC, 2011.

[196] Kenyon, K.M. Excavations at Jericho, 1955. *Palest. Explor. Quart.* **1955**, *87*, 108–117.

[197] Marchetti, N.; Nigro, L.; Sarie, I. Preliminary Report on the First Season of Excavations of the Italian–Palestinian Expedition at Tell es-Sultan/Jericho, April–May 1997. *Palest. Explor. Quart.* **1998**, *130*, 121–144.

[198] Kenyon, K.M. *Digging up Jericho*, 1957.

[199] Nigro, L.; Taha, H. *Renewed Excavations and Restorations at Tell es-Sultan/Ancient Jericho, Fifth Season-march-april 2009*, 2009; pp. 731–744.

[200] Nigro, L.; Taha, H. Results of the Italian-Palestinian Expedition to Tell es-Sultan: At the Dawn of Urbanization in Palestine. In *Tell es-*

Sultan/Jericho in the Context of the Jordan Valley: Site Management, Conservation and Sustainable Development, Proceedings of the International Workshop (Ariha 2005), 2006; pp. 1–40.

[201] Kenyon, K.M. Some Notes on the History of Jericho in the Second Millennium BC. *Palest. Explor. Quart.* **1951**, *83*, 101–138.

[202] Nigro, L.; Sala, M.; Taha, H.; Yassine, J. *The Bronze Age Palace and Fortifications at Tell Es-Sultan/Jericho: The 6th-7th Seasons (2010-2011) by Rome La SapienzaUniversity and the Palestinian Mota-Dach*, 2011; pp. 571–597.

[203] Migowski, C.; Agnon, A.; Bookman, R.; Negendank, J.F.; Stein, M. Recurrence Pattern of Holocene Earthquakes Along the Dead Sea Transform Revealed by Varve-counting and Radiocarbon Dating of Lacustrine Sediments. *Earth Planet. Sci. Lett.* **2004**, *222*, 301–314.

[204] Svetsov, V. Total Ablation of the Debris from the 1908 Tunguska Explosion. *Nature* **1996**, *383*, 697–699, doi: 10.1038/383697a0.

[205] Svetsov, V.B. Thermal Radiation on the Ground from Large Aerial Bursts Caused by Tunguska-like Impacts. *Lunar Planet. Sci. XXXVII* **2006**, *2006*, 1–2.

[206] Kirova, O. Scattered Matter from the Area of Fall of the Tunguska Cometary Meteorite. *Ann. N. Y. Acad. Sci.* **1965**, *119*, 235–242.

[207] Beretta, M. *The Alchemy of Glass: Counterfeit, Imitation, and Transmutation in Ancient Glassmaking*, Science History Publications/ USA, 2017.

[208] Museum_of_London. What happened in the Great Fire of London? Available online: https://www.museumoflondon.org.uk/application/files/6514/5511/5493/what-happened-great-fire-london.pdf (2019). (accessed April 2025).

[209] Hopkins, R.P. *The Historiography of the Allied Bombing Campaign of Germany*, East Tennessee State University, 2008.

[210] Connolly, B.D. *HSE and Re-Os Systematics of the 3.3 Ga Weltevreden komatiites from the Barberton Greenstone Belt, South Africa: Implications for Early Earth's Mantle Evolution*, 2011.

[211] de Silva, S.; Sharpton, V. Explosive volcanism, shock metamorphism and the KT boundary. In *Global Catastrophes in Earth History: An Interdisciplinary Conference on Impacts, Volcanism, and Mass Mortality*, 1988; Volume 673, pp. 38.

[212] Bronk Ramsey, C.; Manning, S.W.; Galimberti, M. Dating the Volcanic Eruption at Thera. *Radiocarbon* **2004**, *46*, 325–344, doi: 10.1017/S0033822200039631.

[213] Sigurdsson, H.; Carey, S.; Devine, J. Assessment of Mass, Dynamics and Environmental Effects of the Minoan Eruption of Santorini Volcano. *Thera Aegean World III* **1990**, *2*, 100–112.

[214] Moore, A.; Hillman, G.; Legge, A. *Village on the Euphrates: From Foraging to Farming at Abu Hureyra*, Oxford University Press, 2000; pp. 585.

[215] Moore, A.; Kennett, D. Cosmic Impact, the Younger Dryas, Abu Hureyra, and the Inception of Agriculture in Western Asia. *Eurasian Prehist.* **2013**, *10*, 57–66.

[216] Hanson, S.K.; Pollington, A.D.; Waidmann, C.R.; Kinman, W.S.; Wende, A.M.; Miller, J.L.; Berger, J.A.; Oldham, W.J.; Selby, H.D. Measurements of Extinct Fission Products in Nuclear Bomb Debris: Determination of the Yield of the Trinity Nuclear Test 70 y Later. *Proc. Natl. Acad. Sci. U. S. A* **2016**, *113*, 8104–8108, doi: 10.1073/pnas.1602792113.

[217] Glasstone, S.; Dolan, P.J. *The Effects of Nuclear Weapons*, 3rd ed.; US Dept of Defense, U.S. Government Printing Office, 1977; pp. 653.

[218] Wheeler, L.F.; Mathias, D.L. Probabilistic Assessment of Tunguska-Scale Asteroid Impacts. *Icarus* **2019**, *327*, 83–96, doi: 10.1016/j.icarus.2018.12.017.

[219] Hermes, R.E.; Strickfaden, W.B. A New Look at Trinitite. *Nucl. Weap. J.* **2005**, *2*, 2–7.

[220] Astapovich, I. Novye materialy po poletu bolshogo meteorita 30 iunija 1908 gv Tsentralnoj Sibiri. *Astron Zh.* **1933**, *10*, 465–486.

[221] Wolbach, W.S.; Ballard, J.P.; Mayewski, P.A.; Parnell, A.C.; Cahill, N.; Adedeji, V.; Bunch, T.E.; Domínguez-Vázquez, G.; Erlandson, J.M.; Firestone, R.B.; et al. Extraordinary Biomass-Burning Episode and Impact Winter Triggered by the Younger Dryas Cosmic Impact ~12,800 Years Ago. 2. Lake, Marine, and Terrestrial Sediments. *J. Geol.* **2018**, *126*, 185–205.

[222] Robertson, D.K.; Mathias, D.L. Hydrocode Simulations of Asteroid Airbursts and Constraints for Tunguska. *Icarus* **2019**, *327*, 36–47, doi: 10.1016/j.icarus.2018.10.017.

[223] Kletetschka, G.; Procházka, V.; Fantucci, R.; Trojek, T. Survival Response of Larix Sibirica to the Tunguska Explosion. *Tree-Ring Res.* **2017**, *73*, 75–90, doi: 10.3959/1536.1098.73.2.75.

[224] Zlobin, A.E. Discovery of Probably Tunguska Meteorites at the Bottom of Khushmo River's Shoal. *arXiv preprint arXiv:1304.8070*, 2013.

[225] Kirova, O.; Zaslavskaya, N. Data Characterizing the Dispersed Matter as Recovered from the Area of Fall of the Tunguska Meteorite. *Meteoritika* **1966**, *27*, 119–127.

[226] Vishnevsky, S.; Raitala, J. Impact diamonds as indicators of shock metamorphism in strongly-reworked Pre-Cambrian impactites. In *Impacts and the Early Earth*, Springer, 2000; pp. 229–247.

[227] Kvasnitsa, V.N.; Sobotovich, E.V.; Kovalyukh, N.N.; Litvin, A.L.; Rybalko, S.I.; Sharkin, O.P.; Egorova, L.N. High-pressure carbon polymorphs in the peats of Tunguska catastrophe region. In *Dopovidi Akademii Nauk Ukrainskoi RSR Seriya B-Geologichni Khimichni Ta Biologichni Nauki*, 1979; pp. 999–1004.

[228] Hryanina, L. The bouquet of the meteorite craters in the epicentre of Tunguska Impact 1908 year. In *Lunar and Planetary Science Conference*, 1999; Volume 1186.

[229] Korina, M.; Nazarov, M.A.; Barsukova, L.D.; Suponeva, I.V.; Kolesov, G.M.; Kolensnikov, E.M. Iridium Distribution in the Peat Layers from Area of Tunguska Event. *Lunar Planet. Sci. Conf.* **1987**, *18*, 501.

[230] LeMaire, T.R. *Stones from the Stars: The Unresolved Mysteries of Meteorites*, Prentice Hall; 1980.

[231] Artemieva, N.; Shuvalov, V. Atmospheric Shock Waves After Impacts of Cosmic Bodies up to 1000 m in Diameter. *Meteorit. Planet. Sci.* **2019**, *54*, 592–608, doi: 10.1111/maps.13229.

[232] Van Ginneken, M.; Goderis, S.; Artemieva, N.; Debaille, V.; Decrée, S.; Harvey, R.P.; Huwig, K.A.; Hecht, L.; Yang, S.; Kaufmann, F.E.D.; et al. A Large Meteoritic Event Over Antarctica Ca. 430 ka Ago Inferred from Chondritic Spherules from the Sor Rondane Mountains. *Sci. Adv.* **2021**, *7*, eabc1008, doi: 10.1126/sciadv.abc1008.

[233] Molnár, M.; Ventura, K.; Svanda, P.; Štaffen, Z.; Rappenglück, M.A.; Ernstson, K. Chrudim-Pardubice: Evidence for a young meteorite impact strewn field in the Czech Republic. In *48th Annual Lunar and Planetary Science Conference*, 2017; Volume 1920.

[234] Poßekel, J.; Molnár, M.; Ernstson, K. The proposed meteorite impact event in the Czech Republic: Evidence strengthened by investigations with the digital terrain model. In *53rd Lunar and Planetary Science Conference*, 2022; Volume 2678, pp. 1558, doi: 10.13140/RG.2.2.17849.65123.

[235] Ernstson, K.; Müller, W.; Gawlik-Wagner, A. The Saarlouis semi crater structure: notable insight into the Saarland (Germany) meteorite impact event achieved. In *49th Lunar and Planetary Science Conference*, 2018; Abstract #1876, doi: 10.13140/RG.2.2.20958.74560.

[236] Ernstson, K.; Portz, D.; Müller, W. Zhamanshinite-Like Black-Glass Melt Rocks from the Saarland (Germany) meteorite impact site. In *52nd Lunar and Planetary Science Conference*; 2021; pp. 1350.

[237] Siegel, U.; Rommelfangen, J.; Müller, W.; Michelbacher, S.; Ernstson, K. Shatter Cones in Litermont Quartzites: Saarlouis/ Nalbach (Saarland, Germany) meteorite impact event strengthened. In *Lunar and Planetary Science Conference*, 2022; Abstract #1842.

[238] Ernstson, K.; Poßekel, J.; Rappenglück, M.A. Near-ground airburst cratering: petrographic and ground penetrating radar (GPR) evidence for a possibly enlarged chiemgau impact event (Bavaria, SE-Germany). In *Lunar and Planetary Science Conference*, 2020; pp. 1231.

[239] Rappenglück, B.; Hiltl, M.; Ernstson, K. Artifact-in-impactite: A new kind of impact rock. Evidence from the Chiemgau meteorite impact in southeast Germany. In *Proceedings of the Modern Problems of Theoretical, Experimental, and Applied Mineralogy*, (Yushkin Readings – 7–10 December 2020, Syktyvkar, Russia), 2020; pp. 365–367.

[240] Rappenglück, B.; Hiltl, M.; Ernstson, K. Metallic artifact remnants in a shock-metamorphosed impact breccia: An extended view of the archeological excavation at Stöttham (Chiemgau, SE-Germany). In *50th Annual Lunar and Planetary Science Conference*, 2019; pp. 1334.

[241] Rappenglück, M.A.; et al. *The Chiemgau Impact Event in the Celtic Period: Evidence of a Crater Strewnfield and a Cometary Impactor Containing Presolar Matter*, Chiemgau-Impakt c/o Kord Ernstson, 2004.

[242] Rappenglück, B.; Hiltl, M.; Poßekel, J.; Rappenglück, M.A.; Ernstson, K. People Experienced the Prehistoric Chiemgau Meteorite Impact – Geoarchaeological Evidence from Southeastern Germany: A Review. *Mediterr. Archaeol. Archaeom.* **2023**, *23*, 1–29.

[243] Rappenglück, B.; Hiltl, M.; Ernstson, K. Exceptional evidence of a meteorite impact at the archaeological site of Stöttham (Chiemgau, SE-Germany). In *Harmony and Symmetry: Celestial Regularities Shaping Human Culture. Proceedings of the SEAC 2018 Conference*; Draxler, S., Lippitsch, M.E., Wolfschmidt, G., Eds. Hamburg, 2020; pp. 116–125.

[244] Rappenglück, B.; Hiltl, M.; Ernstson, K. The Chiemgau impact: Evidence of a Latest Bronze Age/Early Iron Age meteorite impact in the archaeological record, and resulting critical considerations of catastrophism. In *Beyond Paradigms in Cultural Astronomy*; González-García, C., Frank, RM, Sims, LD, Rappenglück, MA, Zotti, G., Belmonte, JA, Šprajc, I., Eds. Oxford, 2021; pp. 57–64.

[245] Waldmann, G.; Herten, F.; Hiltl, M.; Ernstson, K. The Enigmatic Niederrhein (Germany) deposit: evidence of a middle-pleistocene meteorite impact strewn field. In *49th Annual Lunar and Planetary Science Conference*, 2018; pp. 1610.

[246] Ernstson, K.; Schulz-Hertlein, G.; Ernstson, T.; Poßekel, J. A Probable holocene meteorite impact crater strewn field in Lower Franconia (Germany): evidence from Digital Terrain Models and Geophysical Surveys (GPR, Electrical Imaging, Geomagnetics). In *Poster, Proceedings of the AGU Fall Meeting*, 2022.

[247] Ernstson, K.; Poßekel, J.; Kurtz, J. The Enigmatic Sachsendorf Bay structure (Oderbruch, Northeast Germany): evidence of a Pleistocene/Holocene Meteorite impact event. In *12th Planetary Crater Consortium Meeting*, 2021; Volume 12, pp. 2022.

[248] Ahokas, H. *Thirty-Three Previously Unknown Meteoritic Craters of Diameter from 5 to 100 m in Western Kouvola, Finland from a Swarm of Impactors in the Holocene*, Kave, 2023.

[249] Ernstson, K.; Molnár, M.; Poßekel, J. The Enigmatic Luzice (Czech Republic) Megablock and Melt Rock Megabreccia: Evidence of a Meteorite Impact Origin. *LPI Contrib.* **2023**, *2990*, 6059.

[250] Molnár, M.; Ventura, K.; Poßekel, J.; Ernstson, K. The Kolešovice 20 km-Diameter Structure (Czech Republic): Evidence of an Airburst Impact Crater. *LPI Contrib.* **2023**, *2806*, 1428.

[251] Tankersley, K.B.; Meyers, S.A.; Stimpson, D.I.; Knepper, S.M. Evidence for a Large Late-Holocene Strewn Field in Kiowa County, Kansas, USA. *Airburs. Crater. Imp.* **2023**, *1*, 20230005.

[252] Tankersley, K.B.; Meyers, S.D.; Meyers, S.A.; Jordan, J.A.; Herzner, L.; Lentz, D.L.; Zedaker, D. The Hopewell Airburst Event, 1699-1567 Years Ago (252-383 CE). *Sci. Rep.* **2022**, *12*, 1706, doi: 10.1038/s41598.022.05758.y.

[253] Bronikowska, M.; Artemieva, N.; Wünnemann, K. Reconstruction of the Morasko Meteoroid Impact—Insight from Numerical Modeling. *Meteorit. Planet. Sci.* **2017**, *52*, 1704–1721, doi: 10.1111/maps.12882.

[254] Schultz, P.H.; Harris, R.S.; Perroud, S.; Blanco, N.; Tomlinson, A.J.; Valenzuela, M. Late pleistocene fireballs over the Atacama Desert, Chile. In *50th Lunar and Planetary Science Conference*, 2019; Volume 50.

[255] Schultz, P.H.; Harris, R.S.; Perroud, S.; Blanco, N.; Tomlinson, A.J. Widespread Glasses Generated by Cometary Fireballs During the Late Pleistocene in the Atacama Desert, Chile. *Geology* **2022**, *50*, 205–209, doi: 10.1130/G49426.1.

[256] Andronikov, A.V.; Andronikova, I.E. Sediments from Around the Lower Younger Dryas Boundary (USA): Implications from LA-ICP-Analysis. *Geogr. Ann. A* **2016**, *98*, 221–236.

[257] Ballard, J.P.; Bijkerk, A.K. Quartz melt structures in European coversands may support Younger Dryas extraterrestrial impact hypothesis. In *UT Geography Research Symposium 2014 "Mapping Outside the Lines: Geography as a Nexus for Interdisciplinary and Collaborative Research"*, 2014.

[258] Bement, L.C.; Madden, A.S.; Carter, B.J.; Simms, A.R.; Swindle, A.L.; Alexander, H.M.; Fine, S.; Benamara, M. Quantifying the Distribution of Nanodiamonds in Pre-Younger Dryas to Recent Age Deposits Along Bull Creek, Oklahoma Panhandle, USA. *Proc. Natl. Acad. Sci. U. S. A.* **2014**, *111*, 1726–1731, doi: 10.1073/pnas.1309734111.

[259] Moore, C.R.; West, A.; LeCompte, M.A.; Brooks, M.J.; Daniel, I.R. Jr; Goodyear, A.C.; Ferguson, T.A.; Ivester, A.H.; Feathers, J.K.; et al. Widespread Platinum Anomaly Documented at the Younger Dryas Onset in North American Sedimentary Sequences. *Sci. Rep.* **2017**, *7*, 44031, doi: 10.1038/srep44031.

[260] Wolbach, W.S.; Ballard, J.P.; Mayewski, P.A.; Adedeji, V.; Bunch, T.E.; Firestone, R.B.; French, T.A.; Howard, G.A.; Israde-Alcántara, I.; Johnson, J.R.; et al. Extraordinary Biomass-Burning Episode and Impact Winter Triggered by the Younger Dryas Cosmic Impact ~12,800 Years Ago. 1. Ice Cores and Glaciers. *J. Geol*. **2018**, *126*, 165–184, doi: 10.1086/695704.

[261] Moore, A.M.T.; Kennett, J.P.; Napier, W.M.; LeCompte, M.A.; Moore, C.R. West, A. Abu Hureyra, Syria, Part 3: Comet Airbursts Triggered Major Climate Change 12,800 Years Ago that Initiated the Transition to Agriculture. *Airbursts and Cratering Impacts* **2023**, *1*, 1–24, doi: 10.14293/ACI.2023.0004.

[262] Moore, C.R.; Brooks, M.J.; Goodyear, A.C.; Ferguson, T.A.; Perrotti, A.G.; Mitra, S.; Listecki, A.M.; King, B.C.; Mallinson, D.J.; Lane, C.S.; et al. Sediment Cores from White Pond, South Carolina, Contain a Platinum Anomaly, Pyrogenic Carbon Peak, and Coprophilous Spore Decline at 12.8 ka. *Sci. Rep.* **2019**, *9*, 15121, doi: 10.1038/s41598.019.51552.8.

[263] Moore, C.R.; Brooks, M.J.; Hemmings, C.A.; Feathers, J.K. Geoarchaeological investigations at Wakulla Springs, Florida. Southeastern archaeological conference (SEAC). In *Proceedings of the 76th Annual Meeting, November 6-9*, 2019.

[264] Napier, W.M. Palaeolithic Extinctions and the Taurid Complex. *Mon. Not. R. Astron. Soc.* **2010**, *405*, 1901–1906, doi: 10.1111/j.1365.2966.2010.16579.x.

[265] Napier, W.M. The Hazard from Fragmenting Comets. *Mon. Not. R. Astron. Soc.* **2019**, *488*, 1822–1827, doi: 10.1093/mnras/stz1769.

[266] Smith, J.R.; Kleindienst, M.R.; Schwarcz, H.P.; Churcher, C.S. Kieniewicz, J.M.; Osinski, G.R.; Haldemann, A.F.C. Potential Consequences of a Mid-Pleistocene Impact Event for the Middle Stone Age Occupants of Dakhleh Oasis, Western Desert, Egypt. *Quat. Int.* **2009**, *195*, 138–149, doi: 10.1016/j.quaint.2008.02.005.

[267] van Ginneken, M.; Harvey, R.P.; Goderis, S.; Artemieva, N.; Boslough, M.; Maeda, R.; Gattacceca, J.; Folco, L.; Yamaguchi, A.; Sonzogni, C.; et al. The Identification of Airbursts in the Past: Insights From the BIT-58 Layer. *Earth Planet. Sci. Lett.* **2024**, *627*, 118562, doi: 10.1016/j.epsl.2023.118562.

[268] Koeberl, C. Libyan Desert Glass: Geochemical Composition and Origin. *Silica'96* **1997**, 121–131.

[269] Collins, G.S.; Melosh, H.J.; Marcus, R. Earth Impact Effects Program: A Web-based Computer Program for Calculating the Regional Environmental Consequences of a Meteoroid Impact on Earth.

Meteorit. Planet. Sci. **2005**, *40*, 817–840, doi: 10.1111/j.1945.5100.2005.tb00157.x.

[270] Clifton, J.R.; Davis, F.L. *Mechanical Properties of Adobe*; Department of Commerce, National Bureau of Standards, 1979; Volume 13.

[271] Torrealva, D.; Cerrón, C.; Espinoza, Y. Shear and out of plane bending strength of adobe walls externally reinforced with polypropylene grids. In *Proceedings of the 14th World Conference on Earthquake Engineering, Beijing*, 2008; pp. 12–17.

[272] Silveira, D.; Varum, H.; Costa, A.; Martins, T.; Pereira, H.; Almeida, J. Mechanical Properties of Adobe Bricks in Ancient Constructions. *Constr. Build. Mater.* **2012**, *28*, 36–44, doi: 10.1016/j.conbuildmat.2011.08.046.

[273] Zipf Jr, R.K.; Cashdollar, K.L. Effects of Blast pressure on structures and human body. In *Explosions and Refuge Chambers*, 2007; Volume 125 (NIOSH Docket).

[274] Aftosmis, M.J.; Mathias, D.L.; Tarano, A.M. Simulation-based Height of Burst Map for Asteroid Airburst Damage Prediction. *Acta Astronaut.* **2019**, *156*, 278–283, doi: 10.1016/j.actaastro.2017.12.021.

[275] Artemieva, N.A.; Shuvalov, V.V. From Tunguska to Chelyabinsk Via Jupiter. *Annu. Rev. Earth Planet. Sci.* **2016**, *44*, 37–56, doi: 10.1146/annurev.earth.060115.012218.

[276] Boslough, M. Computational modeling of low-altitude airbursts. In *AGU Fall Meeting Abstracts*, 2007; Volume 2007; pp. U21E-03.

[277] Boslough, M. Airburst Modeling. *First International Workshop on Potentially Hazardous Asteroids Characterization, Atmospheric Entry and Risk Assessment*, 2015.

[278] Collins, G.S.; Lynch, E.; McAdam, R.; Davison, T.M. A Numerical Assessment of Simple Airblast Models of Impact Airbursts. *Meteorit. Planet. Sci.* **2017**, *52*, 1542–1560, doi: 10.1111/maps.12873.

[279] Shuvalov, V.V.; Artemieva, N.A.; Kosarev, I.B. 3D Hydrodynamic Code SOVA for Multimaterial Flows, Application to Shoemakerlevy 9 Comet Impact Problem. *Int. J. Impact Eng.* **1999**, *23*, 847–858, doi: 10.1016/S0734.743X(99)00129.3.

[280] Baldwin, E.; Milner, D.; Burchell, M.; Crawford, I. Shock wave propagation and damage to the target in oceanic impact events. In *Bridging the Gap II: Effect of Target Properties on the Impact Cratering Process*, 2007; pp. 13–14.

[281] Baldwin, E.; Vocadlo, L.; Crawford, I. Validation of AUTODYN in replicating large-scale planetary impact events. In *36th Annual Lunar and Planetary Science Conference*, 2005; pp. 1380.

[282] Robertson, N.J.; Hayhurst, C.J.; Fairlie, G.E. Numerical Simulation of Explosion Phenomena. *Int. J. Comput. Appl. Technol.* **1994**, *7*, 316–329, doi: 10.1504/IJCAT.1994.062536.

[283] Saito, T.; Kaiho, K.; Abe, A.; Katayama, M.; Takayama, K. Hypervelocity Impact of Asteroid/Comet on the Oceanic Crust of the Earth. *Int. J. Impact Eng.* **2008**, *35*, 1770–1777, doi: 10.1016/j.ijimpeng.2008.07.046.

[284] Saito, T.; Kaiho, K.; Abe, A.; Katayama, M.; Takayama, K. Numerical Simulations of Hypervelocity Impact of Asteroid/Comet on the Earth. *Int. J. Impact Eng.* **2006**, *33*, 713–722, doi: 10.1016/j.ijimpeng.2006.09.012.

[285] Birnbaum, N.K.; Cowler, M.; Hayhurst, C. Numerical simulation of impact using AUTODYN. In *Proceedings of the 2nd International Impact Symposium; Beijing, China*, 1996.

[286] Deller, J.; Lowry, S.; Snodgrass, C.; Price, M.; Sierks, H. A New Approach to Modelling Impacts on Rubble Pile Asteroid Simulants. *Mon. Not. R. Astron. Soc.* **2016**, *455*, 3752–3762, doi: 10.1093/mnras/stv2584.

[287] Jones, A.P.; Price, D.G.; DeCarli, P.S.; Price, N.; Clegg, R. Impact decompression Melting: a possible trigger for impact induced volcanism and mantle hotspots? In *Impact Markers in the Stratigraphic Record*, Koeberl, C.; Martínez-Ruiz, F.C. Eds.; Springer: Berlin, Heidelberg, 2003; pp. 91–119, doi: 10.1007/978.3.642.55463.6_4.

[288] Nishizawa, M.; Matsui, Y.; Suda, K.; Saito, T.; Shibuya, T.; Takai, K.; Hasegawa, S.; Yano, H. Experimental Simulations of Hypervelocity Impact Penetration of Asteroids Into the Terrestrial Ocean and Benthic Cratering. *J. Geophys. Res. Planets* **2020**, *125*, e2019JE006291, doi: 10.1029/2019JE006291.

[289] Stickle, A.; Barnouin, O.S.; Bruck Syal, M.; Cheng, A.; El Mir, C.; Ernst, C.M.; Michel, P.; Oklay, N.; Owen, M.; Price, M.; AIDA Impact Simulation Working Group. et al. Impact simulation benchmarking for the double asteroid redirect test (DART). In *47th Annual Lunar and Planetary Science Conference*, 2016; pp. 2832.

[290] Wie, B.; Barbee, B.; Pitz, A.; Kaplinger, B.; Hawkins, M.; Winkler, T.; Premaratne, P.; Wagner, S.; Vardaxis, G.; Lyzhoft, J.; et al. *An Innovative Solution to NASA's NEO Impact Threat Mitigation Grand Challenge and Flight Validation Mission Architecture Development*, 2014.

[291] Caldwell, W.K.; Euser, B; Plesko, C.S.; Larmat, C.; Lei, Z.; Knight, E.E.; Rougier, E.; Hunter, A. Benchmarking Numerical Methods for Impact and Cratering Applications. *Appl. Sci.* **2021**, *11*, 2504, doi: 10.3390/app11062504.

[292] Birnbaum, N.; Cowler, M.; Itoh, M.; Katayama, M.; Obata, H. AUTODYN - An interactive non-linear dynamic analysis program for microcomputers through supercomputers. In *Transactions of the 9th International Conference on Structural Mechanics in Reactor Technology*, 1987; Volume B, pp. 1–4.

[293] Marcus, R.; Melosh, H.J.; Collins, G.S. Earth Impact Effects Program. Available online: https://impact.ese.ic.ac.uk/ImpactEarth/ImpactEffects/ (2004) (accessed April 2025).

[294] Silber, E.A.; Boslough, M.; Hocking, W.K.; Gritsevich, M.; Whitaker, R.W. Physics of Meteor Generated Shock Waves in the Earth's Atmosphere–A Review. *Adv. Space Res.* **2018**, *62*, 489–532, doi: 10.1016/j.asr.2018.05.010.

[295] Zhilyaev, B.; Petukhov, V.; Reshetnyk, V.; Vidmachenko, A. Meteor Colorimetry with CMOS Cameras. *arXiv preprint arXiv:2106.07403* **2021**.

[296] Alekseev, V.; Konkashbaev, I.; Konkashbaev, I. *Possible Explanation of Total Ablation of the 1908 Tunguska Asteroid*, 1998.

[297] Galli, P. Active Tectonics Along the Wadi Araba-Jordan Valley Transform Fault. *J. Geophys. Res. Solid Earth* **1999**, *104*, 2777–2796, doi: 10.1029/1998jb900013.

[298] Abed, A.M. An Overview of the Geology and Evolution of Wadi Mujib. *J. Nat. Hist.* **2017**, *4*, 6–28, doi: 10.13140/RG.2.2.33625.98406.

[299] Neev, D.; Emery, K.O. *The Destruction of Sodom, Gomorrah, and Jericho: Geological, Climatological, and Archaeological Background*, Oxford University Press, New York, NY, 1995.

[300] Frumkin, A.; Elitzur, Y. Historic Dead Sea level Fluctuations Calibrated with Geological and Archaeological Evidence. *Quat. Res.* *57*, 334–342 (2002), doi: 10.1006/qres.2002.2330.

[301] Kagan, E.J.; Langgut, D.; Boaretto, E.; Neumann, F.H.; Stein, M. Dead Sea Levels During the Bronze and Iron Ages. *Radiocarbon* **2015**, *57*, 237–252, doi: 10.2458/azu_rc.57.18560.

[302] Hennessy, J.B. Preliminary Report on a First Season of Excavations at Teleilat Ghassul. *Levant* **1969**, *1*, 1–24, doi: 10.1179/lev.1969.1.1.1.

[303] Gustafsson, Ö.; Bucheli, T.D.; Kukulska, Z.; Andersson, M.; Largeau, C.; Rouzaud, J.-N.; Reddy, C.M.; Eglinton, T.I. Evaluation of a Protocol for the Quantification of Black Carbon in Sediments. *Global Biogeochem. Cycles* **2001**, *15*, 881–890, doi: 10.1029/2000GB001380.

[304] Wolbach, W.S.; Gilmour, I.; Anders, E. Major Wildfires at the Cretaceous/Tertiary Boundary. *Geol. Soc. Am. Spec. Pap.* **1990**, *247*, 391–400, doi: 10.1130/SPE247.p391.

[305] Wolbach, W.S.; Lewis, R.S.; Anders, E. Cretaceous Extinctions: Evidence for Wildfires and Search for Meteoritic Material. *Science* **1985**, *230*, 167–170, doi: 10.1126/science.230.4722.167.

[306] Wolbach, W.S.; Gilmour, I.; Anders, E.; Orth, C.J.; Brooks, R.R. Global Fire at the Cretaceous-Tertiary Boundary. *Nature* **1988**, *334*, 665–669, doi: 10.1038/334665a0.

Appendix

A1. Geological context

The Middle Ghor is marked by a major tectonic boundary separating the Arabian and African Plates (Sinai-Palestinian subplate), running through the Gulf of Aqaba/Dead Sea/Jordan Valley region. The resulting Dead Sea Rift is a highly active pull-apart strike-slip fault with largely horizontal left lateral motion. For the past 15 million years, motion along the plate boundary has been in a north-south direction (Figure 1). Geological evidence indicates an average horizontal displacement rate of at least one cm per year along this fault system, producing a recurring cycle of strong earthquakes (M ≥7) approximately every 1400 years [297].

Exposed rock formations on the eastern slopes of the Jordan Valley near the Dead Sea shoreline are of late-Cambrian age (~500 Ma) and consist of ~300 m of brick-red, fluvial, quartz-rich sandstone [298]. These sediments are unconformably overlain by a basaltic sequence ~5 Myr in age. The eastern edge of the Jordan Valley contains an even younger sequence consisting of reddish conglomerates and laminated marls interlayered with gravels and sandstones. These, in turn, are capped by a Late Quaternary sequence of alluvial and colluvial sediments exposed on the valley floor on the eastern side of the Middle Ghor near TeH.

Lake Lisan, the precursor to the modern Dead Sea, began to fill about 80,000 years ago, reaching a maximum level of 170-185 mbsl by ~18,000 cal BP [299]. What remains of Lake Lisan is now known as the Dead Sea, landlocked and considered "dead" because of its hypersalinity at ~34 wt% salt. Consequently, the sea does not support higher organisms like aquatic plants and fish. During Middle Bronze Age I (MB I; ~2000-1800 BCE), rainfall was more plentiful than during MB II, and the level of the Dead Sea rose to about 370 mbsl, at least ~50 m higher than its current elevation of 430 mbsl. At that time, the eastern shore of the Dead Sea was likely several km closer to the [300]. Toward the end of MB II, the lake level dropped as low as 430 mbsl, as indicated by a windblown sand layer in Dead Sea sediment cores [300, 301].

A2. Human occupation of the Jordan Valley

Located in a generally arid region, the Jordan Valley is among the best-watered areas in the southern Levant (Jordan, Israel, and Palestine). In addition to numerous springs created by a disgorging Transjordanian aquifer, the area had hydrological conditions for human habitation somewhat analogous to the Nile Delta region, which is also bordered by arid terrain. The Middle Ghor near TeH supported a large human population. During MBA peak occupation, at least an estimated 50,000 people occupied three major cities, plus satellite towns, villages, and hamlets spread across ~400 km^2 of the eastern Kikkar [302].

The earliest significant human settlement in the Middle Ghor area was Tuleilat Ghassul near the northeast corner of the Dead Sea, ~5 km from TeH, initially settled during the Late Neolithic Period (>6600 cal BP). By the Chalcolithic Period (~6600-5500 cal BP), the inhabitants had developed considerable skill as pottery makers [302], and by the Early Bronze Age, the Middle Ghor was extensively settled at >100 separate locations.

The three largest settlements in this area were TeH, Tall Nimrin, and Jericho (aka, Tell Es-Sultan), urban anchors of three city-state clusters, each surrounded by numerous smaller satellite towns and villages. At 36 hectares of fortifications (0.36 km^2) and an additional 30 hectares of "suburban sprawl," TeH at its zenith was >4× larger than Tall Nimrin [186] and >5× larger than Jericho [197], and, thus, was likely to have been the area's politically dominant MBA urban center for many centuries [20, 21]. TeH was initially occupied during the early Chalcolithic Period (~6600 cal BP) and was a well-established fortified urban center by the Early Bronze Age (~5300 cal BP). The city reached its peak of hegemony during the MBA and dominated the eastern half of the Middle Ghor and, most likely, the western half as well. Then suddenly, the occupation of TeH ceased at ~1650 BCE (~3600 cal BP) at the end of MB II, followed by an enigmatic ~600-year occupational hiatus. The site was not substantially occupied again until much later in the Iron Age.

A3. Methods. All methods followed standard procedures

Optical photographs

For clarity, the authors of Bunch et al. [1], Silvia et al. [2], and this article often enlarged, cropped, and globally adjusted the photographs' contrast, brightness, and sharpness; they have not been otherwise altered. Most photographs of potsherds display a north arrow, or in other cases, N-S and E-W excavation string lines are visible, allowing us to establish a north direction. In the other cases, directionality was inferred using the time of day recorded in the metadata of the original photographs with sun-shadow software (https://app.shadowmap.org/) to determine the photograph's north compass direction, estimated to be accurate within approximately ± 25°.

Optical and electron microscopy

Samples were processed and analyzed using previously published protocol [63, 120, 123, 124]. After size-sorting with multiple screens (American Society for Testing and Materials) ranging from 4.75 mm to 53 µm, spherules and meltglass were examined using optical and electron microscopy. SEM-EDS analyses were conducted in low-vacuum mode using a JEOL-6000 SEM system and a ThermoFisher Apreo 2. Using SEM-EDS, we manually selected for detection of Fe, Ni, Mo, Ru, Rh, Pd, Os, Ir, and Pt, if present, with uncertainties of approximately ±100% for concentrations

<1.0 wt% and ±10% for larger concentrations. T.D.B., Gary Chandler, M.A.L, A.V.A., T.E.B., J.H.W., C.M., D.B., K.L., and A.W. performed measurements and analyses.

Shocked quartz analyses

(i) Sediment was treated with HCl to remove carbonates. **(ii)** Sedimentary grains were wet-sieved and sorted to ≥150 μm and ≤850 μm. **(iii)** Mixed grains were embedded in blue-tinted epoxy on 26 × 47 × 1 mm slides for better visibility; thin-sectioned to ~30 μm; and highly polished for microprobe analyses at Spectrum Petrographics http://www.petrography.com/ No cover slide was used. **(iv)** Next, the slides were etched by immersion for ~1-2 min in a 30% solution of hydrofluoric acid (HF) liquid or, alternately, exposed to HF vapor for ~1.5 min to dissolve amorphous quartz and make any lamellae more visible. The vapor produced more consistent results. **(v)** After treatment with liquid HF, we performed a dH_2O rinse; neutralized with 5% sodium carbonate solution; rinse with dH_2O again; and then treated with 5% HCl to remove carbonates. After treatment with HF vapor, we performed a dH_2O rinse. **(vi)** Candidate grains were identified on the polished slides using optical microscopy (transmitted light, reflected light, and epi-illumination under both plane and crossed polarization). **(vii)** The compositions of candidate grains were then investigated using SEM-EDS, and **(viii)** using a cathodoluminescence detector (CL). Analyses were performed on uncoated thin sections in low-vacuum mode on a ThermoFisher Apreo 2 SEM. CL Images were acquired at ~10 mm working distance using 10 kV and 3.2 nA of beam current, with 50 Pa of chamber pressure to balance charge. Individual images using red, blue, and green wavelength filters on the CL detector were acquired and composited to form the final CL images. **(ix)** Then, the relative angles of lamellae on candidate grains were measured using a Leitz universal stage mounted onto a Leitz polarizing microscope. The accuracy of U-stage measurements is estimated at ±5°. **(x)** Finally, the relative angles of lamellae to the c axis were compared to known crystallographic axes of quartz and plotted using a computer program, A.N.I.E, Automated Numerical Index Executor [104]. K.L., A.W., M.A.L., A.V.A., and T.E.B. performed analyses.

Electron microprobe analyses

Standard practices were followed for all samples investigated by electron microprobe. Selected samples of melted pottery were embedded in epoxy, mounted to 25 x 51 x 1 mm slides, and polished to a microprobe finish at a thickness of ~30 μm. Nelia Dunbar and T.D.B performed analyses.

Neutron activation analysis

Sediment samples were analyzed by ActLabs, Canada, using INAA to measure elemental abundances. For 56 elements, including Pt, Pd, and Au, along with LOI and salinity, bulk sediment samples of ~50 g each and magnetic fractions of ~1 g were analyzed using INAA, fire assay, and/or inductively coupled plasma mass spectrometry (ICP-MS) with a lower detection limit of 0.1 parts per billion (ppb). The accuracy of the laboratory results was verified with blanks and known standards.

Heating experiments

For the furnace experiments, a 26-mg powdered sample of unmelted TeH pottery was heated at 10°C/minute under argon purge using simultaneous Differential Scanning Calorimetry with Thermogravimetric Analysis (DSC-TGA). The cooled sample was investigated for signs of melting using optical microscopy. Experiments were performed by Allison Sikes, Bhavesh Patel, and M.P.

Remanent magnetism

Two pottery samples from TeH were weighed and affixed to a holder designed to measure the variation of the magnetization vector through stepwise laboratory-induced demagnetization in three perpendicular axes. The remanent magnetism instrument measures weak magnetic fields enabled by a superconducting quantum interference device containing Josephson junctions made by 2G Enterprises. The noise level of this instrument was 1e-8 A/m of the measured magnetic moment. The magnetic acquisition was acquired with pulse magnetizer ASC Model IM-10-30. G.K. performed the analyses.

Diamondoids and diamond-like carbon

A standard protocol for isolating nanodiamonds and other acid-resistant carbon species has been developed and used successfully at several dozen sites [31]. For this study, there was one modification: diamond-containing residues were treated with sulfuric acid following their extraction to dissolve gypsum ($CaSO_4 \bullet 2\, H_2O$) to release potentially encapsulated diamonds. Details can be found in **SI Figure S10** [7] and **SI Methods S1** [7]. Images were acquired using transmission electron microscopy (TEM). W.S.W. and J.K. conducted extractions.

Soot analyses

Soot carbon was extracted from sediment samples following a chemothermal oxidation procedure (CTO-375) [303]. Samples were demineralized sequentially at 0.2, 2, and 6N HCl until effervescence ceased and dried. Dried samples were manually ground in a mortar and pestle to fine dust and then thermally oxidized in a muffle furnace. The furnace was set to a 24-hour cycle, with 6 hours to ramp the temperature up to 375°C, where it was held for twelve hours, followed by a six-hour cool-down period. The isolated residue is operationally defined as soot. Soot samples were ground using a mortar and pestle and then gravimetrically placed in small tin capsules sent to the UC Davis Stable Isotope Facility to quantify carbon abundance and its stable isotopic signature. S.M. and A. M-B conducted experiments.

Aciniform carbon (AC)

A standard protocol was used to extract AC/soot from bulk sediment [31, 221, 260, 304–306]. The process consists of multiple steps: (1) demineralization through multiple treatments of hydrofluoric acid (HF) and hydrochloric acid (HCl); (2) oxidation to separate organic material from elemental carbon using acidic potassium dichromate; (3) SEM analysis to differentiate between AC/soot and non-soot carbon; and (4) examination of micrographs to quantify soot vs non-soot carbon abundances using particle size analysis. W.S.W. and J.K. conducted experiments.